

---

**PLASMA PROCESSING STUDIES  
WITH APPLICATION TO  
CARBON NANOTUBE  
FLUORINATION**

---



A dissertation submitted by  
**Anders Barlow**

for the degree of  
**Doctor of Philosophy**

School of Chemical and Physical Sciences  
Flinders University

OCTOBER 2011



---

# DECLARATION

I certify that this thesis does not incorporate without acknowledgment any material previously submitted for a degree or diploma in any university; and that to the best of my knowledge and belief it does not contain any material previously published or written by another person except where due reference is made in the text.

---

**Anders Jack Barlow**  
**October 2011**



---

## SUMMARY

The fluorination and growth of carbon nanotubes using plasma is a possible means towards controlling their properties. To develop a deeper understanding of these processes, a series of fundamental experiments were performed that studied sulphur hexafluoride ( $\text{SF}_6$ ) plasma, its exposure to carbon nanotubes and finally the growth of nanotubes within a plasma environment. Plasma was characterised using a single cylindrical Langmuir probe, while carbon nanotube modification and growth treatments were studied using X-ray photoelectron spectroscopy, Raman spectroscopy and electron microscopy. Methods that allowed the fluorination and growth of nanotubes with desired properties are discussed.

Using an established Langmuir probe apparatus, plasma ignited within sulphur hexafluoride was characterised. Initially, a curious instability was observed within the main plasma density that oscillated with a frequency of ten's of Hertz. This instability was characterised with respect to experimental parameters such as applied power, gas pressure and probe position within the plasma chamber. From this research the instability is hypothesised to manifest as a wave that moves radially throughout the chamber from the plasma source with a speed of  $\sim 16 \text{ ms}^{-1}$ . The instability interfered with Langmuir probe experiments by inducing fluctuations in the measured probe currents. The experiment was refined to account for this interference and allow the characterisation of the plasma with respect to experimental parameters.

The electron density within  $\text{SF}_6$  plasma was observed to increase with absorbed rf power. Only marginal variations were observed with gas pressure. Typical densities were found to be  $\sim 10^8 \text{ cm}^{-3}$ . Ion densities display a stronger dependence on the gas pressure in comparison with rf power and overall were significantly greater than that of the electron density,  $\sim 10^9 \text{ cm}^{-3}$ , despite the assumption that plasma maintains quasineutrality. This is attributed to the strong electronegativity of the  $\text{SF}_6$  molecule. The space potential of  $\text{SF}_6$  plasma remained largely constant irrespective of applied rf power and gas pressure, while the floating potential is found to decrease with increasing power and pressure. For most  $\text{SF}_6$  plasma the electron temperature is found to remain constant across the powers studied, although for high pressures the presence of a second population of high temperature electrons is observed.

---

Single-walled carbon nanotubes were exposed to sulphur hexafluoride plasma resulting in the attachment of fluorine moieties to the structures. Initial analysis found that smaller diameter nanotubes result in greater levels of functionality. Nanotubes with metallic band structure are also observed to show a greater susceptibility to the plasma fluorination mechanism. By varying the absorbed rf power the extent of these functionalities could be tuned, with a general increase in fluorination as power was increased. The oxygen content on the nanotube surfaces acted to interfere with the fluorination mechanism whereby increased oxygen content at the surfaces prior to a treatment resulted in a greater amount of fluorine attachment after exposure. This observation was then used to develop another level of control over the fluorination mechanism. Sulphur hexafluoride plasma containing low amounts of either oxygen or water vapour produce much greater levels of functionality. The cause of this was elucidated as an enhanced breakdown of the parent sulphur hexafluoride molecule resulting in a greater concentration of reactive fluorine ions in the plasma and thus greater reactivity overall.

Pure sulphur hexafluoride plasma resulted in carbon-fluorine bonding at the nanotube surface that was a mixture of covalent and semi-ionic types, thereby decreasing the overall quality of the functionalised sites. Through the addition of oxygen, either into the plasma or at the nanotube surface via pretreatments, the relative amounts of covalent and semi-ionic bonding could be tuned. Pretreatments using oxygen plasma result in almost purely covalent carbon-fluorine bonds.

The plasma chamber was modified to enable the growth of carbon nanotubes from mixed methane/argon plasma. The resultant nanotube growth displayed predominantly single-walled nature with very high homogeneity. The yield was very low however, with the nanotubes hypothesised to be very short in length. The variation of experimental parameters, such as time and temperature, afforded the growth of nanotubes with tailored diameters. Through Raman spectroscopy a transition from single- to multi-walled growth was observed to occur with increasing growth time and decreasing growth temperature. For temperature this is explained through a decrease in the energy of growth species at the catalytic sites and thus insufficient energy for the formation of single-walled nanotubes. The transition observed for growth time is explained through the enhanced etching of the smaller diameter nanotubes by plasma species, an effect that the larger multi-walled nanotubes could withstand for longer periods of time.

---

# CONTENTS

Declaration .....	iii
Summary .....	v
Contents .....	vii
Acknowledgements .....	xi
Publications .....	xiii
<b>Chapter 1. ....</b>	<b>1</b>
Introduction .....	1
1.1. Nanotechnology and Nanotubes .....	2
1.2. The Single-Walled Carbon Nanotube.....	5
1.3. Plasma Processing .....	13
1.4. Aim and Scope of this Research.....	22
<b>Chapter 2. ....</b>	<b>25</b>
Experimental .....	25
2.1. The rf Induction Plasma Reactor .....	25
2.2. Langmuir Probes.....	29
2.3. Surface Characterisation Techniques.....	33
2.4. Preparation of Samples .....	48
2.5. Plasma Surface Modification.....	49
<b>Chapter 3. ....</b>	<b>53</b>
Preliminary Langmuir Probe Diagnostics of rf Plasma.....	53
3.1. I-V Characteristic Curves .....	53
3.2. Electrostatic Probe Theory .....	55
3.3. Understanding the Langmuir Probe Experiment: N <sub>2</sub> Plasma .....	59
3.4. Langmuir Probe Characterisation: Application to SF <sub>6</sub> Plasma.....	66
<b>Chapter 4. ....</b>	<b>69</b>
The Characterisation of SF <sub>6</sub> Plasma .....	69
4.1. Fluctuations in Probe Current.....	69
4.2. Dependence on Experimental Conditions.....	73
4.3. Spatial Distribution.....	79
4.4. Previous Literature on SF <sub>6</sub> Plasma Instabilities.....	87
4.5. Effect on Sample Functionalisation.....	92
4.6. Refinement of the Langmuir Probe Experiment.....	93
4.7. Langmuir Probe Characterisation of SF <sub>6</sub> Plasma .....	95
4.8. Summary of Langmuir Probe Studies.....	105

---

<b>Chapter 5.....</b>	<b>107</b>
Fluorination of Carbon Nanotubes.....	107
5.1. X-ray Photoelectron Spectroscopy.....	107
5.2. Transmission Electron Microscopy.....	117
5.3. Raman Spectroscopy.....	119
5.4. The Plasma Fluorination of Carbon Nanotubes.....	127
5.5. Summary of the Plasma Fluorination of CNTs.....	137
<b>Chapter 6.....</b>	<b>139</b>
Synchrotron Studies of Fluorinated Nanotubes I - SXR187: Round 2 2008.....	139
6.1. Introduction.....	139
6.2. Synchrotron XPS Studies of Fluorinated SWCNTs.....	143
6.3. Summary of Synchrotron Studies I.....	161
<b>Chapter 7.....</b>	<b>163</b>
Synchrotron Studies of Fluorinated Nanotubes II - FI2751: Round 2 2010.....	163
7.1. Introduction.....	163
7.2. Quantification of PES Results at Varying Excitation Energy.....	167
7.3. Fluorination in the Presence of Oxygen.....	169
7.4. Summary of Synchrotron Studies II.....	181
<b>Chapter 8.....</b>	<b>183</b>
PECVD Growth of Carbon Nanotubes.....	183
8.1. Introduction.....	183
8.2. Experimental Design.....	186
8.3. PECVD Growth of Carbon Nanotubes.....	189
8.4. Patterned Growth of SWCNTs.....	205
8.5. Summary of PECVD Nanotube Growth Studies.....	209
<b>Chapter 9.....</b>	<b>211</b>
Conclusion.....	211
9.1. Key Outcomes.....	211
9.2. Future Work and Recommendations.....	214
<b>References.....</b>	<b>217</b>
<b>Appendix A.....</b>	<b>231</b>
Ancillary Information for Langmuir Probe Studies.....	231
A.1. Derivation of Electrostatic Probe Theory.....	231
A.2. Mean Free Path Calculations and the Debye Length.....	239
A.3. RF Compensation.....	241
<b>Appendix B.....</b>	<b>243</b>

---

---

Ancillary Information for XPS Studies .....	243
B.1. Calibration of the Binding Energy Scale .....	243
B.2. The Dependence of XPS Peak Positions on Photon Energy .....	247
B.3. XPS Peak Widths .....	250
B.4. XPS Peak Curve Fitting .....	255
<b>Appendix C. ....</b>	<b>261</b>
Calculation of Atomic Sensitivity Factors for sXPS .....	261
C.1. Photoelectron Intensity .....	261
<b>Appendix D. ....</b>	<b>267</b>
XSpec: Data Acquisition Software for the LHS-10 at Flinders .....	267
D.1. The XSpec Front Panel and its Operation .....	268
<b>Appendix E. ....</b>	<b>273</b>
Units, Symbols and Abbreviations .....	273
E.1. Units .....	273
E.2. Symbols .....	274
E.3. Abbreviations .....	275



---

## ACKNOWLEDGEMENTS

I endured the highs and lows of PhD candidature alongside many of my peers. As I was writing this dissertation it was interesting to note the many different interpretations of what made a PhD thesis. Naturally everyone had different ideas about the body of the dissertation; from reference styles to page layouts, but it was *this* section that seemed to draw the greatest contrast in opinion. Personally, I felt it to be an opportunity to give thanks, not just to those who offered scientific input throughout my research, but also to those who have supported me through motivation, inspiration and compassion.

Before all else, I must thank my supervisor, Jamie Quinton. From the outset you guided me into an ideal project that was both engaging and novel. Although we never anticipated the troubles we faced during my candidature, and I know that you would never wish such problems upon any student, I am fairly certain that without those hard times I would not have the confidence that I now carry. You instilled upon me knowledge, experience, and patience. But most of all you taught me to be a careful scientist, to think before I act, and to make sure I consider all possibilities before arriving at a conclusion. Although my candidature was not as fruitful as it could have been with a working instrument, there is no doubt in my mind that my training was anything less than the most worthwhile experience of my life to date. I must also thank you for supporting me financially during the final stages of my candidature. Without that support I honestly do not know if I would have been successful.

Thank you to my co-supervisor, Joe Shapter. We didn't spend a tremendous amount of one-on-one time during my PhD, but any contact we did have regarding my work was always productive. Even if you weren't aware, you helped strengthen my scientific and critical thought process, and gave me the motivation to aim higher than I otherwise would.

The Smart Surface Structures Group at Flinders is an ensemble of fantastic scientific minds. Every time I would stand in front of the group to give a talk about my work I always came out inspired and motivated and often with new ideas to test. The group provided companionship and a great sense of camaraderie, especially when on conference trips where the downtime together was essential to surviving a PhD intact. To the entire group, including the many peers who have come and gone over the years, thank you.

---

There are some specific names from the group I must acknowledge. Cameron Shearer provided the oxidised and cut CNT samples that were part of the 2010 study at the Australian Synchrotron. While the PECVD research was in the back of my mind for a long time during my candidature, the research of Mark Bissett on carbon nanotube photovoltaics became the final push to attempt to grow CNTs and I am certainly glad we did. The 2008 synchrotron trip was exhausting as I was alone almost the entire time. In 2010 however, myself, Jamie, and two peers Adam Blanch and Ashley Slattery arrived at the synchrotron *en masse* to perform research into nanotube fluorination. To all of you, thank you for dedicating some of your precious time to my work, we couldn't have achieved what we did if we hadn't worked so well together as a team. Chris Gibson managed the Raman instrument used in this work and as such trained me and imparted as much of his knowledge as he could, so thank you Chris. Thank you also to Alec Deslandes. Not only did you show that it was in fact possible to complete a PhD, by doing so right in front of me, you have always provided a different level of insight into my research, especially with the Langmuir probe work. I am extremely grateful.

There is also a myriad of support staff I must acknowledge. Thank you to the Electronics and Mechanical Workshops in the School of Chemical and Physical Sciences. Specifically Bill Drury, Wayne Peacock, Mark Ellis, Mike Mellow, Bob Northeast and Chris Price. Throughout all the troubles we had with the XPS, each and every one of you were willing to drop things at a moment's notice to provide assistance. We would never have the LHS in such fine working order without your help. Thank you to Bruce Cowie, Lars Thomsen and Anton Tadich of the soft X-ray beamline at the Australian Synchrotron. Your assistance during our research was invaluable. On an official note I must also thank the Australian Synchrotron Research Program for funding assistance during each of our trips.

To all my friends and family, thank you. You have provided me with friendship and compassion for the duration of my candidature, even if I was somewhat of a hermit towards the end. I am eternally grateful. To my mum and grandmother, thank you for always being there for me and for pitching in whenever possible, I love you both.

And finally, to Kate, thank you for dealing with me through this the final stage in my education. Thank you for putting up with my rollercoaster emotions, and loving me regardless. I know that it has been equally hard on you as it has me, especially while I was writing this dissertation, but I could never have survived without you. I love you.

---

# PUBLICATIONS

The following is a list of publications made during the author's candidature resulting from work either directly related to the research herein or performed as a result of the research.

## *Journal Articles*

**Barlow, A.J.**, Deslandes, A. and Quinton, J.S., Langmuir Probe Characterization of Low-Frequency Oscillations in Radio-Frequency SF<sub>6</sub> Plasma. *Plasma Sources Sci. Technol.*, **20**, 065011 (2011).

Bissett, M.A., **Barlow, A.J.**, Shearer, C., Quinton, J.S. and Shapter, J.G., Carbon Nanotube Modified Electrodes for Photovoltaic Devices. *Carbon*, doi:10.1016/j.carbon.2012.01.065 (2012).

Bissett, M.A., **Barlow, A.J.**, Shapter, J.G. and Quinton, J.S., Transition from single to multi-walled carbon nanotubes grown by inductively coupled plasma enhanced chemical vapor deposition. *J. Appl. Phys*, **110**, 034301 (2011).

Quinton, J.S., Deslandes, A., **Barlow, A.J.**, Shapter, J.G., Fairman, C., Gooding, J., & Hibbert, D.B., RF Plasma Functionalized Carbon Surfaces for Supporting Sensor Architectures. *Curr. Appl. Phys.*, **8**, 376-379 (2008).

## *Refereed Conference Proceedings*

Bissett, M. A., **Barlow, A. J.**, Shapter, J. G., Quinton, J. S., Raman Characterisation of Carbon Nanotubes Grown by Plasma Enhanced Chemical Vapour Deposition. *Materials Science Forum*, **700**, 112-115 (2011).

**Barlow, A.J.** and Quinton, J.S., Radio Frequency SF<sub>6</sub> Plasma Modified Single-Walled Carbon Nanotubes: Synchrotron Spectroscopy and Plasma Characterisation Studies, *International Conference on Nanoscience and Nanotechnology, 22-26 February, Sydney Australia* (2010).

**Barlow, A.J.** and Quinton, J.S., Synchrotron Soft X-ray Studies of Single-Walled Carbon Nanotubes Functionalized by Radio-Frequency SF<sub>6</sub> Plasma. *AIP Conference Proceedings*, **1151**, 21-24 (2009).

**Barlow, A.J.**, Shapter, J.G., & Quinton, J.S., Fluorinated carbon surfaces using radio frequency plasma modification. *Proceedings of the 18th Biennial Australian Institute of Physics Congress*, 85-88 (2008).



---

## Chapter 1.

# INTRODUCTION

The ignition of a gaseous species into the plasma state produces a reactive environment capable of modifying surfaces and structures.<sup>1</sup> Plasma affords the use of low reactant volumes compared to many wet-chemical techniques, with the additional benefit of a clean, low-pressure regime. The relative ease of scalability to industrial sizes means that such processes could enable the large-scale production of future nanoscale devices. Carbon nanotubes (CNTs) are a material that shows promise for the manufacturing of such devices. CNTs display fascinating properties although their suitability towards the development of future devices and materials hinges on the ability to controllably produce, functionalise and tune their properties to suit a given application. The attachment of fluorine species to CNTs is one possible route towards this goal of nanoscale ‘building blocks’.<sup>2</sup> Through the application of fluorine-rich plasma to the surface modification of nanotubes, controllable CNT functionality could be achieved. Moreover, the plasma state can also be employed to controllably grow CNTs themselves. Before they can be successfully employed however, a greater level of understanding surrounding these processes is necessary. This requires knowledge of how the plasma behaves under certain experimental conditions through detailed characterisation, thus elucidating ways in which the plasma environment can be tailored to provide the most desirable CNT material.

## 1.1. Nanotechnology and Nanotubes

The advent of the electron microscope in the 1930's, along with subsequent developments over the decades that followed, gave scientists the capability to view the world on a scale that had not as-yet been seen. Much of the motivation for this work stemmed from a desire to image individual cells, which exist on micrometre scales, and viruses, which exist on sub-micrometre scales (tens to hundreds of nanometres).<sup>3</sup> The ability to view these fundamental structures began a rapid development in understanding that continues onward in modern medicine. The ability to view the world on such a small scale led to a lecture by Physicist and Nobel Laureate Richard Feynman to the American Physical Society in 1959, where he posed a multitude of possibilities related to using these new abilities to manipulate the very 'building blocks' of the universe; namely atoms.<sup>4</sup> This lecture was titled "There's Plenty of Room at the Bottom", a statement suggesting that conventional 'top-down' approaches to solving problems may be superseded by the unconventional, and not yet realised, 'bottom-up' approach, a regime where gravity may no longer be important and instead, surface tension and Van der Waals forces are dominant. In 1981, Binnig and Rohrer, while at IBM, advanced the original ideas of the 'Topografiner' (a scanning field emission microscope) first demonstrated in the early 1970s by Russell Young (at the National Bureau of Standards, now NIST, MD, USA). They demonstrated that the world could indeed be viewed at such a small scale with the development of the scanning tunnelling microscope (STM), a feat which earned them the Nobel Prize in Physics in 1986 alongside Ernst Ruska for his work with electron microscopy.<sup>5</sup> For the first time, a surface of silicon was viewed with atomic resolution, allowing individual atoms and even their interactions to be imaged. In 1989 Don Eigler, also at IBM, demonstrated the direct manipulation of atoms for the first time, where he was able to construct the letters of his employer using 35 xenon atoms using an STM. This work demonstrated the capability of such an instrument, and truly showed that the 'bottom-up' approach could be realised better than ever before, earning him the Kavli Prize for Nanoscience in 2010 alongside Nadrian Seeman.<sup>6</sup> This new level of technology on the nano-scale, i.e. a length scale of  $10^{-9}$  metres, spawned the field of science now known as Nanotechnology. While Eigler demonstrated the practical manipulation of atoms and potentially the birth of Nanotechnology, Feynman's lecture should be considered the initial inspiration for these developments and perhaps even the seed for the idea itself. Contemporary Nanotechnology

covers a broad range of disciplines, but the fundamental concept remains the same; the manipulation of nanoscale materials with nanometre level precision.

While Binnig, Rohrer and Eigler were investigating the application of scanning probe techniques, simultaneous discoveries were made during the middle 1980s and early 1990s that brought Nanotechnology further into the spotlight. In 1985, in *Letters to Nature*, Harold Kroto and others presented time-of-flight mass spectrometry results from laser ablated graphite discs. Prominent peaks in the spectra were observed at masses related to species consisting of 60 and 70 carbon atoms. The lower mass species was concluded to be from a unique aromatic molecule of formula  $C_{60}$  with a structure likened to that of a soccer ball; a truncated icosahedron with 60 vertices, 12 pentagonal and 20 hexagonal faces. From the work of Richard Buckminster Fuller with geodesic domes, the authors named the new material the Buckminsterfullerene and Harold Kroto, Robert Curl and Richard Smalley won the 1996 Nobel Prize in Chemistry for their discovery.<sup>7</sup>

In 1991 an article published in *Letters to Nature* by Sumio Iijima of NEC, and simultaneous *Nature* publications in 1993 by Iijima and Donald Bethune of IBM, documented other members of the fullerene family.<sup>8-10</sup> These structures were observed to be tubes of carbon capped with what were essentially half of the  $C_{60}$  molecule, discovered years earlier. From transmission electron micrographs the tubes in 1991 were observed to have multiple walls and in 1993 tubes were observed with a single wall. These species came to be known as the multi- and single-walled carbon nanotubes (MWCNTs and SWCNTs) respectively. From electron diffraction experiments, Iijima determined the tubes to be constructed from carbon in a manner analogous to taking a single or multiple sheets of the graphite lattice (known as graphene) to form a tube as depicted in figure 1.1. In the single-walled case the nanotubes were reported to have diameters as small as 0.7 nm by Iijima, although a broad range of diameters were found up to ~1.6 nm. Bethune reported a more consistent diameter distribution of ~1.2 nm. In each case the nanotubes were observed to have lengths far exceeding their diameter, with maxima reported by Iijima to be 700 nm and by Bethune to be in the order of microns.

There is an interesting point of contention among the scientific community regarding who should be credited for the discovery of carbon nanotubes. In scientific literature surrounding the study of carbon nanotubes it is not uncommon to find some variant of the phrase; “since their discovery in 1991 by Iijima”, and indeed a literature search using this

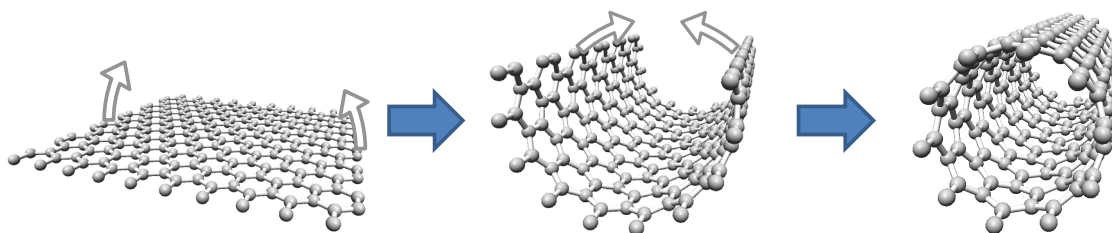


**Figure 1.1. A visualisation of the formation of a single-walled carbon nanotube via the rolling of a graphene sheet.**

exact phrase gives a great number of results. Monthioux, in a guest editorial for the journal *Carbon* in 2006, presented evidence and literature to suggest that very small fibres consisting purely of carbon may have been produced as early as 1889 through the decomposition of methane.<sup>11</sup> However it was not until the emergence of electron microscopy techniques that it was possible for scientists to view fibres on a small enough scale to deem them ‘nano-sized’. Monthioux revisited literature from Russian scientists Radushkevich and Lukyanovich in 1952 showing transmission electron micrographs of carbon fibres with diameters  $\sim 50$  nm.<sup>11,12</sup> Thus the first discovery of multi-walled carbon nanotubes could potentially be credited to that work. Nevertheless, the author reinforced that while the discovery of multi-walled CNTs may have been much earlier than Iijima’s 1991 article, it was this paper that spurred the enormous amount of current research around these structures. The author also stressed that the discovery of *single*-walled CNTs should unequivocally be credited to Iijima and Bethune.

The realisation of the potential of single-walled carbon nanotubes was seemingly immediate. Independent theoretical calculations by Mintmire and Hamada in 1992 showed that SWCNTs could behave electrically as either a semiconductor or a metal depending on the adopted physical structure, i.e. the way the graphene was ‘rolled’.<sup>13</sup> The structures displayed a property known as ballistic transport, whereby electrons could travel along the tube length without scattering, and thus with no heat loss. As a result, the current carrying capacity of SWCNTs has been shown to be as high as  $10^9$  A.cm<sup>-2</sup>, proclaimed to be as much as  $10^3$  times greater than that of noble metals.<sup>14,15</sup> Since the electronic structure could be tuned to behave as desired, CNTs quickly became prime candidates for molecular and nanoelectronic devices. Additionally, this electronic flexibility was coupled to a structure with incredible mechanical resilience. Due to their seamless graphite sidewalls, carbon nanotubes were found to have Young’s moduli, a measure of material stiffness, in the order of a few TPa (note that steel is commonly  $\sim 0.2$  TPa).<sup>16</sup> Other work has also shown that the

structures could be repeatedly buckled and deformed through large angles without failure.<sup>17</sup> With all of these properties in mind it is thus no wonder that carbon nanotubes have garnered much attention from many research groups around the world.

## 1.2. The Single-Walled Carbon Nanotube

### 1.2.1. The Structure of Carbon Nanotubes

Carbon nanotubes are commonly visualised as sheets of graphene rolled to form a tubular structure. Although this is not the way in which they are formed it is a useful explanatory tool and enables one to draw comparisons between the other forms of carbon and nanotubes. Carbon has two natural crystalline structures; graphite and diamond. The hybridisation of the electronic orbitals for each of these structures differs however, with graphite consisting of  $sp^2$ , and diamond  $sp^3$  carbon. In pristine graphite, each carbon atom is bonded to three other carbon atoms through  $\sigma$  bonds, with a bond length of 1.42 Å. This results in a trigonal planar arrangement with an angle of  $120^\circ$  between each neighbouring atom in the hexagonal lattice. There exists a delocalised  $\pi$  orbital with a pair of lobes out-of-plane from the graphite lattice.<sup>18,19</sup> This arrangement within a carbon lattice is highlighted in figure 1.2(a). Each layer within graphite is atomically flat, meaning that the  $\pi$  orbitals are normal to the surface and parallel to each other. In graphite, the  $\pi$  orbitals are responsible for weak interlayer Van der Waals forces. The properties of the sidewalls of a single-walled CNT mimic those of a graphene sheet and accordingly, an ideal SWCNT consists of all  $sp^2$  carbon atoms in a hexagonal arrangement with  $\pi$  orbitals protruding normal to the nanotube axis. Multi-walled CNTs consist of multiple tubes of varying diameter arranged concentrically to produce a layered structure.

The ‘rolling’ of the graphene sheet is not limited to a single possible arrangement and many of the fascinating properties of CNTs arise due to variations in the structure.<sup>20,21</sup> Figure 1.2(b) shows a single sheet of graphene upon which two vectors  $\mathbf{a}_1$  and  $\mathbf{a}_2$  have been defined. These vectors correlate directly to the atoms in the hexagonal lattice through the relations

$$\mathbf{a}_1 = \left(\frac{\sqrt{3}}{2}, \frac{1}{2}\right) a \quad \text{and} \quad \mathbf{a}_2 = \left(\frac{\sqrt{3}}{2}, -\frac{1}{2}\right) a$$

where  $a$  is commonly  $\sqrt{3}$  times the C-C bond length in graphite.<sup>20</sup> It should be noted that due to strain induced by tube curvature an elongation of the C-C bond length is observed. As such, in place of the graphite C-C bond length a slightly larger value of 1.44 Å is found

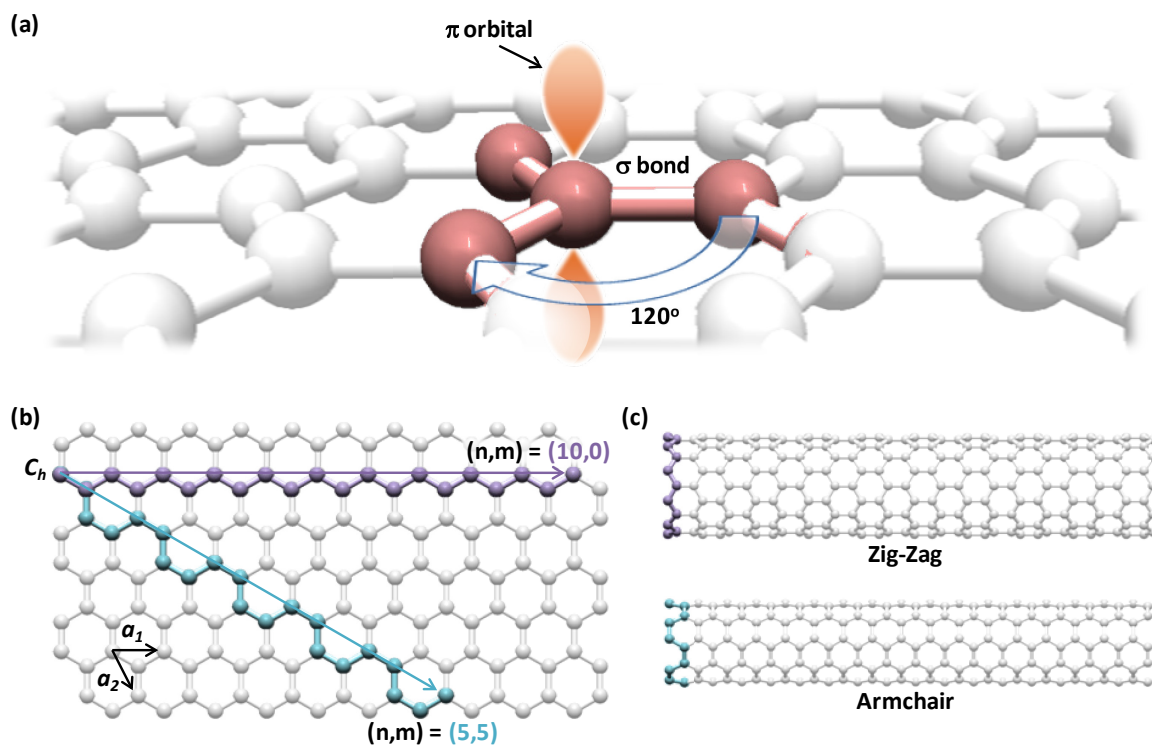


**Figure 1.2.** (a) The arrangement of carbon atoms in the hexagonal lattice of graphene with bond types and angles noted and (b) a representation showing how graphene may be rolled along the arrows to produce different types of single-walled carbon nanotubes (modified from Dresselhaus).<sup>20</sup> Although the sheet may be rolled so that any ‘chirality’  $(n,m)$  is possible, the two limiting cases of ‘Zig-Zag’  $(n,0)$  and ‘Armchair’  $(n,n)$  are shown in (c).

to be a better approximation for carbon nanotubes.<sup>22</sup> When describing nanotube geometry a third vector is defined along which the graphene sheet is rolled to produce the CNT. This is known as the chiral vector,  $\mathbf{C}_h$ , and is represented by a linear combination of the vectors  $\mathbf{a}_1$  and  $\mathbf{a}_2$  such that

$$\mathbf{C}_h = n\mathbf{a}_1 + m\mathbf{a}_2$$

where  $n$  and  $m$  are integers. This vector is also known as the ‘roll-up’ vector since it indicates the direction in which the sheet is rolled. This quantity alone entirely describes the carbon nanotube structure, with the exception of the nanotube length. The integer pair  $(n, m)$  becomes the ‘chiral assignment’ for a given nanotube. To demonstrate this, overlaid onto the graphene sheet in figure 1.2(b) are two chiral vectors with assignments of  $(10,0)$  in purple and  $(5,5)$  in blue. The nanotubes that result from these chiral vectors are given in figure 1.2(c) where the colour coded atoms in the sheet relate to those in the nanotube structure. The assignments presented here were chosen specifically because they demonstrate the two limiting cases of nanotube structure. The angle  $\theta$  defined relative to the vector  $\mathbf{a}_1$  is known as the chiral angle. In the  $(10,0)$  case  $\theta = 0^\circ$  while in the  $(5,5)$  case

$\theta = 30^\circ$ . Due to the way in which each of the vectors and the angles between them are defined the chiral angle can always be found within the range  $0^\circ \leq \theta \leq 30^\circ$ .<sup>20</sup> Nanotubes that result from each of these limiting cases are named the Zig-Zag and Armchair nanotubes respectively. Note that the nomenclature arises from the pattern created by the carbon atoms around the circumference. Any nanotube defined by a chiral vector with an angle between  $0^\circ$  and  $30^\circ$  is labelled as a Chiral (or alternatively Helical) nanotube.<sup>20</sup> This can be further generalised by using the chiral assignments. That is, all nanotubes where  $(n,m) = (j,0)$  will be Zig-Zag and those where  $(n,m) = (j,j)$  will be Armchair ( $j$  is an integer) with all others Chiral.<sup>23</sup>

The chiral assignment can also be used to determine the electronic structure of a given carbon nanotube. Although this has important implications towards the design of future devices, it is beyond the scope of this thesis and will only be mentioned here in brief.

It has been mentioned already that depending on the way in which the graphene is rolled, i.e. the chiral vector, a nanotube can display metallic or semiconducting band-structure. Additionally, the band-gap in the semiconducting case is variable, giving a small or large band-gap. In general it can be shown that all  $(n,n)$  nanotubes are metallic, while  $(n,m)$  nanotubes with  $n - m = 3j$  are small-gap semiconductors and those with  $n - m = 3j \pm 1$  are large-gap semiconductors.<sup>23</sup> This level of control is extremely desirable for nanoscale electronics where semi-conductors with very specific electronic structure would be useful. A method for reliably producing a single type of nanotube however is still yet to be achieved although extensive research continues.<sup>24</sup>

### 1.2.2. Reactivity of Carbon Nanotubes

Graphite is a particularly stable form of carbon. It follows that pristine carbon nanotubes are also quite resistant to chemical attack.<sup>25</sup> That said, they are not inert structures and some level of reactivity exists due to inherent nanotube curvature.<sup>2</sup> Multiple reviews on the covalent surface chemistry of CNTs have been published with extensive literature surveys<sup>2,25-30</sup> and the intention is not to reproduce that here, except to point out some of the key phenomena observed that lead to CNT reactivity and help to explain some observed results later in this dissertation.

Given that the nanotube can be formed by the rolling of a graphene sheet, then it is somewhat intuitive to realise that the bonds between the  $sp^2$  hybridised carbon atoms must

undergo some level of strain due to the curvature of the tube. In effect this forces the carbon atoms away from the ideal trigonal planar arrangement that is found in graphite. This results in curvature induced ‘pyramidalisation’ of the carbon atoms, an effect demonstrated in the left side of figure 1.3. By curving the graphene lattice, strain on the  $\sigma$  bonds increases the angle relative to the  $\pi$  orbital from the ideal value of  $90^\circ$ , as it is in graphite, to values as great as  $110^\circ$ .<sup>30</sup> It follows that nanotubes of smaller diameter will experience greater pyramidalisation and thus greater bond strain. Ultimately, reactions at these sites become energetically favourable since the breaking of bonds within the nanotube structure allows for some of the strain to be relieved through conversion to  $sp^3$  hybridisation, or by introducing vacancies and decreasing the spatial constraint of the carbon atoms.<sup>30</sup> The bonds within the caps typically experience even greater strain in SWCNTs with closed ends. Thus the ends become preferential sites for chemical attack, and consequently chemical functionalisation is commonly expected to be more favourable at the nanotube ends than along the sidewalls.<sup>30</sup>

Nanotube curvature gives rise to another aspect to their reactivity. There are generally two types of C-C bonds in a CNT; those that are parallel with the nanotube axis, and those that are at some angle to the axis. In figure 1.3 these two cases are highlighted in blue and green respectively, where the arrows indicate the viewpoint for the extracted atoms on the left and right respectively. Recall that in the  $sp^2$  hybridised carbon atoms making up the CNT structure,  $\pi$  orbitals protrude normal to nanotube axis. In the case where the C-C bond is parallel to the tube axis (blue) the  $\pi$  orbitals are aligned, i.e. the angle between them is zero. However, for the C-C bond at an angle to the tube axis, the curvature induces a twist along the bond axis and as a result the angle between the  $\pi$  orbitals is *not* zero. Similar to pyramidalisation this misalignment increases with decreasing nanotube diameter. This is known as  $\pi$  orbital misalignment and acts to reduce the stability of the nanotube structure. Any reaction that may reduce this misalignment becomes energetically favourable, giving rise to further chemical reactivity.<sup>30</sup>

Defects in the sidewall structure of carbon nanotubes are also expected to display greater reactivity compared to pristine sites.<sup>27</sup> This defect-induced reactivity can be caused by vacancies, dopants and imperfect lattice structures such as pentagonal and heptagonal carbon rings.<sup>2</sup> A unique defect caused by these imperfect structures is the Stone-Wales defect, where 2 pentagons and 2 heptagons are fused together within the nanotube

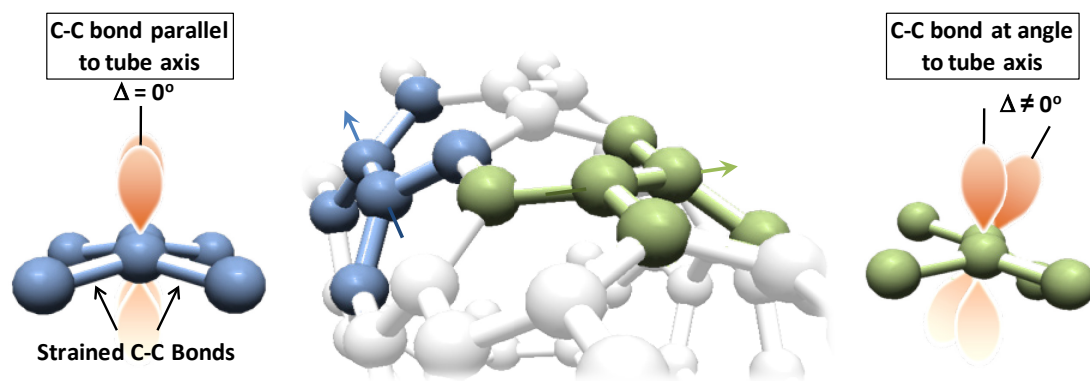


**Figure 1.3. Pictorial representation of curvature induced pyramidalisation and p orbital misalignment that leads to CNT reactivity.**

sidewall.<sup>31,32</sup> Lu *et al.* showed through density functional calculations that while the centre of this defect was no more reactive than a pristine site, the periphery of the defect, i.e. where it meets with the perfect nanotube structure, results in a significant increase in reactivity.<sup>32</sup>

### 1.2.1. Synthesis of Carbon Nanotubes

Since the surge in carbon nanotube research in the early 1990s, numerous synthesis routes have been reported.<sup>8,10,33-40</sup> Some methods have proven to be more successful than others yet the ability to reliably grow one type of CNT in high yields, i.e. either single- or multi-walled, remains elusive. Rather than discussing all possible methods, only those synthesis routes of direct relevance to the nanotubes and research in this thesis are detailed here.

The first SWCNT growth was achieved through an electric arc discharge between two graphite rods, although the yield was very low.<sup>8,10</sup> Soon after, Smalley's group developed a method capable of producing SWCNT yields in excess of 70% using laser vaporisation of solid graphite.<sup>34</sup> While this was an improvement over the arc discharge method, it was not amenable to large-scale commercial synthesis of nanotubes. In 1997 Journet adapted the electric-arc method using mixed transition metal catalysts to establish a gram-scale synthesis route suitable for commercialisation.<sup>37</sup> The consumption of the graphite electrodes established a limitation and as such was considered a 'batch' rather than a 'continuous' process as would be desired for commercialisation.

It was soon realised that a gas-phase reaction where the carbon source and catalyst could be constantly replenished within a reactor may be a more suitable method capable of continuous nanotube production. Smalley's group achieved this goal in 1999 through a method of nanotube synthesis now known as the high pressure carbon monoxide (HiPCO)

process. Carbon monoxide in the gas phase was decomposed in the presence of a gaseous iron catalyst (such as iron carbonyl) at high temperature and pressure.<sup>40</sup> Yields of ~20 mg/hour were initially achieved and this was later improved to ~450 mg/hour through an in-depth study of the process.<sup>41</sup>

The arc discharge and HiPCO processes are now commercialised and CNTs generated through these methods are used around the world in nanotube research. Indeed the nanotubes used in this work were generated from these two techniques. Each of the methods produce single-walled CNTs in high yield with the arc discharge CNTs having a 60-70% purity, and >65% for the HiPCO CNTs. The HiPCO method is known to produce smaller diameter nanotubes (~0.8 – 1.2 nm) compared to arc discharge (~1.4 nm). Given the earlier discussion it could therefore be expected that HiPCO CNTs be more reactive than those created by arc discharge.

#### *Chemical Vapour Deposition*

The synthesis methods to this point have been aimed towards the large-scale production of CNTs, with their discussion motivated by these types of CNTs being used in the nanotube research presented in this dissertation. These processes provide nanotube material in a form that is convenient for use in wet-chemical procedures such as the dissolution into a solvent for further treatment, or the incorporation into another substance such as a polymer matrix to produce composite materials. The ability to have CNTs directly attached to a substrate is also highly desirable however, particularly for device applications.

The HiPCO mechanism is a specialised gas-phase variant of the chemical process known as chemical vapour deposition (CVD).<sup>39,41</sup> Traditionally, this technique involves the deposition of a solid film from a gas phase at elevated temperatures onto a substrate that is often coated with a catalytic species. CVD is used in research pertaining to catalysis,<sup>42</sup> thin-film deposition,<sup>43</sup> synthetic diamond<sup>44</sup> and most importantly here, the growth of carbon nanotubes.<sup>35</sup> While the specifics may differ, the growth of carbon nanotubes using CVD requires some common elements. A desired substrate is coated in a thin film (~nm) of catalyst material. This surface is placed into a high temperature environment usually in the order of 750 – 1000 °C under an inert atmosphere. At such high temperature the catalyst forms into nanoparticles. The surface is then exposed to a carbon-containing feedstock; often methane (CH<sub>4</sub>), acetylene (C<sub>2</sub>H<sub>2</sub>) or ethylene (C<sub>2</sub>H<sub>4</sub>). Although the mechanism underpinning nanotube growth is a contentious issue many possibilities have

been proposed. The feedstock is thought to decompose at the surface of the catalyst and carbon is dissolved into the nanoparticles where, upon supersaturation,  $sp^2$  carbon is formed as the most energetically favourable structure.<sup>35,45</sup> Nanotubes then grow from the particles either outward from the base (base or root growth) or pushing upward against the catalyst particle (tip growth).<sup>33,46</sup>

Nessim described two broad groups of nanotube synthesis methods; ‘grow-then-place’ and ‘grow-in-place’.<sup>39</sup> The arc discharge and HiPCO methods fall into the former category while CVD enables the latter to be possible. This is particularly desirable for device applications where nanotubes are likely to be tethered to a substrate. Growing them in-place allows greater control over nanotube placement, as well as good physical and electrical contact with the substrate. A major failing of the application of CVD towards this goal is the particularly high process temperatures required. This limits the applicable substrates to only those that can endure the extreme environment.

### 1.2.2. Fluorination of Carbon Nanotubes

Multiple reviews on the covalent surface chemistry of carbon nanotubes have been performed. From these, and the references within, the high number of possible CNT functionalities becomes clear. A figure presented by Banerjee, and reproduced in part in figure 1.4, showed that from pristine nanotube material the addition of fluorine to the sidewalls enables multiple reaction pathways to produce CNTs with amine, hydroxyl and alkyl functionalisation.<sup>2</sup> Fluorination has also been used as a first step towards incorporation into polymer composites.<sup>47</sup> Despite the typical strength of C-F bonds, these addition reactions are made possible by the weakened nature of the C-F bonds in fullerenes caused by curvature (6.2 eV in  $CF_4$  and 5.33 eV in  $C_{60}F_{60}$ ).<sup>48-50</sup> By tailoring the amount of fluorine attached to the CNTs to begin with, the level of further functionalisation could be controlled. Exposure to stoichiometric quantities of hydrazine affords this control through ‘defluorination’ and gives a significant level of control over the amount of fluorine left attached to CNTs.<sup>51</sup> While it is important to note the broad functionality achievable through fluorination, the initial process itself also gives rise to interesting phenomena. For example, the addition of active fluorine sites to CNT sidewalls makes them more receptive to hydrogen bonding. Mickelson *et al.* showed that after fluorination CNTs could be more readily solubilised via sonication in a wide range of alcohol solvents. The solutions were found to be metastable, with the nanotubes remaining in solution for up to a week.<sup>52</sup>

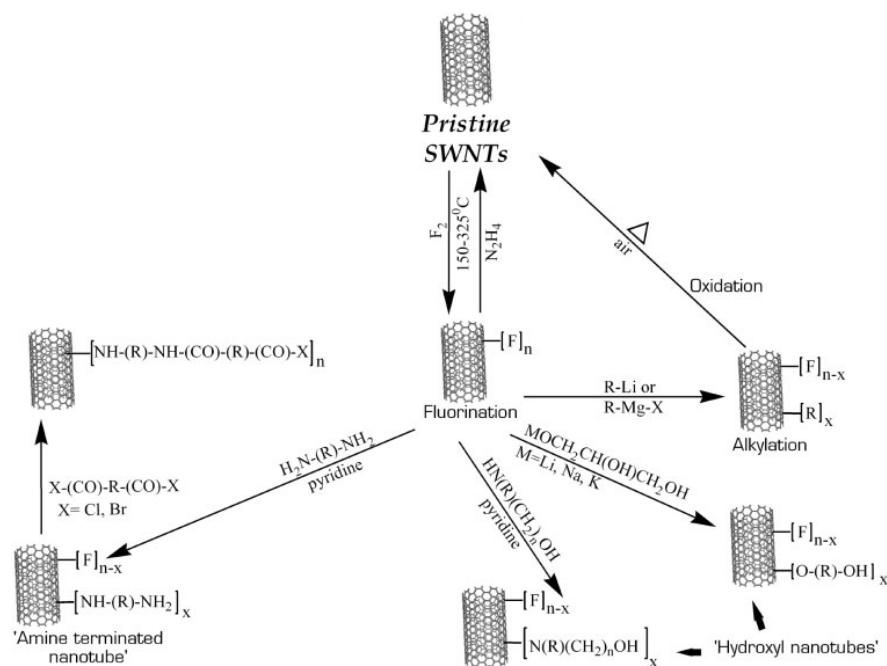


**Figure 1.4. The various functional nanotubes possible via an initial fluorination step.**  
**Reproduced from Banerjee.<sup>2</sup>**

Dissolution of CNTs is an important step towards their further use since Van der Waals forces resulting from the delocalised  $\pi$  orbitals promote the formation of CNT ‘bundles’ in the raw material, similar to the interlayer interaction within crystalline graphite.<sup>53</sup>

It has been demonstrated both theoretically and experimentally that fluorine attaches to CNTs in distinct banded structures.<sup>54,55</sup> Through STM measurements it was found that regions of high electron density attributed to fluorine attachment appeared in bands either around the nanotube circumference, or along the nanotube axis. Calculations showed that depending on the site at which the initial fluorination occurred, additional fluorine atoms would arrange themselves to minimise repulsive forces and thus either spread around the circumference or along the length of the tube. These calculations also showed that after the initial fluorination event additional species tended to attach nearby to these sites, with further fluorination being energetically favourable after the first attachment.<sup>54,55</sup> This phenomenon allowed for the controlled cutting of CNTs into smaller fragments. Gu demonstrated that by using the fact that fluorine preferred to attach near to other functionalised sites, localised defects and vacancies could be introduced in a controlled fashion throughout the nanotube structure. Pyrolysis of the nanotubes at 1000 °C resulted in a decreased length distribution.<sup>56</sup> Ziegler also demonstrated this using fluorination to first functionalise the nanotubes, then de-fluorinate the samples using hydrazine to induce

vacancies. The nanotubes were then etched in an acid solution where a significant narrowing of the length distribution, along with a decrease to a lower average length was observed.<sup>57</sup>

Fluorination has also been observed to modify the electronic structure of CNTs.<sup>58,59</sup> Using four-point probe measurements, An *et al.* found that by increasing the level of fluorination of CNTs, their specific resistivity was increased. This was further complemented by photoelectron spectroscopy results where the valence band spectra showed an increase to higher binding energies, indicating an increase in the band gap of the material.<sup>58</sup> This was directly attributed to a reduction in the electron density around the Fermi level thus converting the otherwise metallic CNTs into semiconductors.<sup>59</sup> These changes in electronic structure have been applied to electrochemical cells where fluorinated CNTs were used in place of the standard fluoro-graphite (carbon monofluoride) cathodes.<sup>60</sup> The fluorinated CNT cathodes displayed a greater cell potential than the standard cathode. The CNT cells also showed an increased discharge rate, an effect attributed to the weaker C-F bonding in CNTs compared to carbon monofluoride. The authors noted that while it was promising to observe improved behaviour with fluorinated CNTs, the cost of producing such cathodes (at the time) was a severe drawback.<sup>60</sup> Improved fluorination methods, as well as nanotube synthesis techniques, could very likely improve the outcomes within this field of research leading to high quality, small scale batteries.

### **1.3. Plasma Processing**

#### 1.3.1. Plasma: The Fourth State of Matter

Along with the solid, liquid and gas phases, there exists a fourth state of matter known as plasma. Neglecting exotic forms of matter, most of the observable universe is in the plasma state in the form of nebulae, solar winds and stellar interiors.<sup>61,62</sup> On Earth however, there are a few examples of plasma that one may encounter on a daily basis, both naturally and man-made.<sup>61</sup> The intense glow produced during a lightning strike is possibly the most impactful, with the sudden extremely high voltage discharge producing such intense electric fields as to ionise the surrounding air. While far more benign, the ionosphere surrounding our planet is plasma and shields the surface of solar winds to create the Aurora Borealis, also plasma.<sup>61</sup> Synthetic examples of plasma include the discharge within fluorescent tubes or neon signs, and the generation of light and colour within a plasma

display panel.<sup>61,62</sup> Needless to say, one is inevitably exposed to plasma in some form on a day-to-day basis. Over the last few decades the plasma state has also become one of the most important industrial tools.

It could be argued that the semiconductor industry would not have reached the capabilities of today without the usage of processing methods involving plasma. Much of the silicon based technology relies on this highly reactive and energetic state to develop intricate integrated circuit components. For example, using plasma, trenches narrow enough to fit onto a single human hair hundreds of times across can be etched into silicon to produce circuitry.<sup>1</sup> The process can be used to deposit various metals in precisely controlled quantities, as well as to grow oxides or films of specific thicknesses. Ion implantation can also be performed, which is an extremely important process for the production of p- or n-type silicon components.<sup>1</sup> Each of these processes can be used in tandem to produce an integrated circuit of incredibly small dimensions, and extreme intricacy. While this industry is a very large and important one today, its usage of plasma processing methods is not unique. The medical technologies and food industries use plasma in various forms to sanitise surfaces. In medicine new operating tools are being developed to sanitise local areas of tissue, such as open wounds, by using a plasma-based torch generated from an inert gas.<sup>63,64</sup> The food industry uses plasma to sanitise surfaces and materials used in the packaging of consumables.<sup>65</sup> Due to the very high energies required for the fusion of deuterium atoms, plasma has been investigated as a possible way of creating and containing a controlled nuclear fusion reactor. This research has existed since the 1950's and continues today to ever increasing scales.<sup>61</sup> In possibly the grandest challenge, plasma is even being investigated as a method of propulsion in space, with the development of ion thrusters.<sup>66-68</sup> The abundance of fields making use of plasma gives rise to some questions; *what exactly is plasma; how is it generated and why is it so useful?*

Simply put, plasma is the ionised form of a gas. However, the Saha equation gives the ratio of ionised,  $n_i$ , to neutral,  $n_n$ , density in a gas of temperature  $T$  such that, when simplified,

$$\frac{n_i}{n_n} \approx 2.4 \times 10^{21} \frac{T^{3/2}}{n_i} e^{-U_i/k_B T} \quad (1-1)$$

where  $U_i$  is the ionisation potential of the gas and  $k_B$  is Boltzmann's constant.<sup>61</sup> From this it could be argued that all gas is in the plasma state to some degree, although granted at room temperature the result is extremely low ( $n_i/n_n \approx 10^{-122}$ ).<sup>61</sup> Thus a more rigorous definition of plasma is required.

To quote Chen<sup>61</sup>;

*“A plasma is a quasineutral gas of charged and neutral particles which exhibits collective behaviour”.*

The two important terms within this definition are *quasineutral* and *collective behaviour*. The first term refers to the fact that when viewed on a large enough scale a given plasma will appear to be neutral, i.e. all the positive and negative charges will balance each other to result in no net charge density. However, if one views the plasma on scales below a specific length, then the Coulomb potentials of the charge carrier are observed and the plasma is no longer neutral. This length is known as the Debye length, and is defined by

$$\lambda_D = \left[ \frac{k_B T_e}{4\pi e^2 n_e} \right]^{1/2}$$

where  $k_B$  is Boltzmann's constant,  $T_e$  is the electron temperature,  $e$  is the elementary charge and  $n_e$  is the electron density.<sup>69</sup> At length scales greater than the Debye length, the Coulombic interactions between the charge carriers in the plasma are mutually shielded, resulting in the appearance of neutrality. This leads to another criterion for a gas to be considered plasma; the density of the charged species must be great enough so that the Debye length is much less than the dimensions of the plasma as a whole.<sup>69</sup>

Collective behaviour also relates to the fact that individual plasma species are charged. In a neutral gas, molecules moving due to thermal motion can only change trajectory through collisions with other species or with the walls of the container. In plasma however, the species are charged and the motion of the particles in turn generates localised electric fields. The motion of the particles results in currents within the plasma and ultimately localised magnetic fields. Each of these fields is then capable of acting upon remote charged particles, influencing their motion. Collective behaviour therefore refers to the fact that charged species within a plasma not only react to the local environment, but also the state of the plasma as a whole.<sup>61</sup>

Plasma can be generated through various means. The simplest to consider is that of gas temperature. Consider again equation (1-1) where the ratio of ionised density,  $n_i$ , to neutral density,  $n_n$ , varies with temperature,  $T$ . As the temperature rises, a point is reached where the thermal energy  $k_B T$  nears the ionisation potential  $U_i$  of the gas and the ratio of ionised to neutral atoms increases abruptly. At this point the gas can be considered to be in a plasma state.<sup>61</sup> If one were to take nitrogen as the gas under study,  $U_i$  would be 14.5 eV, which would equate to a temperature of  $\sim 168,000$  K (from a treatment in Appendix A).

---

Due to the high energy tail of the thermal distribution of velocities in the gas,  $k_B T$  need only be a few times less than  $U_i$  before sufficient ionisation could occur to consider it plasma, but this still requires tens of thousands of Kelvin in temperature. Since this is not practical in a laboratory environment, other methods of plasma generation are used.

The ionisation of atoms can also be enacted by the application of strong electric or electromagnetic fields.<sup>1</sup> In these systems the atoms are ionised through either the dissociation of an electron from the atom resulting in two charged species, or the collision of an atom with an electron that has been accelerated by the fields. In either case, charged species result which act to continue the ionisation of the gas and provided energy is continuously delivered into the system the gas will remain in the plasma state. The degree of ionisation can be controlled by the magnitude of the applied fields (among other factors), i.e. more energy delivered to the charged species results in a greater number of collisions and thus more ionisation. Typical lab-based plasma has a degree of ionisation less than 1%, and is commonly referred to as ‘cold’ plasma.<sup>1</sup>

To initiate ionisation some plasma systems utilise a static high voltage ( $\sim$ kV) electric field setup between two parallel plates immersed within the gas. The sample stage often takes the place of one electrode. These systems can be generally referred to as dc (direct current) plasma sources. Examples include sputter ion coaters and glow discharge tubes. These systems suffer from very high directionality since the electric field is static. Charge flow becomes unidirectional with electrons and negative ions flowing towards the cathode and positive ions towards the anode. This is desirable in an ion coater where the intention is to sputter a given target material onto a substrate. However the sputtering of a material may be a serious inconvenience when chemical functionalisation alone is the desired outcome.

To alleviate this issue to some extent, plasma can also be ignited using ac (alternating current) electric fields. A myriad of frequencies can be used from kHz to GHz, but a commonly used value is 13.56 MHz, corresponding to a special band set aside for scientific purposes. These are commonly referred to as radio frequency (rf) sources. Ionisation in these systems occurs in much the same way as their dc counterpart, however the electric field from the source is not static and thus the system ideally displays little to no directionality. Practically however, this is not strictly true as through other means the source can develop what is known as a ‘self-bias’ voltage which can lead to sputtering. This is discussed later in Chapter 4. A range of source geometries (antennae) exist for rf

plasma systems. Many utilise an external antenna where the electric field is generated from a source that is external to the chamber and plasma density, and the electromagnetic field permeates through some dielectric material such as glass or quartz. These are often either planar or helically coiled in nature and require large input powers (100 – 1000 kW) to generate significant plasma density.<sup>1</sup> Also, sputtering of the dielectric material can be problematic. Other systems utilise the similar geometries (planar or helical coil) but have the source internal in direct contact with the density. These systems generally require less power input but substitute the sputtering of the dielectric with the antennae.

One of the biggest advantages of an rf plasma system driven by an antenna is the decoupling of the plasma source from the sample.<sup>1</sup> In a dc system the plasma is generated between the plates and the sample sits upon the bottom electrode, which is often Earthed. The field is then varied via the top electrode to control the plasma density. In some processes it is desirable to not only control the plasma density but also the energy of the plasma species impacting the surface. In a dc system it is not possible to vary these quantities independently since the method of plasma generation relies directly on the potential at the surface. Thus variation of the field to control the density will also act to change the impact energy of the ions. In an rf system the method of plasma generation and the potential at the surface are decoupled, meaning they can be varied independently giving much greater control over the type and extent of surface modification. While this is possible in most rf plasma systems, it is not always necessary however and in these cases the common practice is to keep the surface electrically Earthed.

Most plasma is generated within stainless steel vacuum systems where the walls are conductive and Earthed. In cold plasma the electron velocity is generally much greater than the ion velocity due to the substantial mass difference.<sup>1,70</sup> Electrons from the plasma are therefore lost to the walls more readily than positive ions. The net result is a loss of neutrality at this interface and the development of a layer known as a ‘sheath’ across which a strong potential difference develops known as the space (or plasma) potential. The thickness of this sheath is given by the Debye length. Strong electron and ion density variations exist across the sheath. Due to the rapid loss of electrons to the wall the space potential is positive within the plasma density, quickly dropping to the surface potential (usually Earth). An ion passing into the sheath may be accelerated towards the wall due to the large potential variation, where the strength of the potential determines the magnitude

of the acceleration. This is an important phenomenon to consider in materials processing using plasma since control of the space potential intrinsically gives control over the energy of the impacting species in the absence of other applied fields. Across the sheath both the electron and ion densities vary as the surface is approached, with the electron density decreasing at a rate greater than that of the ions. Within the main density however these two quantities are expected to be essentially equal, due to quasineutrality discussed previously. In cold plasma the energy of these species are expected to vary drastically however, with the electron energy very much greater than the ion energy, again due to the mass difference. In fact, it is commonly accepted that the ion temperature may be comparably close to room temperature, while electrons could have temperatures of many thousands of Kelvin.<sup>1,62</sup> It is the electron and ion densities that are expected to perform surface modifications through ion impacts, reactions with radicals or by simply imparting energy to the surface. It is therefore particularly important to quantify these densities and their energies, along with the potentials within the plasma.

### 1.3.2. Characterisation of Plasma

Although the initial observation of plasma was made by Sir William Crookes in 1879, significant understanding of the science of plasma was not furthered until the 1920s, during the work of Irving Langmuir.<sup>71,72</sup> Since then many developments have been made regarding the theory behind the state, how to generate and contain it and possibly most importantly, how it can be characterised. With many decades of research come many characterisation methods. Examples include atomic emission and absorption spectroscopy, interferometry, fluorescence, and electron scattering. Many of these techniques give useful information about the chemistry of the plasma. The oldest characterisation technique however is that of the electrostatic probe, also known as the Langmuir probe after the aforementioned scientist and Nobel Laureate.<sup>73</sup> In practice these devices are very simple, and give extensive information about the *physics* of the plasma.

#### *Langmuir Probes*

The premise behind Langmuir probe characterisation is quite simple; a conductive probe is immersed into direct contact with the plasma density. The geometry of the probe can vary somewhat between experiments although common variants include spherical, planar and cylindrical collectors.<sup>69,74</sup> More exotic designs include probes with multiple tips arranged in such a way as to simplify theoretical treatments, allowing for very easy determination of

certain quantities.<sup>75</sup> Other work has used two dimensional Langmuir probe arrays to determine spatial information about the plasma.<sup>76</sup> Possibly the most common geometry however is that of the single cylindrical Langmuir probe, which in practice is often simply a thin piece of conductive wire. Connected to the probe are voltage supply and current measurement components. The voltage is swept and the current measured to produce a current versus voltage characteristic. Analysis of this curve gives details about the electron and ion densities, electron temperature and various potentials. It is worthwhile noting that information about the ion temperature is not obtainable using single cylindrical Langmuir probes.<sup>77</sup> Such a determination requires more sophisticated experimental setups, or alternate techniques such as Doppler broadening spectroscopy.<sup>78</sup>

Details regarding the experimental nature of the Langmuir probe experiment are given in Chapter 2, including the probe material and its dimensions. The theory behind electrostatic probes is given in brief in Chapter 3, and in detail in Appendix A.

### 1.3.3. The Plasma Fluorination of Carbon Nanotubes

Much of the work surrounding the fluorination of CNTs already presented has made use of fluorine ( $F_2$ ) gas at elevated temperature to achieve the desired functionality. Fluorine gas is extremely reactive, as evidenced by fluorine attachment to CNTs being achieved at room temperature,<sup>79</sup> albeit from an extreme exposure time.<sup>80</sup> Elemental fluorine is considerably toxic which complicates its handling during an experiment.<sup>81</sup> Reactants capable of providing fluorination without the toxicity of  $F_2$  are therefore desired.

More recently, the usage of plasma-based processes have been identified as a very useful tool towards controllable fluorination. Multiple research groups have investigated the use of this reactive state using fluorine rich gases such as carbon tetrafluoride ( $CF_4$ ) and sulphur hexafluoride ( $SF_6$ ).<sup>47,82-93</sup> Each of these species has significantly greater stability than  $F_2$ . In fact  $SF_6$  has been used extensively as an insulating gas in high voltage switch-gear due to its very high breakdown potential.<sup>94</sup> Furthermore, the toxicity is greatly reduced with these substances, particularly with  $SF_6$  which is commonly used to display the opposite effect to breathing in helium; its significant density lowers ones voice. The improved stability of these molecules requires reactivity to be induced through ionisation into the plasma state where it produces radicals and ions that can functionalise surfaces.

In 2003 Plank *et al.* detailed the fluorination of SWCNTs using CF<sub>4</sub> plasma generated within a commercial reactive ion etching system.<sup>89</sup> After exposure for only 2 minutes the authors noted significant fluorine presence on the surface. The ratio of fluorine to carbon was found to be 0.22. This was noted as being less than what was found from F<sub>2</sub> gas exposure.<sup>89</sup> The advantages of a room temperature process with greatly reduced exposure time is however noteworthy.

In 2004 Tressaud *et al.* performed a direct comparison between F<sub>2</sub> gas and CF<sub>4</sub> plasma exposure on graphite samples.<sup>83</sup> It was found that while the high temperature fluorine exposure gas had an increased level of C-F bonding, the CF<sub>4</sub> plasma provided a greater level of covalency to those bonds (as determined via photoelectron spectroscopy).<sup>83</sup> Thus the choice between these two techniques, at least on graphite, appeared to be a balance between quality and quantity. While not strictly the same material the similar structure of graphite to CNTs allows its comparison here.

Within the reactor used earlier, Plank *et al.* in 2004 performed a comparison of the fluorination of CNTs obtained using either plasma generated within CF<sub>4</sub> or the more fluorine-rich molecule SF<sub>6</sub>.<sup>87</sup> Some particularly interesting points arose from this work. While each of the exposures resulted in similar levels of fluorine attachment over the bias range studied, the sample exposed to the SF<sub>6</sub> plasma resulted in essentially purely covalent C-F bonding, while the CF<sub>4</sub> treatment gave mixed covalent/ionic bonding. This result was made more curious by the fact that the SF<sub>6</sub> flow rate was half that of the CF<sub>4</sub>. The authors suggested that this was a result of the greater atomic fluorine pressure in the SF<sub>6</sub> plasma, a conclusion based on a plasma diagnostic study. Thus, for half the flow rate, SF<sub>6</sub> produced a greater concentration of fluorine ions than CF<sub>4</sub>. Further to this, the authors suggested the presence of (CNT)-CF<sub>2</sub>=CF<sub>2</sub> functionality on the surfaces after exposure. This presence was most notable for the CF<sub>4</sub> plasma treatment. Whether the CF<sub>4</sub> plasma resulted in some level of carbonaceous film deposition was not mentioned. However, given the capability of hydrocarbons to deposit carbonaceous films of varied properties from plasma, the presence of such a mechanism would seem plausible.<sup>95-97</sup>

Much of the work involving fluorination of CNTs is aimed towards the further functionalisation of the material, using fluorination merely as an initial step. As such, many fluorination techniques are recycled without too much thought for the fundamental mechanism. The literature detailed here however provides some key pieces of information

regarding the advantageous nature of using plasma processes to achieve functionalisation. One of the strongest points is the fact that it can be a room temperature process. This expands the applicability of substrates and materials to those that would not typically survive under elevated temperatures. Plasma fluorination can also be performed in a matter of minutes due to the high reactivity of the environment, compared to hours for the fluorine gas methodology. As a result, sample throughput is greatly improved. Reactant volumes in the plasma processes are significantly lower, with all systems operated in low pressure regimes. Reactant flow rates of only 20 – 40 sccm (standard cubic centimetres per minute) have been reported.<sup>87</sup> This is vastly different to the fluorine gas processes where F<sub>2</sub> is diluted into a carrier gas at atmospheric pressure and flowed across the sample for hours at a time.<sup>51</sup> Finally, fluorine gas has been found to result in greater levels of functionality, but the plasma processes using CF<sub>4</sub> and SF<sub>6</sub> resulted in greater covalency to that functionality. Furthermore, SF<sub>6</sub> was found to provide greater covalency than CF<sub>4</sub> for a particular system.<sup>87</sup> This high quality of C-F functionality would likely be far more desirable in the long term for device development where stability and longevity could be far more desirable than the extent of functionalisation.

#### 1.3.4. Plasma-Enhanced Synthesis of Carbon Nanotubes

Thermal CVD processes have been established as a successful method towards large-scale production of nanotubes. An issue with the typical thermal CVD process however is that processing temperatures in excess of 800 °C are generally required to result in single-walled CNT growth.<sup>98</sup> Below this, multi-walled growth is predominant. When SWCNTs are desired such high temperatures limit the applicability of the CVD process to only those substrates that are particularly resilient. The high temperature is required largely to initiate the decomposition of the feedstock into components suitable for growth. By using the plasma state, much of this energy can be supplied by the collisions of electrons at high energy, and thus decomposition can occur without the need for the gas to be heated significantly.<sup>38</sup> This is the principle of plasma-enhanced CVD (PECVD), which in many ways is the same as thermal CVD, except that it is performed at reduced pressure where the feedstock can be ignited into plasma to facilitate decomposition. Over recent years, multiple extensive reviews of the current state of knowledge of plasma nano-science have been performed with particular focus on PECVD growth of nanostructures.<sup>38,98-101</sup>

Using PECVD, SWCNT growth has been achieved with substrate temperatures as low as 450 °C, and MWCNT growth at room temperature.<sup>99</sup> Although very desirable, low temperature synthesis is not the only advantage to PECVD over thermal CVD. Due to the formation of a sheath above a growth substrate, nanotubes grown via PECVD have a natural vertical alignment. Upright forests of CNTs have been produced via CVD, as have arrays of vertical columns, however detailed inspection finds that the nanotubes within these structures are not necessarily well aligned, and appear more like the traditional nanotube ‘spaghetti’ that has been pushed upward from the surface. PECVD on the other hand has been used to generate well aligned freestanding vertical CNT arrays of very small dimensions.<sup>38</sup> This level of precise control over morphology is paramount for device development, especially field emission, photovoltaics, sensing and filtration, where vertical alignment is highly desirable.

The fact that PECVD is performed under vacuum also gives the process intrinsic cleanliness, since atmospheric contaminants become negligible. Furthermore, in PECVD the sample can be easily cooled under either a pure inert atmosphere or vacuum. Following growth via thermal CVD, the atmosphere must be precisely controlled as the surface is cooled to ensure that oxidation from atmospheric species does not occur.

#### **1.4. Aim and Scope of this Research**

So far this chapter has discussed the highly desirable nature of both carbon nanotubes as a material and plasma processing as a means towards the controllable functionalisation and growth of these materials. Further to this, fluorination has been established as a means towards new functionalities, as well as a method of modifying the intrinsic properties of CNTs. Issues have been identified however, with the typical elemental fluorine procedures resulting in high quantity, yet low quality C-F functionality. Plasma within CF<sub>4</sub> partially aids this issue but the deposition of carbonaceous films is a potential drawback. The usage of SF<sub>6</sub> plasma environments appears to solve both of these issues, however a detailed study of the characteristics of this environment in the context of carbon nanotube fluorination is somewhat lacking in the literature. Plasma enhanced CVD has been identified as a desirable process towards the controlled growth of CNTs. It can be performed at reduced temperatures compared to its thermal counterpart, has intrinsic cleanliness and results in natural CNT alignment. The development of such a technique would therefore be very useful in nanotube research and as yet it has not been achieved at Flinders.

This dissertation endeavours to bridge this gap in knowledge and technology through the investigation of plasma processing towards the fluorination and growth of CNTs with the following research aims in mind:

- i) *To investigate the physical nature of sulphur hexafluoride plasma within a plasma system with respect to experimental parameters that would typically be altered for surface modification treatments.*
- ii) *To investigate the application of sulphur hexafluoride plasma towards the fluorination of carbon nanotubes.*
- iii) *To investigate the viability of carbon nanotube growth within the same plasma system used for fluorination studies.*

As there are multiple facets to this work, each element will be isolated, investigated and discussed individually, with successive arguments built upon the knowledge gained from each section of the research.

#### 1.4.1. Characterisation of Plasma Chamber

The plasma chamber used in this research has been studied previously using methane and hydrogen plasma towards the hydrogenation of carbon surfaces.<sup>102</sup> However, the usage of SF<sub>6</sub> plasma in this system had not been studied in any significant detail prior to this work. Thus it was deemed imperative to establish an understanding of the nature of this plasma environment to aid its application to surface modification. The characterisation of the chamber would be performed using an existing Langmuir probe apparatus.

##### *Proof of Concept*

Initially the application of the existing Langmuir probe experiment in the plasma system will be investigated within an environment that has already been characterised; nitrogen plasma.<sup>103</sup> Direct comparisons will be made between results obtained here, and those already published to establish a thorough understanding of the experiment.

##### *Characterisation of SF<sub>6</sub> Plasma*

With operational parameters established, the Langmuir probe will then be applied to SF<sub>6</sub> plasma. Characterisation of the plasma will be performed with variation of experimental parameters such as gas pressure, applied rf power and the position within the chamber.

#### 1.4.2. Characterisation of Carbon Surfaces Exposed to SF<sub>6</sub> Plasma

##### *Proof of Concept and Preliminary Characterisation*

Once the plasma environment is well understood, carbon nanotube surfaces will be exposed to the SF<sub>6</sub> plasma. The effect of the exposure will be characterised using surface analysis techniques such as photoelectron spectroscopy, transmission electron microscopy, and Raman spectroscopy, each of which are introduced and discussed in the following chapter. The proof-of-concept will establish the applicability of this system towards the fluorination of CNTs, as well as to establish any failings of the methodology which can then be investigated and improved upon.

##### *Advanced Characterisation of Functionalised Surfaces*

Upon establishing a proof-of-concept, the surfaces will then be modified under varying experimental conditions, such as rf power and the modification of the plasma chemistry through gaseous mixtures. Efforts towards improving the fluorination methodology will be investigated, characterised and discussed. These experiments will utilise advanced characterisation performed on the soft X-ray beamline at the Australian Synchrotron.

#### 1.4.3. PECVD Growth of Carbon Nanotubes

The CNT growth performed at Flinders prior to this work resulted in multi-walled growth where for many applications single-walled carbon nanotubes would be preferable due to their semiconducting nature, and thus better electron-hole pair separation in photovoltaic applications.<sup>104</sup> As part of this research then the possibility of growing carbon nanotubes using a plasma-enhanced CVD technique will be investigated and discussed.

##### *Proof of Concept and Preliminary Characterisation*

Through a brief literature survey a methodology that should afford the growth of CNTs in a plasma environment will be established, along with chamber modifications that will be required to succeed in this goal. Initial experiments will be performed establishing the viability of this method, with characterisation by photoelectron and Raman spectroscopy. The flexibility of the method will then be demonstrated through modification of the treatment parameters to produce differing types of CNT growth. Finally, a simple method towards the patterned growth of CNTs will be established and characterised.

---

## **Chapter 2.**

# **EXPERIMENTAL**

### **2.1. The rf Induction Plasma Reactor**

#### 2.1.1. A Brief History

The reaction vessel used to perform plasma studies is pictured in figure 2.1. This system was originally built at the University of New England (UNE) in New South Wales as a sister chamber to a system at the Australian Nuclear Science and Technology Organisation (ANSTO) utilised for the investigation of gaseous impurities and neutrals on the nitriding of stainless steel.<sup>105-107</sup> The chamber was transported to Flinders University in South Australia in 2005 where it was re-commissioned as a general purpose rf plasma reactor under the supervision of Dr Jamie Quinton. Alec Deslandes, a PhD candidate and student of Dr Quinton, began work on the hydrogenation of carbon surfaces using the reactor,<sup>108</sup> and since that time the system has become an integral part of multiple post-graduate research projects. While some modifications have been made to the chamber during its lifetime at Flinders, it remains largely the same as it was at UNE, with only the pumping system undergoing any significant change.

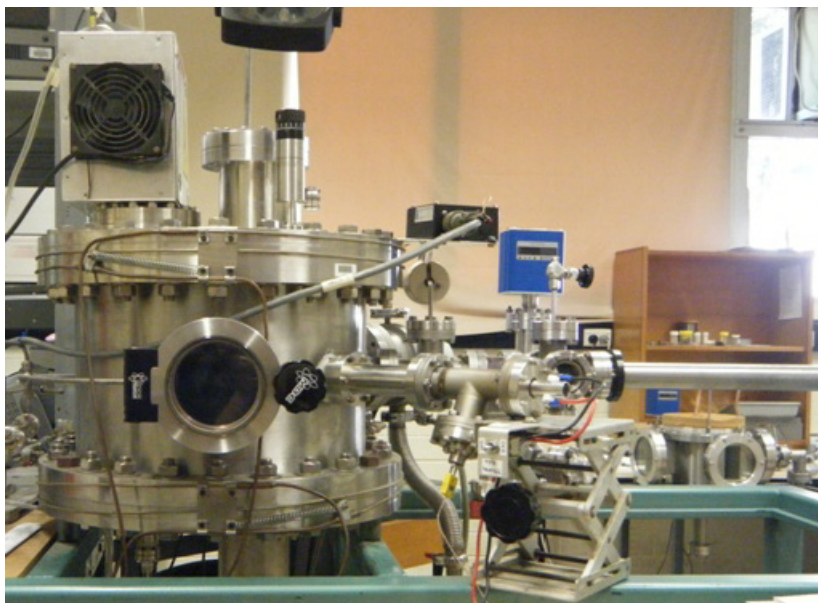


**Figure 2.1.** The plasma reactor at Flinders University used in this research.

### 2.1.2. Experimental Setup and Control Over the Plasma

A schematic of the plasma reactor is presented in figure 2.2. The system consisted of two chambers separated by a manually actuated gate valve. The main chamber, made from AISI-316 stainless steel, was cylindrical in shape and measured 0.4 m in diameter and 0.3 m in height (internally). Vacuum was achieved via a  $110 \text{ L s}^{-1}$  turbo-molecular pump backed by a rotary vane pump. The chamber could routinely achieve pressures of better than  $10^{-5}$  Torr, although when not in regular use the base pressure was seen to reach  $<5 \times 10^{-6}$  Torr. The second chamber was a load-lock system for the easy transfer of samples in and out of the main chamber, removing the requirement to break vacuum in the reaction volume, affording significantly improved sample turn-around times while also maintaining the cleanest possible reaction environment. The load-lock was pumped by a rotary vane pump and achieved a base pressure of  $1 \times 10^{-3}$  Torr. Although higher than the base pressure of the main chamber, research is commonly performed in the  $10^{-3} - 10^{-1}$  Torr range (1 – 100 mTorr) and consequently deemed suitable for sample transfer during experiments.

Plasma was generated by coupling rf power to a given reactant gas via a single loop antenna made from hollow stainless steel tube. During treatments, the antenna was cooled by flowing compressed air through its core. Power was supplied by a 100 W Kalmus 161 Linear Amplifier, driven by a Stanford Research Systems DS345 Function Generator. The frequency applied to the antenna was 13.560 MHz, pursuant to the rf band set aside for ‘Industrial, Scientific and Medical’ purposes (the ISM band).

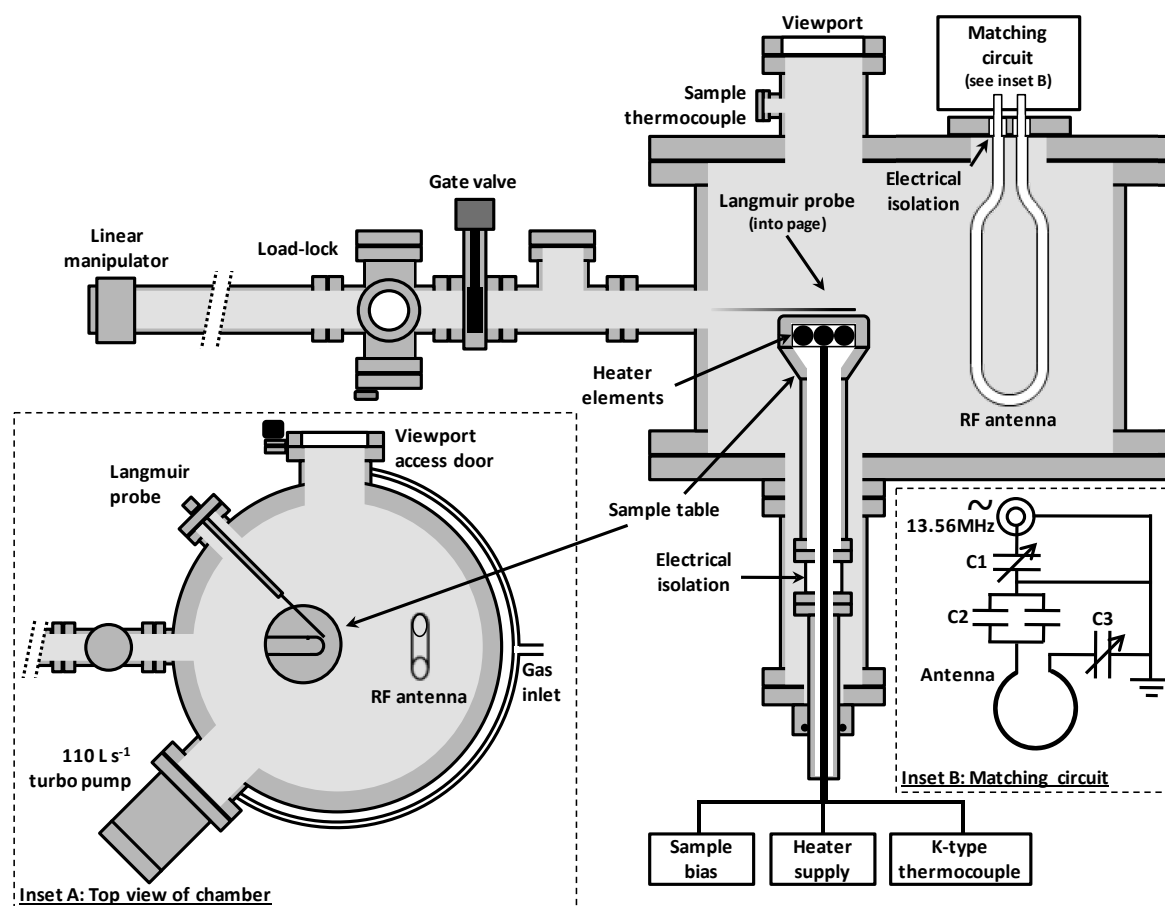


**Figure 2.2.** A schematic of the plasma reactor at Flinders University. Inset A shows the top view of the chamber. Inset B shows the circuit used to match impedances.

The amount of rf power delivered to, and reflected from the plasma was measured using a Bird 4381 rf Power Analyst power meter. The total absorbed power, or the total power coupled to the plasma, was taken as the reflected power subtracted from the applied power. Ideally the reflected power would always be zero, meaning that 100% of the applied rf power was used to generate the plasma, however in reality this was not the case. To minimise the amount of reflected power a matching circuit, depicted in figure 2.2, inset B, was used to ‘match’ the impedance of the source electronics with the impedance of the antenna-plasma system through variation of capacitors C1 and C3. The value of this match was generally found to be strongly dependent on the applied rf power and gas pressure, although the gas type also had a significant influence. The circuit was housed within the matching unit, which was designed and built at ANSTO.

Control over the amount of applied power, and thus the absorbed power when appropriately tuned, was given by adjustment of the peak-to-peak voltage ( $V_{p-p}$ ) of the input wave from the DS345. Generally, steps of 0.1 V were utilised ultimately resulting in rf power increases of  $\sim 10$  W, although this was dependent on the gas being ignited.

Whenever possible, samples were placed on a stainless steel mount that was inserted directly into a fixed sample stage within the reaction volume. Three resistive elements embedded within the stage allow for samples to be heated from room temperature to  $\sim 400$  °C. Temperature was monitored via a K-type thermocouple. The table surface and sample could also be biased up to  $\pm 2.1$  kV by a Fluke 412B High Voltage Power Supply. Although this feature was not used in this research, it is mentioned here for completeness.

The base pressure of the system was monitored with a Bayard-Alpert type ionisation gauge that was mounted underneath the chamber. The suitability of this type of gauge above  $\sim 10^{-3}$  Torr was questionable and so during plasma treatment the ionisation gauge would be switched off. A Granville-Phillips Series 375 Convectron gauge was attached to the system and allowed pressure measurement from atmospheric pressure down to  $\sim 1 \times 10^{-4}$  Torr. Although useful during venting procedures, this gauge becomes compromised during a plasma treatment since it relies on heat transfer from a sensor wire, which was not a reliable measure within a plasma environment. This quantity was also dependent on the gas being measured (the gauges would typically be calibrated using nitrogen) resulting in significantly different pressure readings for different gases. Instead a MKS Baratron 615A (1 Torr range) was used to monitor gas pressure during plasma treatments. This gauge operated purely on the physical interaction between the gas within the chamber and two parallel plates, between which a capacitance was measured and correlated with a gas pressure. This type of gauge was therefore not vulnerable to interference due to plasma species, and was independent of the nature of the gas being measured. The chamber allowed two gases to be introduced at the same time, creating the possibility of complex plasma environments. One gas line was controlled via a Granville-Phillips (GP) Series 203 Manual Leak Valve while the other was controlled by a GP Series 216 Automatic Pressure Controller (APC). The APC would monitor the total pressure from the Baratron gauge and adjust a servo controlled valve accordingly to bring the chamber pressure to a user defined set point. In the case of gaseous mixtures, the partial pressure of one reactant was first set by the manual leak valve, with the total gas pressure then set and controlled by the APC.

## 2.2. Langmuir Probes

The concept of studying the physics of a gaseous discharge using an immersed conductive electrode was introduced by Mott-Smith and Langmuir in a series of articles in 1924.<sup>71,72</sup> This work detailed a practical approach towards extracting important details regarding the physical nature of a discharge under study, such as the electron temperature, ion and electron densities, and various electric potentials within the plasma.

In practice a Langmuir probe is a relatively simple device. It commonly consists of a single thin conductive wire that is immersed in the plasma under study at which point a bias is applied with respect to Earth potential (0 V). Since the plasma is an ionised gas, species local to the probe will respond to the bias and a current is induced within the probe. The amount of current that flows through the probe depends upon the magnitude and polarity of the bias that is applied. If one were to assume that the discharge consists only of electrons, positive ions, and neutrals then the current flowing through the probe will be due to both electron current ( $I_e$ ) and ion current ( $I_i$ ) depending on the bias. The bias voltage would be swept from a large negative potential to a large positive potential while measuring the resultant current that flows through the probe. Details regarding the plasma would then be extracted from the resultant Current-Voltage (I-V) characteristic. While practically simple, the theory describing how electron and ion currents are collected by Langmuir probes is very complex.<sup>72</sup> An in-depth theoretical treatment of Langmuir probe operation is presented in Appendix A.1. Discussion regarding the I-V characteristic collected from a Langmuir probe and how it is related to plasma species is presented in Chapter 3.

### 2.2.1. Probe Design Considerations

Although it is true that any conductive surface could be used to elucidate information about a given discharge,<sup>73</sup> there are certain requirements that must be considered by the experimentalist before designing and building a Langmuir probe. These include the dimensions of the probe and the material from which the probe is made, as well as electronic concerns such as the filtering of noise induced by the plasma source and the avoidance of loading the probe with unwanted voltages.

#### *Probe Material and Physical Dimensions*

Plasma is a harsh environment. Many processes can occur at the surface of a probe tip once it is immersed in a discharge. The probe material and its support must therefore be able to

withstand both high temperature, and physical sputtering. A suitable probe material that is commonly used is tungsten as it has a high melting point (3700 K), is workable and easily obtainable as a thin wire, is strong and retains its strength across a wide temperature range, and can withstand plasma environments without excessive sputtering.<sup>77</sup> The dimensions of the probe tip must also conform to some constraints to allow the suitable application of the theory detailed in Appendix A. Firstly, to ensure the probe does not behave like a sink and drain the plasma in a localised region, the radius of the probe,  $r_p$ , must not be greater than the mean free path,  $\lambda$ , of the species under investigation.<sup>69</sup> The mean free path is the average length scale a particle within the plasma will travel before an interaction with another particle. In this work the minimum mean free path for fluorine ions in these plasma studies was found to be 0.8 mm and so chosen as the maximum size for the probe diameter. Second, the probe must have a high aspect ratio.<sup>73</sup> That is, its length must be much greater than its radius. This allows the probe surface to be treated like an infinite plane, provided that the plasma sheath dimensions are sufficiently small in comparison with the probe dimensions. Further details regarding the constraints underpinning Langmuir probe design, as well as the method for the mean free path calculation, is discussed in Appendix A.

#### *RF Compensation*

Unlike a simple dc glow discharge, an rf plasma is not steady-state.<sup>77</sup> The plasma potential has a temporal nature that is present across the probe sheath, and consequently interferes with measurements of the I-V characteristic. This interference can cause the entire I-V characteristic to shift relative to the voltage axis. A simple yet effective way to eliminate this interference is through 'rf compensation' whereby a compensating electrode in the sampling region of the probe coupled to the tip across a capacitance (such as an insulating layer) superimposes the time-varying plasma potential onto the probe tip. Further discussion of the theory behind this technique is given in Appendix A.3.

#### *Filtering*

In the presence of an rf emitter the probe itself essentially behaves like a second antenna that will receive the rf signal and transmit this signal to the measurement circuit. This signal will then appear as high frequency noise on top of the measured current that the analyst is interested in, often accompanied by a higher frequency harmonic further complicating matters. For this reason the probe requires a filter within its circuit

(preferably as soon after the probe as is practicably possible), that is designed to have highest possible impedance at the drive frequency and its first harmonic, in this case 13.560 MHz and 27.120 MHz respectively.

### 2.2.2. The Langmuir Probe Used in This Research

The previous discussion arrived at the following set of constraints that must be considered in a Langmuir probe design:

- the tip must be of suitable material, such as tungsten to withstand the plasma environment;
- the tip radius must be much less than the minimum mean free path of the species under investigation, i.e.  $<0.8$  mm;
- the tip length must be much greater than the radius, and
- both rf compensation and filtering should be employed to obtain I-V characteristics from the Langmuir probe without undesired artefacts.

Figure 2.3 shows a photo and schematic of the Langmuir probe used in this work. The probe tip was tungsten wire, 0.3 mm in diameter, and extended 20 mm from its support. This resulted in a surface area of  $1.8 \times 10^{-5}$  m<sup>2</sup>. The tip was encased in ceramic, supported by a stainless steel (1.8 mm in diameter) compensating electrode. The entire probe assembly was supported by a copper plate attached to a 2¾ inch ConFlat™ fitting. The filter circuit used to remove the drive frequency and its first harmonic is shown in figure 2.4. This filter was located outside the vacuum space but was attached directly to the feed-through, minimising its distance from the probe. This design was deemed to satisfy all the constraints outlined previously.

### 2.2.3. Ramp Generation and Current-Voltage Measurement

The I-V measurement electronics and software, along with the method of generating the voltage ramp for the probe, have been detailed thoroughly by Deslandes<sup>108</sup> and as such will only be briefly discussed here.

The voltage ramp was supplied by an Agilent 33220A Programmable Function Generator. It consisted of a function with a linear sweep from -2.29 V to +2.29 V across a period that could be set by the analyst. This signal was then amplified to give a final probe bias sweep of  $\pm 50$  V. The sweep was triggered by a TTL pulse from a National Instruments (NI) data

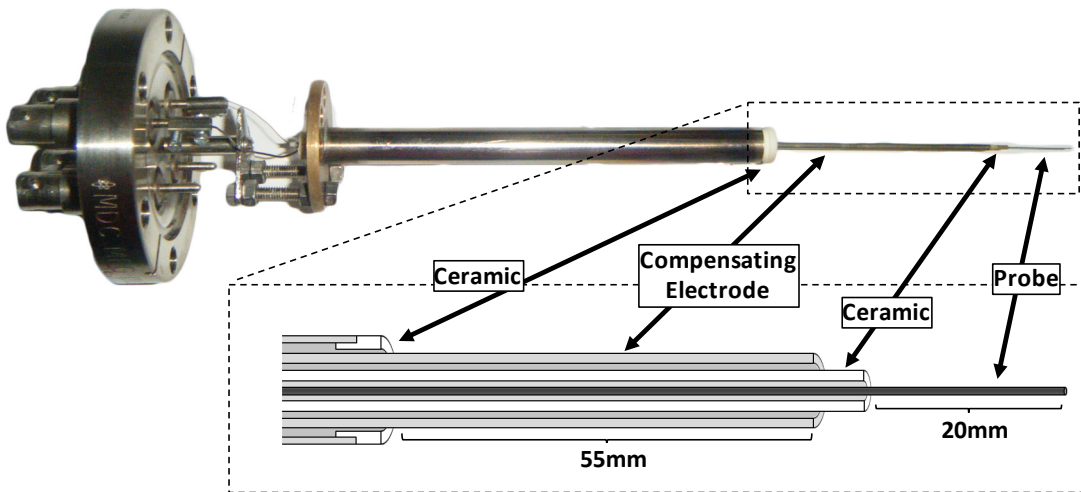


Figure 2.3. A photo and schematic of the Langmuir probe used in this research.

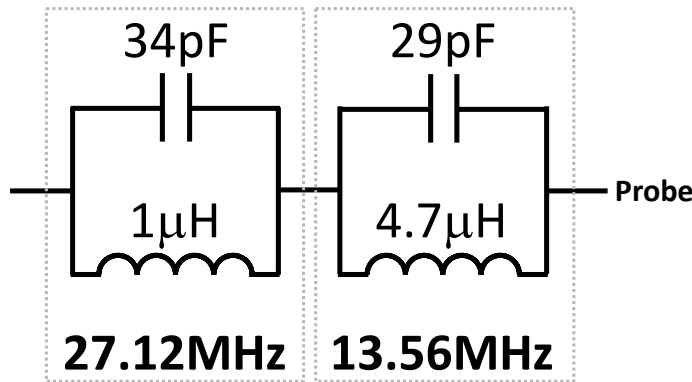


Figure 2.4. The filtering circuit used to remove the drive frequency and its first harmonic.

acquisition device, controlled by software written in the LabVIEW™ graphical programming environment. Analysis of the I-V curve was performed within the software, and was user operated.

#### 2.2.4. Analysis Procedure

Each I-V characteristic used for analysis was generated by taking the average of 100 individual I-V characteristics. In chapter 3, triggering and data collection was performed by a National Instruments (NI) USB-6008 device capable of collecting samples at a rate of 10 kS/s. This resulted in a typical I-V curve being collected in a 100 ms period. For reasons yet to be described in Chapters 3 and 4, the USB device was later swapped for a NI PCI-6024E data acquisition card that was capable of collecting data at a rate of 200 kS/s. For this device, the sweep was re-programmed so that each I-V measurement was collected in a 2.5 ms period.

## 2.3. Surface Characterisation Techniques

### 2.3.1. X-ray Photoelectron Spectroscopy

X-ray Photoelectron Spectroscopy (XPS) has been an invaluable surface characterisation tool since its main stream acceptance after extensive work by Kai Siegbahn, who received the Nobel Prize in 1981 for his work on the technique he named Electron Spectroscopy for Chemical Analysis (ESCA).<sup>5,109</sup> Since this time, XPS and ESCA are interchangeably used to describe the same technique. It is based on the photoelectric effect, discovered by Heinrich Hertz in 1887<sup>110</sup> and discussed by Albert Einstein in 1905,<sup>111</sup> who won the Nobel Prize in 1921 primarily for this work.<sup>112</sup> In this phenomenon, electrons are emitted from a material when it is exposed to radiation of sufficiently high energy. In XPS, samples under examination are irradiated by high energy (~keV) photons, and as a result electrons are emitted from the surface with some amount of kinetic energy. This energy is dependent on the binding energy of the element from which it was ejected. Using a spectrometer capable of distinguishing between and subsequently detecting electrons of varying kinetic energy, a spectrum comprised of multiple peaks from the elemental makeup of the surface is gained. This spectrum then becomes a ‘fingerprint’ for the chemical composition of the surface. It is this feature, along with its high surface sensitivity, that has allowed the technique to receive strong recognition as an important tool for the characterisation of material surfaces.

#### *XPS Theory*

Presented in figure 2.5 are the processes involved in XPS. Upon irradiation with a photon of energy  $h\nu$ , energy is absorbed by a usually core-level electron of binding energy  $E_b$ . This electron, provided it has sufficient energy, is then ejected from the element with kinetic energy  $E_k$ , leaving a hole in the shell. Electrons liberated in this way are labelled photoelectrons. The atom, now in an excited state, relaxes via an electronic transition from a higher energy shell which in turn releases energy either through the emission of an X-ray photon, or the liberation of a further higher level electron. The latter process is known as the Auger effect, and the electron an Auger electron, named after Pierre Auger<sup>113</sup> despite the fact that Lise Meitner discovered the process in 1922, a few years earlier.<sup>114</sup>

The amount of kinetic energy the electron has after it escapes depends upon the binding energy of the shell from which it left, and the incident photon energy, by the relationship

$$E_k = h\nu - E_b - \Phi_{sp} \quad (2-1)$$

where  $\Phi_{sp}$  is the spectrometer work function, a term used to account for the work function of the material under study,  $\Phi_s$ , and the work function of the analyser, as seen in the energy level diagram in figure 2.6.<sup>115</sup> This term can be experimentally determined as detailed in Appendix B.1, and accounted for prior to data collection. The kinetic energy of the Auger electron in figure 2.5 is given by

$$E_k = E(K) - E(L_1) - E(L_{2,3}) \quad (2-2)$$

and it would be labelled as a KLL Auger electron.

The spectrometer work function can be accounted for experimentally, and thus it is often removed from equation (2-1) to give

$$E_k = h\nu - E_b \quad (2-3)$$

and hence the binding energy of an element can be determined through measurement of the kinetic energy of an electron ejected under irradiation of a known photon energy. It should be noted that this analysis is only valid when the Fermi level,  $E_F$ , is the same for both the sample and the spectrometer. This requires that samples be both conductive and in electrical contact with the spectrometer during analysis.

From equations (2-2) and (2-3), it can also be shown (through discussion in Appendix B) that when plotted on a binding energy scale, the energy at which Auger peaks will appear is dependent on the incident photon energy. This property can be very useful when dealing with Auger peaks that overlap with photo-peaks of interest, as it means that by simply changing excitation energy, one can deconvolute these peaks from one another.

A lab-based XPS system will commonly utilise X-rays generated by a source that accelerates electrons thermionically emitted from a filament, the cathode, into a metal target, the anode, at high energy. This produces X-rays of a specific wavelength that is dependent on the type of metal anode used. The most common anodes used in XPS systems are aluminium (Al) and magnesium (Mg), which produce  $K\alpha$  radiation of energy 1486.6 eV and 1253.6 eV respectively. X-rays of this energy are capable of penetrating  $\sim 1 \mu\text{m}$  into the bulk of the sample. However, electrons that are ejected from irradiated atoms only escape from a very shallow depth within the surface, and depending on the kinetic energy of the electron this depth is usually between 1 – 10 nm. The distance that an electron travels through matter without losing energy due to collisions is called the inelastic mean free path (IMFP, denoted  $\lambda$ ) and is plotted in figure 2.7.<sup>116,117</sup> The fact that  $E_k$  is sufficient to result in this shallow escape depth gives XPS its surface sensitivity.

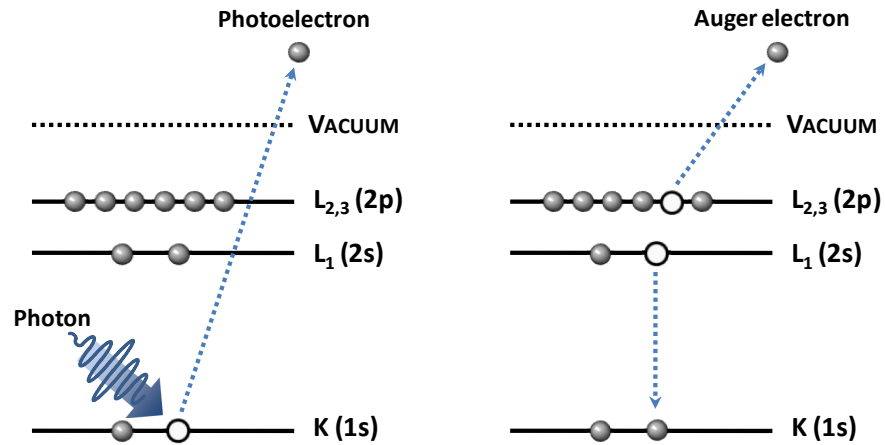


Figure 2.5. The two processes involved in XPS. Modified from Kibel.<sup>115</sup>

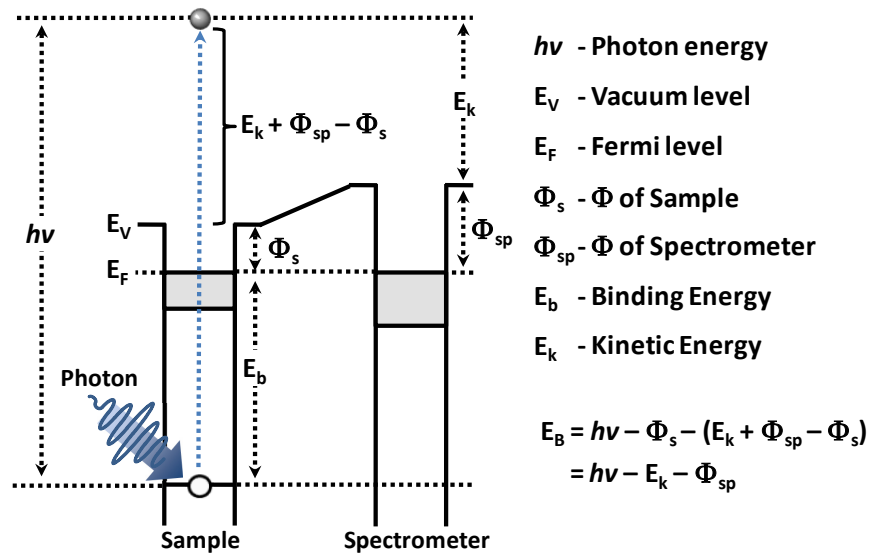


Figure 2.6. An energy level diagram representing the photoemission process and its relation to the spectrometer work function. Modified from Kibel.<sup>115</sup>

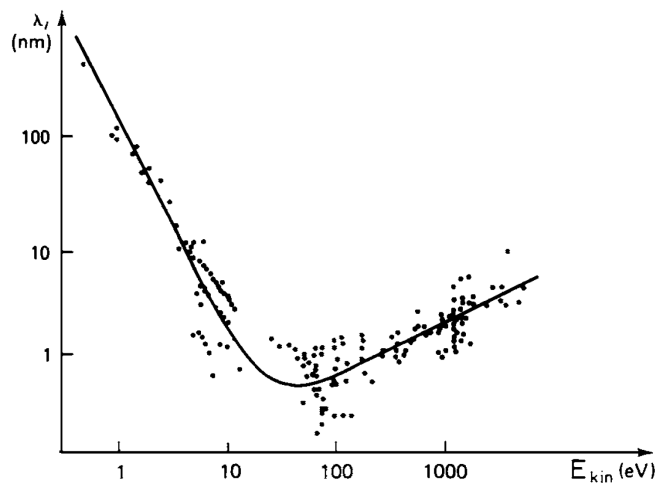


Figure 2.7. The inelastic mean free path of an electron plotted against its kinetic energy. Reproduced from Sigle,<sup>117</sup> originally published by Seah and Dench.<sup>116</sup>

*The LHS-10 XPS System*

Pictured in figure 2.8 is the XPS system used in this work. Originally commissioned circa 1980, the Leybold-Heraeus LHS-10 was capable of performing XPS, Auger electron spectroscopy, and ion scattering spectroscopy, although during this work it was configured to perform only XPS measurements.

The system, similar to the plasma reactor discussed previously, consisted of a main analysis chamber, and a smaller load-lock chamber. Both volumes were pumped by turbo-molecular drag pumps, and backed by rotary vane pumps. XPS requires ultra-high vacuum (UHV) conditions to allow the electrons ejected from the sample to be detected without significant loss in energy due to interactions with gaseous species. Therefore, the main chamber had an ultimate pressure of  $\sim 10^{-10}$  Torr, although under regular use it maintained a pressure of  $\sim 1 \times 10^{-9}$  Torr when no sample was present, and better than  $\sim 10^{-8}$  Torr during analysis.

The LHS-10 employed an EA-10/100 concentric hemispherical analyser (CHA) electron spectrometer. This type of analyser, represented in figure 2.9, consists of two stainless steel hemispheres of radii  $r_1$  and  $r_2$ , positioned concentrically on top of one another. The surfaces are biased with negative voltages  $V_1$  and  $V_2$  respectively, with  $V_2$  greater than  $V_1$ . Consequently there exists an equipotential surface between the hemispheres with

$$V_0 = \frac{V_1 r_1 + V_2 r_2}{2r_0}$$

along the surface defined by

$$r_0 = \frac{r_1 + r_2}{2}$$

where  $r_0 = 97$  mm for the EA-10/100. An electron focused onto the entrance slit from the electrostatic lens system that has kinetic energy of  $E = eV_0$ , where  $e$  is the elemental charge, will travel along the surface defined by  $r_0$  and consequently be focused onto the exit slit and detected. An electron that enters the analyser with energy significantly less than  $eV_0$  will be accelerated towards the inner hemisphere and therefore not focused onto the detector. Likewise, a higher energy electron entering the analyser will be accelerated towards the outer hemisphere. Since  $r_1$  and  $r_2$  are fixed, sweeping the voltage  $V_1$  and  $V_2$  allows the CHA to selectively pass and subsequently detect only electrons of a specific energy. The electron kinetic energy that will traverse through the analyser and be detected is known as the pass energy  $E_0$ .



Figure 2.8. The LHS-10 XPS System at Flinders University.

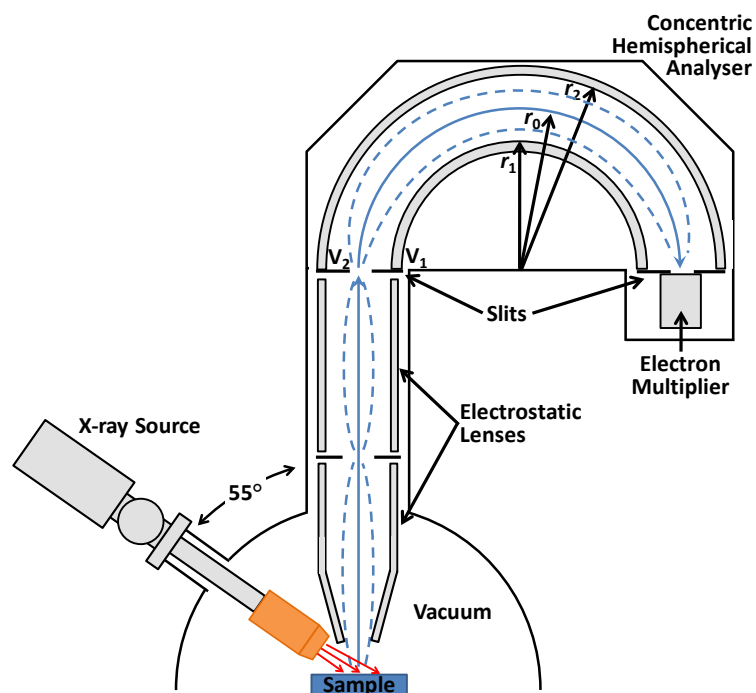


Figure 2.9. A schematic representation of the concentric hemispherical analyser (CHA) and its lens system. CHA modified from Kibel.<sup>115</sup>

The CHA and its lens system can be operated in two modes, a fact that becomes important in later chapters when analysing XPS data. Traditionally the voltages on a CHA are not scanned, but instead are fixed at a certain value of  $V_0$ , and hence allow only a fixed  $E_0$ . This relies then on the lens system to slow electrons down to the required energy by the use of a retarding field so that they may pass through the analyser. That is, if the pass energy of the CHA is set to 50 eV, then electrons of kinetic energy 500 eV must be slowed

**Table 2.1. X-ray sources and related energies and line widths. From Kibel.<sup>115</sup>**

Anode Type	Energy (eV)	Line Width (eV)
Al K $\alpha$	1486.6	0.85
Mg K $\alpha$	1253.6	0.70

by 450 eV to be allowed to pass through the analyser. This mode is known as fixed analyser transmission (FAT) mode, also known as constant analysis energy (CAE) mode. This mode provides a constant analyser resolution across the entire energy range under study. A second mode, called constant retarding ratio (CRR) mode, sweeps both the CHA voltages and the lens system. This mode slows electrons by a constant ratio of the electron energy to be detected. That is, if a 500 eV electron is to be detected, and the retarding ratio,  $B$ , is set to 10, then the electrons are slowed to 50 eV and  $E_0$  is set to 50 eV. This analysis method does not have a constant resolution like FAT mode, but instead maximises signal across the entire energy range. In summary, FAT mode gives constant energy resolution; CRR mode gives constant resolving power. Therefore in this research, CRR mode was used for wide energy sweeps for qualitative analyses and FAT mode was used for high resolution scans of narrow energy bands for quantitative analyses.

The LHS system utilised a Specs XR-50 Dual-Anode X-ray source mounted such that the angle between the source and the analyser lenses was 55°. Installed in 2008, the XR-50 replaced the previous source after a failure of the anode allowed water to enter the UHV system, effectively forcing a complete rebuild of the instrument. The XR-50 was capable of providing either Al K $\alpha$  or Mg K $\alpha$  radiation, details of which are provided in table 2.1, which afforded certain advantages to the experimentalist. One such advantage was the access to the narrower width of the Mg K $\alpha$  X-ray line, giving rise to increased spectral resolution. Another, and perhaps more useful advantage was that with multiple excitation energies, one had the ability to deconvolute Auger peaks from photopeaks should they interfere with one another, simply by changing anodes. As discussed earlier in brief, and in detail in Appendix B, on a binding energy scale Auger peak position is dependent on the excitation energy. For example, an Auger peak that would appear at an energy of 700 eV under illumination by Al K $\alpha$  radiation would be shifted by 233 eV when exposed to Mg K $\alpha$  radiation and appear at an energy of 467 eV. The importance of this dependence becomes crucial in chapters 6 and 7 when discussing synchrotron based XPS.

*Development of a New Data Acquisition System*

To replace the X-ray source the LHS-10 system was decommissioned for a significant period of time during which the dated computer system that was used to acquire data, a Microbits PC with Intel 486 CPU running Windows™ 3.1, was also replaced. This required the design and commissioning of a new data acquisition system that would bring the LHS more in line with modern instruments.

Figure 2.10 shows a simplified flow diagram for the conventional data acquisition process on the LHS-10. Scan parameters such as sweep width, start energy and scan time were input to the sweep generator by the analyst. This unit would then output a 0-10 V signal to both the data-logging PC and the high voltage bipolar amplifier according to those settings. The amplifier related the 0-10 V to a 0-2000 eV energy sweep, and set the voltages for the CHA and the lenses accordingly. When the user started the scan, the sweep generator would ramp the voltage across the range specified and likewise the analyser was ramped across the energy range by the amplifier. Pulses due to electron detection were output from the detector preamplifier and counted by the ratemeter as the energy was swept. The ratemeter would then output a 0-10 V signal to the PC related to the count rate. The signals from the sweep generator and the ratemeter were finally combined to produce the spectrum. This method effectively made the PC a ‘dumb’ data logger; it had no real control over the scan itself. It also limited the flexibility of the instrument in that the user could only select values for the scan time and sweep width that were available on the unit.

The solution to this was to replace the sweep generator with a computer controlled device capable of a 0-10 V analog signal output. Voltage resolution was however an important issue regarding the design of a new sweep generator. The old system would output 1800 points regardless of the magnitude of the sweep. Across a 1000 eV range this equated to 0.555 eV/step, or 2.775 mV/step ( $10\text{ V} \equiv 2000\text{ eV}$ ), which was achievable with many analog output devices such as the NI PCI-6024E card used with the Langmuir probe. However, XPS analyses would frequently require much narrower scans, in the order of tens of eV. Across a 20 eV range then, the required step width was only 0.055 mV. The PCI-6024E card had a 12-bit digital to analog converter (DAC) and was therefore capable of a maximum voltage resolution of 2.5 mV across 10 V, meaning at best it could do steps of 0.5 eV. The desired energy resolution for high quality XPS spectra would be 0.01 eV which would require at least an 18-bit DAC. To this end a computer controlled sweep

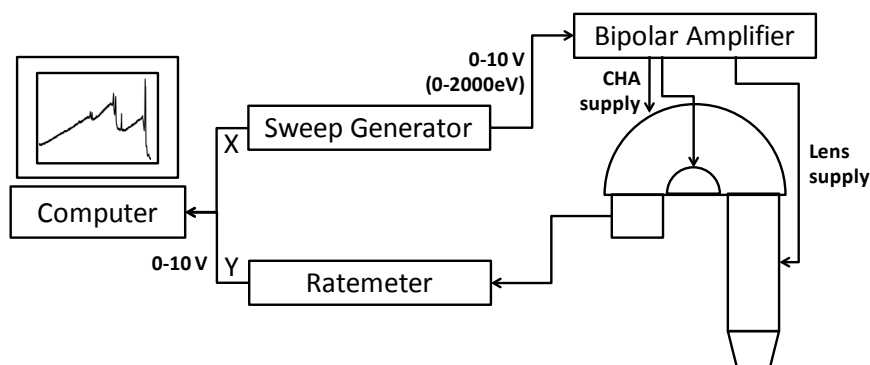


**Figure 2.10.** Simplified flow diagram for the data acquisition process on the LHS-10.

generator using a 24-bit DAC was built in-house by the electronics workshop in the School of Chemical and Physical Sciences. Voltage output from the DAC was set by a micro-controller, and controlled via a USB-Serial interface by simply writing a voltage value to the micro-controller. This output was connected to the bipolar amplifier via the existing connection. The photoelectron signal was recorded by direct measurement of the ratemeter output (0-10 V) using a NI USB-6008. To produce the final photoelectron spectrum the two signals were combined in software written in LabVIEW™, a screenshot of which is shown in figure 2.11. The software, named XSpect, gave the user absolute control over all scan parameters, as well as the ability to perform a series of scans across multiple regions, to average multiple data sets, and to save and re-use scan parameters, aiding consistency between experiments. Data was saved as comma separated value (.csv) files. The energy scale was also calibrated within the software, reducing post-processing requirements. Detailed discussion surrounding the design and operation of the XSpect software is given in Appendix D.

#### *Sample Requirements for XPS*

Pictured in figure 2.12 are the sample mounts that were available for use with the XPS. The standard mount was machined from aluminium and allowed multiple small samples, or a single large sample to be mounted. The total sample size was required to not exceed the dimensions of the top of the mount otherwise problems could arise during transfer to and from the chamber. Samples could be mounted via carbon tape, a conductive adhesive tape, or by mechanical attachment using screws. As discussed earlier, due to the requirement of UHV conditions to conduct XPS experiments, samples needed to be ‘vacuum compatible’. That is, they needed to be free of excess solvent and mounted such that particulates would be prevented from entering the chamber uncontrolled. Samples also needed to be conductive to ensure excessive charging did not occur during analysis.

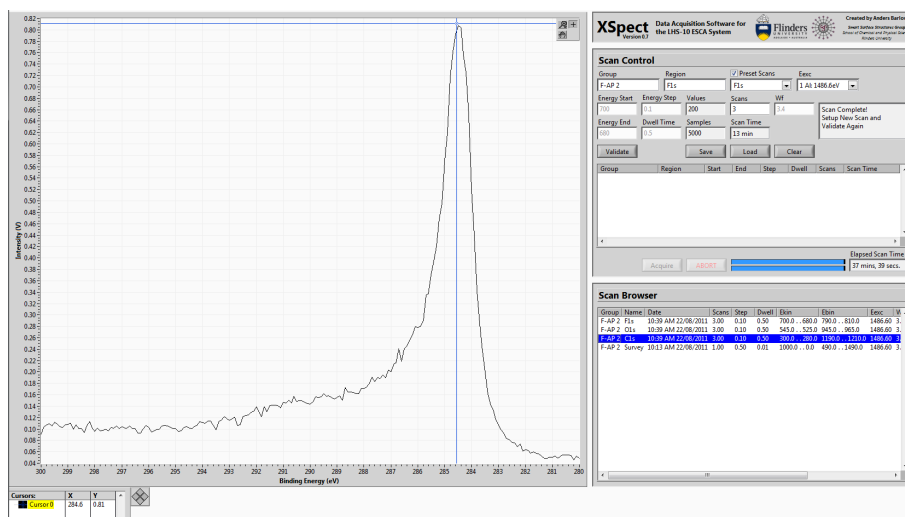


Figure 2.11. A screenshot of XPSpect, the software programmed during this work.

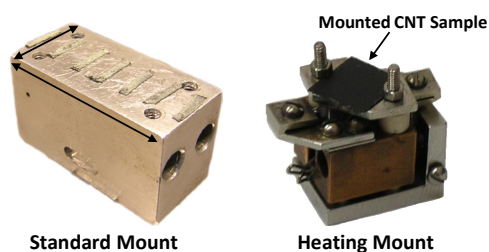


Figure 2.12. The sample mounts available for use with the LHS-10.

### Data Analysis

The analysis of XPS spectra was performed using a combination of software packages; Fityk and CasaXPS. Fityk (version 0.8.3) is a freeware software package for general purpose peak fitting and spectral analysis.<sup>118</sup> CasaXPS is a licensed peak fitting software package designed almost exclusively for the analysis of XPS spectra. Each software package enabled the fitting of mixed Gaussian-Lorentzian peaks (or Voigt shapes as in Fityk) with control over the position, shape and total area of the fitted components.

### 2.3.2. Raman Spectroscopy

Raman spectroscopy is a technique that probes the vibrational and rotational modes of a system. It utilises monochromatic light typically in the visible or near IR spectrum to excite vibrations and phonons via inelastic scattering processes. The result is a small fraction of light being scattered with energy different to that of the incident light and this variation in energy is measured against the excitation energy to obtain a Raman spectrum.

*The Raman Effect*

When light impinges on a medium it can be transmitted, absorbed or scattered. For the latter case, light may be scattered elastically; *without* change in energy, or inelastically; *with* change in energy. The elastic scattering of a photon, shown in figure 2.13, is named Rayleigh scattering after Lord Rayleigh used this phenomenon to explain how sunlight is scattered by air molecules to produce the blue sky.<sup>119</sup> When light is incident on a molecule it may excite that molecule from its ground state up to some higher ‘virtual’ energy level (dashed line in figure 2.13). This level is unstable for the molecule and so it may scatter a photon and relax back to its initial ground state. Since there is no net change in the energy of the molecule the scattered photon therefore has the same energy as the incident photon.

C.V. Raman described a second type of scattering now known as the Raman effect whereby photons incident on a molecule are scattered with either a gain or loss in energy, work for which he received the Nobel Prize in 1930.<sup>120</sup> In figure 2.13, after the molecule has been excited by the incident photon, rather than relaxing back to the ground state the molecule may drop in energy to an excited vibrational state, emitting a photon in the process. In this case the scattered photon has energy equal to the incident photon energy *minus* the energy of the excited vibrational state, thus having a longer wavelength than the excitation wavelength.<sup>121</sup> This is known as Stokes scattering, named after Sir George Stokes who posited that fluorescent radiation must occur at longer wavelengths than that of the incident radiation.<sup>122</sup>

The third case in figure 2.13 results when the molecule is already in an excited state and the incident photon raises its energy to a higher virtual level than that in Stokes scattering. The molecule may then relax down to its ground state, in which case it scatters a photon of energy equal to the incident photon energy *plus* the energy of the initial excited state. Since this photon has wavelength shorter than that of the incident photon, the process is known as anti-Stokes scattering.<sup>121</sup> Experimentally one observes a different intensity for the Stokes and anti-Stokes lines. From Boltzmann statistics, it can be shown that at room temperature the probability of finding a molecule in its ground state is much greater than that for an excited state. This leads to the Stokes process being far more favourable at room temperature than the anti-Stokes process and the Stokes lines being more intense than the anti-Stokes lines. Rayleigh scattering remains the dominant process however, with only 1 in  $\sim 10^6$  photons being scattered inelastically.<sup>121</sup>

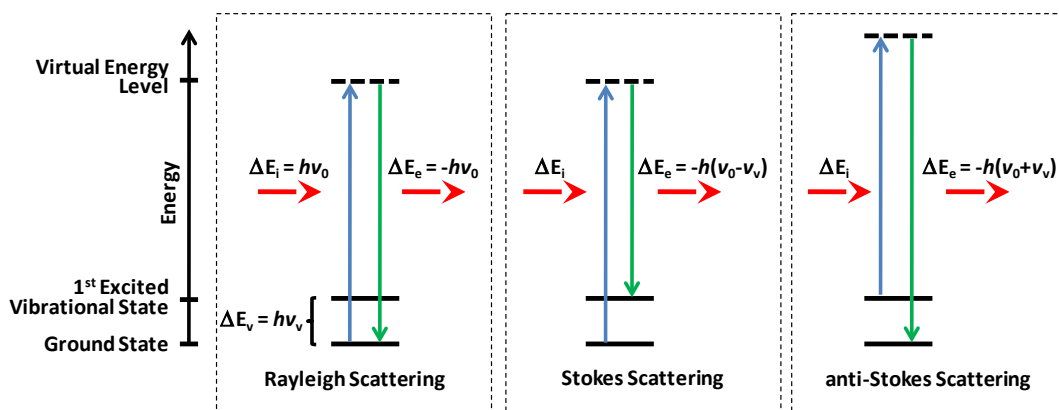


Figure 2.13. The Raman effect. Modified from Smith and Dent.<sup>121</sup>

It is the change in photon energy due to inelastic scattering that is measured in Raman spectroscopy to generate a spectrum, with the intensity plotted against a wavenumber (a unit of energy) shift relative to the original laser photon energy (thus the units of  $\text{rel. cm}^{-1}$ ).

#### *Resonant Raman Processes*

Discussion of the Raman effect up to this point has assumed that the energy of the incident photon does not match real electronic transitions within the system, and the excited energy levels are considered ‘virtual’ levels. However, it is entirely possible to have an excitation energy that matches an electronic transition in the molecule and when this occurs the intensity of the associated Raman line is greatly increased, sometimes by as much as a factor of  $10^3$ .<sup>123</sup> Resonant Raman spectroscopy makes use of this phenomenon with tuneable excitation energies. The idea of resonant enhancement extends further when applied to single-walled carbon nanotubes. If the energy of the incident or scattered light matches the energy of a van Hove Singularity (vHS) in the Joint Density of States (JDOS) then the Raman signal becomes very intense for any tube in resonance.

#### *The Witec Alpha 300*

Pictured in figure 2.14 is the Witec Alpha 300 Raman instrument used in this work. It combined a conventional Raman spectrometer with a confocal microscope, giving the dual ability to collect spectra and images of samples under study. Excitation was achieved through a laser of wavelength 532 nm (frequency doubled Nd:YAG, 1064 nm). The Alpha system used a charge coupled device (CCD) spectroscopic detector with a spectral resolution defined by the monochromator grating used (and thus the width of the scan) and the resolution of the DAC, which in the case of the Witec instrument is 10 bit, resulting in 1024 bins across the spectrum. Most spectra were obtained using a 600 lines/mm grating, giving an ultimate spectral resolution of  $\sim 4.7 \text{ cm}^{-1}$  across a range of  $\sim 3900 \text{ cm}^{-1}$ . Some

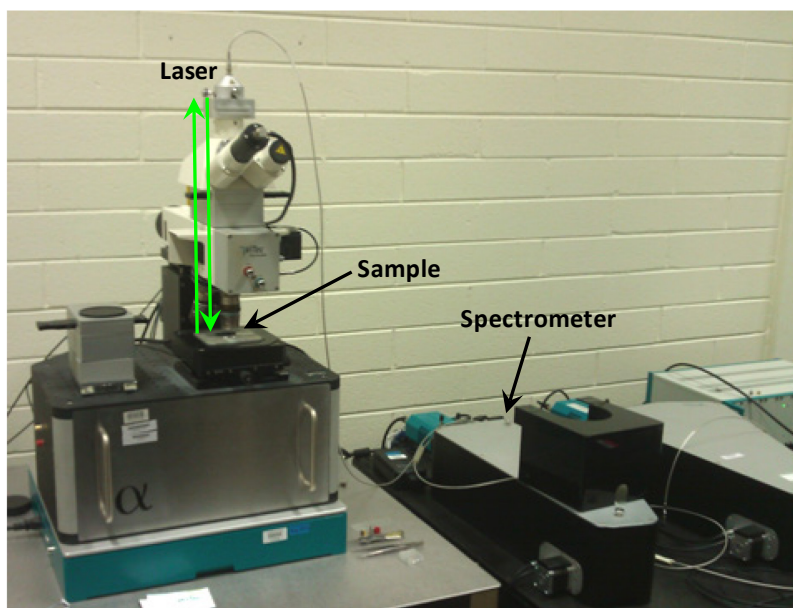


**Figure 2.14. The Witec Alpha 300.**

spectra were also obtained using a higher resolution grating with 1800 lines/mm, which gave an ultimate resolution of  $\sim 1.2 \text{ cm}^{-1}$  but a range of only  $\sim 1200 \text{ cm}^{-1}$ . Thus the high resolution grating could only be used for narrower scans across specific peaks.

#### *Sample Requirements for Raman*

Requirements for Raman spectroscopy were not as stringent as those for XPS since the technique was performed in ambient conditions. Samples needed to simply be flat, and reasonably bound to a substrate for ease of handling and to prevent particulates from entering the lenses of the Witec instrument. Substrate choice was not of concern provided the sample covered enough of the material to prevent any signal from the underlying surface being detected. It was prudent however to choose a substrate that provided the flattest surface to make focusing of the laser easy to achieve and maintain while scanning.

#### *Analysis*

Data analysis of Raman spectra was performed using the Witec Project 1.90 software packaged with the instrument.

### 2.3.3. Electron Microscopy

Some of the work discussed in this dissertation involved the use of electron microscopy to image CNTs and the surfaces made using them. In simplest terms, there are two types of electron microscope; the transmission electron microscope (TEM) and the scanning electron microscope (SEM). The main difference between these two techniques comes

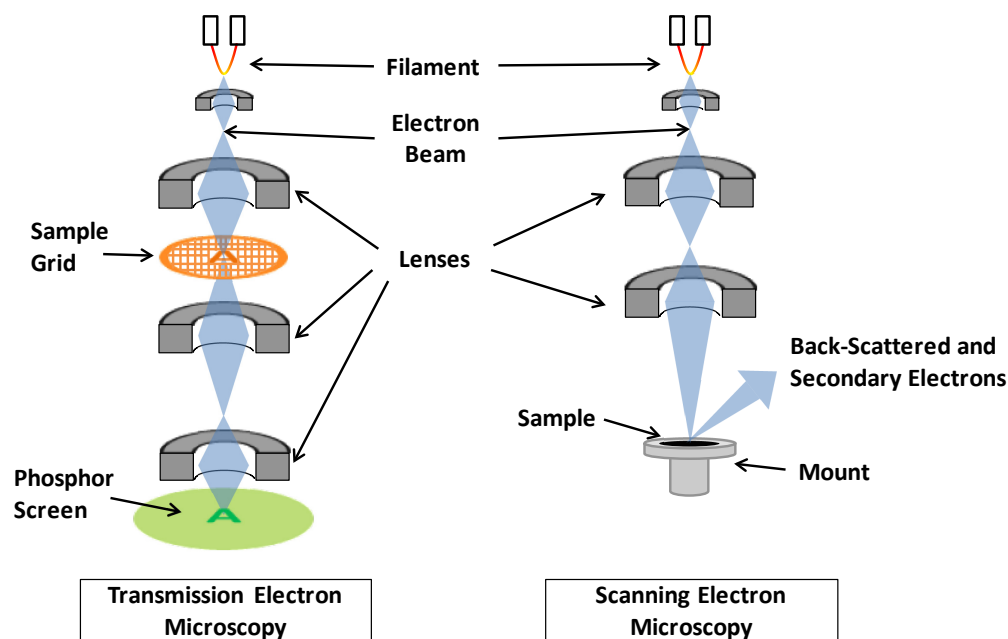


**Figure 2.15. A pictorial representation of the two electron microscopy techniques; transmission (left) and scanning (right) electron microscopy.**

from the way in which a beam of electrons interacts with a specimen under analysis, and how this interaction is detected. Figure 2.15 shows a simple pictorial representation of the way these techniques operate. In TEM, electrons are generated through the thermionic emission from a filament. This beam is then passed through the sample under analysis which must therefore be sufficiently thin to avoid total attenuation of the beam. The electrons are incident on a detection medium such as a phosphor screen, or a CCD camera, which generates the image. When operated in the most common mode the contrast in TEM comes from the attenuation of the electron beam, and is related to the thickness of the sample as well as the material from which it is composed. In a typical TEM image the light areas represent sections of the sample that provided little attenuation, while dark areas represent sections that provided significant attenuation. This mode is called ‘bright field’ TEM.<sup>124</sup> Other methods of contrast formation are available although not used in this work. While the electron generation as well as the focusing and magnification optics remain largely the same between the techniques, the formation of an image in SEM is quite different. In this case electrons incident on the surface can interact with the sample in a variety of ways. They may elastically scatter from the atoms in the sample, in which case the detection is provided by a ‘back-scatter’ detector. Inelastic scattering may occur, which subsequently results in the ejection of a secondary electron from the atoms in the surface the detection of which is performed by a secondary electron detector. Finally, inelastic

scattering may give rise to the emission of X-ray radiation, which can be detected by a fluorescent X-ray detector and can be used to identify the chemical makeup of the sample.

In initial work TEM was used to confirm the presence of CNTs after plasma exposure as the Raman instrument was not yet readily available at Flinders. The instrument used was a Philips CM100 TEM, which was part of the suite of microscope facilities at Adelaide Microscopy. Samples were required to be mounted onto TEM supports which in this work were copper grids with 50  $\mu\text{m}$  holes on top of which was a carbon support film known as 'lacey carbon'. This film was present across the entire grid and allowed CNTs to lie across holes that were sufficiently large to enable TEM analysis, but not so large that the CNT was not supported at each end. CNTs were deposited directly onto the grids from solution (details of which are given in Section 2.4.2) and allowed to dry at elevated temperatures under vacuum for a period of hours to ensure their compatibility to the vacuum of the TEM instrument. Requirements for SEM were not as stringent, with CNT surfaces mounted onto SEM 'stubs' using carbon tape. The surfaces were generally coated with 5 nm of platinum prior to analysis to provide surface conductivity and minimise the effects of charging.

#### 2.3.4. Synchrotron Soft X-ray Absorption and Photoemission Spectroscopy

To complement lab-based XPS studies, experiments were also performed on the Soft X-ray (SXR) beamline at the Australian Synchrotron in June 2008 and August 2010. The Australian Synchrotron is a 3 GeV third generation synchrotron light source located in Clayton, Victoria. Advantages of synchrotron based techniques are detailed where relevant in Chapters 6 and 7, and only experimental details are given here.

##### *The SXR Beamline (SR14ID01) and its End-Station*

Pictured in figure 2.16(a) is a representation of the optics along the SXR beamline from the storage ring to the experimental end-station.<sup>125</sup> Highlighted in red boxes is the plane grating monochromator (PGM) and elliptically polarised undulator (EPU). These components were varied continuously and simultaneously by the user via the end-station highlighted in the blue square. This allowed the EPU to be adjusted such that the fundamental photon energy output from the insertion device remained as desired, while the monochromator was always tuned to this energy providing the highest possible spectral resolution at all times. Details regarding the specifics of the beamline as well as deeper technical and performance aspects have been published elsewhere.<sup>126</sup> The end-station,

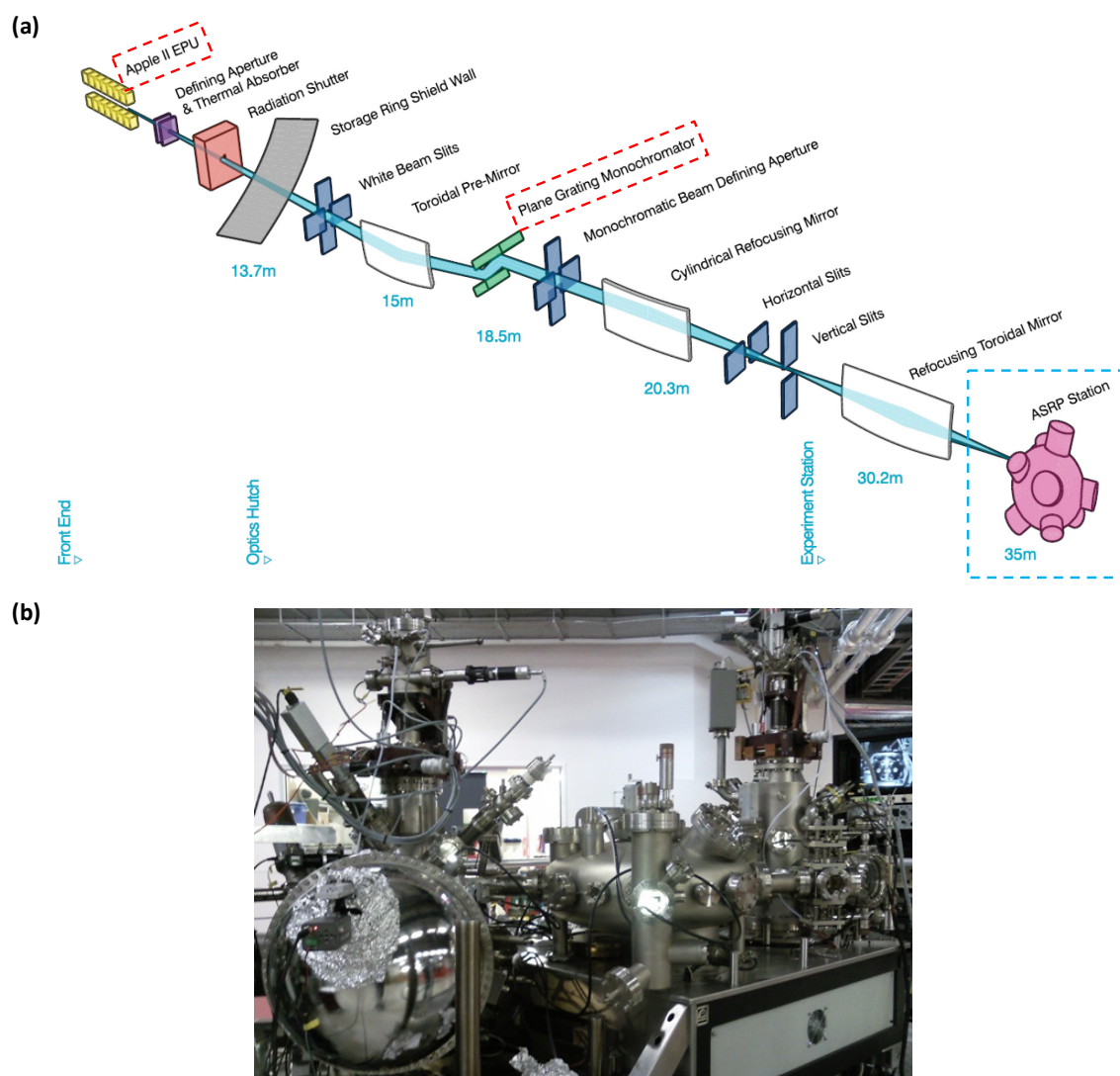


**Figure 2.16. (a) Pictorial representation of the soft X-ray beamline at the AS<sup>125</sup> and (b) a photo of the experimental end-station.**

designed by Precision & Vacuum Technologies, is photographed in figure 2.16(b). Analysis of the electron energy was performed by a SPECS Phoibos 150 CHA. Detection was achieved by nine single channel electron multipliers. This meant the analyser was essentially capable of measuring nine spectra at once, greatly improving signal to noise. Samples were mounted on a stage capable of linear movement along three axes;  $x$ ,  $y$  and  $z$ ; as well as rotation about the  $z$ -axis and the sample stage normal.

#### *Sample Requirements for Synchrotron Studies*

The requirements for samples used in synchrotron studies were much the same as those for XPS due to the techniques being performed under UHV conditions. Additionally however, samples under study in the end station on the SXR beamline benefited from being as thin as possible. This allowed more accurate alignment of the sample angle to the X-ray beam.

## 2.4. Preparation of Samples

### 2.4.1. Highly Ordered Pyrolytic Graphite

HOPG (10 mm x 10 mm, ZYH grade) was purchased from Coherent Scientific, Australia. Prior to experiments the surfaces were cleaved using adhesive tape to expose a fresh layer of graphite. This method of preparation did not produce any detectable impurities on the HOPG surface during analysis, and ensured a consistent surface chemistry prior to a given plasma exposure. The HOPG used in this work was self-supporting, requiring no underlying substrate to be used during analysis. The samples were flat enough to be used in the Raman instrument without significant problems, and have conductive, vacuum compatible surfaces allowing them to be suitable for lab-based and synchrotron photoelectron spectroscopy techniques.

### 2.4.2. Carbon Nanotubes

Single-walled CNTs were purchased from Carbon Solutions (produced by Arc discharge, nickel-yttrium catalyst) and CNI (produced by HiPCO, iron catalyst). In both cases the nanotubes were purchased in their as-produced, un-purified state, resulting in some catalyst contamination being detectable, particularly in the case of HiPCO CNTs.

Nanotube material was dispersed in a solution of N,N-dimethylformamide (DMF) at a concentration of 2 mg/mL (20 mg into 10 mL of DMF) via bath sonication for 30 minutes at room temperature. The chosen substrate was placed at the bottom of a glass vial and 0.5 mL of the nanotube solution deposited on top, completely submerging the substrate. This was then baked at 150°C to evaporate the solvent, leaving behind a dense ‘bucky paper’ firmly adsorbed onto the substrate. Once appropriately dried, these surfaces were highly vacuum compatible, requiring minimal pump-down times.

### 2.4.3. Substrate Choice

The choice of the supporting substrate for CNTs depended largely on the analysis technique to be employed. As discussed throughout Section 2.3, there were certain constraints regarding the way in which samples needed to be handled in order for them to be accommodated within each instrument. To summarise, samples needed to be vacuum compatible, flat, and conductive. Additionally, samples to be produced for analysis using the SXR beamline needed to be as thin as possible without compromising strength.

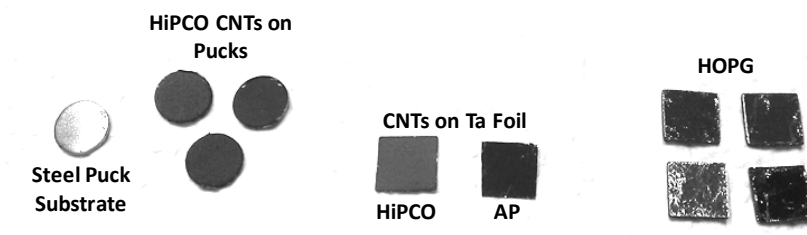


**Figure 2.17. Pictures of various substrates supporting deposited bucky papers, and the self-supporting HOPG samples.**

To this end, two substrates were chosen to support the bucky paper samples; silicon wafer and tantalum sheet, both cut to appropriate sizes. Silicon allowed for very flat samples to be produced for analysis under Raman, while also giving suitable conductivity for XPS. Tantalum sheet allowed for very flat samples to be produced, while also giving excellent conduction from the surface through to the substrate, making it ideal for use in synchrotron experiments. The use of tantalum has the added benefit of the element not being present anywhere else in this work, and as such can be used to indicate when the substrate is being detected, and hence when measurements may be compromised.

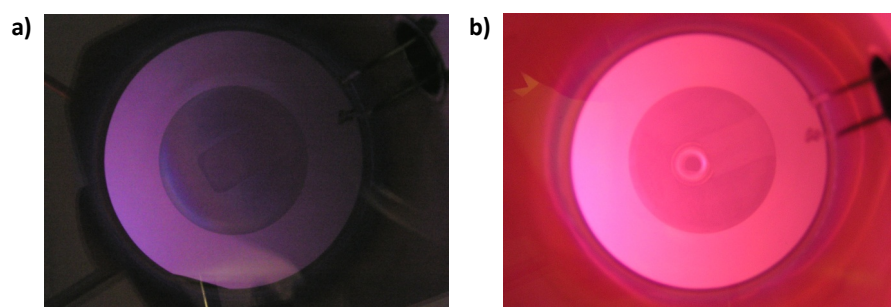
## 2.5. Plasma Surface Modification

### 2.5.1. Gases

Table 2.2 shows the gases used in this research along with suppliers and percentage purities. All gases used in this research were of high purity research grade and were supplied to the experimental chamber via stainless steel Swagelok™ tubing. All gas lines were evacuated prior to experiments to test vacuum tightness and then purged with the reactant to ensure maximum purity at all times. Prior to an experiment, ‘test’ plasma would be ignited to check for visible signs of contaminant within the chamber. Fortunately pure SF<sub>6</sub> plasma presented as a deep purple colour that was barely visible at low power, and was localised around the antenna. In contrast, nitrogen plasma at the same power and pressure was bright pink in colour, and also well dispersed throughout the chamber. Consequently, SF<sub>6</sub> plasma that was contaminated with nitrogen, either due to a vacuum leak in the system or to improper preparation of the gas lines, was easy to spot from the colour of the plasma, as depicted in figure 2.18.

**Table 2.2. Gases used in this research including the purity and supplier.**

Reactant Gas	Purity (%)	Supplier
Sulphur Hexafluoride, SF <sub>6</sub>	99.9	Coregas
Oxygen, O <sub>2</sub>	99.95	BOC
Hydrogen, H <sub>2</sub>	99.99	CIG
Nitrogen, N <sub>2</sub>	99.9	BOC
Argon, Ar	99.99	Linde
Methane, CH <sub>4</sub>	99.95	BOC

**Figure 2.18. Photographs of test plasma showing a) pure SF<sub>6</sub> and b) SF<sub>6</sub> contaminated with nitrogen from improperly cleaned and purged gas lines.**

### 2.5.2. Variations in Experimental Parameters

Specific details regarding each experiment will be given in the thesis chapters when necessary, however the detailed description here is the experimental protocol that was followed when modifying any of the experimental parameters.

#### *RF Power and Gas Pressure*

As any change in the experimental parameters also changed the match between the electronics, the antenna and the plasma, experiments were designed and performed in such a way as to ensure measurements of a particular quantity remained valid between each experiment.

In the plasma reactor at Flinders University, for a given gas pressure the change in match did not vary significantly over the accessible rf power range. However, if one were to minimise the reflected rf power at a low power, such as 10 W, then it was likely that at a much higher power, the reflected component would be found to be significant. This was not necessarily indicative of a change in the match required, but more that the appropriate match was not achieved at the low power in the first place. It would merely appear as

though the match was correct due to the very low applied power. This led to the protocol of matching all plasma at the highest obtainable rf power first, and then reducing the power to the lowest desired value for the experiment without varying the acquired match.

In contrast with power, variations in gas pressure in turn required significant variation of the matching unit values in order to minimise reflected power. As a general trend, increasing pressure required C1 (within the matching circuit presented in figure 2.2) to also be increased in value, with C3 often remaining constant once matched at the starting pressure. Thus, when trying to ascertain the effect of changing gas pressure on the properties of the plasma and its effect on functionalisation, care needed to be taken to ensure both variations in pressure and match were suitably accounted.

#### *Gaseous Mixtures*

With the experimental setup used in this research, a maximum of two gases could be introduced into the chamber at any one time, however only one gas line was automatically controlled. This meant that when performing experiments involving mixtures, the partial pressure of the gas on the manual leak valve line needed to be set first, and then the total desired pressure set on the APC. This presented a possible source of error in that if the partial pressure supplied by the manual valve were to change, the APC would compensate by opening the second line further, and overall the total pressure would not change. This kind of drift in pressure was quantified over the nominal experimental timeframe and found to be insignificant.



---

## **Chapter 3.**

# **PRELIMINARY LANGMUIR PROBE DIAGNOSTICS OF RF PLASMA**

The first two sections of this chapter introduce and describe the physical processes behind Langmuir probe characterisation. In particular, the I-V characteristic curve obtained from Langmuir probe measurements, its features, how they relate to physical characteristics of the plasma, and the underlying theory behind electrostatic probes will be presented. This theory will then be applied to a well-known experimental environment with an aim to establish a thorough understanding of the behaviour of the Langmuir probe used in our laboratory. Finally, Langmuir probe characterisation will be subsequently applied to sulphur hexafluoride plasma.

### **3.1. I-V Characteristic Curves**

As briefly mentioned in Section 2.2, the I-V characteristic is collected when the bias voltage of a Langmuir probe is swept from a sufficiently large value through zero to another sufficiently large value of opposing polarity, while simultaneously collecting and measuring the current flow through the probe. An idealised representation of an I-V curve is presented in figure 3.1 with regions of interest labelled. The voltage sweep programmed

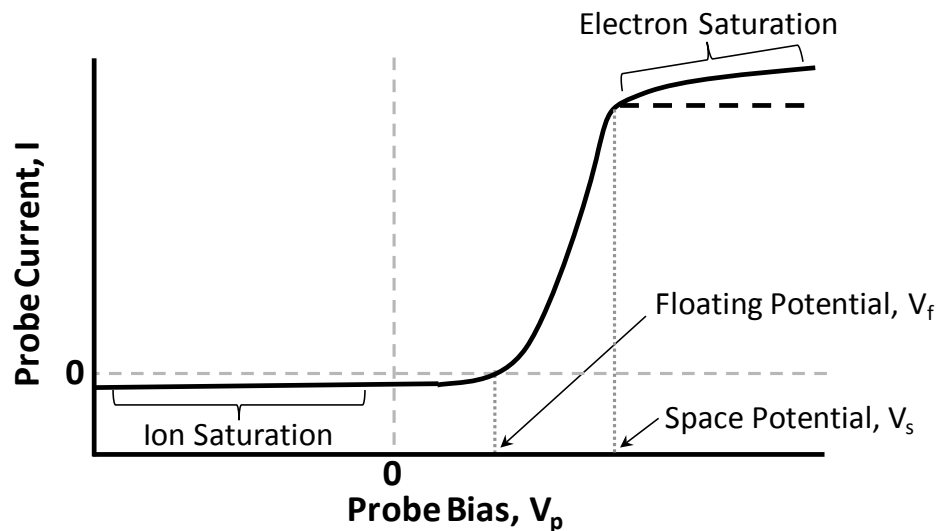


Figure 3.1. An idealised I-V curve.

for the Langmuir probe in this research began at a negative voltage and linearly ramped to a positive voltage. For clarity, the features of the I-V curve will be discussed sequentially.

When the probe bias, defined as  $V_p$ , is sufficiently negative the current measured by the probe is generated almost entirely from positive ions, as electrons and negative ions are strongly repelled. This region of the I-V curve is labelled the ion saturation region as indicated in figure 3.1. As  $V_p$  is decreased in magnitude towards zero volts the repulsive potential, given by  $V_s - V_p$  where  $V_s$  is the space potential (also known as the plasma potential), in turn decreases in magnitude. As the repulsive potential decreases, the most energetic of electrons are able to surpass the sheath surrounding the probe and consequently be collected, contributing to the overall current measured. As the value of  $V_s - V_p$  gets smaller and approaches zero, more electron current is collected until eventually a point is reached where the ion and electron currents are equal in magnitude but opposite in sign, and no net current flows. The bias at which this occurs is called the floating potential,  $V_f$ , and is also the potential that a surface that is not Earthed will accrue upon contact with a plasma. Most analyses, including that used in this work, assumes that for all probe biases above the floating potential no ions are collected, and the resultant probe current is purely generated from electrons.<sup>108</sup>

From  $V_f$  to  $V_s$  the electrons are modelled as having a Maxwellian distribution of energies, enabling the analysis in Section 3.2. As a result the probe current is expected to rise exponentially between these potentials. Details regarding the electron density and

temperature come from this region of the I-V curve. When the probe bias reaches the space potential all electrons within the collection volume contribute to the total current, from the ‘hottest’ to the ‘coldest’, and the probe current saturates, producing a distinct inflection in the I-V curve. Intuitively, if the probe current saturates at the space potential, then further increases in probe bias should not change the current collected and the I-V characteristic will exhibit a plateau in current beyond  $V_s$  as depicted by the black dashed line in figure 3.1. In actuality the probe current continues to rise slowly beyond  $V_s$  due to the sheath around the probe expanding, thus increasing the collection volume and draining the plasma local to the probe.

### 3.2. Electrostatic Probe Theory

The theory governing Langmuir probes was first introduced in 1924 by Langmuir and Mott-Smith<sup>71,72</sup> and has since been studied in-depth by many other authors.<sup>69,73,77,78</sup> The following discussion is a brief summary of the key results obtained from this theory and how they allow the analyst to extract useful information from I-V characteristics. A more thorough treatment of the theory presented in Sections 3.2.1 and 3.2.2 can be found in Appendix A. Some of the equations resulting from this analysis were embedded within the data acquisition software to reduce the amount of calculation required by the analyst, and remove random errors associated with erroneous calculations.

#### 3.2.1. The Space Potential, Electron Density and Temperature

The mass of an electron is significantly less than the mass of ions within plasma, and thus the electrons have much greater mobility. As a result, much of the current flowing through a biased electric probe arises due to electron current. This is particularly true when the bias is near the space potential. Therefore, by modelling the electron density much of the physical nature of plasma can be elucidated. Foremost however, to suitably apply the theory prescribed by Langmuir and Mott-Smith<sup>71,72</sup> some assumptions must be made regarding the probe and its relationship with the plasma. Namely;

- $r_p \gg \lambda_D$
- $r_p \ll \lambda_e, \lambda_i$
- $T_e > T_i$
- $n_e = n_i$

where  $r_p$  is the radius of the probe,  $\lambda_D$  is the Debye length,  $\lambda_e$  and  $\lambda_i$  are the electron and ion mean free paths,  $T_e$  and  $T_i$  are the electron and ion temperatures and  $n_e$  and  $n_i$  are the electron and ion densities.<sup>69</sup> These assumptions state that the probe radius must be greater than the Debye length, but less than the electron and ion mean free paths; the electron temperature is greater than the ion temperature; and the densities of both ions and electrons is equal (i.e. quasineutrality is maintained). If one assumes the energy distribution of the electrons to be Maxwellian, then the distribution function can be represented by

$$f(\vec{x}, \vec{v}, t) = n_e \left( \frac{m_e}{2\pi k_B T_e} \right)^{3/2} \exp \left( - \left( \frac{m_e v^2}{2k_B T_e} \right) \right) \quad (3-1)$$

where  $m_e$  is the electron mass,  $k_B$  is Boltzmann's constant and  $v$  is the electron velocity.<sup>73</sup>

The force of attraction or repulsion between the charged plasma species and the Langmuir probe depends on the potential difference between the space potential and the probe bias, given by  $V_s - V_p$  as described experimentally in Section 3.1. There exists a minimum electron velocity given by

$$v_{min} = \left( \frac{2e(V_s - V_p)}{m_e} \right)^{1/2} \quad (3-2)$$

whereby any electrons with velocity equal to or greater than this can overcome the repulsive potential and be collected by the probe.<sup>73</sup>

By setting up the problem in a particular way (as discussed in Appendix A), and using the definition of  $v_{min}$ , the current density can be shown to be

$$j = en_e \left( \frac{k_B T_e}{2\pi m_e} \right)^{1/2} \exp \left( \frac{-e(V_s - V_p)}{k_B T_e} \right). \quad (3-3)$$

Multiplication of the current density by the total probe collecting area  $A$  leads to the electron current flowing through the probe,  $I_e$ , as a function of  $V_p$ ,

$$I_e(V_p) = Aen_e \left( \frac{k_B T_e}{2\pi m_e} \right)^{1/2} \exp \left( \frac{-e(V_s - V_p)}{k_B T_e} \right) \quad \text{for } V_p \leq V_s. \quad (3-4)$$

As discussed previously, the electron saturation current is achieved when the probe bias is set to be equivalent to the space potential. An expression for the electron saturation current can therefore be found from the above when  $V_p = V_s$

$$I_{e,sat} = Aen_e \left( \frac{k_B T_e}{2\pi m_e} \right)^{1/2} \quad (3-5)$$

and thus the total probe current can be re-written as

$$I_e(V_p) = I_{e,sat} \exp\left(\frac{-e(V_s - V_p)}{k_B T_e}\right). \quad (3-6)$$

Taking the natural logarithm of both sides yields

$$\ln(I_e) = \left\{ \ln(I_{e,sat}) - \frac{e}{k_B T_e} V_s \right\} + \frac{e}{k_B T_e} V_p \quad (3-7)$$

where one can see that a plot of  $\ln(I_e)$  versus  $V_p$  should result in a straight line with slope of value  $\frac{e}{k_B T_e}$ , allowing determination of the electron temperature. Making linear fits in the electron saturation region and the transition region of the I-V characteristic will result in an intersection point of  $[V_s, \ln(I_{e,sat})]$ , allowing determination of the space potential and electron saturation current. This fitting procedure is diagrammatically represented in figure 3.2 with idealised data. With this knowledge, the electron density can be calculated from the relationship for the electron saturation current. The exponential nature of the outlined method can result in larger than desired errors when care is not taken in the judgment of the best linear fits. This motivates secondary methods for determination of  $V_s$  and  $n_e$ .

When the probe bias is at the floating potential,  $V_f$ , the ion and electron currents are equal and opposite. If the ion current is estimated to be equal to the Bohm current

$$I_B = \frac{1}{2} n_e e A \left( \frac{k_B T_e}{m_i} \right)^{1/2}, \quad (3-8)$$

then this can be equated with the previously determined electron current. This analysis results in the expression

$$V_f = V_s - \frac{k_B T_e}{2e} \ln\left(\frac{2m_i}{\pi m_e}\right) \quad (3-9)$$

whereby the space potential can be calculated once the floating potential and electron temperatures are known.

A secondary method to calculate the electron density comes from the total electron current expression (3-4) which, when  $V_p = 0$  and with knowledge of  $V_s$  and  $T_e$ , can be rearranged to show that the electron density can be calculated from

$$n_e = \frac{I_e(V_p=0) \cdot \exp\left(\frac{eV_s}{k_B T_e}\right)}{A e \left(\frac{k_B T_e}{2\pi m_e}\right)^{1/2}}. \quad (3-10)$$

### 3.2.2. The Ion Density

A relatively simple theory describing the behaviour of ions around a cylindrical probe is that of Orbital Motion Limit (OML) theory, developed by Langmuir and Mott-Smith.<sup>72</sup> It

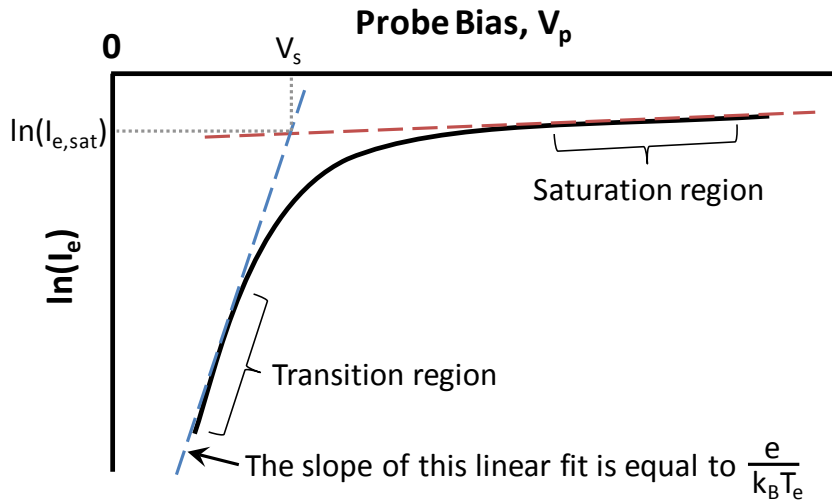


**Figure 3.2.** An idealised  $\ln(I_e)$ - $V$  curve with linear fits to the transition (blue) and saturation (red) regions. The slope of the blue fit gives information about the electron temperature while the intersection of the lines occurs at the point defined by the space potential and the electron saturation current.

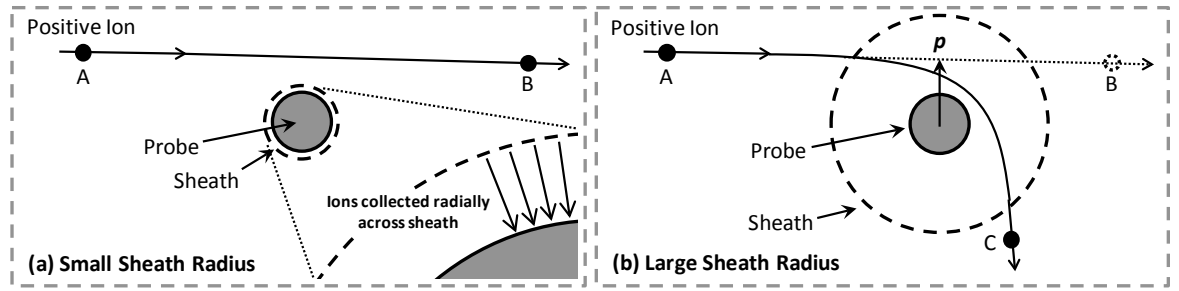
is limited in its general applicability due to certain approximations within the theory, but it is appropriate when dealing with low density plasma such as those employed in this work,<sup>77</sup> and is therefore the theory chosen for analysis in this dissertation.

Figure 3.3 depicts the trajectory of a positive ion with velocity  $v_0$  passing by a negatively biased probe. When the probe's sheath dimensions are small compared to that of the probe radius, as represented in figure 3.3(a), an ion following the path described by the line AB would pass by the probe without being collected. In this case when the sheath dimensions are sufficiently small, the ions are consequently assumed to have been collected radially, i.e. following a trajectory normal to the probe surface, and the probe current is described simply by  $I_p = Aj$  where  $A$  is the collecting area and  $j$  is the current density.<sup>73</sup> This does not hold when the sheath dimensions are significantly larger than the probe radius, at which point the orbital motion of the particle around the probe must be considered.

Figure 3.3(b) depicts the case where the probe's sheath dimensions are significantly larger than the probe radius. The electric field within the probe sheath exerts a force on the particle, resulting in the trajectory being altered and following the line AC. If the distance from the centre of the probe to the line AB is defined as  $p$ , then from a treatment detailed in Appendix A, conservation of energy and angular momentum can be used to show that if

$$p \leq r \left( 1 + \frac{V_p - V_s}{v_0} \right)^{1/2} \equiv p_r \quad \text{where} \quad -eV_0 \equiv \frac{1}{2} m v_0^2 \quad (3-11)$$

then the particle will be collected by the probe.<sup>77,103</sup>



**Figure 3.3.** The trajectory of a positive ion around a negatively biased probe with (a) small sheath dimensions and (b) large sheath dimensions. In (a), the inset shows the radial ion collection resulting from the small sheath dimensions. Modified from Chen<sup>77</sup> and Priest.<sup>103</sup>

The above comes from an analysis that assumes mono-energetic particles and as such is not realistic for experimental plasma. Langmuir expanded the analysis to Maxwellian distributions of ion velocities.<sup>71</sup> This analysis allowed the following expression for the ion density to be determined

$$N_i^{+2} = \frac{2\pi^2 m_i}{A^2 e^3} \cdot \left. \frac{dI^2}{dV_p} \right|_{V_p < V_f} \quad (3-12)$$

which allows the experimentalist to calculate the ion density in the ion saturation region, i.e. for  $V_p < V_f$ , by using the slope of a plot of  $I^2$  versus  $V_p$ .

### 3.3. Understanding the Langmuir Probe Experiment: N<sub>2</sub> Plasma

The Langmuir probe detailed in Section 2.2 was commissioned by Deslandes.<sup>108</sup> It saw limited use prior to this thesis and although the design was well considered by Deslandes, it was deemed prudent to study the behaviour of the probe in plasma of a simple ideal gas, namely nitrogen, to allow comparison with results obtained in previous experiments.<sup>103</sup>

#### 3.3.1. Averaging

Regarding the collection of I-V characteristics, there were multiple factors to consider before an appropriate standard protocol could be established. One area worthy of investigation was the collection of multiple characteristics and subsequent averaging of the data, implemented to improve data quality (i.e. signal to noise). However, like most averaging techniques a point is inevitably reached beyond which no measurable benefit is achieved. Thus it was desirable to determine the most suitable number of I-V characteristics to be obtained for a given experiment.

Presented in figure 3.4 are I-V curves obtained from the averages of one to one hundred data sets taken by Langmuir probe measurements in nitrogen plasma with a supply

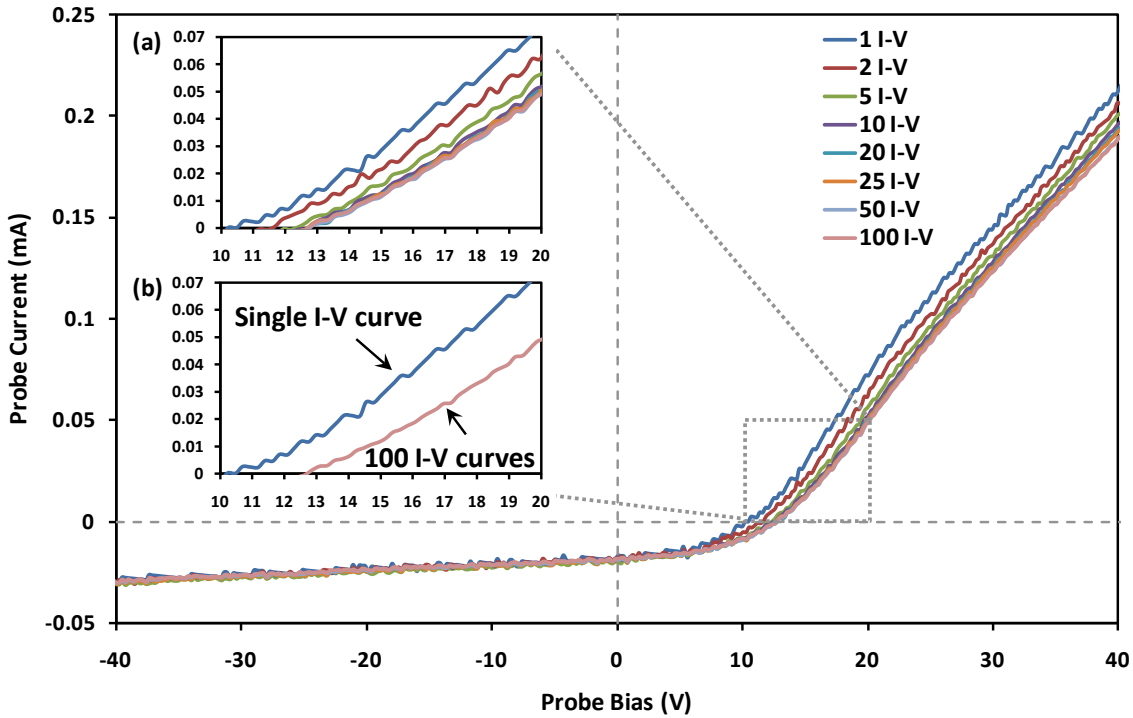


**Figure 3.4.** I-V curves obtained from 2.5 mTorr pure  $N_2$  plasma at 10 W. Acquisition was performed using single I-V curves up to an average of 100 curves.

pressure of 2.5 mTorr and an absorbed rf power of 10 W. While the main figure presents the entire I-V characteristics, the inset (a) presents the same data focused on the transition region, between the floating and space potentials, which is the region of most interest for analysis. Initially, there was an observed translation of the transition and saturation regions along the abscissa as the number of collected data sets was increased. This is likely caused by the deposition of plasma species onto the probe tip, effectively contaminating the probe and interfering with the collection of ions. Beyond an average of ten I-V curves, the variation between collected characteristics up to an average of one hundred did not appear to vary significantly within the transition region of the curve. This was an important result to consider as beyond an average of ten curves the calculation of certain plasma properties were not affected, especially the values of both the floating and space potentials since they were taken directly from the collected I-V curve.

Although improvements in data quality were not immediately apparent with all of the I-V curves plotted together, the inset (b) separates the two extreme cases; a single I-V curve, and the average of one hundred curves. The single I-V curve presented itself with sawtooth-like noise across the entire data set. While this was not of particular concern during the linear fitting process for the transition and saturation regions (as this relied on

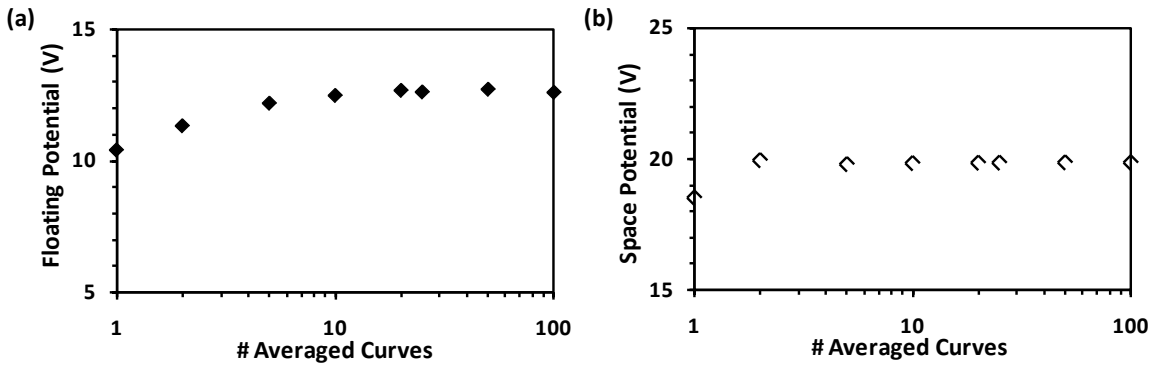
the analyst's judgement), it did present a problem for the calculations of ion density which involve the derivative of this data. Since it was a numerical calculation performed by the software, noise within the data inherently added significant error to the calculation. The characteristic generated by an average of one hundred curves, although not flawless, presented with less noise, and was thus a more desirable data set for analysis.

Figure 3.5 shows measured values of (a) the floating potential and (b) the space potential against the number of averaged curves, taken from the data presented in figure 3.4. In both cases the measured values from the single collected curve differed from that measured by average curves. In the case of the floating potential this presented itself as a gradual increase from 10.4 for the single curve up to 12.5 V for the average of ten curves. Beyond an average of ten curves the value of the floating potential was not seen to vary significantly with an average value of  $12.6 \pm 0.1$  V. The space potential however displayed different behaviour with the initial value measured as 18.5 V and each successive measurement producing a value of  $19.8 \pm 0.1$  V.

Of particular importance when diagnosing plasma systems are the densities of the ions and electrons. Figure 3.5 illustrates the measured value of these densities, again taken from the data presented in figure 3.3. Neither quantity showed considerable overall variation with increasing numbers of averaged data sets, with only the electron density showing a minor perturbation at 2 curves. This was actually to be expected from figure 3.4 since the values of the ion and electron densities come from the slope of fits in the ion saturation and electron saturation regions of the I-V characteristic. In figure 3.4 it can be seen that these slopes did not change considerably, an observation that was particularly evident in the ion saturation region.

### 3.3.2. Stability Over Time

Another concern that needed to be addressed was the stability and reproducibility of the measurements made by the Langmuir probe over a given experimental time frame. To assess any variations that may occur over a nominal time period, Langmuir probe measurements were performed in nitrogen plasma (with experimental parameters held constant at a gas pressure of 2.5 mTorr and an rf power of 10 W) over a 30 minute time frame. Figure 3.7 presents the floating and space potentials over this period with figure 3.8 showing the ion and electron densities.



**Figure 3.5. Values of (a) floating and (b) space potential for an increasing number of averaged curves. Taken from the data in figure 3.3.**

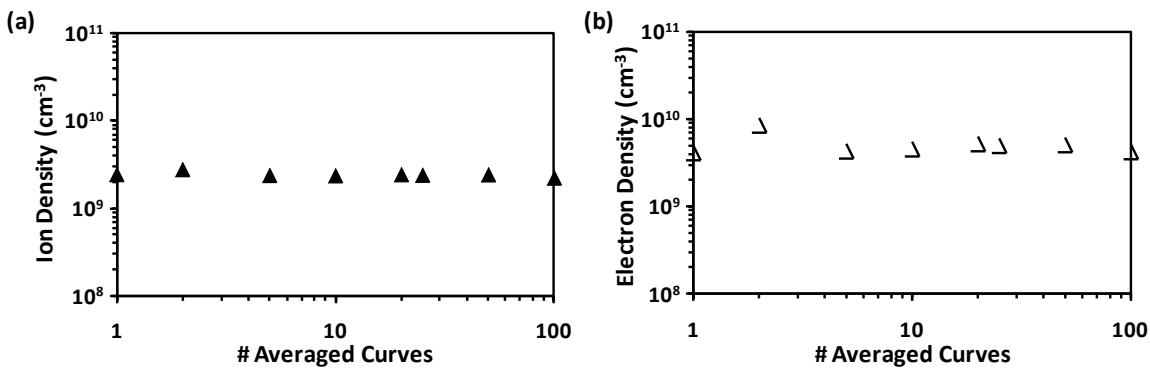


**Figure 3.6. Values of (a) ion and (b) electron densities for an increasing number of averaged curves. Taken from the data in figure 3.3.**

Both the floating and space potentials display similar behaviour over the time frame studied. An initial rapid increase in magnitude for both quantities occurs over the first few minutes of the experiment followed by a steady, linear increase across the entire time frame. It should not be considered unusual for both potentials to display a similar trend since equation (3-3) shows they are co-dependent, and the space potential is calculated directly from the floating potential. It is worthwhile also to note the range across which the potentials varied. The floating potential displayed a total variance of 1.5 V while the space potential varied by only 0.1 V over the full 30 minutes of data collection.

The measured ion and electron densities maintain considerable stability for the entire 30 minute period, as evidenced in figure 3.8. This fact is particularly important to note from two points of view. Firstly, it shows that the system could maintain a stable plasma condition for an extended duration, a characteristic that is paramount when performing surface modification. It is not quite correct to then carry this through to other source gases, such as SF<sub>6</sub>, and assume that they too would be stable, but it provides evidence that the system is capable of stable operation. Secondly, it shows that the Langmuir probe can

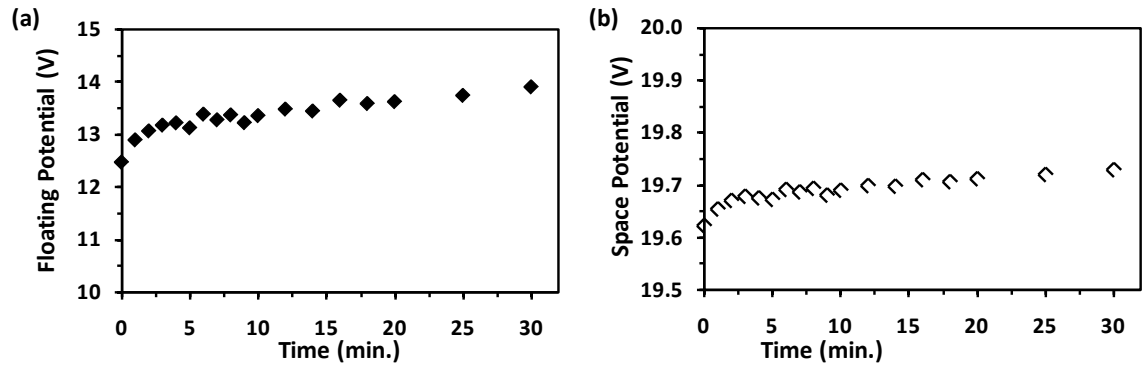


Figure 3.7. Values of (a) floating and (b) space potential over a 30 minute time frame for nitrogen plasma at constant power and pressure.

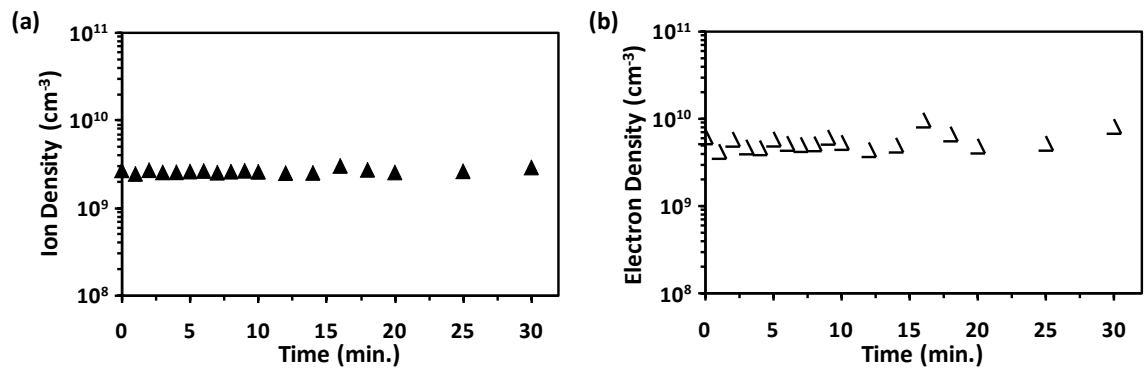


Figure 3.8. Values of (a) ion and (b) electron densities over a 30 minute time frame for nitrogen plasma at constant power and pressure.

maintain stability for an extended exposure to plasma. Again, it should perhaps not be presumed that this will be the case with every gas that could be used, but it establishes the proof-of-principle operation of the Langmuir probe with the nitrogen plasma case.

Another quantity that could be recorded during plasma experiments was the so-called self-bias voltage, or  $V_{dc}$ . This is a voltage that naturally accrues on the antenna during operation and arises largely due to the greater mobility of electrons in comparison with ions. Aanesland discusses the phenomenon by presuming the time-averaged space potential to be positive and constant, with the driving rf antenna voltage oscillating about zero Volts and greater in magnitude than the space potential.<sup>127</sup> When the rf voltage is *greater* than the space potential there is a net flow of electrons to the antenna and conversely, when *below* the space potential, a net flow of positive ions. The electrons experience a greater acceleration than the heavier ions and consequently more electrons strike the antenna than ions. The net result of this phenomenon is thus an overall negative dc potential on the antenna, dubbed the self-bias voltage ( $V_{dc}$ ), which consequently leads to a capacitive sheath surrounding the antenna surface.<sup>127</sup>

Antenna self-bias has been shown to lead to sputtering of the antenna material and hence contamination of samples by metal particles.<sup>108</sup> Deslandes investigated this phenomenon in the Flinders reactor and found sample surface contamination by sputtered iron from the antenna to be at most ~2 at.% by XPS. Realistically, an acceptable detection limit for the LHS-10 used in that work would be no better than 1 at.%. Furthermore, in this work contamination by iron nanoparticles was much more prevalent, since this was the catalyst for nanotube growth. Thus contamination by antenna sputtering, though expected to be present, is deemed to be of little significance in the work presented here.

The self-bias voltage is usually found to be primarily dependent on the applied rf power, with some dependence on gas pressure.<sup>103,108</sup> Assuming an ideal match, there are no other parameters that the experimentalist would typically alter that could cause a variation in  $V_{dc}$ , other than changing the source gas entirely. Figure 3.9(a) shows how the measured self-bias voltage changed over the same 30 minute time period discussed in figures 3.7 and 3.8. Note that the self-bias voltage is negative on the ordinate of the plot. Over approximately the first 10 minutes the magnitude of  $V_{dc}$  (i.e. its absolute value) decreases, varying from an initial maximum value of -196.6 V to a minimum around -193 V. The average measured voltage from 10-30 minutes was found to be  $-193.2 \pm 0.4$  V.

During a plasma experiment the antenna generates significant heat which, if left unabated, could be potentially damaging. To alleviate this heating a constant flow of compressed air is directed through the core of the hollow antenna material. Due to the large potentials that were evidently present on the antenna a direct measurement of its temperature is not possible, however the temperature of the exhaust air coming immediately from the antenna provides an indirect measure. Figure 3.9(b) shows this measurement and how it varied with time. Upon ignition, the temperature of the antenna increases somewhat linearly over the first 5 minutes until a transition from 5-10 minutes to a plateau in temperature beyond 10 minutes at which point the temperature of the air exiting the antenna, and presumably the antenna itself, remains constant over the entire period. Immediately evident is the similarity between the trends in the quantities presented in figure 3.9. The dotted lines are placed at the 10 minute mark, and it would appear that there is a direct connection between the temperature of the antenna and the measured self-bias voltage.

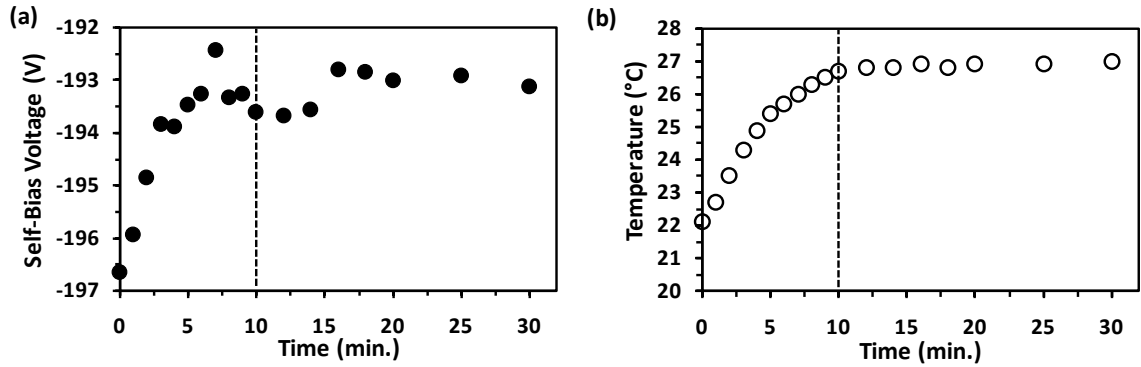


**Figure 3.9. (a) The antenna self-bias voltage and (b) antenna cooling air temperature over a 30 minute time frame for nitrogen plasma at constant power and pressure.**

To summarise, the results presented here lead to the conclusion that one should allow the system to equilibrate for at least 10 minutes prior to taking Langmuir probe measurements. This is deemed necessary to obtain an invariant measure of the floating potential, space potential, ion and electron densities and the antenna self-bias voltage.

### 3.3.3. Comparison with Previous Work

As discussed in Section 2.1, the experimental vessel used in this research was originally designed for the nitriding of stainless steel.<sup>105,107</sup> The work using this chamber that was published by Priest largely dealt with the spectroscopic analysis of surfaces after plasma treatment, with little discussion focussed on the diagnostics of the plasma generated. Prior to reporting in literature however, Priest presented an Honours thesis with work dedicated solely to the study of nitrogen plasma in this chamber using a cylindrical Langmuir probe that was very similar in design to the one used in this work.<sup>103</sup> Since the study was performed on the same chamber with only minor experimental differences, this afforded a unique opportunity for comparison.

Table 3.1 presents data extracted from the thesis by Priest. The floating and space potentials, the self-bias voltage and the ion and electron densities as measured by Priest are directly compared to the measurements made from the work presented here. Overall the data agrees very well across the experimental parameters studied with the measured potentials, the self-bias voltage and the densities all displaying very similar values. This shows that the Langmuir probe experiment applied here provided sound experimental results and could confidently be applied to SF<sub>6</sub> plasma, which is the plasma environment of particular interest in this thesis.

**Table 3.1. A comparison of plasma parameters extracted from this work with that previously found by Priest.<sup>103</sup>**

Parameter	Priest	This Work
Floating Potential, $V_f$ (V)	25 → 2	16 → 0
Space Potential, $V_s$ (V)	28 → 5	30 → 2
Self-Bias Voltage, $V_{dc}$ (-V)	500 → 250	600 → 195
Ion Density, $n_i$ ( $\text{cm}^{-3}$ )	$3 \times 10^9 \rightarrow 5 \times 10^8$	$2.0 \times 10^9 \rightarrow 3.5 \times 10^8$
Electron Density, $n_e$ ( $\text{cm}^{-3}$ )	$\sim 4 \times 10^8$	$4.0 \times 10^8 \rightarrow 1.0 \times 10^8$

### 3.4. Langmuir Probe Characterisation: Application to SF<sub>6</sub> Plasma

The motivation behind this experimentation was to ultimately develop the ability to characterise plasma ignited within SF<sub>6</sub> with respect to gas pressure, rf power and any other experimental parameter of interest. The development of a deeper understanding of SF<sub>6</sub> plasma could ultimately lead to novel ways of performing surface modification treatments using this environment.

#### 3.4.1. Fluctuations in I-V Characteristics from SF<sub>6</sub> Plasma

Following on from the established experimental protocol developed using nitrogen plasma, the Langmuir probe experiment was applied to SF<sub>6</sub> plasma. I-V characteristics obtained from pure SF<sub>6</sub> plasma at a supply pressure of 2.5 mTorr with increasing rf powers are presented in figure 3.10. The I-V curves display a similar overall shape to that of the standard Langmuir probe I-V characteristic collected in nitrogen plasma. Most notably however, for probe bias greater than  $\sim 35$  V the I-V characteristics display severe fluctuations in the probe current and appear to do so independently of the rf power chosen to generate the plasma. For comparison, an I-V characteristic taken from N<sub>2</sub> plasma is provided as an inset within the figure.

The observed fluctuations dominate the electron saturation current, i.e. the region of the curve for which the probe bias is greater than the space potential. This is one of the regions of the I-V characteristic that would be used in the analysis presented in Section 3.2.1 by generating a linear extrapolation, ultimately allowing for the determination of the space potential and the electron saturation current. This fitting procedure is performed using a semi-log plot of  $\ln(I)$  versus  $V$ , an example of which is shown in figure 3.11(a) for N<sub>2</sub>

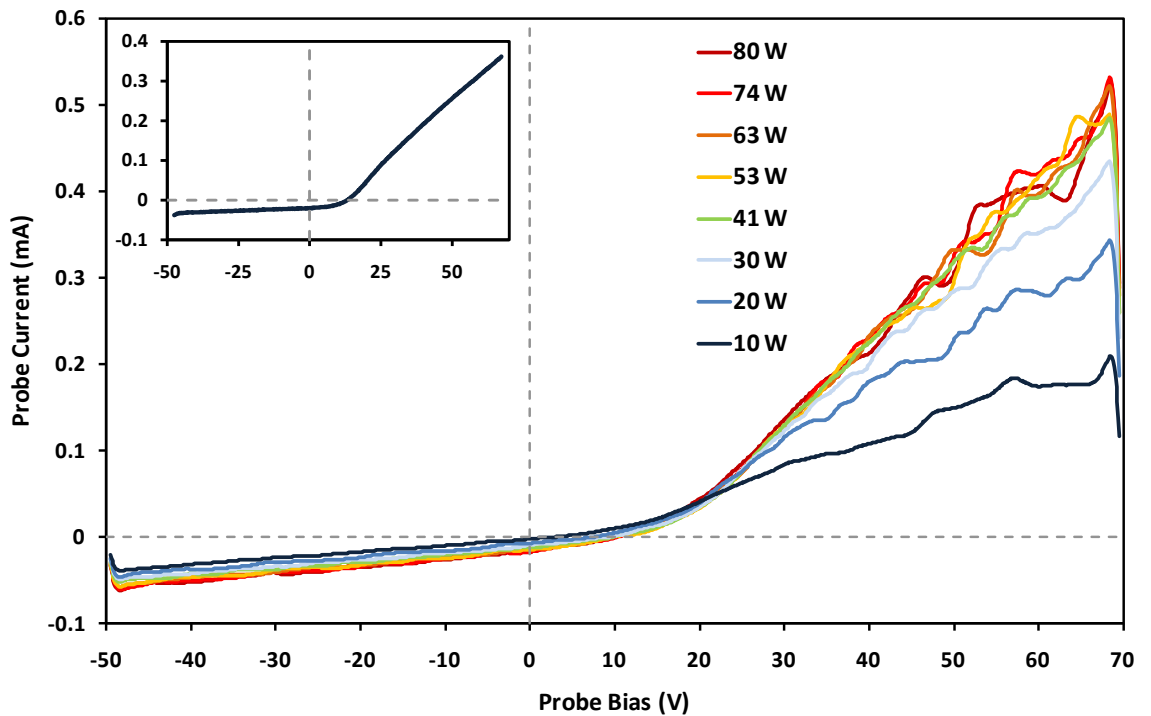


**Figure 3.10.** I-V curves obtained from 2.5 mTorr pure SF<sub>6</sub> plasma with increasing rf power. Acquisition was performed using an average of 10 I-V curves. For comparison the inset shows a typical I-V characteristic from N<sub>2</sub> plasma at 2.5 mTorr.

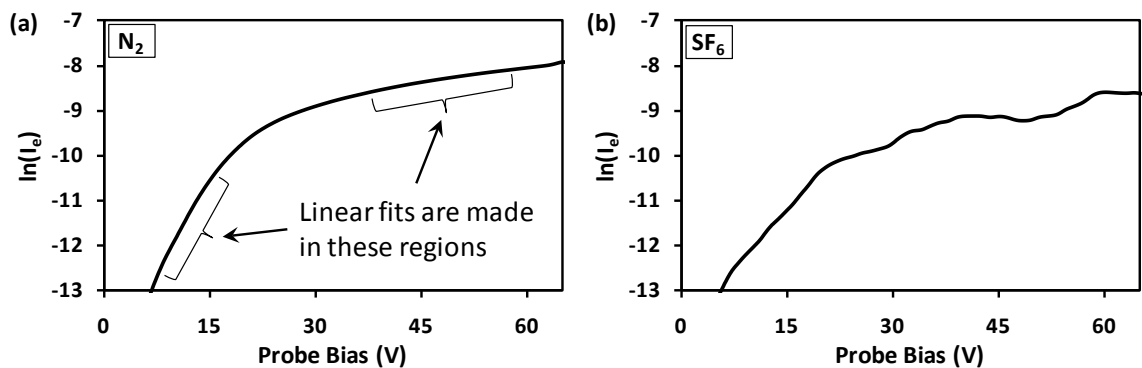


**Figure 3.11.** An example of  $\ln(I_e)$ -V curves for (a) N<sub>2</sub> plasma (b) and SF<sub>6</sub> plasma, showing the distorted nature of the curves in the latter case.

plasma. As can be seen the plot was smooth with two distinct regions where the linear fits would be made using the procedure presented in figure 3.2. The fluctuations observed in figure 3.10, however, carry through to the  $\ln(I_e)$ -V curve for SF<sub>6</sub> as shown in figure 3.11(b). The end result is that data is difficult to reliably fit with linear trend lines for each of the two regions and therefore quite problematic for accurate Langmuir probe analysis of SF<sub>6</sub> plasma.

One possible solution to this issue was to simply average a greater number of data sets in an effort to ‘smooth out’ the fluctuations in the measured probe current. Figure 3.12 shows

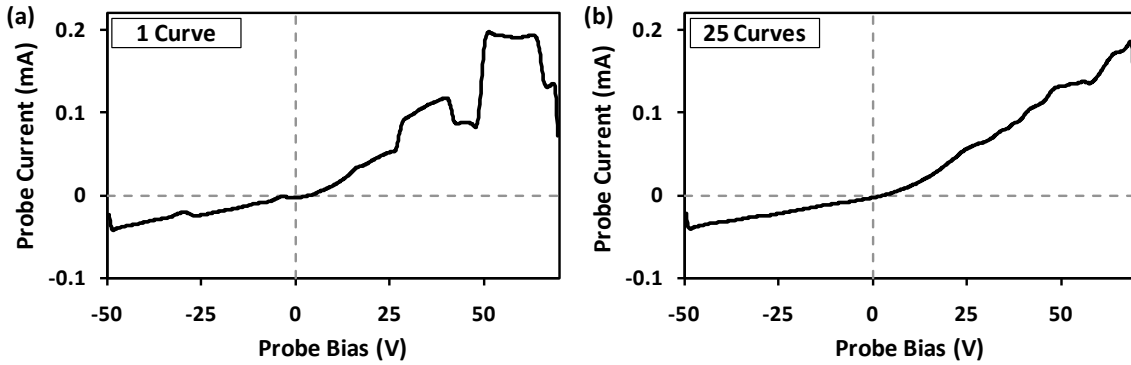


**Figure 3.12. I-V curves obtained from 2.5 mTorr pure SF<sub>6</sub> plasma at 75 W rf power using (a) a single I-V curve and (b) the average of 25 I-V curves.**

two I-V characteristics taken from the same plasma. In figure 3.12(a) the characteristic was obtained from a single I-V curve while in figure 3.12(b) the characteristic was obtained from the average of 25 I-V curves. While the data appeared to improve in apparent signal to noise with an increasing number of data sets, its effect remained noticeable. Ultimately this still resulted in reduced confidence in analyses performed on such data sets.

The conclusion drawn from this study was that to facilitate further application of the Langmuir probe to SF<sub>6</sub> plasma, the fluctuations observed in the probe current first required careful and detailed characterisation. Once this characterisation was performed, steps could then be implemented to allow the successful characterisation of SF<sub>6</sub> plasma by Langmuir probe.

---

## Chapter 4.

# THE CHARACTERISATION OF SF<sub>6</sub> PLASMA

This chapter explores in greater detail the fluctuations observed when the Langmuir probe experiment was applied to SF<sub>6</sub> plasma. The fluctuations are characterised with respect to experimental parameters such as gas pressure and rf power, and the spatial dependence throughout the chamber is examined. A review of previously observed fluctuations in SF<sub>6</sub> is provided, and the influence of these on surface modification is discussed. A refinement to the experiment is proposed to ultimately facilitate the characterisation of SF<sub>6</sub> plasma by Langmuir probe without interference from the observed phenomenon. Finally, this modification is used to characterise the plasma conditions in experimental regimes of relevance for the SF<sub>6</sub> plasma modification of surfaces.

### 4.1. Fluctuations in Probe Current

The probe current fluctuations that were introduced in Chapter 3 were observed as distorted I-V characteristic curves. The bias on the probe was not steady-state during these measurements and thus the measured probe current was a combination of the ramping probe bias inducing a varying current flow, and the observed fluctuations. This is evidenced in figure 4.1. The trace in (a) shows the applied probe bias with respect to time. From 0-100 ms the bias applied to the Langmuir probe is ramped linearly from -50 V to

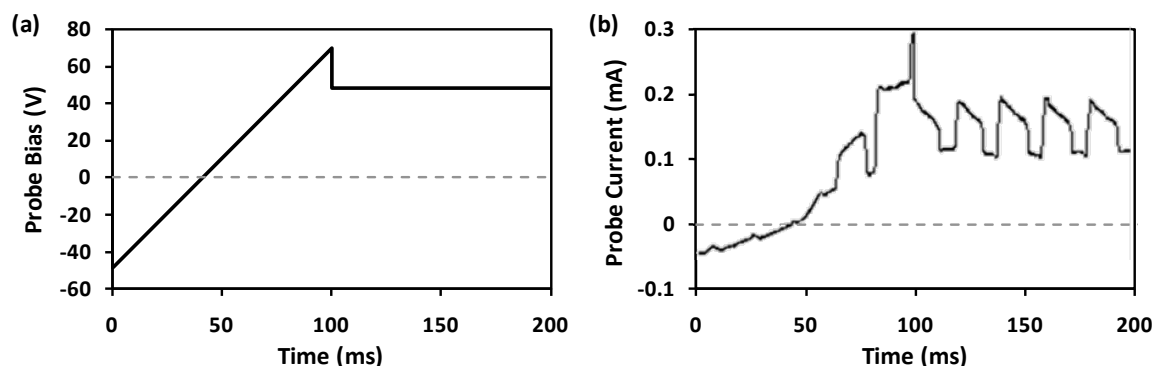


**Figure 4.1.** With respect to time, (a) the probe bias waveform used to perform the Langmuir Probe experiments and (b) the measured probe current from SF<sub>6</sub> plasma when the bias waveform is applied.

+70 V. This is the region that would generate the I-V curve. At 100 ms the bias is reduced to +50 V and held constant for a period of 100 ms, inducing electron bombardment that facilitates the cleaning of the probe tip of any adsorbed species that may be present. Applying the waveform to the probe resulted in a measurable current flow through the tip, which is presented in figure 4.1(b). In the region of 0-100 ms the trace appeared similar to that introduced in Chapter 3, with the combination of the I-V curve and the previously described fluctuation. However, during the ‘cleaning’ cycle, where the probe bias was held constant, fluctuations were elucidated. From the trace the fluctuations, which were first thought to perhaps consist of somewhat random noise, now clearly display a periodic oscillation in the observed probe current.

#### 4.1.1. The Observed Oscillation

Figure 4.2 shows probe current traces for plasma ignited in varying source gases. The probe was biased with a constant voltage, in this case +50 V, and the resultant current flow through the probe was measured. Figure 4.2(a) presents the case for pure SF<sub>6</sub> plasma and clearly shows the oscillatory behaviour. When the period of the oscillation was measured an average value of 21 ms was found across a 200 ms time frame, corresponding to an oscillation frequency of 48 Hz. As this value is close to the frequency of mains power, i.e. 50 Hz, this would immediately lead one to question whether the observed oscillation was an artefact arising from electrical mains interference.

Plasma ignited from a variety of source gases are routinely utilised in the Flinders reactor including argon, nitrogen, oxygen, and of course sulphur hexafluoride. It is immediately apparent from figure 4.2(b) that all of the gases studied *except* for SF<sub>6</sub> are quiescent and

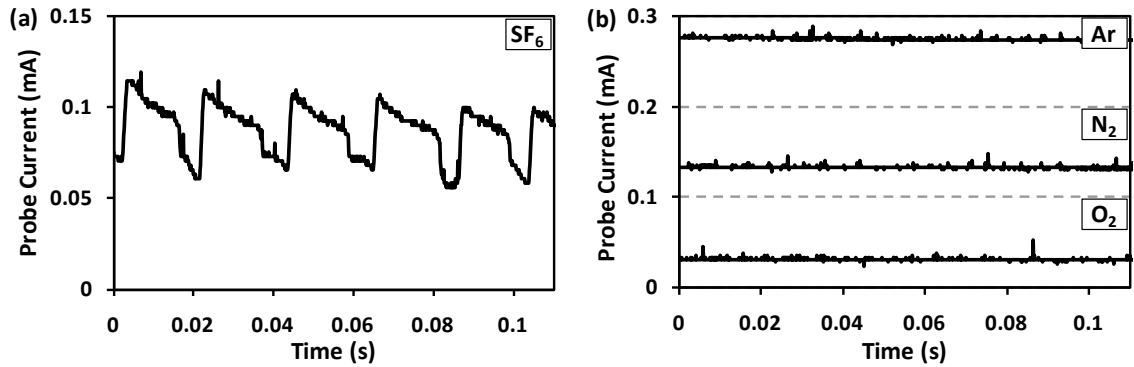


**Figure 4.2.** Probe current traces for (a) SF<sub>6</sub> plasma at 10 W and (b) argon, nitrogen and oxygen plasma at 10 W. Note that for the traces in (b) nitrogen is offset by 0.1 mA and argon is offset by 0.2 mA. The probe bias was held constant at 50 V for all traces.

show no oscillatory behaviour. If the cause of the observed fluctuations in measured current was indeed due to interference from 50 Hz electrical noise then it should be observed in all traces regardless of the source gas used. The fact that the oscillation was only observed for SF<sub>6</sub> plasma suggests the effect was perhaps due to some intrinsic property of SF<sub>6</sub> plasma and not an external influence. This is further evidenced in figure 4.3, showing probe current traces for varying applied bias. If the oscillations were due to an external influence one might expect that the effect be observed across the entire I-V curve, and thus for all probe biases. However it only appears in the electron saturation region, i.e. for probe bias much greater than the floating potential. From figure 4.3, at a bias of +50 V the current oscillated in the same manner already observed. As the bias is reduced however, the magnitude of the oscillation also decreases until its presence was barely detectable above the background noise at a bias of +20 V. For all other biases, even to the opposite end of the scale at -50 V, the resultant probe current appeared stable. Not only did this result further imply that the oscillation was related to the nature of SF<sub>6</sub> plasma, it also suggests that the oscillation occurs within the electron or negative ion current, collected at large *positive* biases, and not the positive ion current, which is collected at large *negative* biases.

Furthermore, the fluctuations were also directly observable to the naked eye in viewing the plasma through a chamber viewport. It appeared as instability within the SF<sub>6</sub> plasma that caused a fluctuation and an apparent ‘fluttering’ of the plasma density. This resulted in a corresponding variation in light intensity allowing its direct observation. Unfortunately the changes in light intensity were too rapid and subtle for photographic evidence to be appropriately reproduced here, but figure 4.4 illustrates this behaviour diagrammatically.

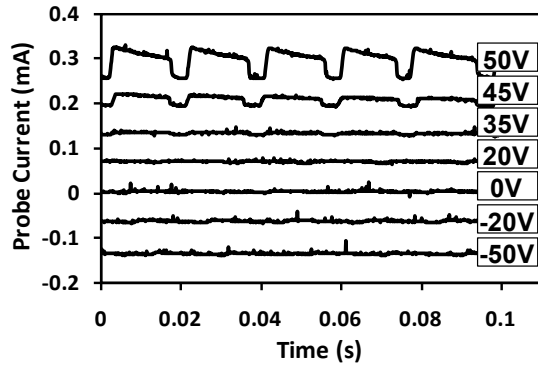


Figure 4.3. Measured probe current for different probe biases. Traces are offset for clarity.

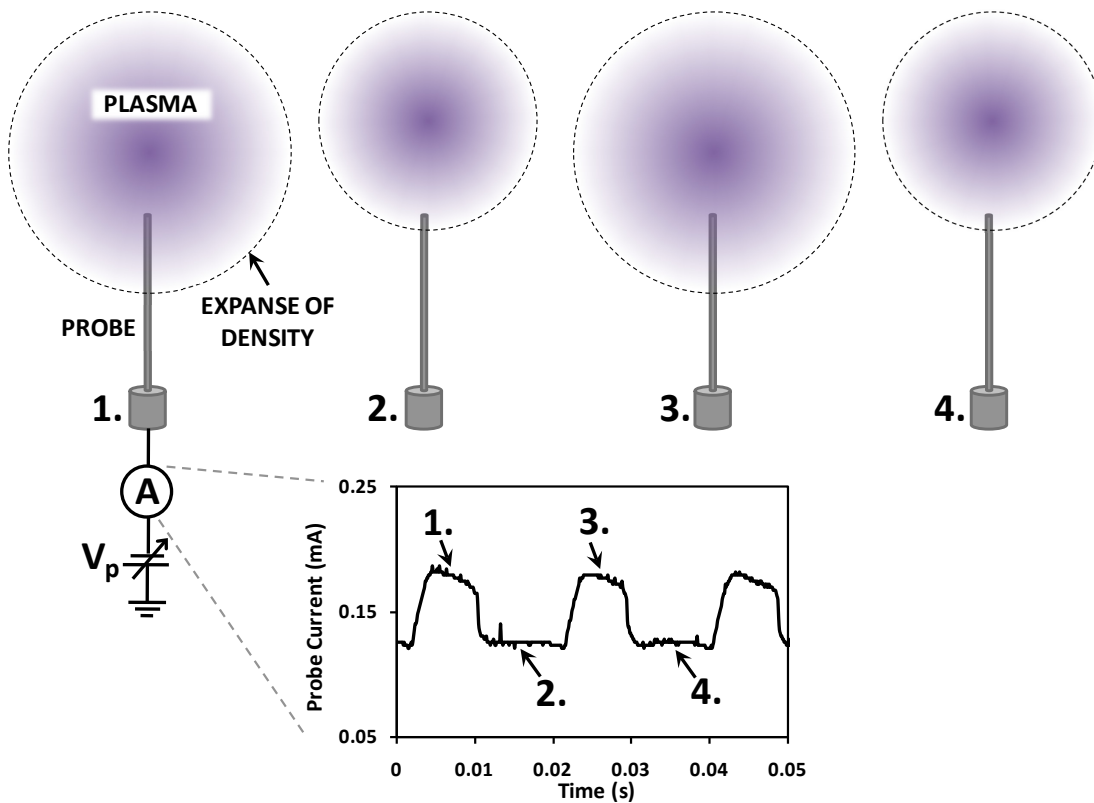


Figure 4.4. A representation of the observed density fluctuations in SF<sub>6</sub> plasma. The radial expanse of the density fluctuated and in turn caused the measured probe current to oscillate.

The plasma density was observed to fluctuate between two limiting states which, by the naked eye, appeared to be one of greater expanse throughout the chamber, and one of lesser. The Langmuir probe observed this as a fluctuation in the ion density localised around the probe tip. When the plasma was at its maximum expanse the Langmuir probe ‘sensed’ a greater number of ions within its collection volume and thus a greater current was measured. In contrast, when the plasma was at its minimum expanse, the ion density around the probe was much lower and thus a lower current was measured. In figure 4.4 this

is presented as steps 1 through 4 where the plasma oscillates between its maximum and minimum expanse for two full cycles, with each step associated with a measured current in the inset trace. In step 1 the plasma is at its maximum expanse and thus the current at 1 is at its greatest, while at step 2 the plasma is at its minimum expanse with the current at 2 at its least, and so on.

Despite the ability to directly observe the effect of the instability on the emitted light from the plasma, the rapid nature of the fluctuations made it difficult to elucidate exactly how the instability propagated throughout the plasma chamber. Initially, two simple cases come to mind. The first could be that the instability generates ‘pulses’ of plasma density that travel outward from the source, and upon reaching the sampling volume of the Langmuir probe induces a similar pulse in the measured current. The second case could be that the plasma is ‘breathing’, with the plasma around the source expanding and contracting throughout the chamber. Again, due to the frequency, each of these cases to the naked eye would be indistinguishable and essentially appear as described in figure 4.4 whereby the plasma fluctuates in density around the source. However, using the Langmuir probe, evidence toward one of these two cases could be elucidated.

#### **4.2. Dependence on Experimental Conditions**

The instability was characterised with respect to experimental parameters that would typically be varied during a given plasma experiment. These included gas pressure, rf power, and the value of the matching capacitance that would normally maximise the power delivered into the plasma.

The program designed to collect probe current measurements was modified to perform a fast Fourier transform (FFT) to facilitate the characterisation process. This converted the collected data from traces in the *time* domain to the *frequency* domain, allowing for the simple analysis of variations in oscillation frequency and intensity with experimental conditions. The FFT was performed in real-time, and the frequency spectra were output alongside the current measurement. An example current trace is given in figure 4.5(a) with its corresponding FFT given in figure 4.5(b). The program was able to record multiple current traces, performing an FFT for each trace, and then perform an average over all collected FFTs. Thus the FFT given in figure 4.5(b) is actually the average of one hundred individual spectra.

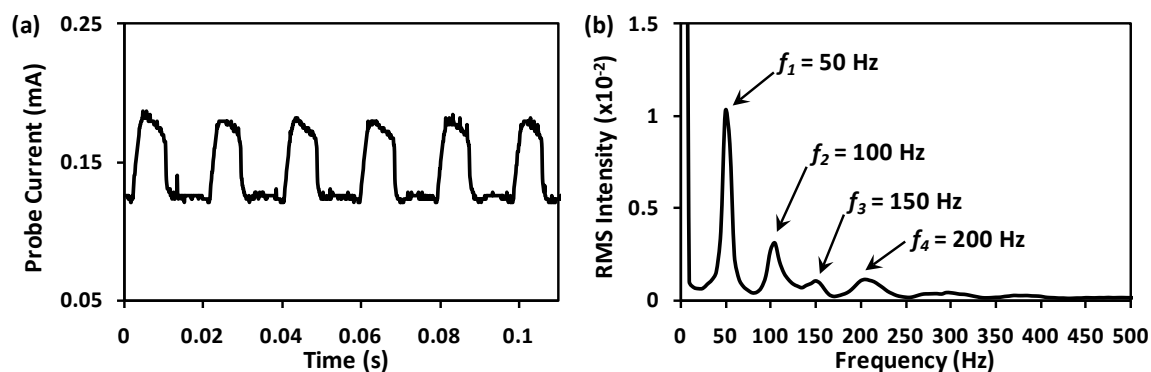


**Figure 4.5. (a) A typical probe current trace showing oscillation due to the inherent SF<sub>6</sub> plasma instability and (b) a corresponding FFT.**

It is evident from figure 4.5(b) that the FFTs showed significant harmonic content for modes greater than the fundamental mode. Along with the primary frequency of 50 Hz, there existed higher frequency modes that were integer multiples of the fundamental, the overtones. These are noted in the figure as  $f_1$ , the fundamental, and  $f_2$  to  $f_4$ , the overtones. For the purpose of this study only the fundamental frequency was analysed, as the overtones were not always present with sufficient intensity compared to the fundamental frequency. It is also worthwhile to note that while the FFTs were determined up to a maximum frequency of 5000 Hz, no features were observed above 500 Hz across any experiment.

#### 4.2.1. A Well-Defined Instability Domain

The instability did not occur across all accessible values of gas pressure and rf power and had a very well defined experimental domain within which the oscillations were observed. Figure 4.6(a) plots this region with respect to gas pressure and rf power. The upper and lower bounds were taken to be the point at which FFTs of the traces no longer showed any discernable features, due to measured probe currents becoming constant and thus the plasma being deemed stable. This is accentuated in figure 4.6(b) with three FFTs chosen from regions A, B, and C in (a). For regions A and C, where the plasma was considered to be stable, the FFTs were featureless. However for B, in the experimental regime where the plasma was observed to display significant instability, the FFT showed strong features similar to those already presented at 50 and 100 Hz, along with higher order modes of oscillation. For gas pressures greater than 30 mTorr the plasma was found to be stable across the entire rf power range. This was not the case for the lower pressure bound, where it was found that as the rf power was increased, the minimum gas pressure that was

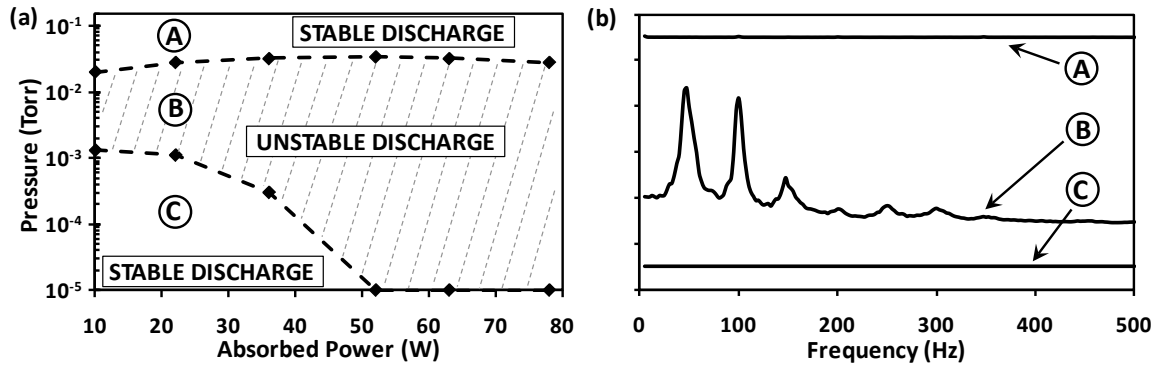


**Figure 4.6. (a) The experimental domain within which SF<sub>6</sub> plasma displays instability and (b) FFTs for labeled locations within the experimental domain.**

required to maintain a stable discharge was decreased. For rf powers greater than 52 W a lower bound could not be established as it extended beyond the lowest pressure that was measurable by the gauges.

The evolution of the plasma from a stable to an unstable state was found to occur at a well defined pressure. Figure 4.7 presents a series of FFTs taken from probe current traces measured in pure SF<sub>6</sub> plasma at constant rf power of 10 W. While maintaining a plasma in the chamber the supply pressure was increased from 1.0 mTorr, where the plasma was stable, up to 2.0 mTorr, where the instability could be observed, with FFTs collected and presented in (a). The pressure was then reduced back to 1.0 mTorr in (b). The FFTs only displayed meaningful features for pressures greater than 1.3 mTorr, with the intensity of these features increasing as the plasma was further brought into the instability regime. This experiment was repeated multiple times with the same result and similar effects were observed for the upper bound of gas pressure. The lack of hysteresis between increasing and decreasing pressure shows that the formation of the instability occurs at a well defined pressure for a given rf power.

#### 4.2.2. The Influence of Power and Pressure

The frequency of the oscillation was observed to have a dependence on user definable experimental parameters such as absorbed rf power and gas pressure. Presented in figure 4.8 are oscillation frequencies with increasing rf power for three supply pressures; (a) 2.5 mTorr, (b) 5 mTorr and (c) 10 mTorr. Each point was determined by taking the position of the fundamental frequency in FFTs made up of the average of one hundred individual FFTs taken over a number of minutes.

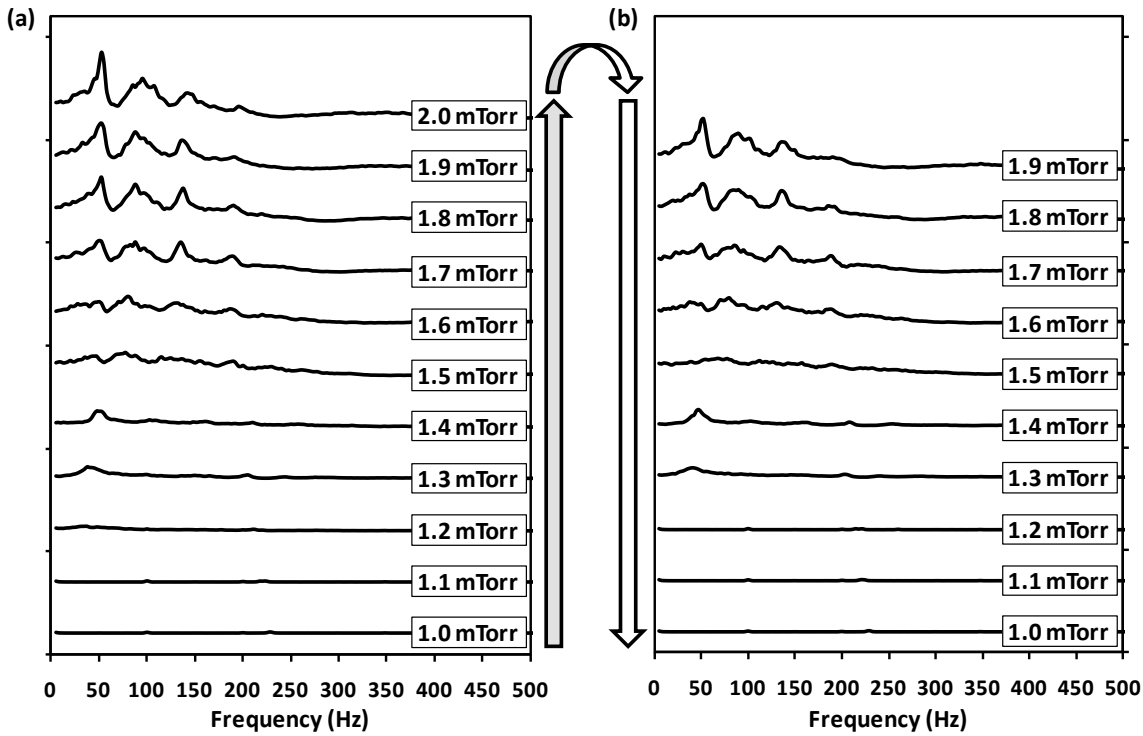


**Figure 4.7.** The onset of the instability at the lower bound of gas pressure for (a) increasing pressure and (b) decreasing pressure within the same pure SF<sub>6</sub> plasma at 10 W rf power.

The trend collected from plasma with a pressure of 2.5 mTorr shows prominent discontinuities at ~20 W and ~40 W, where the measured frequency suddenly changed to a distinctly different value first increasing in frequency and then decreasing. A similar observation can be made from the collected from plasma with a gas pressure of 5 mTorr where at ~30 W the determined frequency suddenly increased. The data taken from plasma at 10 mTorr appeared to be unaffected by these features and a steadily increasing frequency trend with absorbed power was prominent. The cause of these sudden shifts in frequency was unclear. Given the frequency of these oscillations, and the sampling rate of the device used to measure them (10 kS/s), instrumental anomalies such as aliasing can be ruled out. Furthermore, the experiment was repeated multiple times with much the same result. For the lower pressure plasma, where it was most dispersed throughout the chamber, the instability presented itself with distinctly less regularity than at the greater gas pressures. To elucidate, at 10 mTorr the measured probe current oscillations were very regular in the temporal sense, and could be collected over a large time scale (a number of seconds) without noticeable breaks in regularity. At 2.5 mTorr and 5 mTorr however regularity in the oscillations appeared to be more sporadic, with short bursts of high uniformity broken up by random oscillatory features in the FFTs. Put simply, at 10 mTorr

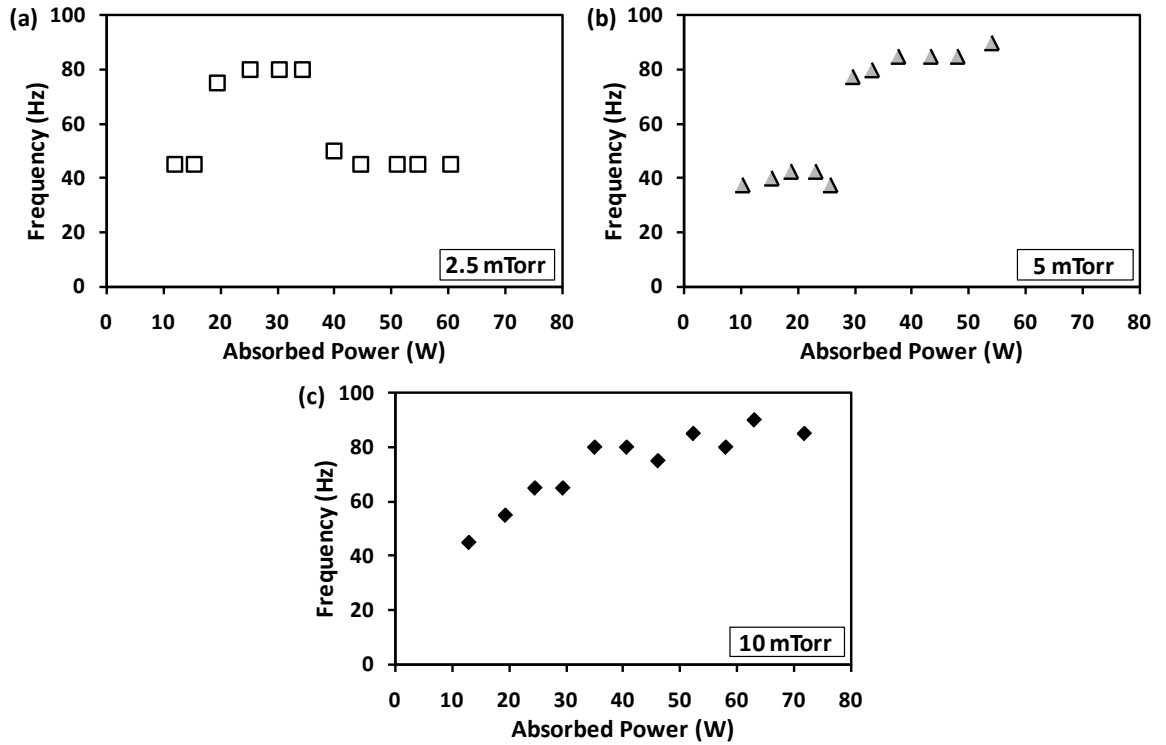


**Figure 4.8.** Variation in the primary oscillation frequency with increasing absorbed power for pure SF<sub>6</sub> plasma at (a) 2.5 mTorr, (b) 5 mTorr and (c) 10 mTorr.

the instability was more uniform and regular than at 2.5 mTorr or 5 mTorr. This lack of uniformity at the lower pressures could lead to the observed behaviour by introducing severe perturbations throughout the measured FFTs.

The frequency of the instability also had a distinct relationship with gas pressure, as observed in figure 4.9(a) which gives a frequency trend with increasing gas pressure for SF<sub>6</sub> plasma at 10 W of rf power. Each point was determined using the aforementioned procedure. Again there was a prominent discontinuity in the trend at around 12 mTorr where the frequency suddenly jumped from 10 Hz to 40 Hz. This feature split the trend into two linear regions with negative slope. The overall trend of these regions was one of decreasing frequency as the pressure was increased. A similar trend was observed when analysing the intensity of the measured oscillations, as seen in figure 4.9(b). The studied pressure range spanned the instability domain presented in figure 4.6(a) for 10 W of power. Accordingly, at the extrema of the trend in (b) the intensity of the oscillations was very low, although these were not isolated minima, with a third minimum intensity around 12 mTorr where the frequency was seen to transition from a lower to higher value.

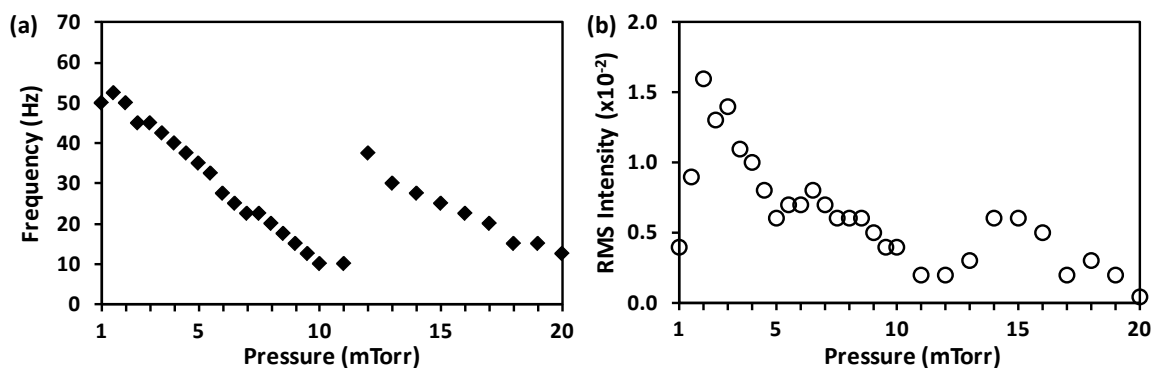


**Figure 4.9.** The oscillation (a) frequency and (b) intensity with increasing gas pressure for SF<sub>6</sub> plasma at 10 W. The trend in this figure spans the entire instability domain as detailed in figure 4.6(a) for this rf power.

#### 4.2.3. The Influence of Impedance Matching

The matching circuit plays an important role in the generation of plasma within the reactor, and as such also had an influence on the instability. In figure 4.10 the relationship between the frequency of the oscillation and the matching capacitance C1 was studied, along with the relationship between C1 and the reflected power (where C1 is one of the variable capacitors in the circuit diagram for the matching unit presented in figure 2.2, Chapter 2). These trends were collected within SF<sub>6</sub> plasma of 10 W rf power for three pressures; (a) 2.5 mTorr, (b) 5 mTorr and (c) 10 mTorr.

The reflected power in figure 4.10 is presented as open triangles. For each pressure there existed minima that corresponded to the value of the capacitance C1 that afforded the optimal match between the drive electronics and the plasma. This minimum was most prominent at 2.5 mTorr where it was found to be between a capacitance of 250 and 300 pF. As the pressure was increased the optimal matching capacitance became less distinct with plasma at 10 mTorr of pressure showing zero reflected power for any value of the capacitance C1 between 350 and 650 pF. Outside of these ranges the reflected power was nominally seen to increase. For values of C1 *above* the optimal matching value this increase occurred quite steadily over a wide range of capacitances. However for capacitances *below* the optimal matching condition, the reflected power increased very rapidly until the plasma was eventually extinguished at a capacitance of 125 pF irrespective of the supply gas pressure. The measured frequency displayed a similar, yet inverse relationship with the matching capacitance. For values above the optimal capacitance the frequency was observed to be relatively stable, with only plasma at

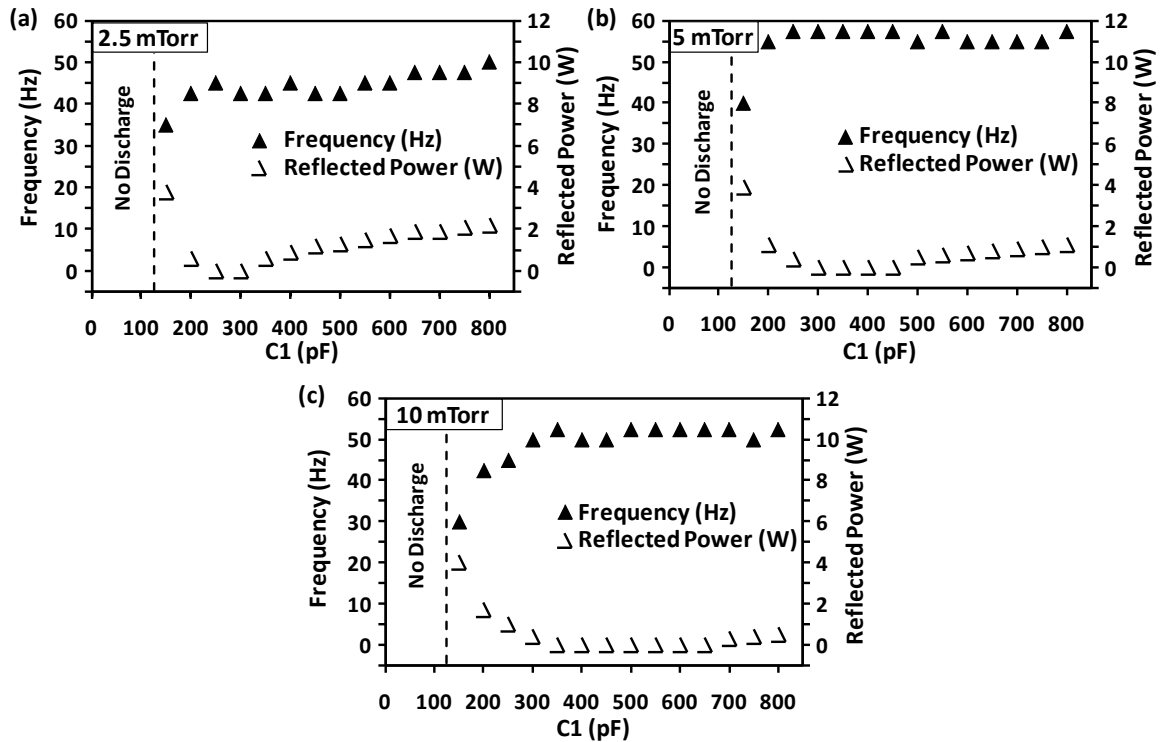


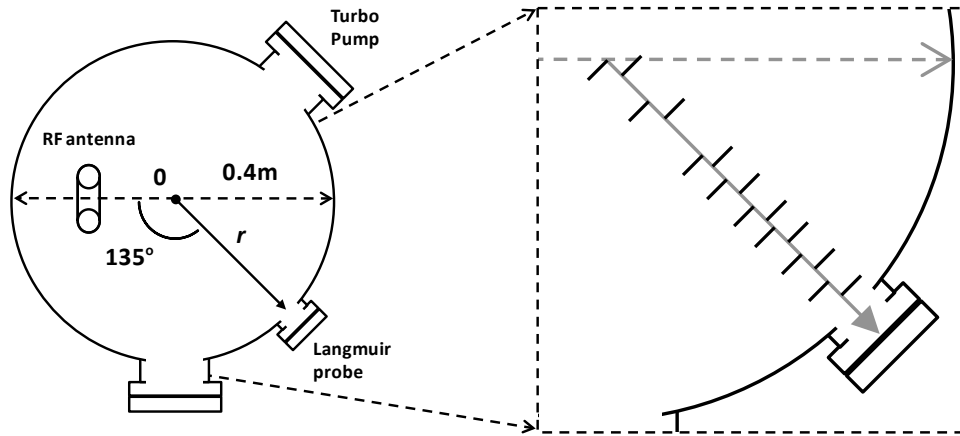
**Figure 4.10.** Variation in the primary oscillation frequency and reflected power with matching capacitance  $C_1$  for (a) 2.5 mTorr, (b) 5 mTorr and (c) 10 mTorr gas pressure.

2.5 mTorr showing a slight increase in frequency as the capacitance was increased. Below the optimal matching value the frequency was observed to drop dramatically until again the plasma was ultimately extinguished at a capacitance of 125 pF.

It is likely that the relationship between the oscillation frequency and the matching capacitance is indirect, and actually a result of the changing reflected power. The amount of *absorbed* power, which is taken as the numerical difference between the applied and reflected power, is seen to decrease as the reflected power increases. Earlier results in figure 4.8 showed that oscillation frequency decreases with absorbed power. Thus the relationship observed in figure 4.10 may actually be a result of the absorbed rf power changing as the matching capacitance is varied.

### 4.3. Spatial Distribution

The instability is hypothesised to manifest itself as either a pulse of high density plasma travelling outward from the source, or an expansion and contraction of the main plasma density around the source. In the case of a pulse travelling away from the source throughout the chamber, the probe should be in contact with this higher density region for the same amount of time irrespective of the probe position and thus the width of the



Position	Distance from Centre (m)	Distance from Source (m)	Position	Distance From Centre (m)	Distance from Source (m)
0	0.000	0.100	8	0.110	0.194
1	0.012	0.109	9	0.120	0.203
2	0.032	0.125	10	0.127	0.210
3	0.045	0.136	11	0.137	0.219
4	0.073	0.160	12	0.147	0.229
5	0.080	0.166	13	0.157	0.238
6	0.090	0.176	14	0.167	0.248
7	0.100	0.185	15	0.177	0.258

**Figure 4.11. The design of the spatial distribution experiment. The probe was moved along  $r$  from the centre of the chamber out to near the edge of the chamber wall. The inset table gives relative distances at each position.**

features in the probe current traces should remain constant. However, if the plasma is ‘breathing’, as described in the second hypothesis, then the width of the features observed in probe currents should be expected to display a significant spatial dependence, i.e. the features in the probe currents would vary depending on the position of the probe within the plasma chamber. Figure 4.11 presents the experiment designed to test each of these hypotheses. The Langmuir probe was positioned on a diagnostic port on the chamber at an angle of 135° from the source. If the axis along the port to the centre of the chamber is defined as  $r$ , then for normal diagnostic experiments, designed to characterise the plasma in the immediate vicinity of a sample undergoing a treatment, the probe would be at position  $r = 0$ , and would consequently be 0.1 m from the antenna. To test the spatial distribution of the instability the probe was moved along  $r$  from  $r = 0$  to  $r = 177$  mm, labelled positions 0 through 15 in figure 4.11, in as regular steps as were possible. Since it is hypothesised that the expansion is directed radially outward from the source, then the distance from the source to the probe was required. This was calculated from the position along  $r$  using the cosine rule with the angle of 135° between  $r$  and the centreline upon which the antenna sat. The distance from the probe to the centre of the chamber and the

source is given in the table in figure 4.11. At each point, current traces were collected and the oscillation was characterised as previously detailed. Plasma ignited in pure SF<sub>6</sub> was maintained at a pressure of 2.5 mTorr with 10 W of absorbed rf power.

Probe current traces for each of the characterised positions along  $r$  are given in figure 4.12(a). As the distance between the probe and the source increases, the features in the measured traces change in shape. The most evident difference between each position was the width of the features along the time axis; the further out from the source the Langmuir probe was placed, the narrower the feature width.

There was also an apparent change in the regularity of these features. For positions 0-3 the features in figure 4.12(a) were not overly distinct and appeared to be a convolution of multiple oscillations. For positions 4 – 12, the features became far more pronounced, with prominent pulse-like structure. With this increase in prominence the decrease in the width with increasing distance became quite clear for these traces. By position 15, which related to a distance of 177 mm from the chamber centre, the probe tip was nearly completely removed from the chamber at which point the oscillations were almost non-existent in the probe current traces. At this position the Langmuir probe was almost completely removed from the chamber and thus the plasma density, leading to the instability being unobservable.

The sudden change in regularity from position 3 to 4 could be explained by the setup of the plasma chamber. The sample table resides near the centre of the chamber and to ascertain the plasma characteristics in the environment most similar to that experienced by the sample, the probe was designed in such a way that it would sit at a height of ~0.5 cm from its surface. The table was approximately 8 cm in diameter, and consequently the probe was nearby to the table surface until position 4, where it was essentially in open vacuum space. The table was electrically connected to the chamber (and thus Earth) and as such there existed a potential difference between it and the plasma resulting in sheath formation. This sheath around the table would interfere with the density measured local to the table and is proposed to have also affected the magnitude and shape of the oscillations observed for positions 0 – 3 in figure 4.12(a).

Quantification of the variation in feature width is given in figure 4.12(b) along with the determined oscillation frequency. The change in the width of the oscillations varies

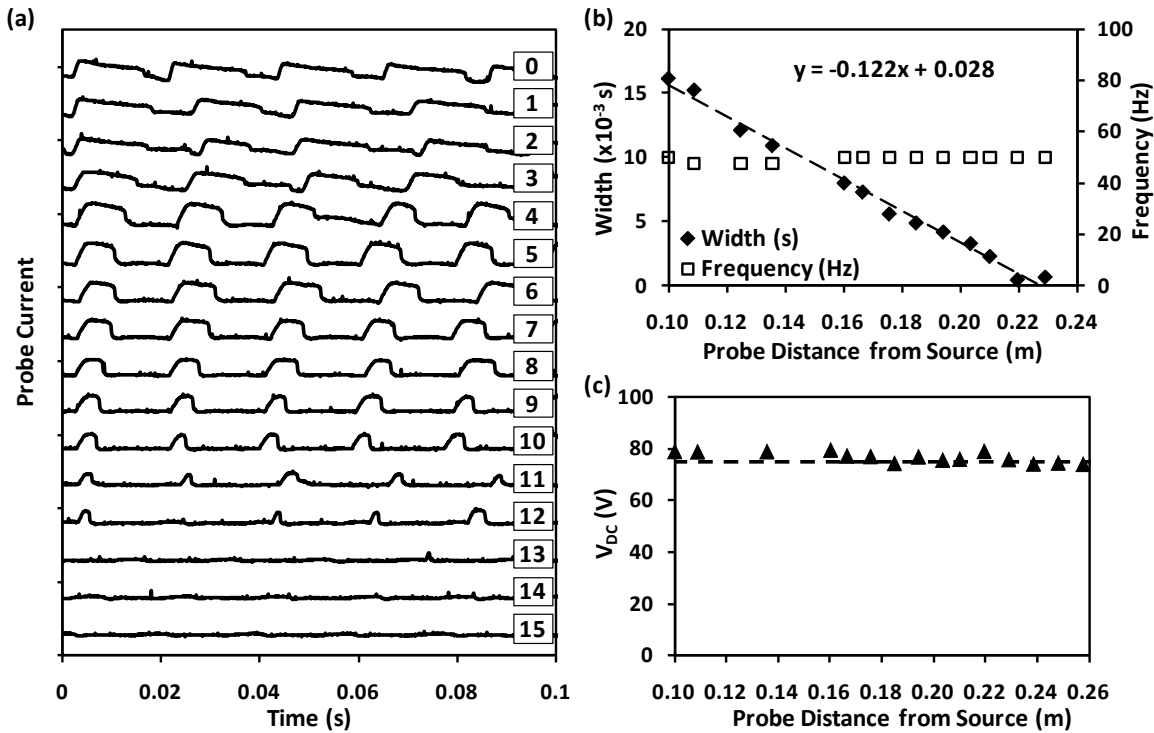


**Figure 4.12.** Results of the spatial experiment with (a) current traces for each of the positions in figure 4.11, (b) quantification of the width and frequency of the observed features as a function of the distance from the source and (c) the self-bias voltage at each measurement.

linearly as the distance from the source was increased. For reference, the equation of the best linear fit is given in the figure. It is important to note here that the frequency of these oscillations appears to be entirely independent of the distance to the source, remaining largely constant over the data range presented here.

Even though the experimental parameters were held at constant values, it was still prudent to have a secondary measure of invariability between each experiment. The Langmuir probe would normally serve this purpose, but since it was being moved for the experiment it could not be used. Thus to ensure the plasma being characterised was as invariant as possible between each successive measurement, the antenna self-bias was also measured. Figure 4.12(c) shows the antenna dc self-bias voltage across the entire experiment. The average measured voltage was  $76.8 \pm 1.9$  V, and is plotted as the dashed line. The lack of significant deviation from this average value over the course of the measurements shows the strong invariability between each measurement, indicating that the environment from which all measurements were taken was essentially constant over the experiment.

The observations presented were consistent with the hypothesis that the instability manifested as an expanding and contracting plasma volume inside of which a higher

plasma density was carried, rather than that of a pulse travelling through the chamber. The edge of this volume of higher density plasma could be likened to a ‘wavefront’ moving throughout the chamber. This hypothesis is pictorially represented in figure 4.13. The high and low density regions are represented by dark and light purple respectively, with the direction of propagation given by the purple arrow. Two hypothetical traces are given relating to what is ‘sensed’ by two probes positioned at  $r_x$  and  $r_y$ . In frame 1, both probes experience the same low plasma density, and thus have the same measured probe current as given by the region labelled 1. As the wavefront passes over position  $r_x$ , represented by the blue probe, the density of ions sensed by the tip increases and thus the measured current also increases as seen in the blue trace at 2. As the wave moves further outward from the source it encounters the second probe, at position  $r_y$  represented in green, at which point the measured current for this tip also increases, noted by step 3. The wave moves onward to a maximum expanse in step 4, before receding, causing the opposite effects to occur at each tip, given in steps 5 and 6.

The features in the two traces in figure 4.13 are centrally aligned with one another, a result of the proposed behaviour of the wave. If the wave indeed behaves in the hypothesised manner and two probes were positioned at distances remote from one another and measuring currents simultaneously while a wave travelled forward and back across both probes, then it should be expected that the traces would be aligned in this way. That they are not aligned this way in figure 4.12(a) should not be taken as indicative of an incorrect hypothesis. Rather it is because of the way in which the experiment was performed. Only a single Langmuir probe was used and thus each trace represented another time period, i.e. no measurements were made simultaneously at any number of points along  $r$ . For clarity each of the traces were shifted with respect to time to align them such that the onset of the first oscillation feature occurred at the same point. No physical significance should be taken from this alignment.

In-depth analysis of the data presented here gives rise to further evidence that the instability manifests as a wave throughout the chamber. If the hypothesis described in figure 4.13 is accurate then the width of the features is a measure of the time it takes for the wavefront of the instability to travel from the probe at a given position, out to some maximum distance and then back again. By making multiple measurements of the width in time of the instability features at varying distances one is in essence taking a measure of

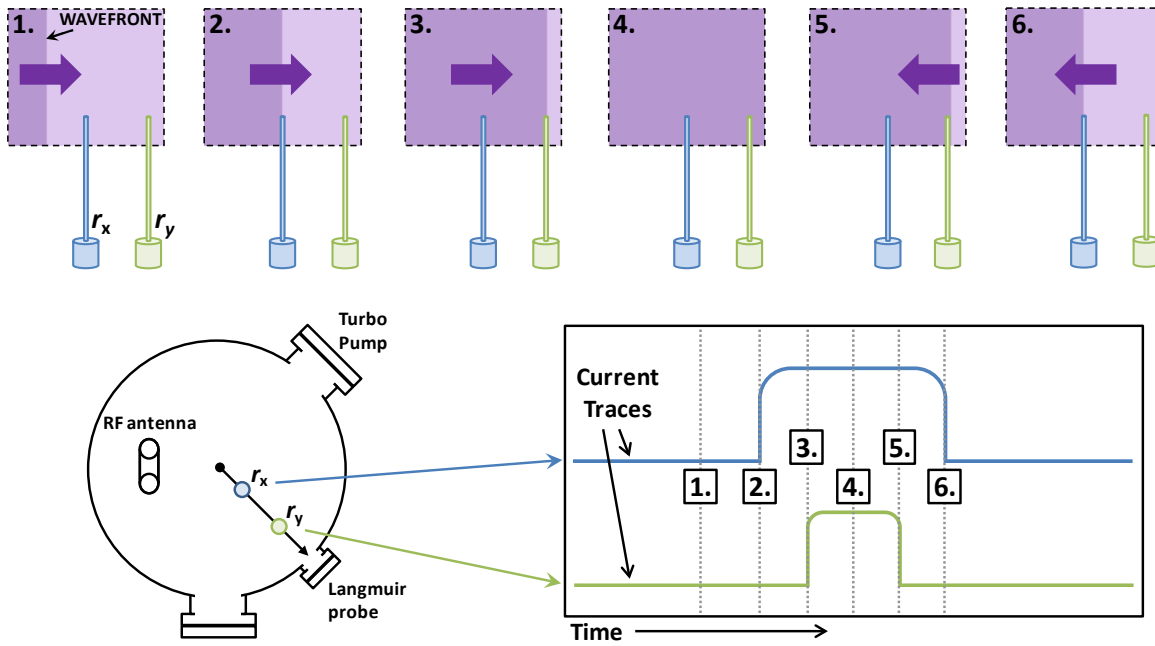


**Figure 4.13.** A pictorial representation of the proposed relationship between the observed probe behaviour and the instability, which is proposed to manifest itself as a wave of higher density plasma moving radially throughout the chamber. Two probes, blue and green, are shown at different positions  $r_x$  and  $r_y$  respectively. The further from the source the narrower the feature width as the probe spends less time at the higher density.

the speed at which this wavefront is moving throughout the chamber. Consider again figure 4.12(b) showing the linear relationship between the width of the features in the probe current traces and the distance between the probe and the source. A dimensional analysis of the linear fit in this figure finds that

$$[slope] = \frac{[time]}{[length]} \equiv \frac{T}{L}$$

which, when inverted, gives

$$[slope]^{-1} = \frac{L}{T}.$$

In other words, by finding the inverse of the slope of the linear fit in figure 4.12(b) one results with a value that has units of metres per second, i.e. a speed. From this analysis a speed of  $16.3 \pm 1.0 \text{ ms}^{-1}$  is found for the instability within pure SF<sub>6</sub> plasma of pressure 2.5 mTorr and rf power of 10 W. This analysis assumes that the speed of the wave was constant for the entire journey (i.e. forward and back) however there is no evidence to suggest this, and the asymmetry in the shape of the features would perhaps suggest that the speed is *not* constant. Nevertheless as the speed given above was generated from multiple measurements, it could be taken as the *average* speed of the wavefront travelling through the plasma. Note that this experiment was performed under one set of conditions and that it might not be quite correct to assume that this speed would apply in all cases.

From this calculated speed, the expected time delay between waves travelling from one point to another separated by a known distance could be determined. In the context of the experiment this allowed the current traces to be translated along the  $x$ -axis and enable direct comparison between each position. Figure 4.14 presents the results of this analysis. For brevity only a subset of the data is presented, with positions 0-3 and 14-15 excluded. The original data is shown in (a) where the onset of the first feature in each trace is aligned. After translating along the time axis with the amount of time it would have taken a wave travelling at the calculated speed to reach each successive position the traces are offset and shown in (b). When this analysis was applied the features behaved as they would if they were taken simultaneously. The data, when treated appropriately, therefore strengthens the hypothesis of a wave moving throughout the chamber.

As the wave moves outward from the source it carries with it a region of higher plasma density compared to the rest of the chamber. As the distance from the source is increased it should be expected that the plasma would expand, consuming a greater volume the further from the source. Thus it should be expected that as distance is increased, the density would decrease and the magnitude of the oscillations in measured probe current should likewise decrease. Figure 4.15 plots the average feature height for positions 0-12 as a function of the distance from the source. This plot shows two distinct regions; Region I consists of positions 0-3, Region II consists of the remaining measurements up to the point where the oscillation was no longer observed. In Region I, the average feature height was somewhat constant, whereas Region II shows the average feature height decreasing with distance from the source. As has been previously mentioned, the measurements taken in Region I carry with them the added complication of the presence of the sample table which was effectively a large Earthed electrode. This is the likely cause of the stark difference between the two regions in the plot. However in Region II, without the presence of the table influencing the measured current, the intensity of the features is observed to decrease as distance is increased. While this decrease was to be expected, the apparent linearity of the trend, as indicated by the fitted linear trend line in figure 4.15(a), was not. If the geometry of the chamber and the plasma source was considered then it should be reasonable to suggest that the density would expand and contract within a cylindrical volume. This volume would have a maximum radius that is dependent on the dimensions of the chamber. If a finite number of plasma species was contained within this volume then as it expands, i.e. as the radius increases, the density would decrease. Now since the

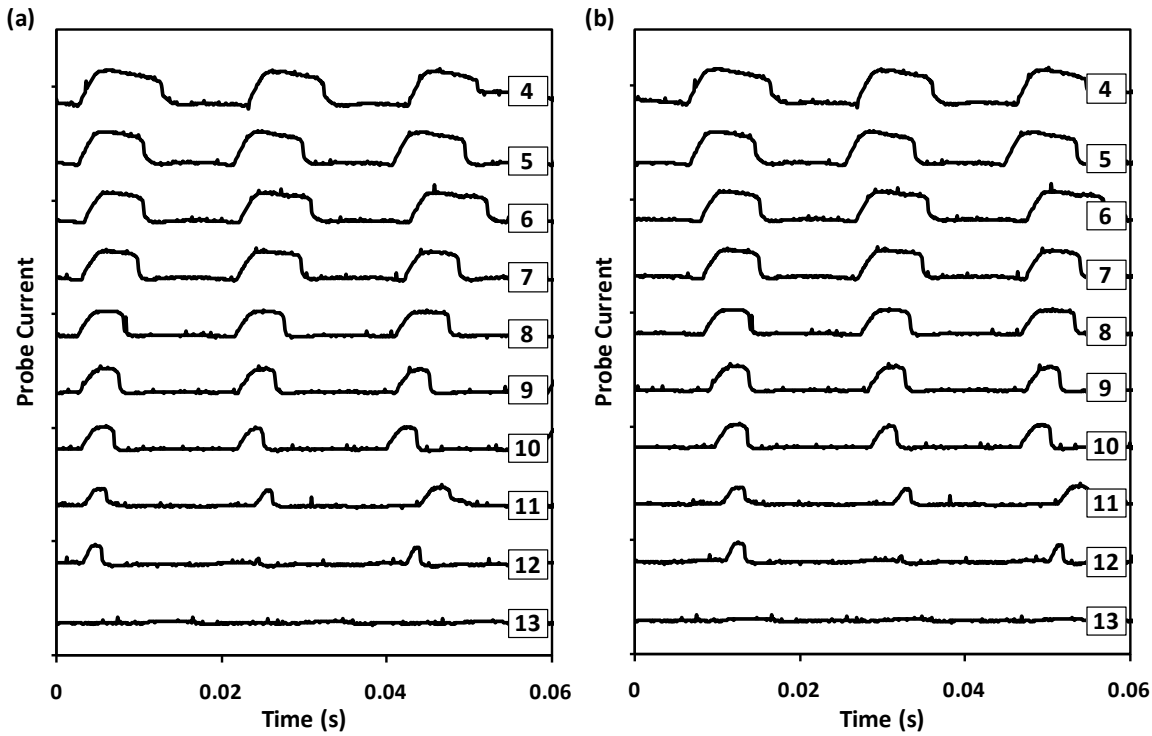


Figure 4.14. A subset of the measured current traces (a) before time adjustment and (b) after time adjustment for the delay between each measurement point.

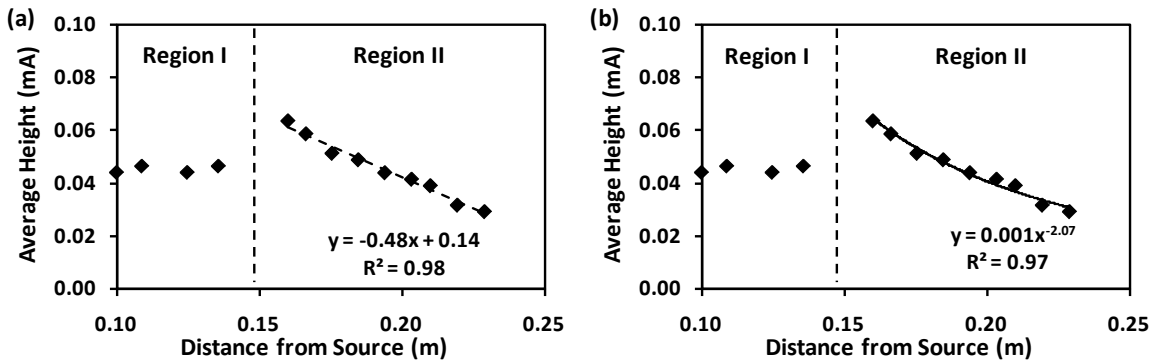


Figure 4.15. The average height of the observed features in measured probe currents as a function of the distance from the source fitted with (a) linear and (b) power law trend lines.

volume of a cylinder is equal to  $\pi R^2 h$  where  $h$  is the height of the cylinder and  $R$  is its radius, then it could be expected that the density would decrease proportional to the inverse square of  $R$ . Figure 4.15(b) presents the same data from (a) with the linear trend line now replaced by a power law. As indicated by the equation inset within the figure, the data can be well modelled by a power law that closely follows the inverse square of the distance between the probe and the source. It should be noted that while the measured quantity in figure 4.15, i.e. the average height of the oscillatory features in probe currents, is expected to depend on the plasma density, it is an indirect result of the density and perhaps should not be expected to display the same behaviour.

#### 4.4. Previous Literature on SF<sub>6</sub> Plasma Instabilities

Plasma environments similar to those being studied in this work are of great interest to many fields of science including most notably fusion research and materials processing. Of particular interest in the field of materials processing is the study of physical and chemical etching of silicon and silica by means of a controlled plasma exposure.<sup>1</sup> In the context of this work sulphur hexafluoride has been shown to have favourable chemical etchant properties, but cause undesirable surface defects.<sup>128</sup> However when it is mixed with another gas that has good *physical* etchant properties such as argon, oxygen or nitrogen, it has been found to become a useful process particularly in the semiconductor and glass industry, where deep etching with high resolution is desired.<sup>128-134</sup> Unsurprisingly then studies have been performed on these plasma processes and instabilities similar to those observed here have also previously been observed.

##### 4.4.1. Previously Observed Instabilities in SF<sub>6</sub> Plasma

In 1996 Tuszewski reported oscillations in measured probe currents in the kHz range for plasma in Ar/SF<sub>6</sub> (85% Ar, 15% SF<sub>6</sub>) and also pure O<sub>2</sub>.<sup>135</sup> The system under investigation was markedly different to that discussed in this work, with notable differences being a much lower drive frequency at 0.46 MHz and the use of an external 12-turn coil surrounding a hemispherical reactor volume. Consequently the power delivery was also much greater with a range of 100 – 500 W. The author reported a strong dependence on experimental conditions such as gas pressure and rf power. As the gas pressure increased from either Ar/SF<sub>6</sub> or pure O<sub>2</sub>, the frequency of the oscillation was seen to decrease dramatically. For oxygen the instability was seen to be present only in a discrete interval of gas pressures across a wide range of applied powers, and appeared most strongly for large negative probe bias. A spatial dependence was also discussed, with results showing the magnitude of the oscillations being the greatest nearest to the source. While this work compared results between the Ar/SF<sub>6</sub> and O<sub>2</sub> plasma, greater focus was given to the latter.

Lieberman *et al.* presented work in 1999 showing a frequency spectrum of collected probe currents with peaks across a wide range of frequencies from 1 – 10 kHz in discharges of pure SF<sub>6</sub>.<sup>136</sup> The experimental setup detailed the use of a planar coil driven at 13.56 MHz from 100 – 1000 W. The authors were also able to correlate the observed oscillations with that of spikes in the intensity of the light emission from the discharge, although it was not

detailed whether this was emission from a particular wavelength or the total emitted light from the plasma. The authors went on to discuss the development of a model in an attempt to explain the effects being observed.

In 2001 Chabert *et al.* reported in-depth experimental work on oscillations in Langmuir probe currents.<sup>137</sup> The experimental setup was similar to that detailed by Lieberman *et al.* with a planar coil driven at 13.56 MHz with two systems studied in the work, Ar/SF<sub>6</sub> at 1:1 and pure SF<sub>6</sub>. Again the oscillations displayed a dependence on the selected power and pressure conditions within the experiment. A development in this work was the addition of optical emission spectroscopy whereby a single emission line, in this case the fluorine line at 703.7 nm, was monitored with respect to time. Interestingly, the intensity of this particular line was seen to oscillate with similar regularity to that of the measured probe currents, although not at the same frequency. The authors discussed the observed instability by considering the plasma to be in a quasi-equilibrium state between a capacitive (E-mode) and inductive (H-mode) discharge. These two modes essentially describe how energy is delivered to plasma species. The E-mode ionises and accelerates the plasma species via the strong instantaneous *electric* field generated from the source while the H-mode induces strong *magnetic* fields, with the corresponding electric field being relatively weak.<sup>62</sup> The electric fields only propagate short distances into the plasma while the magnetic fields propagate further. Consequently, the H-mode commonly generates much higher plasma densities than the E-mode. The transition from E- to H-mode in SF<sub>6</sub> plasma studied by Chabert was concluded to be an unstable one, leading to the observed behaviour.

Transitions between stable capacitive and stable inductive modes have also been discussed and are of particular interest in plasma physics due to marked difference between the two modes in terms of certain properties of the plasma. Lieberman and Boswell developed a model for the transition between the E- and H- modes of a plasma system (and ultimately the W-mode, the so-called wave-sustained or helicon mode).<sup>138</sup> Since the E-mode is sustained largely through the large potentials on the driving antenna, plasma densities moving away from the source are seen to be very asymmetric. Upon transition to the H-mode the density greatly increases throughout a given system. Miyoshi *et al.* characterised E- to H-mode transitions in Ar plasma through the use of computerised tomography with

results showing not only an increased density throughout the system upon transition to the H-mode, but also that the plasma density becomes far more isotropic.<sup>139</sup>

Kim and Aydil detailed the use of a particularly innovative planar probe array incorporated into a silicon wafer used to measure the ion flux throughout a reactor with pure SF<sub>6</sub> plasma driven at 13.56 MHz by an external planar coil.<sup>76</sup> The instability was observed to display similar oscillations in measured Langmuir probe currents. A key difference between this work and that published prior was that these oscillations were observed to have frequencies in the order of only Hz.

In 2003 Tuszewski *et al.* presented results obtained within the same system detailed in 1996. Using a high speed camera images were captured of a higher density ‘refill’ plasma passing across a cylindrical Langmuir probe.<sup>140</sup> The images were directly correlated with measurements of the positive ion density showing that when the density spikes occurred the probe was found to be engulfed in the higher density plasma region. Measurements from an axial array of Langmuir probes were able to elucidate the speed of the wave to be  $\sim 150\text{ms}^{-1}$ . In this same year Tuszewski and White made comparisons between the 0.46 MHz hemispherical reactor and a planar reactor at 13.56 MHz.<sup>141</sup> Not only did the instability domains vary between these two chambers, but the observed oscillations also varied greatly leading to the conclusion that in fact there were two distinctly different oscillations occurring in the strongly electronegative SF<sub>6</sub> environment; that of downstream instabilities and source oscillations. Downstream instabilities were found to be localised phenomena, forming near to the source and travelling outward in the flowing plasma resulting in density fluctuations throughout the chamber. Source oscillations were found to occur as density variations near to the source and were evident in a range of powers between the stable capacitive and stable inductive modes of the system. The authors added that these oscillations were consistent with E- to H-mode transitions.

#### 4.4.2. Summary and Comparison with Instabilities Observed in the Flinders Reactor

Upon reviewing the literature, it becomes clear that instabilities in SF<sub>6</sub> plasma are a seemingly common occurrence. These instabilities lead to oscillations in measured current from electrostatic probes in contact with the plasma. It must be stated though that the nature of these instabilities differs throughout the literature. Table 4.1 summarises key details from the surveyed research including experimental design and the range of

**Table 4.1. A summary of key details from the reviewed literature regarding observed instabilities in plasma containing SF<sub>6</sub>.**

Reference	Source	Gas	Probe	Bias	Frequency
<b>Tuszewski (1996)</b>	External Cylindrical 0.46 MHz	Ar/SF <sub>6</sub> (85:15) O <sub>2</sub>	Cylindrical	Unbiased	Ar/SF <sub>6</sub> : ~4 kHz O <sub>2</sub> : ~10 kHz
<b>Lieberman <i>et al.</i> (1999)</b>	External Planar 13.56 MHz	SF <sub>6</sub>	Cylindrical	Unbiased	1 Hz – 900 kHz
<b>Chabert <i>et al.</i> (2001)</b>	External Planar 13.56 MHz	Ar/SF <sub>6</sub> (1:1) SF <sub>6</sub>	Planar Cylindrical	Pl.: -50 V Cyl.: varied	Ar/SF <sub>6</sub> : 1 – 9 kHz SF <sub>6</sub> : 1 – 90 kHz
<b>Kim and Aydil (2003)</b>	External Planar 13.56 MHz	SF <sub>6</sub>	Planar	-70 V	2 Hz
<b>Tuszewski <i>et al.</i> (2003)</b>	External Cylindrical 0.46 MHz	Ar/SF <sub>6</sub>	Cylindrical	-50 V	0.6 – 1.3 kHz
<b>This Work</b>	Internal Loop 13.56 MHz	SF <sub>6</sub>	Cylindrical	50 V	1 – 100 Hz

frequencies at which the instability was observed to oscillate with the details from this research included.

A majority of the instabilities reported in the literature had measured frequencies on the ~kHz scale, most commonly from 1 – 10 kHz, although frequencies were reported up to 900 kHz.<sup>136</sup> As previously stated, mixtures of Ar and SF<sub>6</sub> are of interest for etching processes and thus much of the research revolved around these mixtures rather than of pure SF<sub>6</sub>. When pure SF<sub>6</sub> was investigated a wider range of frequencies appeared to be observed, and of most importance to this work, gave rise to much lower frequency oscillations in more than one case.<sup>76,136,137</sup> In contrast with this work, the oscillations were also mostly observed in positive ion currents, with either negatively biased or floating probes, rather than in electron or negative ion currents with a positively biased probe.

Perhaps the most critical difference between this work and the literature is the type of source geometry, i.e. the antenna. In the literature, a common arrangement involved an external rf coil, either in a planar form<sup>76,137,141,142</sup> or wrapped around the reactor volume as in the work by Tuszewski.<sup>135,140-143</sup> Power was then transmitted through some dielectric medium, commonly quartz, requiring greater rf power to be delivered. The reactor at Flinders however used an *internal* antenna consisting of a single loop of stainless steel and as a result the required power levels were much lower. Whether this difference in source design is the key to the apparent differences between the instability observed in this work

and that which has already been published is uncertain, however the way in which power is coupled to the plasma is likely to drastically affect how it behaves.

Although the root cause of the observed SF<sub>6</sub> plasma instability in the Flinders reactor is not clear, some possibilities can be discredited. For example, Tuszewski *et al.* concluded that the source oscillation observed within their reactor was due to an unstable E- to H-mode transition.<sup>141</sup> Likewise, Chabert *et al.* used this unstable transition to explain the phenomena observed within that research.<sup>137</sup> A majority of the characterisation of the instability presented here was performed using significantly lower rf powers than the work of Tuszewski, and as such it is expected that the plasma would be driven through capacitive coupling between the antenna and plasma. Moreover, a transition from the capacitive to the inductive mode occurs with a subsequent and significant increase in plasma density. No such phenomenon was observable with SF<sub>6</sub> plasma for any power or pressure range studied. Neither was it observed with any other gas readily available during this research. Consequently the argument of an unstable E- to H-mode transition in the SF<sub>6</sub> plasma would not seem to be amenable here.

The speed of the density ‘refill’ plasma observed by Tuszewski was determined to be  $\sim 150 \text{ ms}^{-1}$ .<sup>141</sup> The authors made a point to note the similarity between this speed, and that of the neutral gas speed of Ar/SF<sub>6</sub> molecules. Furthermore, in 1996 Tuszewski noted the similarity between the observed propagation velocities in that work with the ion acoustic (Bohm) velocity. This quantity is given by

$$v_B = \sqrt{\frac{k_B T_e}{m_i}}$$

where  $k_B$  is Boltzmann’s constant,  $T_e$  is the electron temperature and  $m_i$  is the ion mass.<sup>61</sup> If one were to make conservative assumptions and take the mass to be equal to that of an SF<sub>6</sub> molecule, and the electron temperature to be 1 eV, then the acoustic velocity is found to be  $\sim 800 \text{ ms}^{-1}$ . If the mass of atomic fluorine were substituted instead, the result would increase to  $2200 \text{ ms}^{-1}$ . These values far exceed that of the speed of  $\sim 16 \text{ ms}^{-1}$  determined here. The electron temperature of 1 eV, as will be seen later in this chapter, is a very modest estimate. However increases in this value would only serve to further increase the calculated ion acoustic velocity, and thus make it an even less likely possibility. From this analysis it is therefore suggested that an ion acoustic wave could not be responsible for plasma instability with such a low propagation speed.

#### 4.5. Effect on Sample Functionalisation

Since the aim of this research was primarily to study the functionalisation of carbon nanotubes as a result of exposure to plasma containing SF<sub>6</sub>, it would be remiss to not consider the effect that the instability might have on a surface modification experiment.

The instability was hypothesised to create waves of higher density plasma that propagated throughout the chamber. In the absence of these waves there still remained a background level of plasma density in the reaction volume. Therefore, irrespective of the frequency or intensity of the instability a sample placed inside the reactor would be exposed to plasma at some density for the duration of the experiment. What must be considered is the effect of varying the experimental conditions. Ideally an experiment designed to study the effect of a given parameter on the subsequent functionalisation of a carbon surface would call for a set of controlled samples to be exposed to plasma with that parameter being systematically varied. However the instability has been shown to behave differently under changing conditions. Thus any quantified change in a surface after exposure to varying conditions would be convoluted with changes in the behaviour of the instability.

From the data presented here it would be reasonable to suggest that the primary experimental variable of concern is the radial position of the sample throughout the chamber. At distances far away from the centre of the chamber a sample would experience less time exposed to the higher density wave. Thus over a given experimental time frame, a number of minutes for example, it will have been exposed to a lower average plasma density than a sample in the centre of the chamber, and should be expected to have a different level of functionalisation. This effect would be coupled with an expected overall density gradient as one moved away from the source; the density would be lower at the chamber walls than next to the antenna. The solution to this issue is consistency in sample placement, something made easy by the fixed table position within the chamber.

Variation in parameters such as power and pressure certainly affected the way in which the instability behaved. Changes in the oscillation frequency however do not pose concern for reliable quantification of results as overall the average density that a sample has been exposed to should remain the same. That is, if an instability cycle consisted of 40% of time at a high density and 60% of time at a low density, then by the end of an experiment a surface will have been exposed to a high density 40% of the time and low density 60% of

the time irrespective of the frequency of these cycles. It should however be noted that the *magnitude* of the oscillations may pose concerns for quantification of results. If the oscillation is more intense under a certain set of conditions then in turn this would suggest a higher average density would be experienced. Furthermore, the instability may also impose a fluctuating space potential, something that could not be quantified on a sufficiently short time-scale during this research. If such fluctuations were present, then this would in turn incite ion bombardment at the surface with impact energies that would fluctuate with the space potential. This could be problematic for surfaces sensitive to physical sputtering.

Consideration of the matching circuit is of low priority. When plasma is ignited in the system the matching unit is always tuned in such a way that minimises reflected power using the lowest possible matching capacitances. Thus for multiple experiments, provided consistency in experimental protocol is maintained, the effect on sample functionalisation should be essentially nil.

#### **4.6. Refinement of the Langmuir Probe Experiment**

The motivation behind applying Langmuir probe experiments to SF<sub>6</sub> plasma was to develop an understanding of the way in which certain plasma properties would react upon variation in experimental parameters. This experiment was complicated upon encountering the instability that ultimately results in a distortion of the I-V curves that were necessary to elucidate information about the plasma. One method to resolve this complication was to simply collect a greater number of I-V curves in an effort to ‘average out’ the fluctuations. This approach was only marginally successful and the data still remained somewhat inadequate for reliable analysis. Thus it was deemed that a more thorough method for removing the instability as a source of error was necessary.

When the Langmuir probe experiment was first commissioned by Deslandes, the data acquisition (DAQ) device used to interface between the computer and the measurement circuit was a National Instruments USB-6008.<sup>108</sup> This device was capable of a maximum sampling rate of 10,000 Samples per second (10 kS/s). The entire voltage sweep was performed across 250 ms including the cleaning cycle, with the linear ramp used for generation of the I-V characteristic being collected in 100 ms. Collected I-V characteristics were made up of a total of 1000 points. For instabilities of 1 – 100 Hz, multiple instability

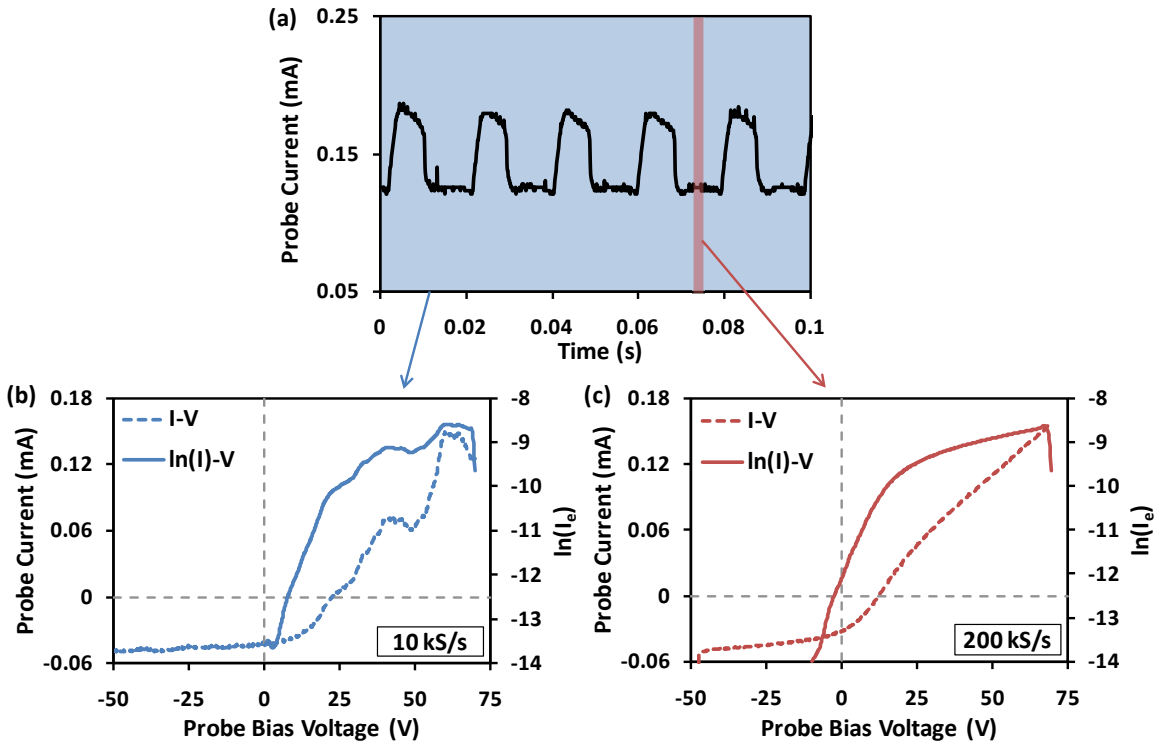


**Figure 4.16.** The effect of improved sampling rate on data collected from unstable SF<sub>6</sub> plasma with (a) a typical oscillation over a 100 ms timeframe (b) data collected at 10 kS/s and (c) data collected at 200 kS/s. The blue shaded area in (a) corresponds to the time taken to collect the data in (b) while the red area corresponds to the sampling time for the data in (c).

cycles may occur during the collection of each I-V characteristic. This is represented in figure 4.16(a) as the blue shaded area. Ultimately this resulted in distorted I-V characteristics, an example of which is presented in figure 4.16(b). The proposed solution to this problem was to sample much faster than was previously possible, allowing characteristics to be collected before a significant density variation could occur.

The NI-USB-6008 was replaced with a NI-PCI-6024E DAQ card. This device was capable of collecting data at 200 kS/s, twenty times faster than the USB-6008. This allowed for the entire sweep to be performed over only 12.5 ms. To further reduce this collection time the number of points collected was halved from 1000 to 500, which was still considered an ample number of points, resulting in a total collection time of only 6.25 ms. The linear voltage ramp and the resulting current response from the probe, the most important part of the process, was therefore collected in only 2.5ms, an overall reduction in collection time of 40 times. In figure 4.16(a) this timeframe is represented by the red shaded area.

Example I-V characteristics with corresponding  $\ln(I)-V$  curves are given in figure 4.16(b) and (c) for data collected at 10 kS/s and 200 kS/s, colour coded to relate to the blue and red

shaded areas in (a) respectively. The improvement in quality through the severe reduction in distorted data in (b) is unquestionable. Not only were measurements such as the floating potential (that come directly from the I-V curve) made less ambiguous, but confidence in linear fits made to the  $\ln(I)$ -V curve is also greatly increased.

The data presented is again an average of multiple data sets; 25 sets were collected in this case, and this results in certain implications. For example the red shaded area in figure 4.16(a) indicates the time frame across which a single data set would be collected. In the indicated position the plasma should be expected to be constant across a time span of approximately 10 ms, ample time for a data set to be collected without any appreciable change and hence resulting in a reliable measurement. However, considering the Langmuir probe software collected data as fast as possible without any controlled timing between each measurement, the red shaded area could have been at any position in (a) and thus data could be collected at any point during the cycle. Taking multiple data sets then assisted in getting a measurement of the *average* state of the plasma. The assumption was that for a majority of the measurements made the data was collected fast enough so that little change occurred from the start of the measurement to the end. It was however inevitable for a data set to eventually be collected at the onset of an instability cycle where the plasma was definitely not steady-state. Each data set was collected and displayed in real-time however and as such the responsibility then fell on the analyst to observe the anomalous behaviour and take appropriate action either restarting the data collection or removing the erroneous data set from the combined average.

#### **4.7. Langmuir Probe Characterisation of SF<sub>6</sub> Plasma**

With the advent of an experimental design that could facilitate the removal of significant I-V curve distortion caused by density fluctuations, the original aim to characterise SF<sub>6</sub> plasma with respect to experimental parameters could be addressed. The parameters of particular interest were gas pressure and rf power. These were deemed the parameters directly related to generation of the plasma that would most likely have an effect on surface functionalisation. To study these parameters, SF<sub>6</sub> plasma was maintained at constant pressure while the applied rf power was increased systematically. To achieve the optimal match prior to each experiment the reflected power was minimised at the highest applied rf power first, and then held constant. The absorbed power, taken as the difference between the applied and reflected power, was varied from 10 – 80 W. The experiment was

performed at three pressures; 2.5 mTorr, 5 mTorr and 10 mTorr, and I-V characteristics were obtained at each variation in power for all three pressures. Upon analysis these characteristics elucidated changes in the space potential, ion and electron densities and the electron temperature with variation in power. The antenna self-bias was also monitored through an independent measurement circuit. Adopting the knowledge gained in Chapter 3, the system was allowed to equilibrate for 10 minutes prior to measurements being performed, and each I-V characteristic was the average of 100 individual I-V curves with a collection time of around 50 seconds ensuring each measurement represented the average state of the plasma as accurately as possible.

#### 4.7.1. The Variation in Antenna Self-Bias

The antenna self-bias voltage was observed to have a linear dependence on absorbed rf power as evidenced in figure 4.17(a). For the three pressures studied the magnitude of  $V_{dc}$  increased with increasing rf power although the rate of increase was not seen to be equal for all pressures. At low powers the differences in  $V_{dc}$  were minimal across the pressure range, with an average value of  $-69 \pm 4$  V. However as the absorbed power increased the trends were seen to diverge, with the rate of increase in  $V_{dc}$  much greater for lower pressure. At the maximum absorbed power  $V_{dc}$  was seen to reach  $-434$  V for the 2.5 mTorr plasma and  $-282$  V for the 10 mTorr plasma, a difference of 152 V. A possible consequence of this effect is that capacitive coupling due to the large static antenna bias may be greater at lower gas pressures.

Consider figure 4.17(b), which helps to describe the evolution of antenna bias.<sup>108,127</sup> The applied rf waveform can be represented in simple terms by

$$V_{rf}(t) = V_{rf} \cos(\omega t)$$

where  $V_{rf}$  is the maximum amplitude of the input wave ( $\omega$  is frequency and  $t$  is time) which oscillates with an equal magnitude above and below zero volts. If the space potential  $V_s$  is assumed to be positive and less than the maximum amplitude of the input wave then whenever  $V_{rf}(t)$  is above  $V_s$ , i.e. more positive than the steady-state potential of the plasma, then there will be a net flow of electrons onto the antenna. Conversely when  $V_{rf}(t)$  is below  $V_s$  there will be a net flow of positive ions to the antenna. Because of the much greater mobility of electrons than ions, the ultimate result is an accumulation of negative charge on the antenna. The applied rf power is varied through changes in the

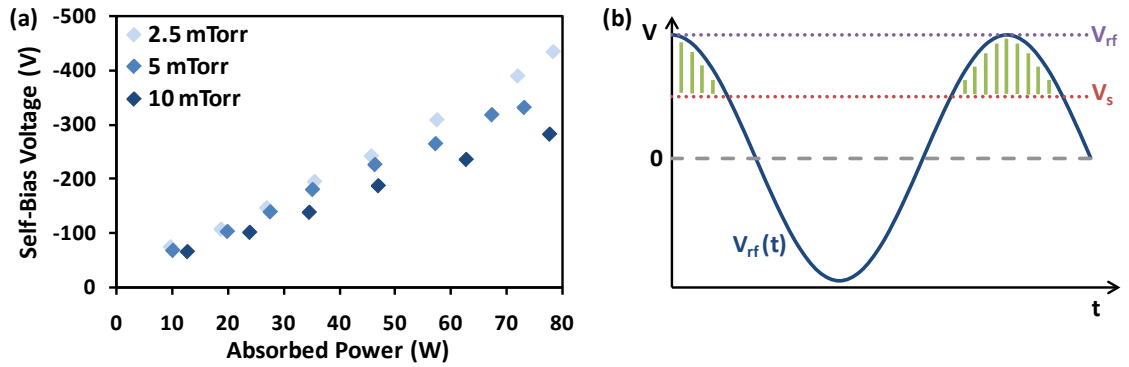


**Figure 4.17. (a) Antenna self-bias measurements with increasing absorbed rf power for three pressures; 2.5 mTorr (light blue), 5 mTorr (blue) and 10 mTorr (dark blue) and (b) the cause of self-bias voltage modified from Deslandes<sup>108</sup> and Aanesland.<sup>127</sup>**

peak-to-peak voltage of the input wave, i.e.  $V_{rf}$ , thus as  $V_{rf}$  is increased the resultant accumulated charge increases and the antenna bias rises. Since the applied rf power was increased linearly then it stands to reason that the antenna self-bias would also increase linearly. As a result, the trends in figure 4.17(a) were not unexpected.

#### 4.7.2. The Variation in Ion and Electron Densities

Ion and electron densities for the three gas pressures are presented in figure 4.18(a) and (b) respectively. At 2.5 mTorr both the ion and electron densities increased with absorbed power. This trend would seem intuitive given that as power is increased the degree of ionisation should be expected to increase through either plasma species having a greater average energy, or perhaps the coupling power from the antenna having a greater influence further throughout the chamber. The plasma at 2.5 mTorr was the only one to show this mutual increase in ion and electron density. While electron densities increased in much the same way for the higher pressures the ion density appeared to remain largely constant at 5 mTorr for all powers and showed a decline for 10 mTorr plasma with a local minimum around 48 W. Although intuitively this may not be expected, given what was observed regarding the instability in SF<sub>6</sub> plasma this could possibly be explained. It was found that there were regions of power and pressure where the oscillation had minimal intensity. Since the measurements given here are time-averaged it is quite possible that the instability adversely affected the average ion density causing the observed decline. That is, when the instability was very intense, on average the density sensed by the probe was greater than when the instability was weak.

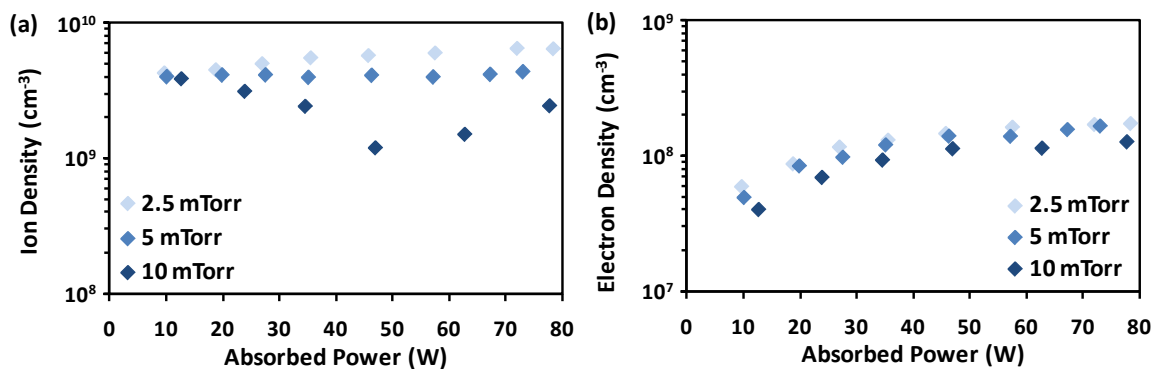


**Figure 4.18.** The variation in (a) ion density and (b) electron density with respect to absorbed power for SF<sub>6</sub> plasma at different pressures.

Overall, the densities measured here agree well with density ranges measured in plasma ignited within other source gases in the Flinders reactor.<sup>103,108</sup> They are also typical of plasma generated through this means of coupling, and are considered a low-density plasma with a degree of ionisation less than 1%.<sup>1</sup> It is curious to note the different orders of magnitude between the electron and ion densities. Since one of the assumptions made regarding the plasma was that of quasineutrality it was expected that the ion and electron densities would be somewhat similar, as was the case while studying the nitrogen system in Chapter 3. The data presented here came from two analyses that determine ion and electron densities independently. It has already been noted that small errors in judgement with the fitting procedure can be magnified greatly by the exponential nature of the electron density calculation, and as such it should not be ignored as a source of error. In the absence of inconsistency in the data analysis procedure, the general trends in the densities should remain similar to that presented here, although if errors due to judgement are propagated the absolute values may be affected. Another factor that should be considered is the nature of the sulphur hexafluoride, which is considered to be strongly electronegative. In the presence of electrons SF<sub>6</sub> may form SF<sub>6</sub><sup>-</sup> ions through electron attachment, and importantly may provide a pathway for electron loss other than to the chamber surfaces. In certain exotic circumstances this has resulted in plasma where the positive ion density is as much as 10<sup>3</sup> times larger than the electron density.<sup>70</sup>

#### 4.7.3. The Variation in Space Potential, Floating Potential and Electron Temperature

Results detailing the dependence of the space potential and floating potential on absorbed power are given in figure 4.19. Similar to that observed by Deslandes for hydrogen plasma, the space potential, seen in figure 4.19(a), showed only minimal variation for increasing

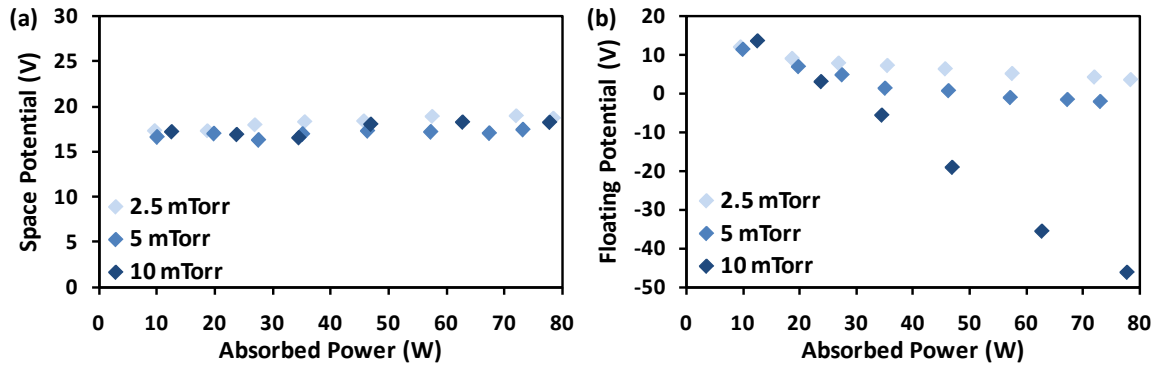


**Figure 4.19.** The variation in (a) space potential and (b) floating potential with respect to absorbed power for SF<sub>6</sub> plasma at different pressures.

absorbed power.<sup>108</sup> The variance within each data set was less than 0.5 V and given that the average value in each case was 17 – 18 V this suggested a very minimal dependence on power. Pressure was observed to have little to no effect on the space potential with the average values being  $18.2 \pm 0.5$  V,  $17.0 \pm 0.2$  V and  $17.5 \pm 0.4$  V for the 2.5 mTorr, 5 mTorr and 10 mTorr plasma respectively.

In contrast to the space potential, the floating potential showed significant dependence on absorbed rf power as seen in figure 4.19(b). At the lower pressures, 2.5 mTorr and 5 mTorr, the floating potential decreased from a value around 12 V to near zero volts in both cases. The difference in  $V_f$  between the extrema of absorbed power was noticeably greater for the 5 mTorr plasma than the 2.5 mTorr plasma. Of more immediate concern though was what was observed at 10 mTorr. The floating voltage was seen to rapidly drop from an initial value of around 13 V, similar to that observed for the lower pressures, down to -46 V. It must be noted here that the voltage sweep applied to the probe to generate I-V characteristics started at -50 V. A value so close to this starting point strongly suggested that something was occurring in the plasma that had not yet been considered. An assumption was made in the theory used to treat ion collection by a Langmuir probe whereby the distribution of electron velocities (or energies) within the plasma would adhere to a single Maxwellian distribution. This assumption is not always valid, and for some plasma two distinct distributions may exist with markedly different energies.<sup>61,70</sup> When this occurs the plasma is said to have a bi-Maxwellian distribution.

#### *A Bi-Maxwellian Distribution of Electron Temperatures*

Experimentally, the presence of a second distribution of electron energies can be observed in semi-log plots of the electron current. Examples of this are given in figure 4.20(a) for

10 mTorr SF<sub>6</sub> plasma where the dark blue and the red traces represent the lowest and highest absorbed powers respectively. The lowest two power increments showed the expected shape of the semi-log, with only two linear regions. This is typical of low density plasma where a majority of the electron current is collected for probe biases above zero volts. Most of the electrons do not have sufficient energy to overcome the repulsive negative potential and thus are only collected at positive bias. These electrons are often labelled the ‘cold’ electrons. Upon increasing the absorbed power, the shape of the curve suddenly changed to include a third region, with a significant increase in measured current for negative bias. The third region was indicative of the emergence of a high-energy population of electrons that had significantly greater velocities and could consequently overcome the negative potential and be collected. These electrons are labelled the ‘hot’ electrons. Inset within figure 4.20(a) are example semi-log plots from 2.5 mTorr plasma under the same systematic variation. At this pressure the plots showed no emergence of a secondary electron velocity distribution.

Presented in figure 4.20(b) are the I-V curves used to generate the semi-log plots in (a). The floating potential is defined as the probe voltage that results in zero net current flow through the circuit. Determination of the floating potential therefore simply came from finding the  $x$ -intercept of the measured I-V curve. The point at which each curve in (b) crossed the abscissa is given in more detail in the inset. From this data the cause of the erroneous  $V_f$  measurements at 10 mTorr becomes clearer; the presence of the secondary distribution of high energy electrons increased the measured probe current for negative bias. This increase shifted the position of the  $x$ -intercept for each trace, convoluting the determination of  $V_f$ . This effect was not observed for lower pressures since at those pressures only a single electron velocity distribution was present.

The measured electron temperatures in plasma of different absorbed power for the pressures studied are given in figure 4.21. At 2.5 mTorr and 5 mTorr the electron temperatures were largely constant at 6 eV across the entire power range. At 10 mTorr though, for powers above 50 W, the electron temperature was separated into two distinct populations with significantly different energies. The cold electrons remained below 10 eV up to the maximum absorbed power while the hot electrons reached 21 eV. Deslandes posited that the cause of the bi-Maxwellian distribution in plasma ignited within the

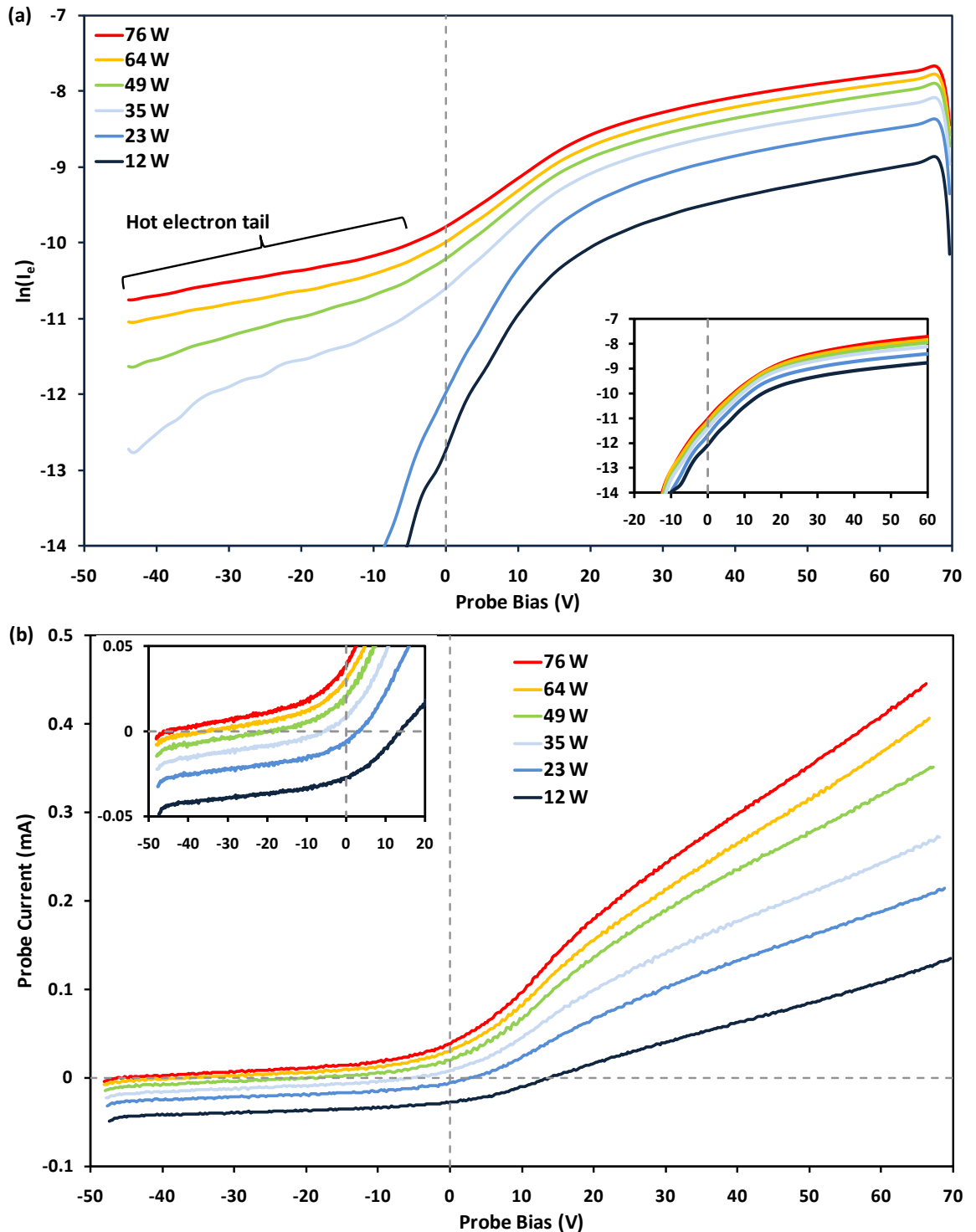
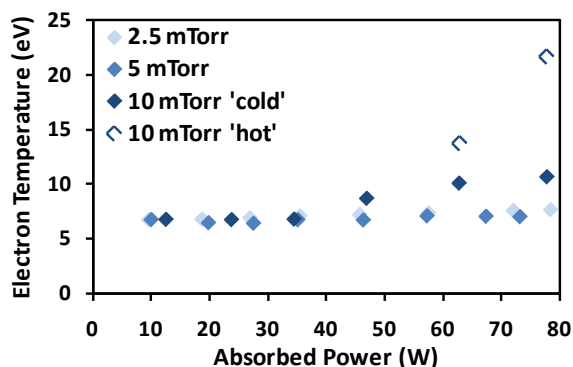


Figure 4.20. (a) Semi-log plots of electron current measured in SF<sub>6</sub> plasma at 10 mTorr for increasing absorbed power showing a tail in the curves at low probe bias resulting from a high energy portion of electrons. The inset shows the comparable result at 2.5 mTorr. (b) The corresponding I-V curves with the inset showing a zoomed area of the abscissa, highlighting the x-intercepts and thus the variation in floating potential. For all plots the absorbed rf powers were 12 W (dark blue), 23 W (blue), 35 W (light blue), 49 W (green), 64 W (orange) and 76 W (red).



**Figure 4.21. Electron temperatures for SF<sub>6</sub> plasma with increasing absorbed power.**

Flinders reactor is due to the way in which rf power was coupled to the plasma species and the geometry of the chamber and its components.<sup>108</sup> The antenna was internal, meaning it was in direct contact with the plasma. As was discovered the dc bias on this antenna could reach several hundred volts, a strong enough potential to drive capacitive coupling in an area somewhat localised around the antenna, producing a region of high energy species. Ionisation can also occur through other processes such as collisions between the gaseous species. Since the mean free path of electrons can be on the order of millimetres in the experimental regime explored in this thesis, this secondary ionisation process can spread the plasma density further throughout the chamber but at the expense of electron energy. Since the Langmuir probe was quite remote from the antenna, most of the time it was likely to sense the low energy electrons spread outward from the source rather than the high energy electrons that remain more localised around the antenna. In some cases however, the high energy electrons can appear as a ‘beam’ of hot electrons that flow throughout the chamber and are subsequently collected by the Langmuir probe.

#### 4.7.4. The Spatial Distribution of Electron Density

The instability that was observed in SF<sub>6</sub> plasma displayed a significant spatial dependence as detailed earlier in Section 4.3. As the Langmuir probe was positioned further from the source, the features observed in the probe current traces were observed to decrease in both width and intensity. It was considered that the hypothesised expansion and contraction of the plasma density that resulted in the probe current oscillations should occur within a cylindrical volume. When a suitable model was generated, an inverse square law was found to be most amenable to the data, lending evidence towards the expansion and contraction of a cylindrical volume. It was noted however that while the intensity of the fluctuations should be dependent upon the plasma density, they may not behave in the

same manner. Thus quantification of the plasma density with respect to the spatial position of the Langmuir probe was performed to attempt to elucidate how it was affected by the instability throughout the chamber.

Presented in figure 4.22 are the measured electron densities as a function of the distance between the Langmuir probe and the source. The probe was moved outward from the source in an identical fashion to that discussed in the spatial distribution experiment presented in figure 4.11. In this case however, one hundred I-V characteristics were collected and averaged enabling the determination of the electron densities at each of the positions. Due to this method, each of these electron densities thus represents the average state of the plasma at each position. Similar to what was observed in figure 4.15, the measured electron densities were affected by the presence of the sample table and thus for brevity only the electron densities measured at positions pertaining to 'Region II' in figure 4.15 are shown here. The data has been fitted with two trend lines; (a) one generated from a linear relationship and (b) one from a power law relationship. The equations of the lines, as well as their determination coefficients ( $R^2$  values) are given in the figures.

Overall the average electron density decreases with increasing distance from the source. This observation makes sense considering both the nature of the plasma generation in the chamber and the instability that has been observed. It is expected that the SF<sub>6</sub> plasma under study in this work would remain in the capacitive mode and thus the ionisation and acceleration of plasma species is enacted by the electric field surrounding the antenna. This field penetrates a short distance into the plasma and ionisation is propagated by interactions and collisions between the gaseous species. Thus the generation of the plasma is expected to be highly distance dependent. The instability is hypothesised to be an expansion and contraction of the main plasma density. The volume within which this density fluctuation occurs is expected to be cylindrical. The plasma density within this volume should therefore be dependent on the inverse square of the radius if the variation occurs in two dimensions and should be expected to decrease as the distance from the source is increased.

Earlier, the intensity of the features in measured probe current traces were also found to decrease with increasing distance. The most suitable fit to the data was found to be that of an inverse square law, despite the apparent linearity of the trend. It was noted that perhaps the plasma density and the intensity of the features, while related, would not behave in the

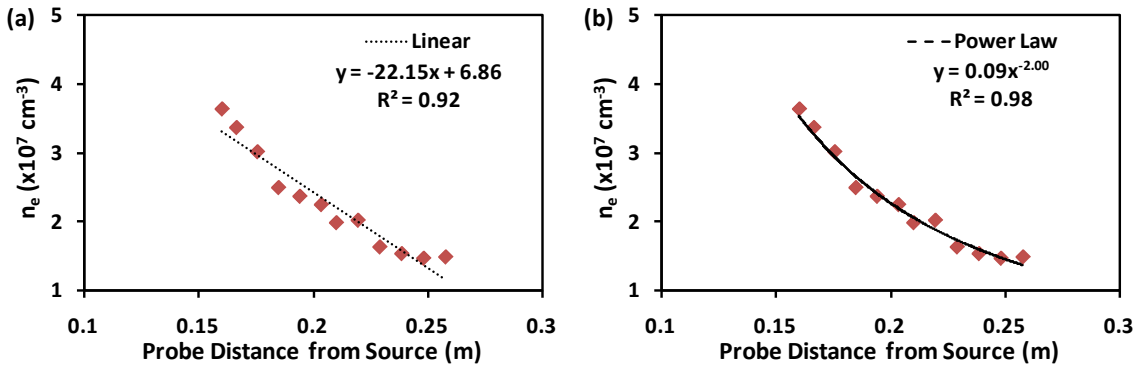


**Figure 4.22. Electron density with increasing distance from the plasma source. The data has been fitted with two trend lines; (a) linear and (b) power law.**

same manner. Fitted to the electron densities in figure 4.22 are two trend lines. Since the intensity of the features initially appeared to decrease linearly, a similar fit was applied to the electron densities as distance was increased, and is presented in figure 4.22(a). It was found that the linear trend line was not particularly amenable to this data set. However when a power law was applied, as presented in figure 4.22(b), a much greater correlation between the data and the trend line was found. The difference in the correlation between the data and the two trend lines is emphasised by the  $R^2$  values, where the power law is observed to have a greater correlation. It must be stressed that while the  $R^2$  value does not necessarily indicate that the power law is the *correct* choice for fitting the data, it does lend evidence towards it being the better correlation and thus a more likely model to predict the behaviour of the electron density than a linear trend.

The equation of the power law is given in figure 4.22(b) which indicates that the electron density has an inverse square dependence on the probe distance from the source. This result was predicted by the hypothesis that the plasma volume was largely cylindrical in nature (due to the chamber geometry) and that the expansion and contraction of the plasma due to the instability was constrained within this volume. As the plasma expands within this cylinder, the volume increases by the square of the radius (since the volume of a cylinder is  $\pi R^2 h$ ) and thus the density, which is defined as the number of plasma species per unit volume, decreases by the inverse of the radius squared. This result also helps to explain the result in figure 4.15(b), where the decrease in the probe current oscillation intensity was observed to decrease following an inverse square relationship with the distance from the source. As the plasma density is decreased, so too must the measured probe current which is generated by this density.

#### 4.8. Summary of Langmuir Probe Studies

Following an initial investigation into Langmuir probe characterisation and analysis within a well-understood environment, nitrogen plasma (as detailed earlier in Chapter 3), the experiment was applied to sulphur hexafluoride plasma. Its application to this environment uncovered an unexpected instability within the plasma that results in measured probe currents that oscillate at frequencies in the order of tens of Hertz. A review of scientific literature detailing instabilities observed in SF<sub>6</sub> plasma found that this frequency is significantly lower than that observed previously. While the fundamental cause of this difference remains unclear, it is likely that the somewhat novel ‘internal antenna’ design of the system is responsible. These oscillations are most strongly observed for large positive probe bias, indicating that the instability occurs in the electron or negative ion density rather than the positive ion density. These features are also only observed in measured probe currents when the plasma is generated within a certain range of rf powers and gas pressures for the system in this study.

The spatial distribution of the plasma and its instability was characterised by systematically shifting the Langmuir probe along a radial axis. A key result from this study was the observation that the features in measured Langmuir probe currents decrease in width as distance from the source is increased. Through careful analysis and interpretation of the data this led to the determination that the instability manifests as an expansion and contraction of the plasma density, with a ‘wavefront’ that travels at  $\sim 16 \text{ ms}^{-1}$  under the experimental conditions used.

An understanding of the instability enabled a refinement of the Langmuir probe apparatus to be made whereby the I-V characteristic could be obtained within a much smaller timeframe than was previously possible. This allows the data to be obtained before any significant change in the plasma local to the probe can occur due to the instability. Characterisation of the SF<sub>6</sub> plasma found that the electron density is strongly dependent on the applied rf power, increasing as the power is increased. It was also found to be strongly dependent on position within the chamber, decreasing in density by the inverse square of the distance from the source. Ion density however is affected more strongly by the gas pressure than by rf power, decreasing as the pressure is increased. Electron temperature also increases with rf power, and at higher pressures, a second high energy population of electrons with temperatures up to 20 eV can be observed.



---

## **Chapter 5.**

# **FLUORINATION OF CARBON NANOTUBES**

As detailed in the previous chapter, characterisation of SF<sub>6</sub> plasma was pursued until its behaviour was well understood. In this chapter, its application to the modification of carbon nanotube surfaces will be presented. The characterisation of single-walled carbon nanotube surfaces using analytical methods such as photoelectron and Raman spectroscopy is detailed. Finally, a study of the fluorination of carbon nanotube surfaces is presented.

### **5.1. X-ray Photoelectron Spectroscopy**

Of the few truly surface sensitive tools available, XPS may be the most widely known and utilised technique. As discussed earlier in Section 2.3, the surface sensitivity of XPS comes from the short IMFP of electrons that are ejected from a surface upon irradiation by photons of sufficient energy. The escape depth, and thus the surface sensitivity, for XPS instruments operating with common excitation sources is typically only a few nanometres. The actual escape depth depends on numerous factors, but mostly the material from which an electron is ejected and its kinetic energy. This level of sensitivity makes XPS an ideal technique to study the chemistry of a surface before and after its exposure to a given treatment. The usage of ‘soft’ X-rays, i.e. excitation energies of only 1 – 2 keV, also means

that XPS is particularly useful for studies of the light elements such as carbon, nitrogen, oxygen and fluorine. This is a result of the reduced photoionisation cross-section for light elements irradiated with X-rays of higher energy ( $\sim 10$  keV).<sup>144</sup> In this research photoelectron spectroscopy was the primary analysis method used to study carbon nanotube surfaces both prior to and after controlled plasma exposure.

#### 5.1.1.1. The XPS Spectra of CNTs

Presented in figure 5.1 are typical XPS spectra of two single-walled carbon nanotube surfaces collected on the LHS-10 at Flinders University. As described in Section 2.3.1, the analyser was operated in CRR mode for survey spectra to obtain maximum signal at the sacrifice of resolution. Thus the survey spectra presented herein are for qualitative analysis.

The single-walled carbon nanotubes studied in this research were produced via two methods; the HiPCO process and the arc discharge process. Unless otherwise stated, in both cases the raw material was used rather than the purified material in an effort to minimise the amount of carboxyl moieties on the nanotube sidewalls, the presence of which were anticipated to interfere with the analysis of C1s spectra. Presented in figures 5.1(a) and (b) are survey spectra of films created from these two materials. The un-purified HiPCO samples were designated 'Raw HiPCO' and presented in (a), while the un-purified arc discharge were designated 'AP' (As Prepared, nomenclature carried over from the manufacturer) and presented in (b). A strong carbon and oxygen signal was present in both spectra, as evidenced by the prominent C1s and O1s peaks. The C1s peaks were found to be at 284.5 eV, in strong agreement with what has been previously observed for SWCNTs, and indeed for  $sp^2$  hybridised carbon in general.<sup>145</sup> The O1s peaks were found to be at 531.5 eV for the raw HiPCO sample and 532.5 eV for the AP sample. An important difference between the two samples was the marked presence of iron in the raw HiPCO sample, a result of residual catalyst left behind after the manufacturing process. Normally acid purification would remove these impurities, along with other non-nanotube carbonaceous species, however since the samples were analysed raw, the catalyst used in their production was still present and observable. This is likely to be the cause of the different O1s peak energies between the samples, since metal oxides are expected to be lower in binding energy than carboxyl/carbonate species.<sup>146</sup> This is also the likely cause of the varied peak intensities.

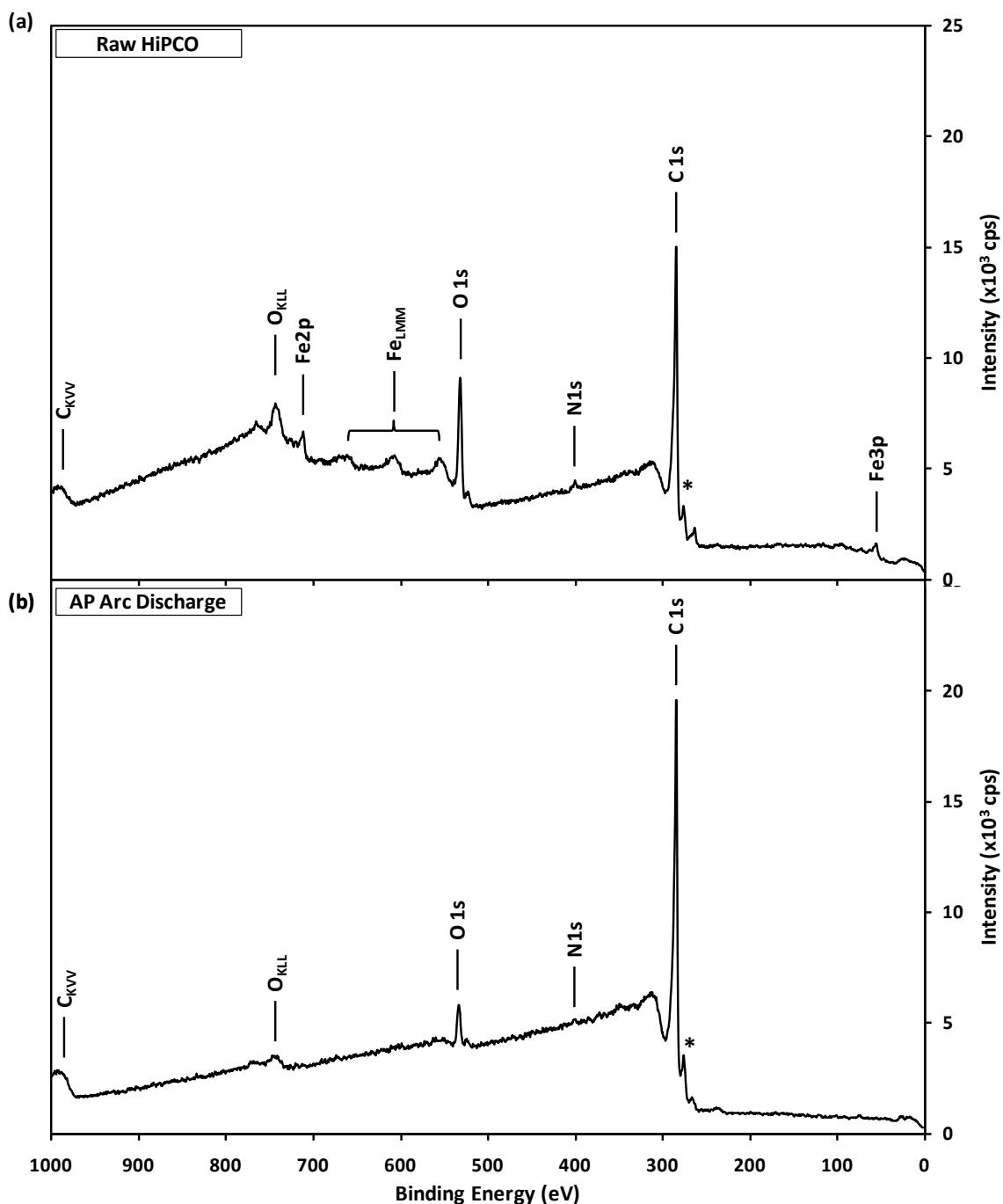


**Figure 5.1.** XPS survey spectra of (a) unpurified CNTs made via the HiPCO process and (b) unpurified CNTs made via the arc discharge process. Nanotube films were dispersed on pure tantalum foil for analysis. Spectra obtained in CRR mode using Mg  $K\alpha$  excitation. The peak labelled with an asterisk (\*) is a satellite peak due to the achromatic source used.

In contrast, the AP sample showed no evidence of metal catalyst, despite the fact that no purification had been performed. The catalyst used to grow AP tubes was a nickel-yttrium mixture which would show strong peaks at 853 eV (Ni) and 158 eV (Y), neither of which was detected in the sample. This does not necessarily mean that the catalyst was not present in the sample, but merely that it was not in high enough quantity to be detected.

Nitrogen was also detectable in both samples, albeit in very small amounts. It is likely that this was due mostly to the solvent, dimethylformamide, that was used to disperse the nanotubes to form the film onto the tantalum substrate, which has a chemical formula of  $(\text{CH}_3)_2\text{NC}(\text{O})\text{H}$ .

Marked with an asterisk (\*) on the lower binding energy side of the C1s peaks is another feature at 276 eV. This is a feature of XPS spectra that sometimes gets confused as pertaining to the chemical nature of the material when in it is actually known as a satellite peak due to the achromatic nature of the X-ray source used. Along with the primary characteristic emission line,  $K\alpha_{1,2}$ , there are satellite lines that arise when a photon is emitted from a multiply ionised state within the anode material. This leads to  $K\alpha_{3,4}$  transitions that are displaced in energy from the primary photon energy. For Mg  $K\alpha$  excitation this displacement is +8.4 eV for the  $K\alpha_3$  transition, meaning that some electrons (around 8 %) will gain more kinetic energy upon ionisation and when detected will thus appear to have originated from an orbital with lesser binding energy than the main photo peak, ultimately resulting in the satellite peak.<sup>115</sup> This feature can be observed for any particularly intense peak in a spectrum, such as the O1s peaks. The nature of characteristic X-ray radiation and its effect on peaks in XPS spectra is discussed further in Appendix B.

Detailed chemical information is obtained from high resolution scans with a narrow width across a peak of interest. Presented in figure 5.2 are O1s and C1s spectra obtained from Raw HiPCO and AP samples. Spectra were recorded with a step size of 0.1 eV, a scan width of 20 eV and pass energy of 20 eV. The difference in oxygen content between the two samples is again made clear in this figure when all spectra are presented on the same scale. With the higher level of resolution the O1s peak positions, shown in (a) and (c), were found to be 531.6 eV and 532.3 eV for HiPCO and AP tubes respectively. At face value these peaks could be simply attributed to oxides of iron for the peak at 531.6 eV, and oxides of carbon for the peak at 532.3 eV.<sup>146</sup> However the O1s peaks were particularly broad suggesting that there were in fact multiple chemical states of oxygen present and contributing to the overall peak position. For example it would not be wise to assume that all of the oxygen content in the HiPCO sample came from oxidised iron; it is expected that there would also be some amount of oxidised carbon in the nanotube sample. This is evidenced by the C1s spectra shown in (b) and (d). The main carbon peak was positioned at 284.6 eV for both samples, in good agreement with what has been shown before for

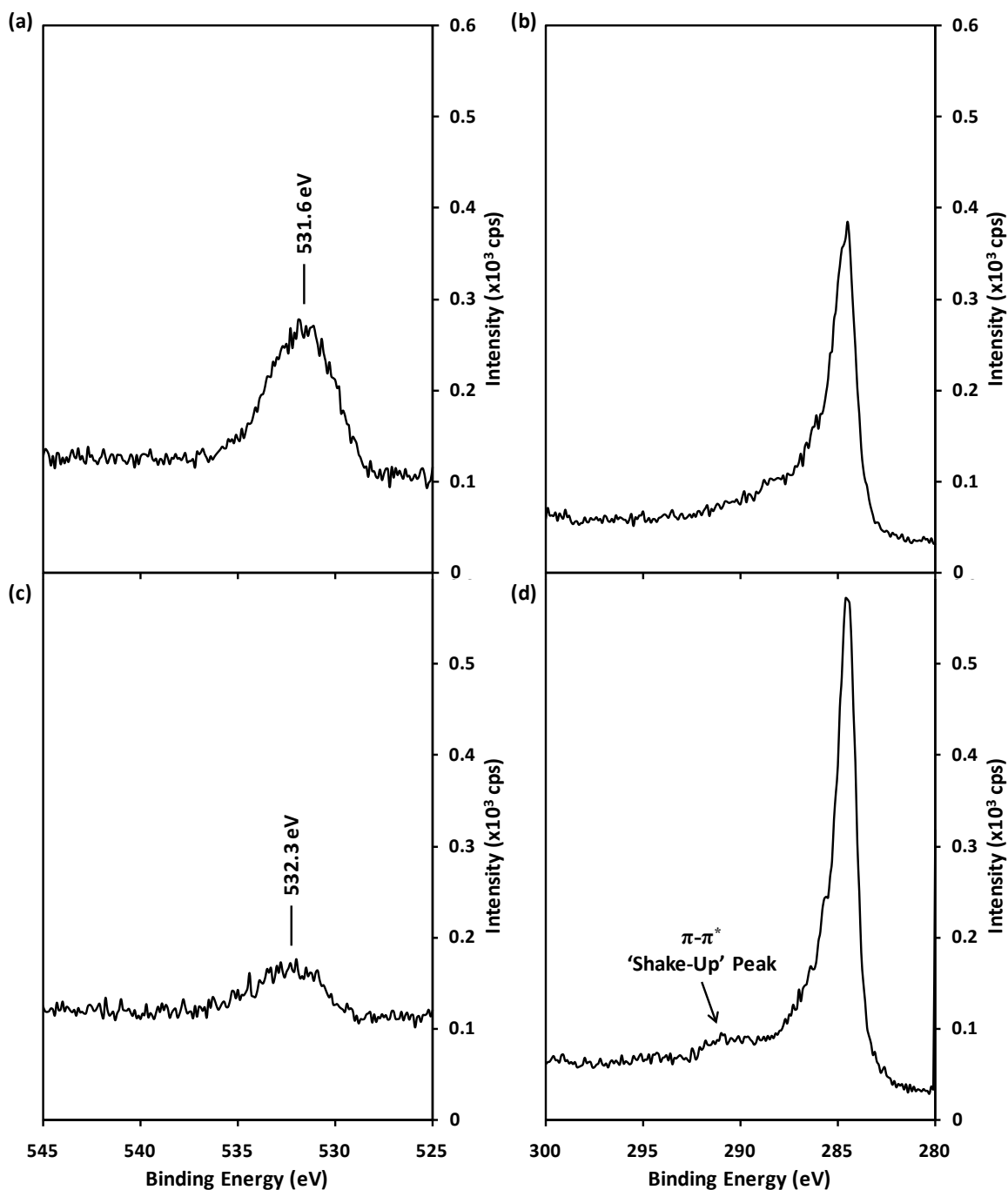


**Figure 5.2.** High resolution O1s and C1s spectra for (a) and (b) HiPCO nanotubes and (c) and (d) AP nanotubes. All spectra obtained in FAT mode with pass energy of 20 eV.

carbon nanotubes and graphitic ( $sp^2$ ) forms of carbon.<sup>58,88,147-154</sup> Both spectra however showed some asymmetry on the high binding energy side of the peaks, which could be attributed to amorphous ( $sp^3$ ) carbon content, as well as the presence carbon oxides.<sup>145</sup> Also highlighted in (d) is another feature of graphitic carbon C1s spectra with the presence of a satellite known as a 'shake-up' peak. This satellite results from the finite possibility that upon photoionisation the atom may simultaneously be promoted into an excited state

that is a few electron volts above the ground state. As a consequence, an amount of photon energy corresponding to the difference between the ground and excited states is lost. This energy is then not available to the liberation of the photoelectron and it will leave the atom with a small deficit in kinetic energy. The result is a satellite peak that is slightly higher in binding energy than the main photopeak.<sup>146,155</sup> For graphitic carbon this peak is generally found at around 291 eV, the difference in energy resulting from the  $\pi$ - $\pi^*$  transition. Thus this satellite is known as the  $\pi$ - $\pi^*$  shake-up peak.

#### *Spectral Dependence on Excitation Energy*

The data presented in figure 5.1 was obtained using Mg K $\alpha$  excitation with photon energy of 1253.6 eV. This would commonly be the source of choice when studying carbon surfaces for two main reasons; of the common characteristic X-ray lines it has the narrowest line width and so can achieve the best resolution (when achromatic), and it has the lowest photon energy and will therefore give the greatest sensitivity to the light elements with low binding energies. Mg K $\alpha$  excitation presents a problem however. In this work the aim is to introduce fluorine functional sites to carbon nanotubes. Thus an XPS spectrum of a treated sample should have, along with the peaks from the untreated samples, a fluorine peak at ~690 eV from the 1s shell.<sup>146</sup> When using a photon energy of 1253.6 eV there were already features in this region due to Auger processes from carbon and oxygen in both samples, and also from iron in the HiPCO sample. Consequently there would be an undesirable convolution of peaks around the fluorine region that would make analysis difficult. It has already been mentioned that when presented on a binding energy scale, the positions of Auger peaks are dependent on the photon energy (with detailed discussion presented in Appendix B.2). Therefore by choosing another excitation source the Auger peaks can be shifted away from the region of interest.

Presented in figure 5.3 are survey spectra of the raw HiPCO and AP samples obtained using the Al K $\alpha$  source with photon energy of 1486.6 eV. The difference in energy between the two X-ray lines is 233 eV and accordingly the Auger peaks shift to higher binding energies by this amount. In both samples the region of interest (650 – 700 eV) under Al K $\alpha$  excitation became clear of features that would interfere with analysis of the F1s photopeak. Noting the intensity scale, the higher photon energy had a detrimental effect on the amount of detected signal, a dual result of the decreased photon flux and the sensitivity of carbon and oxygen to Al K $\alpha$  radiation compared to Mg K $\alpha$  radiation.

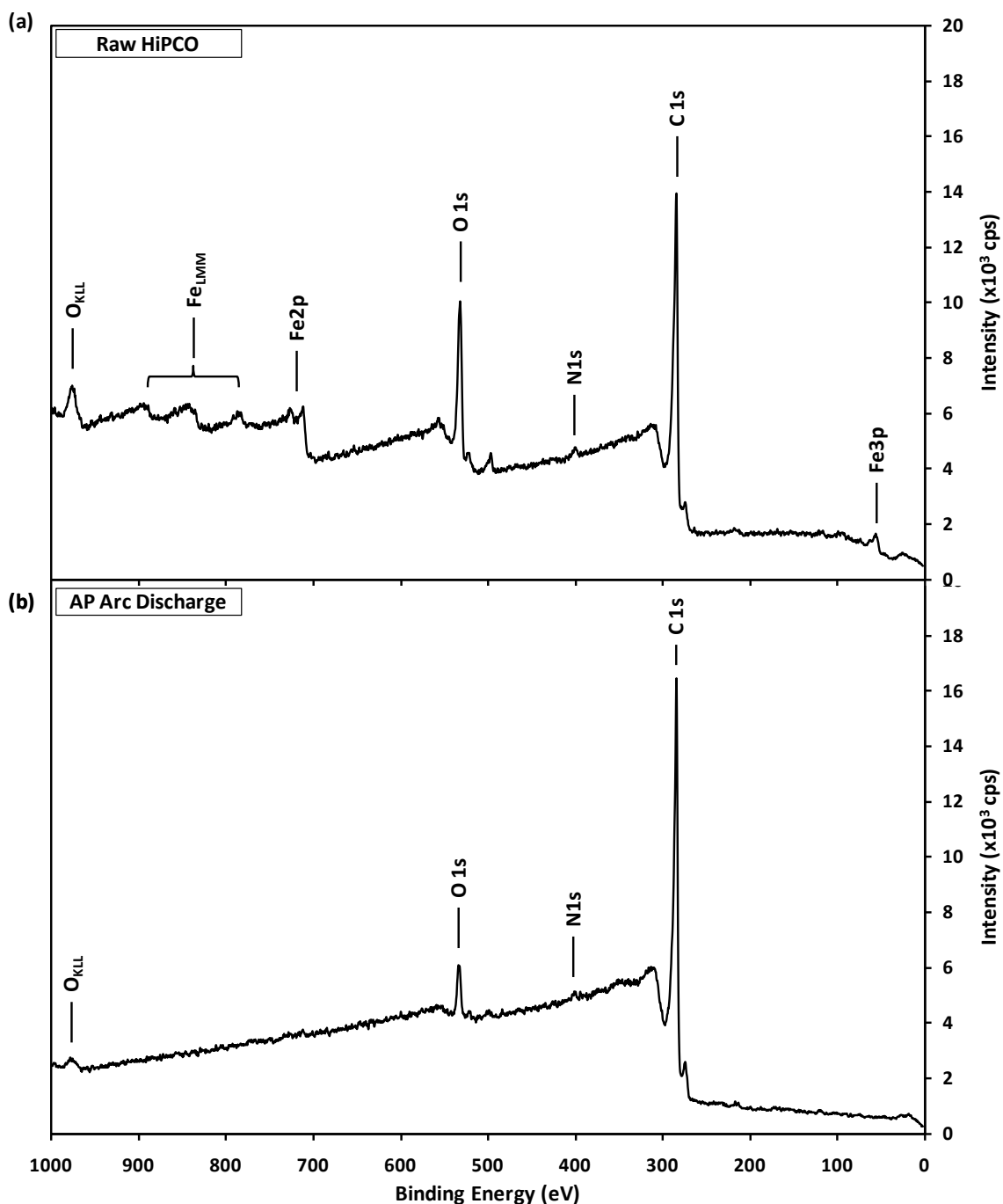


**Figure 5.3.** XPS survey spectra of the same samples as in figure 5.1 however in this case obtained using Al K $\alpha$  excitation.

The change in photon energy also elucidates another potentially common contaminant among these samples. In figure 5.3 there is a feature at 497 eV in both spectra (although it was most prominent in the HiPCO sample). When the Mg K $\alpha$  source was used, as in figure 5.1, the feature was observable at 264 eV, just below the X-ray K $\alpha_{3,4}$  satellite peak from C<sub>1s</sub>. This is a difference of 233 eV and indicated that the feature was an Auger peak. The only element that would suitably explain this feature is sodium (Na). This contaminant was

likely to have come from the oven used to bake the nanotube films onto the metallic substrates, which was often used to also bake samples deposited from surfactant solutions, some of which were in the form of sodium salts. While every effort was taken to minimise this contamination, it remained a potential issue throughout this research.

### 5.1.2. Quantification of XPS Spectra

There are generally two methods of quantification in XPS. The first is to use the survey spectrum to determine total atomic percentages detected on the surface under study. This requires the analyst to apply backgrounds to peaks in a survey spectrum and determine the area underneath that peak. This would then be either compared to the area of another peak to determine a ratio of the two elements, or compared to the total peak area from the entire sample to determine an overall percentage contribution from that element. This method however requires that the survey spectrum be taken in FAT mode, to ensure that the resolution remains constant across the entire spectrum. For modern instruments this is a reasonable constraint since very high signal to noise can be routinely achieved through detector arrays. On the LHS-10 however, survey spectra were obtained in CRR mode and thus this method was not suitable.

The second quantification method would be to take high resolution FAT mode scans of all peaks of interest in a sample. The area underneath each peak could then be determined accurately and the contribution from each element compared. This method was found most suitable for data obtained on the LHS-10.

#### *Total Peak Area*

Figure 5.4(a) presents the C1s region of an XPS spectrum obtained from an AP surface. A Shirley background was fitted to the data from 280 – 295 eV. Details regarding this choice of background are discussed in Appendix B. From within the curve fitting software CasaXPS, the area underneath the data could be calculated. For this data the area was found to be  $1054.3 \pm 48.7$ . Details regarding the error analysis are also given in Appendix B, but briefly it is taken to be

$$\Delta Area \cong 1.5\sqrt{Area} .$$

When the same method was applied to the O1s peak an area of  $246.4 \pm 23.6$  was found. At this stage one could simply take these two areas and determine relative atomic percentages for C and O on the surface, which would result in values of 81.1% and 18.9% respectively.

Taking this approach however ignores the fact that the X-ray photoionisation cross-section is different for each element. Much work has been performed on attempting to accurately determine elemental sensitivities and there are consequently multiple databases of atomic sensitivity factors produced from a range of theories, and determined experimentally on a range of instruments. Ideally the experimentalist would determine a set of sensitivity factors unique to a particular instrument to include its analyser transmission function, however the process is usually too time consuming to be practical (and requires a broad suite of standard materials) and thus one often turns to common databases. In this work the sensitivity factors used were those published in Moulder from the work of Wagner, for X-ray sources at  $54.7^\circ$  to the analyser.<sup>146,156</sup> Corrected peak areas  $n_1$  are then given by

$$n_1 = \frac{I_1}{S_1}$$

and the atomic fraction  $C_x$  is given by

$$C_x = \frac{n_1}{\sum_i n_i} = \frac{I_1/S_1}{\sum_i I_i/S_i}$$

where  $I_i$  is the peak area for element  $i$  and  $S_i$  is its corresponding sensitivity factor.<sup>146</sup> Applying this principle to the measured peak areas resulted in atomic percentages of 91.1% for carbon and 8.9% for oxygen, which are significantly different to that determined without correction for atomic sensitivity.

#### *Component Analysis*

The shape of a peak in XPS can be influenced by a myriad of physical processes at the electronic level. One influence is the chemical state of the atom from which an electron is emitted, which makes XPS a very powerful analytical tool. The C1s region of AP tubes in figure 5.4(a) displays a broad shoulder on the high binding energy side of the peak that extends 7 eV past the main photopeak. This shoulder is in part the result of varying chemical states of carbon. Through careful fitting of synthetic curves the analyst can resolve each of these components and potentially assign chemical functionalities, ultimately elucidating the chemical nature of the surface under study.

Figure 5.4(b) gives the result of this analysis. The raw data is presented as black dots with the fitted Shirley background in green. Each of the synthetic curves is presented as red traces with the sum of these curves given as a blue trace overlaying the raw data. The shape of the synthetic curves comes from a theoretical understanding of the nature of peak shapes in XPS, and is discussed in detail in Appendix B. A mixed Gaussian-Lorentzian

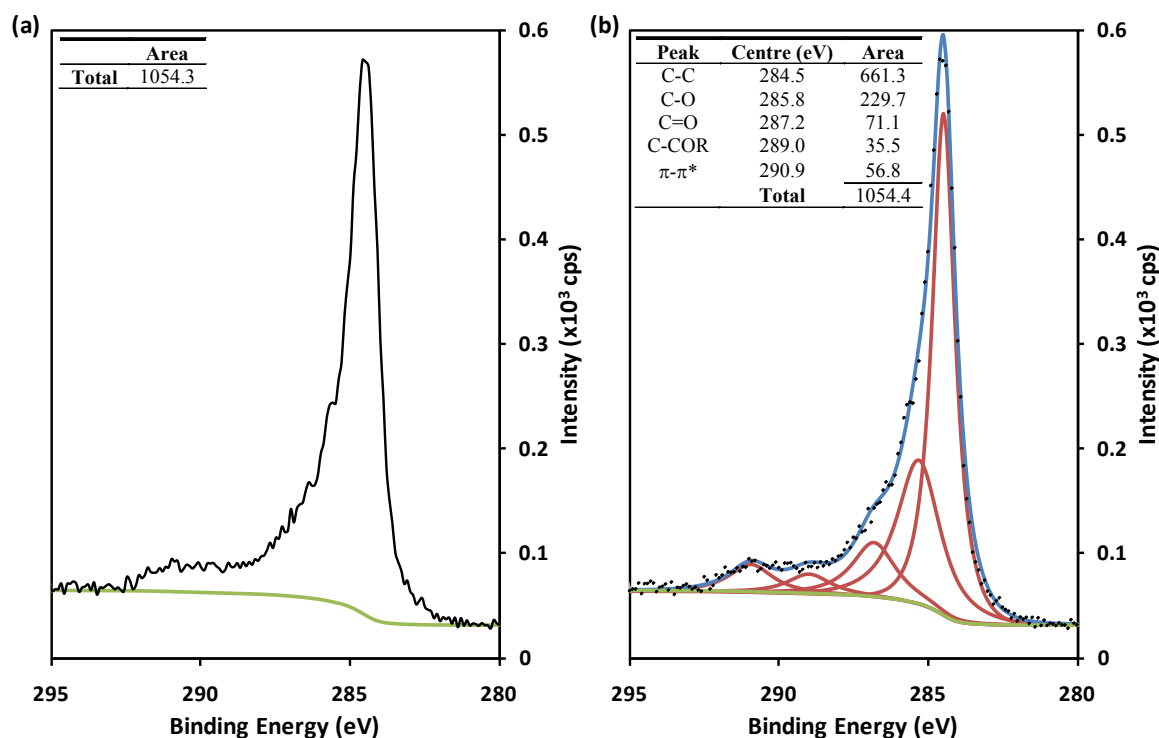


**Figure 5.4. C1s spectrum from AP nanotubes showing (a) the peak with fitted background and calculated area and (b) the same peak fitted and deconvoluted with multiple components for different functionalities. Peak positions and areas are given in the inset table.**

function was applied for each peak, with a mixing ratio of 1:9. That is, the peaks were 90% Lorentzian and 10% Gaussian. CasaXPS utilised a least-squares fitting procedure to optimise peak parameters to most closely match the raw data. The positions of each of the peaks were constrained to lie within a region of the C1s spectrum that was closely associated with the known binding energies of each likely functional group in the system. These assignments, their positions and area are given in the table inset within the figure. From the survey spectrum it was known that only carbon and oxygen was present on the surface in detectable quantities and thus any variation in chemical states was likely to be due to oxides of carbon, or adsorbed gaseous moieties such as O<sub>2</sub> and CO<sub>2</sub>. Thus the fitted functional groups were assigned accordingly, with peaks for carbon singly bound to oxygen, C-O, doubly bound, C=O, and carbon bound to functionalised carbon, C-COR, which encompasses carbonates, carboxyls and carbonyls. It should be noted that the only C-C peak fitted was assigned as sp<sup>2</sup> hybridised (i.e. graphitic) carbon. While it was expected that a majority of the sample material should be SWCNTs and thus graphitic in nature, since they are not purified in any way the presence of sp<sup>3</sup> carbons (i.e. amorphous and adventitious) should not be discounted. In this case there would be a feature at ~285 eV for amorphous carbon that would be convoluted with the sp<sup>2</sup> and C-O peaks.

## 5.2. Transmission Electron Microscopy

TEM was initially used as a method for the confirmation of the presence of CNTs in a given sample, which was of particular concern after a fluorination treatment to ensure that excessive sputtering effects did not destroy the CNT structures completely. This task was later performed by the Raman microscope which was found to be a far more suitable method. Nevertheless, TEM enabled the direct imaging of the CNTs before and after a treatment and was performed early on in the research.

Presented in figure 5.5 are TEM images from CNT samples deposited onto lacey carbon coated copper grids. The TEM grid consisted of  $50 \times 50 \mu\text{m}$  square holes which were far too large to reliably support CNTs for TEM analysis. The grids were therefore purchased with the lacey carbon coating, pictured in (a), which provided a support with voids that were less than  $5 \mu\text{m}$  across (on average).

The CNTs were deposited directly onto the grids via application by a pipette, which resulted in areas of varying material thickness. Around the edges of a deposited area the CNTs were observable as a thin mat covering the support, as seen in (b). The sample pictured here consisted of Raw HiPCO CNTs. Since the material was simply dispersed into a solution of DMF and then deposited onto the grid with no extra purification or separation measures, the sample appeared as a dense web of bundled nanotubes. This was deemed to be suitably representative of the bucky paper surfaces used for fluorination studies, although it should be noted that for plasma exposure the surfaces were much greater in thickness. This CNT mat is further magnified in (c), (d) and (e) where finer details become apparent. Specifically it could be seen that residual metallic catalyst particles were inter-dispersed within the CNT material. This is particularly evident in (e) where the nanoparticles strongly attenuated the electron beam and thus appeared as dark spots throughout the sample. The existence of residual catalyst nanoparticles was of course suggested by the iron signal in XPS spectra and the TEM images provided a direct confirmation of their presence. While a majority of the sample was found to consist of large bundled networks of CNTs, there were some instances where isolated small bundles of nanotubes were found. One such isolated structure is pictured in (f) across a section of the lacey carbon support. From (g) the diameter was estimated to be  $<3 \text{ nm}$ , suggesting either a very small bundle of nanotubes or, since this image was at the limit of the instruments resolution, potentially a single CNT that was not well resolved.

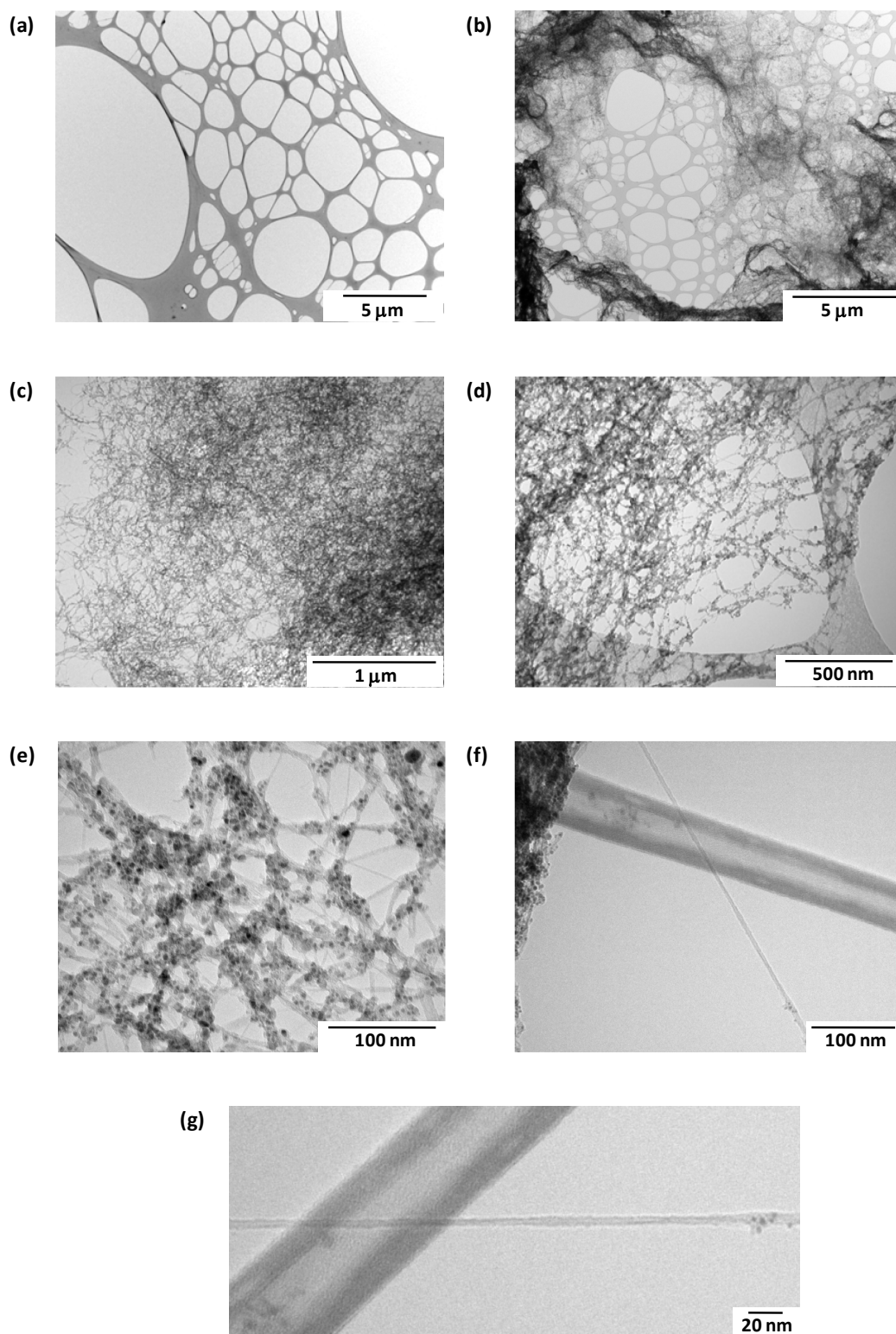


**Figure 5.5.** TEM images of (a) the lacy carbon support film, (b) HiPCO CNTs deposited on the film, (c) magnified view of the CNT ‘spaghetti’, (d) and (e) further magnification of the CNTs showing the dispersion of catalyst particles throughout the material, (f) a single CNT laying across the support and (g) a larger view of this CNT.

### 5.3. Raman Spectroscopy

Raman spectroscopy is an exceptionally powerful tool for the analysis of carbon nanotubes. It is capable of probing the physical, electronic and by extension the chemical nature of a sample through the inelastic scattering of light. There is also a dependence on the energy of the incident photons, with nanotubes of specific electronic structure (for example metallic or semiconducting) displaying resonance with certain photon energies. This can be extended further to show energy dependence with nanotubes of certain chirality. Together these properties enable Raman spectroscopy to characterise a nanotube sample by dimensions, electronic structure and also the level of defects in the nanotube sidewalls.<sup>123</sup>

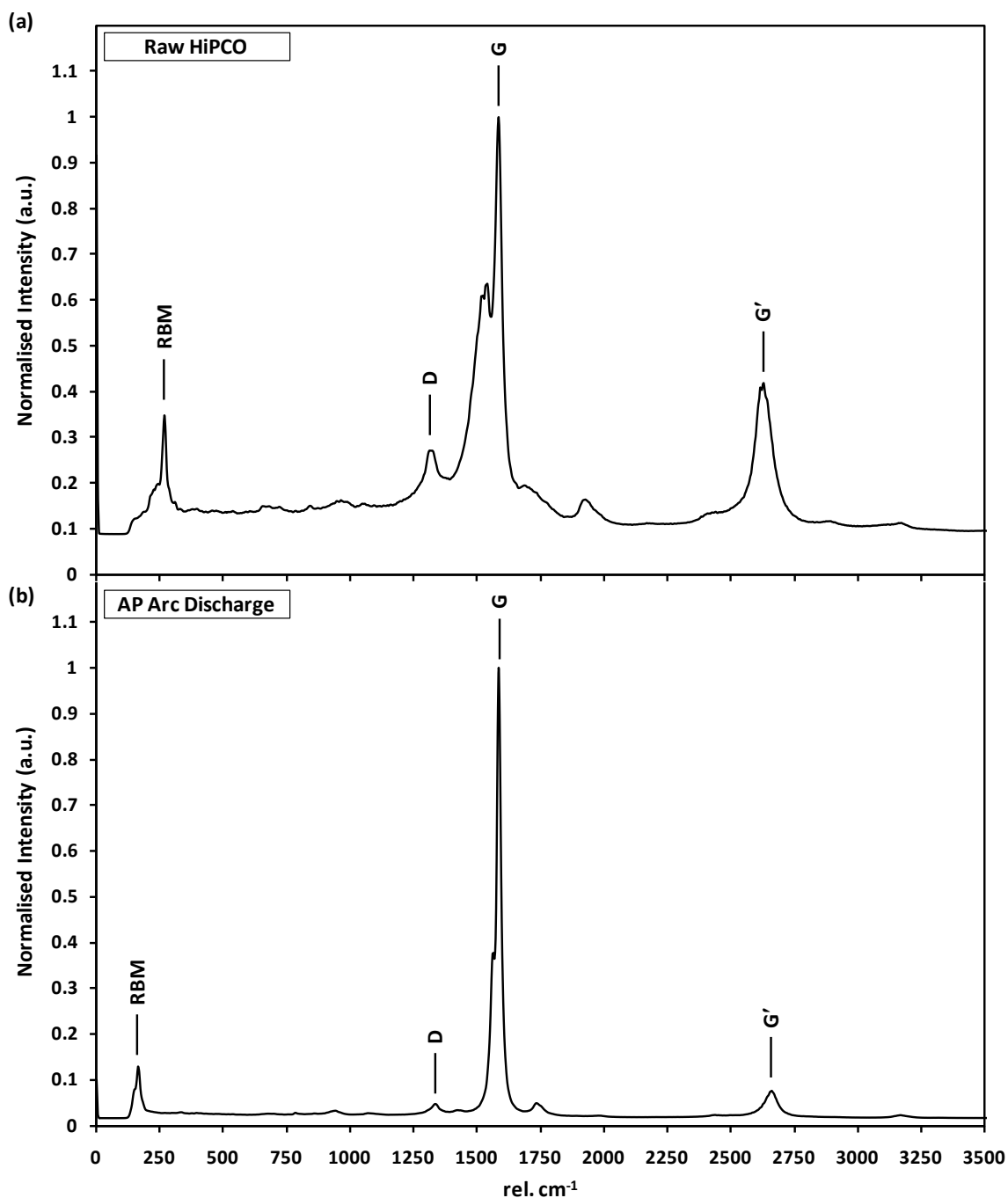
#### 5.3.1. Raman Analysis of CNTs

Figure 5.6 gives the Raman spectra of (a) Raw HiPCO and (b) AP nanotube surfaces across a range of 0 – 3500  $\text{cm}^{-1}$ . The spectra were collected using a frequency doubled Nd:YAG laser at 1064 nm, resulting in a 532 nm excitation wavelength (2.33 eV). Each spectrum has been normalised such that the peak of greatest intensity was set to unity.

There are multiple features that typically appear in the Raman spectrum of carbon nanotubes, each coming from the excitation of a specific vibrational (phonon) mode or scattering process. These features can be broadly separated into two groups; namely first and second order processes, meaning simply that the first order processes result from the foremost event in a set of scattering events induced by photon interaction and second order processes resulting from events that occur after the initial scattering mechanism. In the Raman spectrum of nanotubes the features that generally come under the most scrutiny are the radial breathing mode (RBM), the ‘graphitic’ band (G band), the ‘disorder’ band (D band) and the overtone of the D band (G’ band). The former two features arise from first order processes while the latter two are of second order. In this work the RBM, G and D bands were of the most significance.

#### *RBM*

The RBM is a coherent out-of-plane stretching of carbon atoms radially from the nanotube lattice, giving the appearance of a ‘breathing’ motion as depicted in figure 5.7(a).<sup>157</sup> This phonon mode is specific to carbon nanotubes, and the presence of an RBM in Raman spectra provides direct evidence of a sample containing single-walled nanotubes.<sup>123</sup> The



**Figure 5.6. Raman spectra of (a) a raw HiPCO nanotube surface and (b) an AP nanotube surface. Both surfaces were deposited onto a silicon substrate.**

frequency at which the carbon atoms around the circumference of the tube oscillate depends on the total mass of all the atoms present, which in turn depends on the diameter. Thus the position of the RBM is a direct measure of the size of the nanotubes in a given sample. The dependence of the RBM frequency,  $\omega_{RBM}$ , on the nanotube diameter,  $d_t$ , is an inverse relationship such that

$$\omega_{RBM} \propto \frac{1}{d_t}.$$

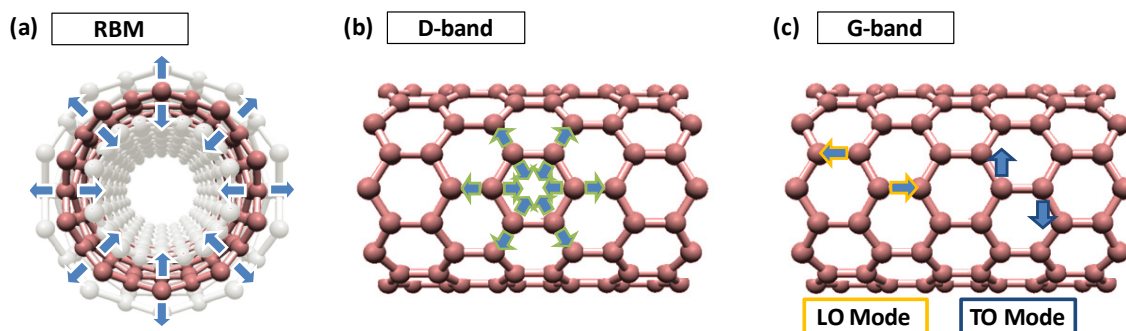


**Figure 5.7.** Atomic displacements within a nanotube due to (a) the radial breathing mode, (b) the disorder (D) band and (c) the graphitic (G) band. For single-walled carbon nanotubes the G band consists of two distinct modes; the longitudinal optical and transverse optical modes (LO and TO modes respectively). Modified from Filho<sup>157</sup> and Dartois.<sup>158</sup>

Therefore as the tube diameter is increased, the position of the RBM decreases. For isolated nanotubes on a silicon substrate it was found that multiplication of the right hand side of the formula by a coefficient  $A$  chosen to be  $248 \text{ nm.cm}^{-1}$  resulted in good agreement between theoretical and experimental values of nanotube diameter.<sup>123</sup> Often however, nanotubes are found to bundle together, with the tube-tube interactions resulting in a change in the RBM frequency. Consequently a modification to the formula was made to account for this effect so that

$$\omega_{RBM} = \frac{A}{d_t} + B$$

where  $A$  and  $B$  have been found to be  $234 \text{ nm.cm}^{-1}$  and  $10 \text{ cm}^{-1}$  respectively.<sup>123</sup>

Typical high resolution spectra of the RBM from both the HiPCO and the AP samples are given in figure 5.8(a) and (c) respectively. The maxima were found to be at  $\sim 270 \text{ cm}^{-1}$  for the HiPCO samples and  $\sim 167 \text{ cm}^{-1}$  for the AP samples. Thus the HiPCO nanotubes were significantly smaller in diameter than the AP nanotubes and when the above formula was applied to the peak values the diameters were found to be  $0.90 \pm 0.10 \text{ nm}$  for HiPCO nanotubes and  $1.48 \pm 0.09 \text{ nm}$  for AP nanotubes. Although these figures came from the maxima within the RBM region it should be noted that both peaks were particularly broad, suggesting a distribution of diameters centred on the values given. Furthermore, for the HiPCO sample there were several smaller peaks on either side of the main RBM peak, providing further evidence indicating the presence of nanotubes of multiple diameters.

#### *D and G bands*

In aromatic systems there is a phonon related to the ‘breathing’ of carbon rings. Ideally this breathing would be symmetric throughout a system giving no net result as depicted in

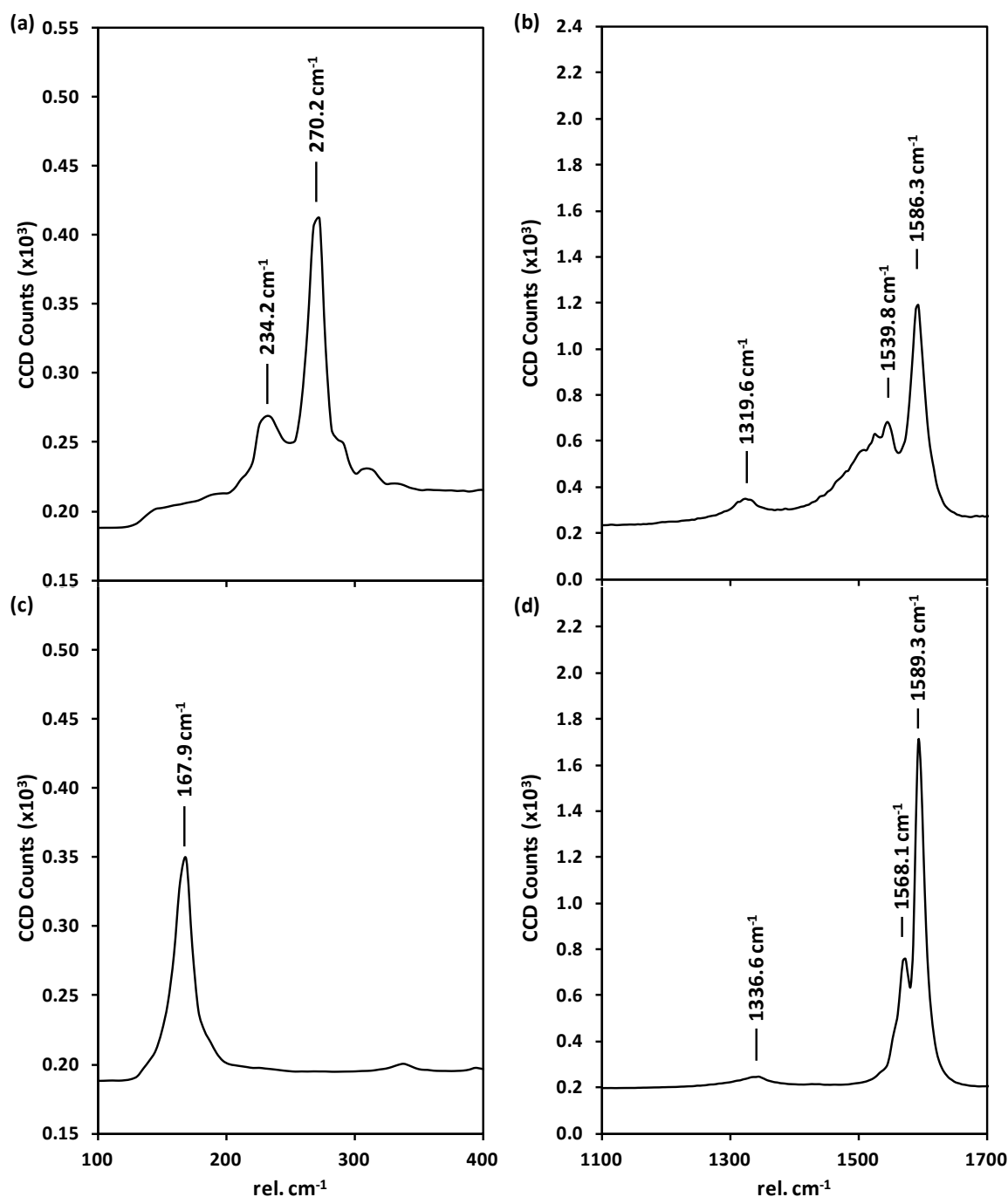


**Figure 5.8. High resolution RBM and D+G spectra for (a) and (b) HiPCO nanotubes and (c) and (d) AP nanotubes.**

figure 5.7(b).<sup>158</sup> However more often than not in large systems, such as the hexagonal carbon lattice of both nanotubes and graphite, there are small defects which create local asymmetry in the breathing of the carbon rings. The result is a Raman active phonon that gives rise to a peak around 1300 cm<sup>-1</sup> known as the ‘disorder’ or D band. This is a second order process and as such the representation given here is a gross over-simplification, although it aids in the visualisation of the process. Since this peak is directly related to

defects within a system it can be used as a measure of the purity or homogeneity of a nanotube sample. Going by peak intensity alone this would suggest that the AP nanotubes had less defects than the HiPCO nanotubes. The D band alone is not enough however to make an accurate determination of how defect free a sample may be, and as such it is often compared in intensity to the ‘graphitic’ or G band. The G band results from a phonon that travels throughout the carbon lattice tangential to the plane normal and is often found around  $1600\text{ cm}^{-1}$ . Only one peak is present in the G band of graphite since the lattice is isotropic (see figure 5.9(c)). In nanotubes however the G band is seen to split into multiple features, the strongest of which arise from two distinct phonon modes that travel either along the nanotube axis or around its circumference. The curvature of the nanotube breaks symmetry resulting in the longitudinal optical (LO) and transverse optical (TO) phonon modes as shown in figure 5.7(c).<sup>157</sup> When assigning peaks in Raman spectra the split G band is labelled as  $G^-$  and  $G^+$  for the lower and higher wavenumber peaks respectively.

The shape and position of the  $G^-$  and  $G^+$  components provides insight into the electronic structure of nanotubes within a sample. Relative shifts in the  $G^+$  position occur for dopant additions that lead to charge transfer within the nanotube structure. Charge acceptors act to increase the  $G^+$  position, while donors decrease this position. The shape of the  $G^-$  peak is sensitive to the electronic structure of the nanotube. It appears as a Lorentzian line shape for semiconducting nanotubes and for metallic nanotubes it presents as the broader Breit-Wigner-Fano (BWF) line shape.<sup>123</sup> These contrasting shapes are evident in figure 5.8(b) and (d) with the HiPCO nanotubes displaying the BWF shape and the AP nanotubes displaying the Lorentzian shape. The spectra therefore suggested that the nanotubes in the HiPCO sample were metallic while the nanotubes in the AP sample were semiconducting. It is unreasonable however to suggest that a sample that has received no purification treatment would contain only one type of nanotube since even with extensive measures it is very difficult to separate nanotubes by electronic type.<sup>24,159,160</sup> To be more accurate, for *this particular excitation energy* the nanotubes that were most resonant in the HiPCO sample were metallic while the most resonant nanotubes in the AP sample were semiconducting. For a different laser wavelength the result may well suggest the opposite.

The relative intensities of the D and G bands can be used as a measure of the homogeneity of a sample; both in terms of purity, i.e. levels of amorphous carbon present in the sample, and also how defective a given nanotube sample may be in terms of the nanotube

structures themselves. The analysis is performed by taking the ratio of the intensity of the D and G bands after some background subtraction. In the literature this ratio is commonly labelled  $I_D/I_G$ , although other forms of nomenclature have been noted (such as D:G, D/G, D-G ratio). This analysis stems from the early application of Raman spectroscopy to the other forms of carbon; diamond, glassy carbon, crystalline graphite and amorphous carbon.<sup>123,161,162</sup>

### 5.3.2. The Influence of Laser Power on Raman Spectra

The Raman instrument used in this work possessed no internal method for the measurement of laser power delivered to the sample. Consequently, between experiments there was no way to ensure the energy density was the same at the laser spot. Aside from the expected variation in the total number of counts that this would cause between experiments, it was also found that this variation caused changes in the spectral features.

Presented in figures 5.9(a) and (b) are Raman spectra of the RBM and G band with increasing laser power taken from AP nanotubes. The laser power was steadily increased with Raman spectra obtained at regular intervals until the maximum laser power was reached (~60 mW). The dotted lines in the figures indicate peak positions of the first (blue) and last (red) spectra taken, corresponding to the lowest and highest laser powers respectively. It was apparent from these spectra that as the laser power was increased the peaks shifted to lower energies (i.e. wavenumber values), a change of as much as 5% in the case of the RBM. The G band was not only seen to shift in position but also to lose definition, with the  $G^+/G^-$  splitting becoming less pronounced at high laser powers.

These peak shifts in the Raman spectra of carbon nanotubes have been reported in the literature. Huong *et al.* in 1995 first observed shifts in the RBM, G and G' bands of nanotubes embedded within resin as the laser power was increased.<sup>163</sup> The temperature was determined to vary from around room temperature at low power to ~370 K at high power, resulting in a shift of the G band by as much as  $22\text{ cm}^{-1}$ . Huang *et al.* performed a more systematic study of the variation in peak position in 1998, determining the sample temperature by comparing the intensities of the Stokes and corresponding anti-Stokes lines.<sup>164</sup> This was possible since the anti-Stokes process becomes more efficient at higher temperatures due to the greater possibility of a molecule being in an excited state. In both pieces of work the cause of the peak shifts was concluded to be a lengthening of the C-C

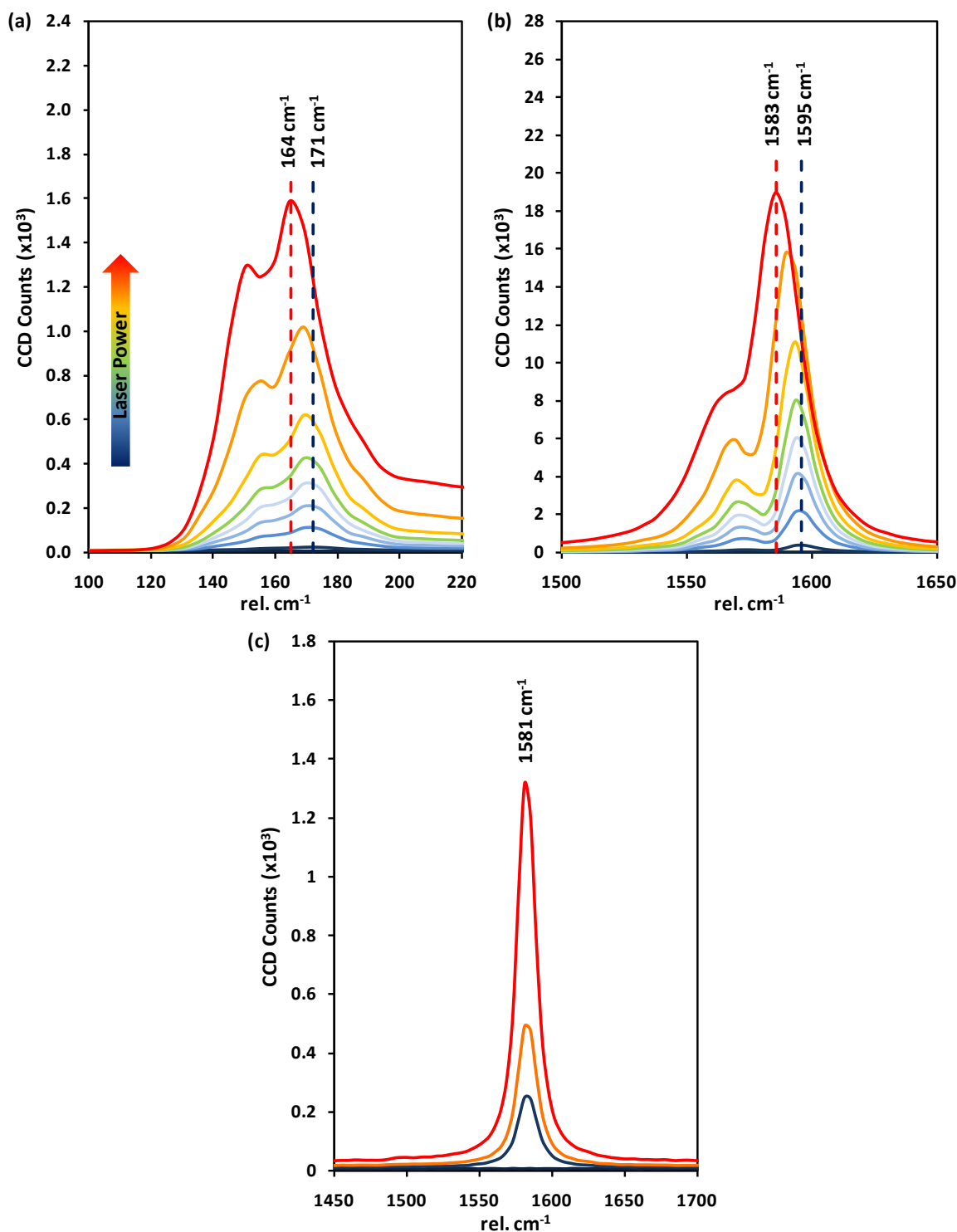


**Figure 5.9.** The effect of laser power on the Raman spectra of graphitic carbon showing the shift in (a) the RBM, (b) the G band from nanotubes and (c) the G band from graphite.

bond distance and thus a downshift in the vibrational frequency. Both authors noted however that HOPG did not display this shift in G band peak position. This is presented in figure 5.9(c) from data obtained within this work. If the cause were as simple as C-C bond lengthening then it could be expected that graphite also presents the same dependence.

Huang postulated that defects within the nanotube structure afford some level of flexibility and thus bond lengthening is allowed to occur, whereas in the graphite system such flexibility does not exist and the change in vibrational frequency is prevented.

Instrumental variations such as these could quite easily be misinterpreted as changes in the structure of the nanotubes, especially between samples that may have had some modification performed that is expected to change the nanotube structure. For example, if the energy density was not constant between two samples, then a small shift in the  $G^+$  position due to laser power could be misinterpreted as a charge transfer effect. This could lead to the false conclusion that a given treatment resulted in the doping of the nanotubes within a sample. Similarly, variation in the ratio of the  $G^-$  and  $G^+$  peaks could be misinterpreted as a change in the electronic structure, such as a reduction of the semiconducting nature of the nanotube, or the destruction of the nanotube itself. Irrespective of this, procedures to ensure the reliable comparison between samples under analysis using Raman spectroscopy were necessary.

To achieve consistency in Raman experiments in this work the entire procedure was undertaken with the laser set once at the start of the experiment and only after sufficient time for the laser to reach a stable operating temperature (around 10 minutes). During the experiment the laser would not be powered down, but rather a shutter closed for sample changeover. This ensured that any heating of the sample due to illumination by the laser would be as constant as possible for each successive sample analysis, enabling reliable comparisons to be made within an experiment. Furthermore, to attempt to maintain some level of comparison between experiments, and in the absence of a reliable power meter, the laser power level was set to give a certain count rate at the start of each session. This was achieved by using a feature of the spectrometer that allowed the real-time collection of spectra, with short integration times. An integration time of 0.05 seconds was selected and the laser power increased until the G band reached a peak intensity of  $\sim 350$  counts. By using this procedure at the start of each experiment it could then be presumed that the laser power was similar between each measurement. This of course assumed that each sample would respond in the same way, which was expected to be strongly dependent upon the amount of material present. However provided the sample preparation protocols set out in Section 2.4 were maintained this was deemed to be constant between samples.

## 5.4. The Plasma Fluorination of Carbon Nanotubes

To establish a proof-of-principle of the fluorination of carbon nanotubes using SF<sub>6</sub> plasma, a sample of both HiPCO and Arc Discharge CNTs were exposed to SF<sub>6</sub> plasma simultaneously. This allowed for a comparative analysis to be performed between the two surfaces both prior to and after a plasma treatment.

### 5.4.1. XPS Analysis of Fluorinated CNTs

Given in figure 5.10(a) are XPS survey spectra of HiPCO and Arc Discharge CNT surfaces that have been exposed to SF<sub>6</sub> plasma. The most noticeable change in these spectra from those of the untreated samples (figure 5.3) is the presence of new features at ~690 eV (the F1s photopeak) and ~830 eV (the F<sub>KLL</sub> Auger peak). As expected from previous discussion, a significant oxygen signal was also detected. For the HiPCO sample residual iron catalyst was again detected with the Fe2p peak visible ~710 eV.

Despite both samples being exposed to the same plasma environment, the amount of attached fluorine was found to be noticeably different between the two cases. The HiPCO CNT surface resulted in 36% fluorine functionalisation compared to 29% for the Arc Discharge CNT surface. Intuitively this result was unexpected, although upon consideration of the Raman results this effect could be explained. From the RBM spectra of these two samples the diameter of the Arc Discharge CNTs was found to be ~1.5 nm while the HiPCO CNTs were ~0.9 nm. The much smaller CNT diameter resultant from the HiPCO process would result in a greater level of strain on the structure and greater  $\pi$ -orbital misalignment. The HiPCO CNTs would therefore be more susceptible to chemical attachment. The attachment of chemical moieties at the surface would then create defects in the structure from the conversion of some carbon atoms to sp<sup>3</sup>, which would in turn alleviate some of the bond strain thus making this attachment energetically favourable. Overall, this would lead to a greater level of functionalisation for HiPCO CNTs compared to Arc Discharge CNTs as observed. It could then be hypothesised that HOPG should display a lower level of functionalisation since in its pristine state there is no strain on the carbon lattice. A survey spectrum taken from HOPG exposed to an identical treatment to that of the two CNT samples is given in figure 5.10(b) where it is seen that the level of fluorination resultant from the exposure was indeed much lower.

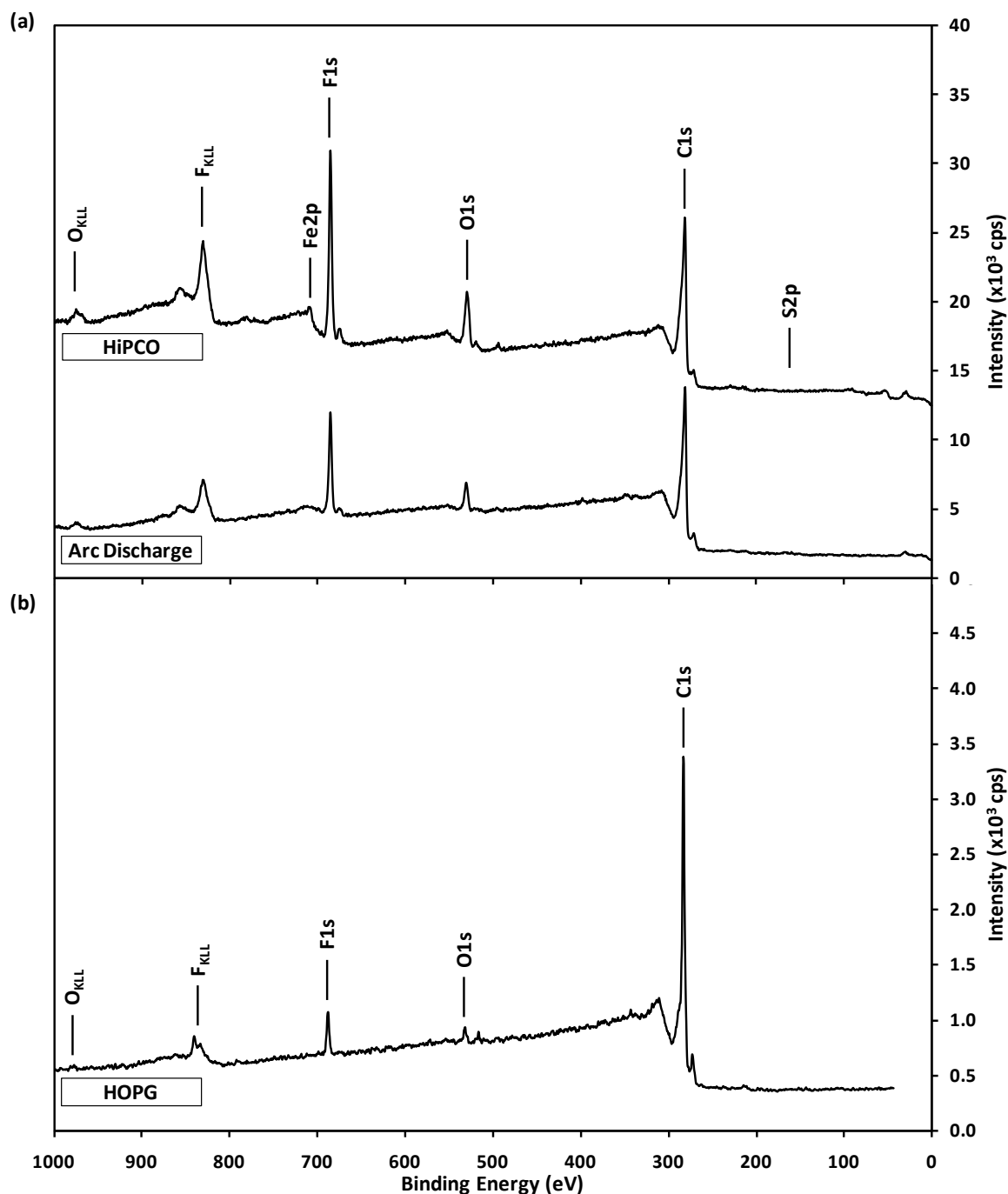


**Figure 5.10.** XPS survey spectra of (a) HiPCO and Arc Discharge CNT surfaces after exposure to SF<sub>6</sub> plasma and (b) HOPG exposed to an identical plasma environment. Spectra were recorded using Al K $\alpha$  radiation with the spectrometer in CRR mode.

The position of the most intense sulphur peak that is measurable in XPS, the S2p line at  $\sim 164$  eV, is also indicated in the spectra. In both cases, no feature was observed here despite the certainty that sulphur containing species should be present in the plasma. This absence suggested that either the fluorination process occurred without contamination by sulphur, or that it was present in such small amounts that it could not be detected.

High resolution spectra from the fluorinated HiPCO and AP samples are presented in figure 5.11. The F1s and C1s spectra from the HiPCO sample are in (a) and (b), while the same for the AP sample is given in (c) and (d).

The F1s spectra in (a) and (c) were observed to have a noticeable level of asymmetry. During peak deconvolution the best agreement between the data and synthetic peaks was achieved when two components were fitted; one at  $\sim 686.5$  eV and another at  $\sim 688$  eV. A similar fit to the F1s spectra of fluorinated nanotubes has been detailed previously where the components were attributed to the covalent C-F bond at 688 eV, and a weaker C-F bonding mode known as semi-ionic (or ionocovalent<sup>165</sup>) at 686.5 eV.<sup>83,87,89,166</sup> By peak area the F1s peak, and thus the C-F bonding in the HiPCO sample, was found to be 75% covalent. Similarly, the AP sample was found to have 78% covalency.

Analysis of the C1s region allowed the elucidation of chemical functionality directly attached to the carbonaceous nanotube structure. Presented in figure 5.11(b) and (d) are the C1s spectra from the fluorinated HiPCO and Arc Discharge CNTs respectively. Also presented for comparison in the figures (as grey data points) are the C1s spectra of the untreated samples. The spectra were fitted with the same components as in figure 5.4(b) and the percentage that each component contributed to the total peak area is given as an inset table within each figure. Originally the components at 285.8, 287.2 and 289.0 eV were all attributed to carbon-oxygen bonding. After fluorination however it should be expected that there be some level of carbon-fluorine bonding and that this would contribute to the peak structure at higher binding energies. However the positions of components related to CF, CF<sub>2</sub> and CF<sub>3</sub> are generally found to overlap significantly with those peaks already assigned, and consequently severe convolution occurs between the components arising from carbon-oxygen and carbon-fluorine functionalities. Thus the peak assignments given here are labelled as convolutions between the overlapping chemical states.

After fluorination it was seen that the high binding energy shoulder to the C1s spectra was made more prominent, a result attributed directly to an increase in the level of functionalisation of the sample surface. This is further evidenced upon quantification of the percentage of the C1s peak area related to CF<sub>x</sub> functionality, which was observed to increase after exposure. However, considering the total amount of fluorine determined to be on the surface this increase was deemed to be somewhat lacking. Quantification of the total C1s and F1s peak areas gave 36% fluorine attached to the HiPCO sample and 29% to

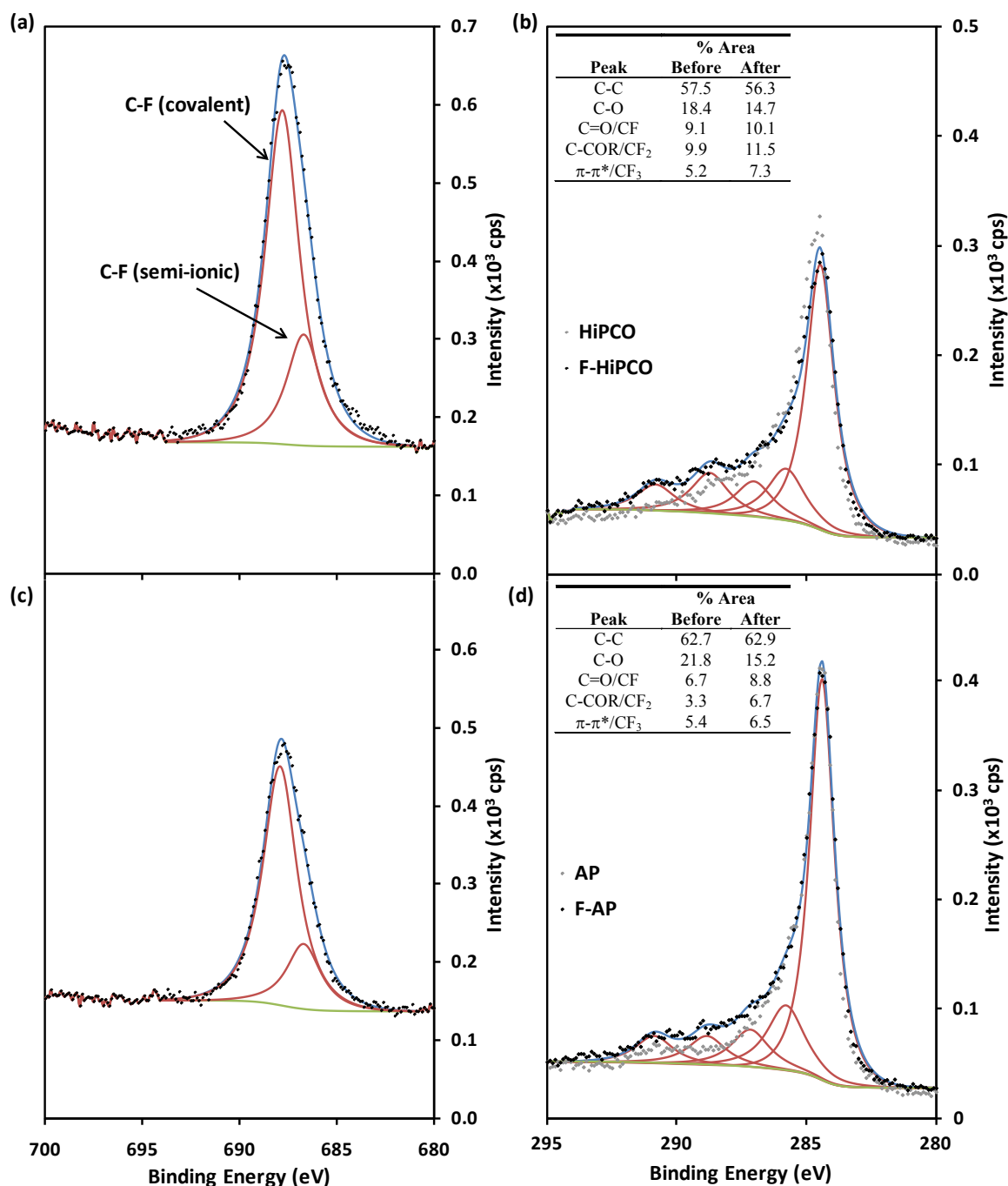


**Figure 5.11. High resolution F1s and C1s spectra for (a) and (b) fluorinated HiPCO nanotubes and (c) and (d) fluorinated AP nanotubes. All spectra were obtained in FAT mode with pass energy of 20 eV.**

the AP sample. If all of this fluorine content were attached to carbon nanotubes then it would seem reasonable to find ~30% of the C1s spectra attributable to CF<sub>x</sub> functionality. Since this was not found, some amount of the detected fluorine signal could be related to an adsorption of species to the CNTs rather than through the formation of a chemical bond. If adsorbed species were in fact present then the surfaces could be expected to show degradation over a given time frame, thereby reducing surface stability.

#### 5.4.2. TEM Analysis of Fluorinated CNTs

HiPCO CNTs mounted on TEM grids were exposed to the same SF<sub>6</sub> plasma treatment. Figure 5.12 presents the images obtained. These results show that after the fluorine treatment the CNT structures still remain, as do the catalyst nanoparticles. Even those nanotubes isolated from the main bundles remained clearly intact after exposure to the plasma environment. It was concluded then that exposure to the plasma was reactive enough to functionalise the CNTs without destroying the structure and leaving behind fluorinated amorphous and non-nanotube graphitic carbon.

#### 5.4.3. Raman Analysis of Fluorinated CNTs

Presented in figure 5.13 are Raman spectra of the untreated (black dotted) and treated (red) HiPCO and AP CNTs. For brevity only the RBM, D and G bands are presented. Due to the protocol set in place to ensure the consistency of the analysis method, the background signal remained essentially constant before and after exposure, allowing convenient comparison of the nanotube features within the spectra. After exposure to SF<sub>6</sub> plasma the peaks resulting from the graphitic carbon of the nanotubes decreased in intensity, a result attributed to a disruption of the CNT structure. Note that the G band spectra have been normalised to accentuate the increased scattering at D band energies.

Prior to fluorination the HiPCO samples showed two significant peaks in the RBM region at 234 and 272 cm<sup>-1</sup>, suggestive of two prominent nanotube diameters being in resonance with the laser wavelength used here. The measured RBM positions correspond to CNT diameters of 1.1 and 0.9 nm respectively. After the plasma treatment the intensity of the peaks in this region decreased overall, however the feature that was present at 234 cm<sup>-1</sup> diminished significantly compared to the main peak at 272 cm<sup>-1</sup>. The AP samples presented with a single large peak at 168 cm<sup>-1</sup>, indicating a single distribution of nanotube diameters around 1.5 nm. After fluorination the intensity of the RBM for this sample was found to decrease although beyond this no other discernable change was observed.

The decreased scattering ~234 cm<sup>-1</sup> in the HiPCO samples would suggest that fluorine preferentially attached to the 1.1 nm diameter CNTs, resulting in a greatly reduced intensity for this RBM feature. Although the conclusion drawn previously was that smaller diameter CNTs would be more likely to undergo significant fluorination due to the greater level of strain on the structure when compared to larger diameter CNTs, this was not

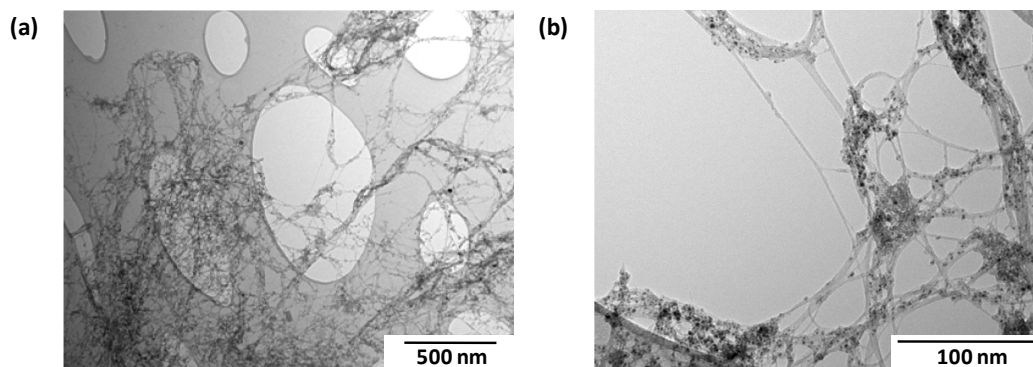


**Figure 5.12. TEM images of the HiPCO CNT sample after exposure to SF<sub>6</sub> plasma.**

expected to be the only phenomenon that could influence the functionalisation. Plasma environments have exhibited selective etching of metallic CNTs previously.<sup>167,168</sup> Furthermore, fluorine has been used by Yang to selectively etch metallic CNTs from HiPCO samples.<sup>169</sup> In that work, a set of peaks  $\sim 230\text{ cm}^{-1}$  in Raman spectra of the samples were attributed to the RBMs of metallic CNTs, as determined by the relationship between diameter, chiral assignment and thus electronic structure.<sup>169</sup> Upon fluorination these peaks were seen to all but completely disappear while the semiconducting RBM features remained with significant intensity. Thus here the peak at  $234\text{ cm}^{-1}$  is attributed to metallic CNTs, and the drastic decline in intensity after fluorination is attributed to the selective etching of these metallic CNTs over their semiconducting counterparts. Yang concluded that the observed selectivity arose from a differing level of charge transfer between fluorine species and the metallic and semiconducting CNTs, with the metallic species displaying a greater charge transfer due to more abundant electron density around the Fermi level. Metallic CNTs were preferentially functionalised because the adsorption barrier between fluorine species and the CNT structure was lowered.<sup>169</sup>

As mentioned, the intensity of the CNT-specific peaks decreased after plasma exposure, an effect attributed to the disruption of the carbon lattice by fluorine functional groups. This was further evidenced by the increase in intensity of the D band  $\sim 1330\text{ cm}^{-1}$  within the Raman spectra of both CNT samples. Quantification of  $I_D/I_G$  found an increase from 0.12 up to  $0.20 \pm 0.05$  for the HiPCO CNTs after exposure. The AP CNTs displayed a similar change in the calculated ratio, where it was found to have increased from 0.03 when untreated to  $0.08 \pm 0.03$  after exposure. Although these changes were not substantial, the absorbed rf power in the plasma used to fluorinate these samples was not particularly high (10 W) and exposure was for only 1 minute. The ratio of the  $G^-$  and  $G^+$  components within

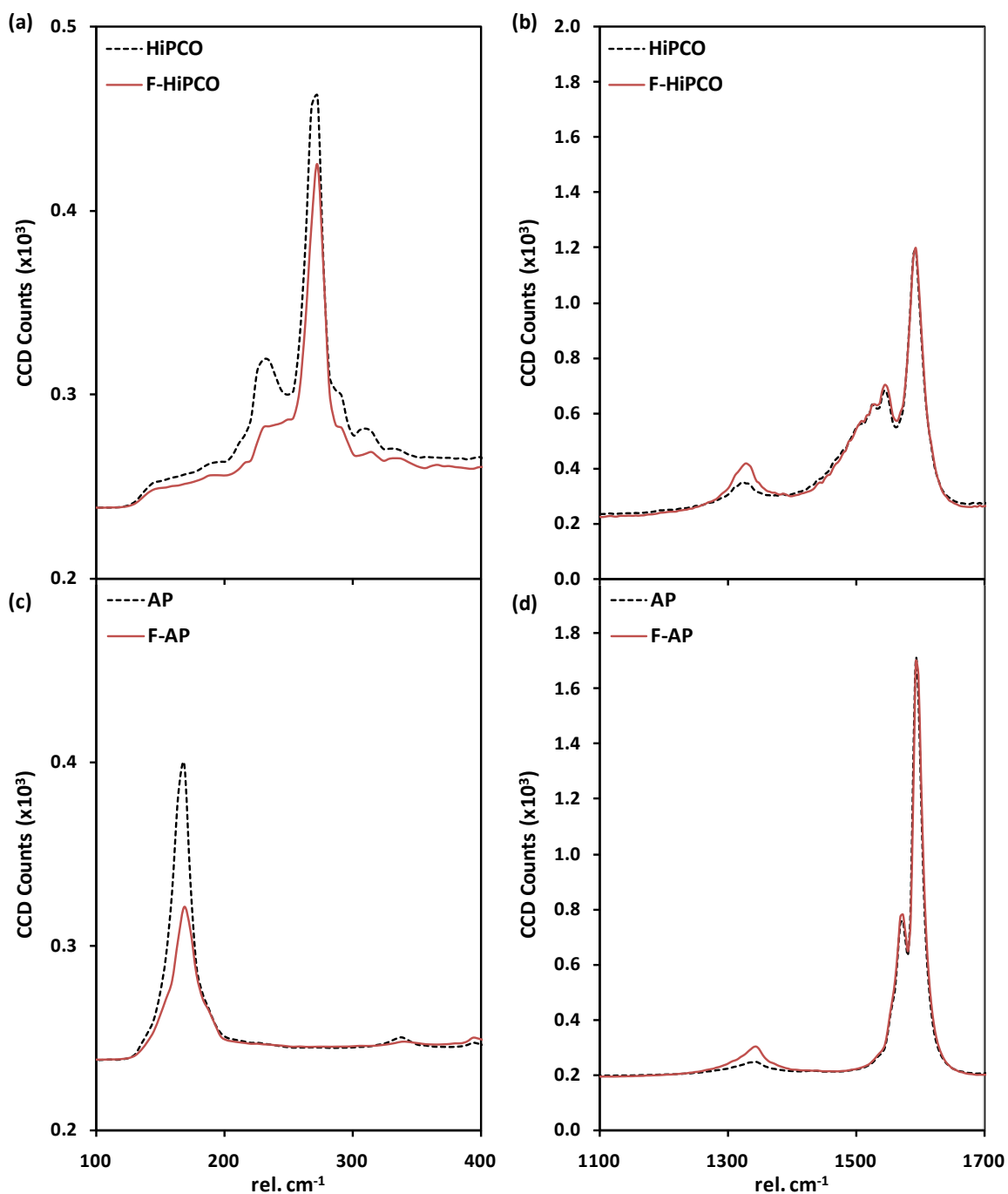


**Figure 5.13.** Raman spectra for CNTs before (black dotted line) and after (red solid line) exposure to  $\text{SF}_6$  plasma. The RBM and D + G band regions are given in (a) and (b) for HiPCO CNTs, and (c) and (d) for AP CNTs respectively.

the G band were not found to vary significantly after fluorination, regardless of the CNT type. Furthermore, the positions of these two components were found to remain constant upon functionalisation. As has already been mentioned the position of the  $G^+$  component can be used as an indicator of the presence of dopants within the CNTs. Since no change was observed in this case, it could be concluded that fluorination did not result in any measurable change in the local electronic structure.

#### 5.4.4. Short-Term Degradation of Fluorinated CNT Surfaces

The spectra in 5.10(a) were obtained 1 day after the samples were exposed to the plasma treatment and during this time they were under vacuum in the XPS instrument's intro chamber. After analysis they were removed and placed into storage in ambient conditions. It was previously found that the level of C1s functionality did not mirror that of the total fluorine content at the surface, thus suggesting that some fluorine species were adsorbed to the CNT surfaces, and over time the surfaces may degrade. The samples were again analysed at a later date where it was found that the fluorine content had decreased significantly. This prompted a brief study to determine if this was reproducible.

Figure 5.14(a) gives XPS survey spectra of an AP CNT sample that had been exposed to SF<sub>6</sub> plasma for 3 minutes. XPS analysis was performed 4 times over a period of 12 days, with the sample removed from the instrument when not under study. The initial (0 days) spectrum was obtained as soon after the fluorination as was possible. That is, it was removed from the plasma chamber and immediately placed under vacuum in the XPS intro chamber. In total the sample would have spent ~1 minute in an ambient atmospheric environment prior to being placed under vacuum.

This first analysis showed the CNT surface having a startling amount of fluorine present. Upon quantification, a fluorine concentration of 66% was found, thus implying that two thirds of the surface species were bound fluorine. After 3 days of storage the sample was again analysed and found to have decreased in total fluorine content to 44%, losing more than 20% of the fluorine species since the initial exposure. This procedure was repeated 6 and 12 days after exposure where it was found that the fluorine content further decreased although beyond 6 days it appeared to have reached a lower limit of ~30%. This trend is plotted in figure 5.14(b), accentuating this decline and plateau in fluorine content.

It is clear that some reaction mechanism acted upon the surface, and that it ultimately lead to the apparent degradation of the fluorinated nanotube surfaces. Between XPS analyses the samples were stored under ambient conditions. This prompted a question regarding whether storage under a less 'reactive' atmosphere would have a measurable effect on the decreasing surface fluorine content. Figure 5.14(c) gives data from an experiment exposing three samples to SF<sub>6</sub> plasma and storing them under ambient, inert (dry nitrogen) and vacuum conditions. Each sample was stored at room temperature and, in the case of the

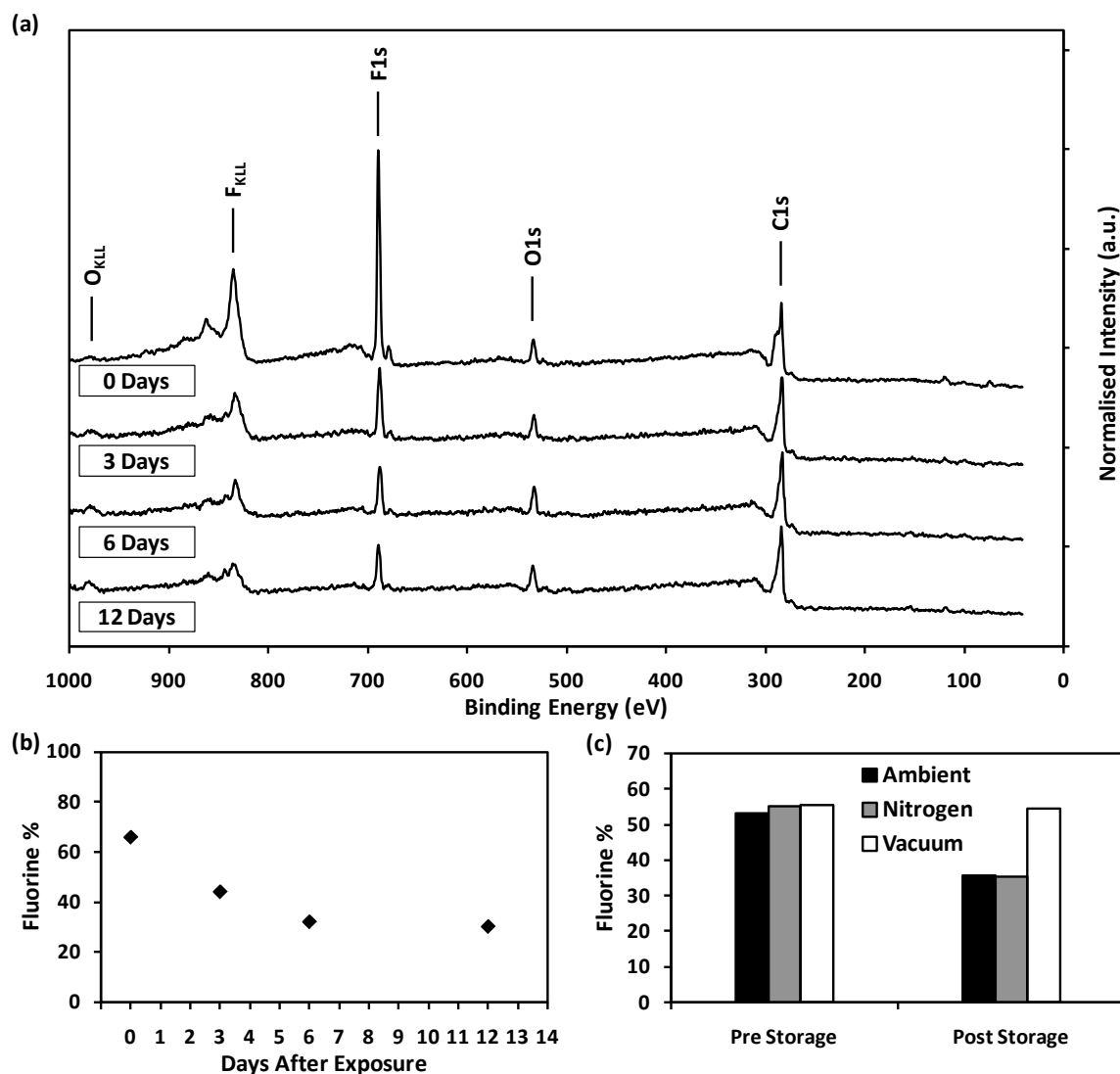


**Figure 5.14. (a) XPS survey spectra of fluorinated CNTs up to 9 days after the initial exposure and (b) the atomic % of fluorine on the surface before and after storage in an ambient and nitrogen atmosphere. Spectra were collected in CRR mode.**

ambient and nitrogen stored samples, at atmospheric pressure. The vacuum sample was stored at a pressure less than  $10^{-6}$  Torr between analyses. The samples were analysed immediately after plasma exposure, and again after storage for 10 days under the different environments. Prior to storage the samples displayed an average fluorine content of  $54.6 \pm 1.2\%$ , similar to that already observed. After storage under the two atmospheric conditions the fluorine content was seen to decrease although the storage conditions did not appear to make any difference to the amount of fluorine depleted from the surface. Overall the average fluorine content between the two samples after storage was  $35.6 \pm 0.2\%$ , again in good agreement with the magnitude of degradation already observed. Interestingly, the sample stored under vacuum for the same amount of time did not show

any significant signs of degradation, with the fluorine content varying by less than 1% between analyses. The sample stored under vacuum showed that the removal of any meaningful atmosphere around the CNT surface ceased the degradation of the fluorinated CNTs. Thus it could be reasonably concluded that the cause of the observed decline in fluorine content was a result of exposure to components within the atmosphere, and not an intrinsic mechanism within the CNT surface, since if the latter were true all three samples should be expected to degrade equally. Furthermore, if the degradation was related to desorption of weakly bound, such as physisorbed, fluorine species at the surface, all samples could again be expected to degrade in the same way. This assumes however that the presence of some atmosphere does not promote desorption. It is then proposed that the fluorinated surfaces react with the atmosphere to liberate fluorine-containing species from the surface, perhaps through some interaction with either gaseous oxygen or water vapour either cleaving chemically bound fluorine species, or promoting the desorption of physisorbed species. It is interesting to note that the same level of degradation was observed between the ambient and nitrogen atmospheres. If some interaction between atmospheric oxygen species and the surface were responsible for the decrease in fluorine content then the storage under nitrogen should have lessened this interaction. This assumes that the nitrogen atmosphere remained dry and inert throughout the course of the storage. Also, independent of the changing fluorine content, the ratio of carbon to oxygen species on all three surfaces was seen to remain largely constant before and after storage, showing that fluorine functionality was not simply replaced by oxygen functionality upon degradation.

Unfortunately, at this stage the XPS instrument suffered a failure that rendered it essentially unavailable for the remainder of the research. Consequently further research is required to clarify the cause of the degradation and possible experiments are discussed later in the Section 9.2. However knowledge that the surfaces did degrade, and the timeframe across which this occurred allowed for experiments to be appropriately designed. That is, to ensure an accurate measure of fluorine content after a given exposure the CNT surfaces were allowed to stabilise for at least 1 week prior to analysis. This also prompted an investigation into possible ways to enhance fluorine bonding at the surface, reducing this degradation and improving the overall stability of the fluorinated CNTs.

### 5.5. Summary of the Plasma Fluorination of CNTs

Pristine and SF<sub>6</sub> plasma fluorinated carbon nanotube surfaces were characterised using XPS, TEM and Raman spectroscopy. The presence of a photoelectric peak at a binding energy of ~690 eV from electrons ejected from the 1s shell of fluorine was taken as direct evidence of the attachment of fluorine to the surfaces. Detailed analysis of the carbon 1s peak found features on the binding energy side of the main C-C peak related to functional moieties, taken as C-F<sub>x</sub> functionality, further evidence of the attachment of fluorine to the carbon nanotubes. This attachment was found to occur with two bonding types; covalent and semi-ionic. It was also observed that fluorination occurred with apparently no contamination from sulphur, a conclusion drawn from the lack of any significant feature in XPS spectra at a binding energy of ~164 eV.

TEM analysis provided clear visual evidence that the CNT structures remained intact after the plasma fluorination technique was applied, however it was found to be very limited in its ability to provide any further chemical information about the nanotube functionality.

Raman spectroscopy of pristine and plasma treated CNT surfaces allowed for the direct observation of changes in the vibrational nature of the nanotubes. This was observed as an increase in the D band relative to the G band, indicative of increased disorder within the nanotube lattice. Furthermore, decreases in the RBM intensity indicated that the nanotubes were being functionalised by the process. This provided strong evidence that indeed the fluorination technique functionalised the CNTs themselves, and not other impurities that may be present within the surface.

The stability of the fluorinated CNT films was also briefly investigated. Fluorinated CNT films were observed to degrade over a relatively short time period. Within ~6 days of exposure the fluorine content on the surface degrades to ~50% of the initial amount. Beyond this time however the surfaces were very stable. Only by storing the surfaces under vacuum could the degradation be prevented, suggesting that it is a direct result of contact with atmospheric species.



---

## **Chapter 6.**

# **SYNCHROTRON STUDIES OF FLUORINATED NANOTUBES I - SXR187: ROUND 2 2008**

### **6.1. Introduction**

Other avenues for the characterisation of fluorinated CNTs were investigated while repairs were being performed to the LHS-10 instrument at Flinders. One technique was of course Raman spectroscopy. While this technique was exceptionally well suited for the physical characterisation of CNT samples it lacked the high degree of sensitivity to chemical changes for which photoelectron spectroscopy is well known. Somewhat fortuitously however the soft X-ray (SXR) beamline at the Australian Synchrotron (AS) began user operations around this time and upon successful application for experimental time, synchrotron-based XPS (sXPS) was used to study the fluorination of carbon nanotubes.

Fundamentally, sXPS does not differ from that of the lab-based technique. X-rays of a given energy are incident upon a surface under analysis liberating electrons from the core shell of the elements of which the sample is composed. These electrons, like in XPS, have a kinetic energy dependent on the incident photon energy and the binding energy of the element from which they came. Synchrotron XPS stands apart from its more common

lab-based parent by the way in which the X-rays are generated. Traditional X-ray sources excite characteristic lines from a material by the acceleration of electrons into a metal at high energies, as outlined in detail in Appendix B. This method does not result in a single X-ray emission, and tends to have a dependence on many secondary effects related to the lifetime of the energy levels in the system as well as other thermal mechanisms. The result is a far from discrete photon emission that directly impacts the achievable spectral resolution of an instrument. Monochromators can be employed to significantly increase this resolution although any improvement is accompanied by a drastic reduction in X-ray intensity at the sample. In contrast, a synchrotron generates radiation by the bending of electrons travelling at relativistic speeds around a circular (or rather, a round cornered polygon) vacuum vessel. This is achieved via the use of strong magnetic fields setup within ‘insertion devices’ designed to either bend or wiggle the electron trajectory. The change in the trajectory of the electron generates electromagnetic radiation that travels tangential to the electron path. This radiation can then be captured by a beamline and an end-station where the user would use it to perform experiments. How the electrons are accelerated to produce the radiation, i.e. whether the electron path is simply bent around a corner, or ‘undulated’ through a straight section, governs the type radiation that is generated. Ultimately, when this method is applied to the generation of X-rays, far greater energy resolution can be obtained at the sample and depending on the experimental setup often the lifetime of the excited state within the atoms making up the sample under study, and thus the natural linewidth of the energy level, becomes the limiting factor governing spectral resolution.

Greater energy resolution is not the only advantage afforded by synchrotron generated X-rays. Compared to a lab-based source the brightness of X-rays generated by an undulator type insertion device can be as much as  $10^{10}$  times greater,<sup>170</sup> and with such high flux the experimentalist can discard some intensity in favour of resolution, both spatially and spectrally. X-rays generated by a synchrotron are also elliptically polarised (an intrinsic result of the way in which the radiation is created and delivered to the end station). This allows advanced sample characterisation to be performed whereby the X-rays interact with the surface in different ways depending on the angle at which the beam is incident. A final advantage, and possibly the most important, is the fact that the X-ray energies that are accessible by the experimentalist is continuously tunable within an energy range defined by the specifications of the insertion device and the beamline. This allows for especially

advanced techniques to be performed, such as X-ray absorption techniques where the photon energy is varied and the resultant sample response monitored rather than the energy of detected electrons being swept such as in XPS. In photoemission studies, a continuously variable photon energy allows one to maximise sensitivity to a particular element. This is afforded by reducing the excitation energy to near the binding energy of the element of interest, thus increasing its photoionisation cross-section. Reduced photon energy not only increases sensitivity to a given element but also to the surface, by lowering the kinetic energy of ejected electrons and decreasing their IMFP, resulting in a reduced escape depth.

Research applying synchrotron radiation based techniques to carbon nanotubes has been limited in recent literature.<sup>19,171-179</sup> Much of the research revolved around the structural characterisation of CNTs and their composites using hard X-ray techniques such as diffraction, scattering and fluorescence microscopy.<sup>19,172-175,178</sup> Application of synchrotron soft X-ray techniques to the fluorine functionalisation of CNTs has only been performed by a few groups. Brzhezinskaya *et al.* have studied both multi-walled and single-walled CNTs using X-ray absorption, photoelectron and photoemission spectroscopy.<sup>172,173</sup> This work was heavily focussed on the C1s core-level and NEXAFS spectra, with minimal discussion of the O1s and F1s presence. Also, the process used was one of high-temperature fluorine gas exposure, expected to have vastly different chemistry to the SF<sub>6</sub> plasma used in this work.

#### 6.1.1. The Application of Synchrotron Radiation to Fluorinated CNTs

The primary goal of the research proposed under SXR187 was the establishment of an understanding of the capabilities of the SXR beamline (SR14ID01) at the Australian Synchrotron, and to apply them to the fluorinated CNT samples being studied in this dissertation. Using the high resolution and flux of the synchrotron X-rays it was anticipated that significantly greater detail could be elucidated from C1s and F1s spectra of CNT samples, giving a greater understanding of the mechanisms behind fluorine attachment via SF<sub>6</sub> plasma exposure. More specifically, the effect of varying applied rf power to the resultant fluorination was to be characterised using high resolution sXPS. Secondary to this main objective were two other aims for this proposal; to use the high flux and sensitivity to investigate whether there was a detectable sulphur presence in the samples (as a result of fluorination using SF<sub>6</sub>), and to investigate how the presence of oxygen containing species in the plasma affects the chemical bonding present on the CNTs at the fluorinated sites.

### 6.1.2. Experimental Design

Samples in this study consisted of raw HiPCO nanotubes deposited on mild steel pucks. Analysis performed prior to this work established that the films deposited were of sufficient thickness to completely mask the underlying substrate and remove it as a source of convolution in XPS analysis. Along with a control, a set of 12 samples were created and exposed to plasma at 2.5 mTorr of gas supply pressure, with absorbed rf powers ranging from 5 – 80 W in regular intervals. Each exposure was performed for 60 seconds.

The second set of samples created would probe the effect of adding gaseous impurities to the SF<sub>6</sub> plasma. Three extra samples were created and exposed to plasma containing pure SF<sub>6</sub>, SF<sub>6</sub> + O<sub>2</sub> and SF<sub>6</sub> + H<sub>2</sub>O. Each plasma treatment was performed for 60 seconds at 15 W rf power. The partial pressure of SF<sub>6</sub> was held constant at 2.5 mTorr while the additive was held at 1 mTorr for each exposure giving a total pressure of 2.5 mTorr for the pure SF<sub>6</sub> treatment and 3.5 mTorr for the mixed-gas treatments. The water used was ultra-pure and degassed under vacuum separately to minimise atmospheric contaminants.

Photoemission characterisation was performed at three excitation energies; 1486.6 eV, 771 eV and 320 eV. The foremost excitation allowed for direct comparison to any results that were obtained on the LHS-10 at Flinders and also enabled the usage of documented atomic sensitivity factors. The lower photon energies enhanced the sensitivity of the light elements under study; C, O and F, to photoionisation. Excitation at an energy of 771 eV allowed the 1s shells of all three elements to be probed. Excitation at an energy of 320 eV maximised sensitivity to carbon, and therefore allowed very high resolution spectra to be obtained around this region. At the time the latter excitation energies (771 eV and 320 eV) were chosen as they enhanced sensitivity without incurring convolution from Auger electrons in the energy ranges of interest.

Since it was expected that any sulphur presence in the samples would be in very small amounts another experiment was performed at various excitation energies, the minimum of which was 249 eV, found to excite electrons from the 2p shell of sulphur with the highest sensitivity without overlapping Auger peaks with the photo peaks. At this energy however no other peaks of interest were observable. As a consequence, quantification was not possible at this photon energy, since to quantify XPS results one requires a comparison with other elements detected at the surface.

## 6.2. Synchrotron XPS Studies of Fluorinated SWCNTs

### 6.2.1. A Detectable Sulphur Presence Using Low Energy Excitation

An observation that had not been clarified prior to the research at the synchrotron was the curious absence of any measurable sulphur signal in the XPS of CNTs after exposure to SF<sub>6</sub> plasma. Intuitively one might assume that in plasma ignited within sulphur hexafluoride the ratio of sulphur to fluorine species should be 1:6, given the structure of the molecule itself, and thus there may be a sulphur presence approximately one sixth that of fluorine. This assumes not only that the molecule is completely dissociated when in the plasma state, but also that the sulphur species react with the CNT surface in the same way and with the same stoichiometry that fluorine would. Nevertheless, the apparent absence of sulphur in the samples was intriguing and warranted further study.

Presented in figure 6.1 is the sulphur 2p region of fluorinated CNTs. The sample used was exposed to 2.5 mTorr SF<sub>6</sub> plasma for 60 seconds at 80 W absorbed rf power. It was proposed that the sample most likely to show any significant sulphur presence after exposure would be the one that had undergone the strongest treatment. The main spectrum in figure 6.1 shows the sulphur 2p region as taken with excitation energy of 249 eV. In contrast the inset used an excitation of 1486.6 eV which was equivalent in energy to the Al K $\alpha$  X-ray source used on the LHS-10 at Flinders. This figure demonstrates the considerable difference in photoionisation cross-section of the S2p state at these two excitation energies. At the high excitation energy no distinct features were discernable in the spectra, which to the analyst would easily lead to the conclusion that there was no sulphur presence after a fluorination treatment. However, at the significantly reduced photon energy a striking feature was resolved at and above the sulphur 2p binding energy, indicating instead that there was indeed a sulphur presence on the sample; it was just in such small concentration that it is below the detection limit of a lab-based instrument.

The cause of this remarkable difference between incident photon energies was two-fold. The first related to the kinetic energy of the ejected electrons. When using 1486.6 eV photons the maximum kinetic energy that an electron ejected from a sulphur atom could receive was 1322.6 eV. Using the TPP2M formula this would result in an IMFP and thus analysis depth of 29.9 Å.<sup>180</sup> At 249 eV this was reduced significantly, to 5.1 Å, meaning a greatly enhanced surface sensitivity. If the sulphur species were present near or at the top

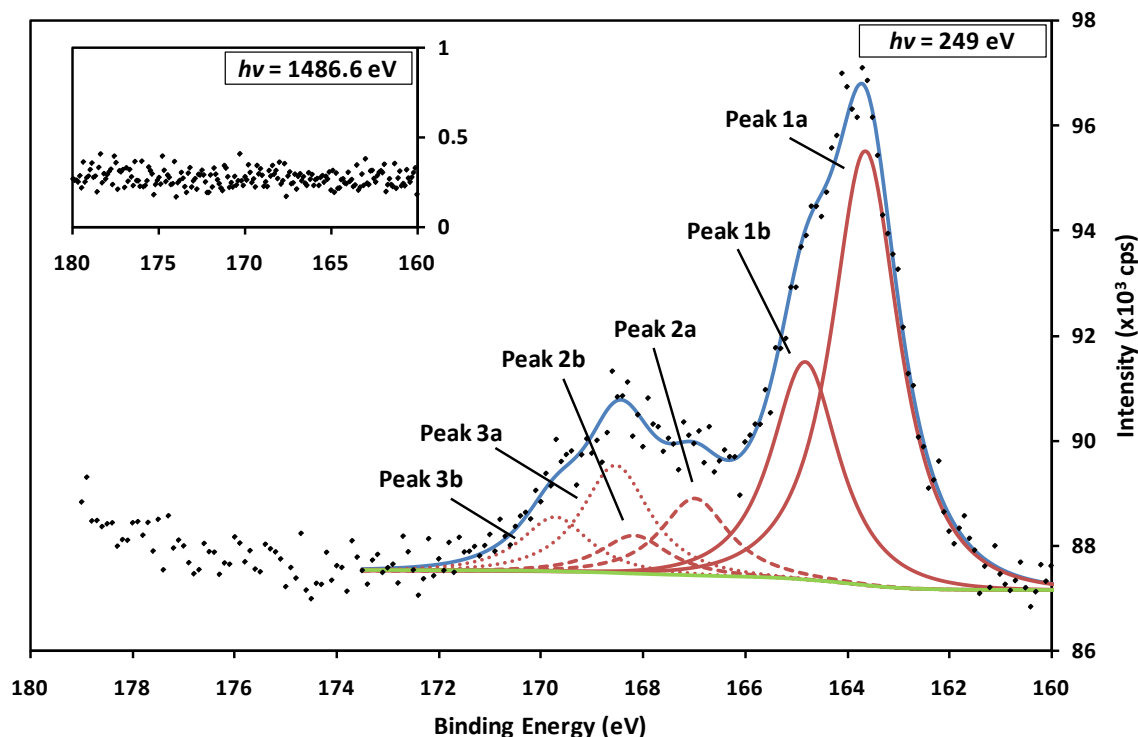


**Figure 6.1.** XPS spectra of the sulphur 2p region from fluorinated CNTs with the main figure taken at 249 eV and the inset at 1486.6 eV. The pass energy was 20 eV for both spectra.

of the CNT surface, then by increasing the surface sensitivity by such a large magnitude the likelihood of detecting the sulphur over the bulk background signal was also increased. Furthermore, at this excitation energy the electrons within the 1s orbital of carbon could not be excited, further enhancing sensitivity towards the sulphur. The second cause of the increased sensitivity was due to the greatly enhanced ionisation cross-section for sulphur at reduced photon energies. Plotted in figure 6.2 is the total photoionisation cross-section of the sulphur 2p subshell for photon energies from 15 – 1500 eV, reproduced from the data published by Yeh and Lindau.<sup>144</sup> As the photon energy is decreased, and thus gets closer to the binding energy of the sulphur 2p shell, the cross section increases and thus the probability of photoionisation is increased as the photon energy decreases. Extracting values from the data for the energies used here gives a cross section (in units of  $10^6$  barn) of 0.045 at 1486.6 eV and 3.322 at 250 eV (note that 250 eV was used due to the limitations of the plotted data). This equates to an increase in ionisation sensitivity by a factor of almost 75, consequently increasing the detectable sulphur signal considerably.

The sulphur 2p shell is spin-orbit split into the  $2p_{3/2}$  and  $2p_{1/2}$  energy levels. This splitting occurs due to coupling of the electronic spin angular momentum ( $S = 1/2$ ) and the orbital angular momentum ( $L = 0, 1, 2, \dots$ ) combining to produce new states described by the total

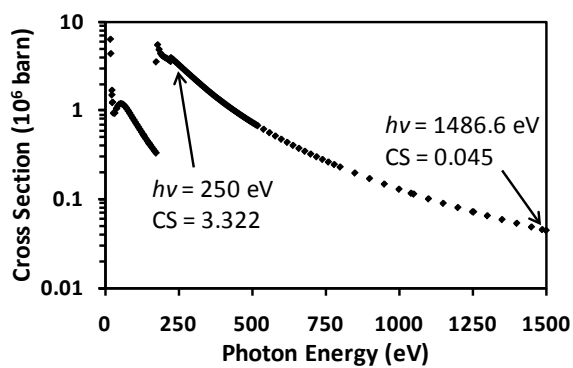


**Figure 6.2.** The total photoionisation cross-section of the S2p subshell for photon energies in the range 15 – 1500 eV. From Yeh and Lindau.<sup>144</sup>

electronic angular momentum ( $J$ ) where  $J = |L \pm S|$ .<sup>115</sup> For the 2p shell in sulphur  $L = 1$  and thus  $J = 3/2, 1/2$  which ultimately produces two discrete peaks in XPS spectra for electrons liberated from this shell. Experimentally these peaks are found to have a separation of 1.18 eV, with the  $2p_{3/2}$  peak being the lowest in energy and found at 164 eV for the elemental solid.<sup>146</sup> To fit a 2p spectrum from sulphur one must then use two synthetic peaks with this separation. Knowledge of the relative intensities is also required and comes from taking the ratio of the degeneracies of the states, which is given by  $2J + 1$  for each value of  $J$ .<sup>115</sup> Upon determination it is found that the ratio is 1:2, where the  $2p_{1/2}$  is half the intensity of the  $2p_{3/2}$  peak. Accordingly the relative intensity of the fitted peaks must follow this analysis.

To achieve good agreement between the sum of the synthetic curves and the data, the spectrum in figure 6.1 was fitted with three pairs of peaks differentiated from one another by the solid, dashed and dotted red lines. The  $p_{3/2}$  and  $p_{1/2}$  peaks are denoted by ‘a’ and ‘b’ respectively. Table 6.1 summarises the parameters of the synthetic peaks. Briefly, each pair was fixed at a separation of 1.18 eV and relative intensity ratio of 1:2, with only the total area and position of the doublets allowed to be adjusted during the fitting procedure.

The fact that the data was best fitted by three doublets suggested that at least three discrete chemical states contributed to the presented spectrum. Unfortunately, at this photon energy no other elemental spectra could be recorded since the photon energy was too low. No comparison could therefore be made with other peaks to test the accuracy of the energy scale. Working under the assumption that the energy scale was accurate, three chemical states with  $2p_{3/2}$  binding energies of ~163.7, 167.0 and 168.5 eV are detected in the spectrum. Foremost, the binding energy of sulphur in the parent molecule, sulphur

**Table 6.1. Parameters for the synthetic peaks used to fit the data in figure 6.1. All peaks were Gaussian-Lorentzian with a mixing ratio of 0.9 and FWHM of 1.5 eV.**

Parameter	Peak 1a	Peak 1b	Peak 2a	Peak 2b	Peak 3a	Peak 3b
Centre (eV)	163.65	164.83	166.99	168.17	168.54	169.72
$\Delta$ (a-b)	1.18		1.18		1.18	
Area (eV.cps)	16279.3	8139.7	2887.4	1443.7	4040.0	2020.0
Ratio (a:b)	2:1		2:1		2:1	

hexafluoride, is accepted to be 174.4 eV from the data in Moulder.<sup>146</sup> This is outside the energy range of the features observed here and the presence of the original molecule can be ruled out. Regardless, adsorbed SF<sub>6</sub> molecules remaining on the surface for a number of days after treatment and after being exposed to the extreme flux of the synchrotron beam would seem unlikely. The covalent attachment of sulphur rich moieties that can be derived from the parent molecule SF<sub>6</sub> therefore become better candidates to explain the feature in figure 6.1.

The simplest sulphur functionality that could exist is the attachment of a single sulphur atom to the CNT surface resulting in a covalent C–S bond. Elemental sulphur, polysulphides and organic sulphides are usually found in the range 163 – 165 eV.<sup>181</sup> Clark and Thomas studied a series of homopolymers with sulphur containing constituents using XPS and found that direct bonds between carbon and sulphur gave a sulphur 2p binding energy of 163.7 eV.<sup>182</sup> Similar results were found for compounds containing sulphides of the form S<sup>2-</sup>, where the binding energies were found on the order of 163 eV.<sup>183,184</sup> These systems are of course markedly different to that of nanotubes. However, Nakamura *et al.* functionalised SWCNTs using cyclic disulphides to produce thioakylthiolated CNTs (authors terminology), where the CNT sidewall was directly bonded to a thioakyl group resulting in a –C–S–C– bond arrangement. Similarly, using XPS the S2p<sub>3/2</sub> binding energy was found to be 163.7 eV.<sup>185</sup> From these examples it would seem reasonable then to suggest that the lowest binding energy and the most intense peak in figure 6.1 was from an organic sulphide, where sulphur was bound directly to carbon.

It has already been established that the HiPCO CNT surfaces used in this study had a considerable amount of oxygen present at the surface. As part of research discussed in the

next section studying the effects of oxygen on plasmas of SF<sub>6</sub>, work by Ryan and Plumb found that under the presence of oxygen sulphur hexafluoride is capable of breaking down into many different species, including SO and SO<sub>2</sub>.<sup>186-188</sup> This was not only found to be true for oxygen present in a gaseous form, but also when on a surface, catalysing the further degradation of the parent molecule into smaller constituents rich with sulphur and oxygen at the interface. McIntyre and Chan noted that when studied using XPS the sulphur-oxygen groups tend to fall in the range of 165 – 169 eV, with the higher end dominated by the inorganic sulphates.<sup>189</sup> A similar observation can be made from the data tables in Moulder.<sup>146</sup> Indeed when studying the effect of irradiation of aliphatic polysulphones, Iacona and Marletta noted peak energies of 166.9 eV and 168.0 eV attributed to –SO– and –SO<sub>2</sub>– (sulphoxy and sulphonyl) functionality in the materials.<sup>190</sup> Since the likelihood of species such as these has been established through surface reactions it is then proposed that the second and third doublets are a result of sulphonyl groups attached to the CNTs.

There is a noticeable difference (of ~0.5 eV) between the fitted position for the –SO<sub>2</sub> functionality in this work and that chosen by Iacona. One possible source for this variation comes from a constituent of the surface not yet considered in the assignment of peaks in the S2p region; the residual iron catalyst. As noted earlier, the S2p peak for inorganic sulphates tends to occur near 169 eV. Pratt provides a detailed list of reference binding energies for various oxidised forms of iron, including FeSO<sub>4</sub> where the S2p<sub>3/2</sub> peak was found at 168.5 eV.<sup>183</sup> A comprehensive study of the XPS binding energies of sulphur species by Lindberg *et al.* notes another sulphate for Fe(III) of the form Fe<sub>2</sub>(SO<sub>4</sub>)<sub>3</sub> where the binding energy is found at 169.3 eV.<sup>181</sup> Since iron was known to be present in small amounts in these samples it seems plausible then that some of the reactive sulphur species may react with these particles producing inorganic sulphates, the presence of which would likely contribute to fitted peaks tending towards higher binding energies.

A further possible source of convolution comes from fluorine, known to be present on the surface. It must be noted that the 2p binding energies of sulphur species containing fluorine (and oxygen) have been published as being generally greater than 169 eV for a wide range of compounds. Moieties such as –RSO<sub>2</sub>F and –SOF<sub>2</sub> are found as high as 170 eV.<sup>181</sup> Since no significant presence was notable above ~169 eV that was not already accounted for as part of an assigned doublet, it is suggested that if these species did exist they are in very

small amounts. Considering the already minute sulphur presence these fluorine species must then be so scarcely present as to render their contribution moot.

A summary of the proposed chemical assignments for the states observed in the S2p spectrum in figure 6.1 are given in table 6.2. It is interesting to note that upon reviewing the literature studying sulphur compounds, the most plausible species that would contribute to the observed S2p peak did not involve fluorine. In fact, from the data presented it would appear as though fluorine-sulphur species are unlikely to be present at all, with oxygen-sulphur groups a much more favourable alternative both as an attached moiety to carbonaceous species and to residual iron catalyst as an inorganic sulphate. This would suggest that any SF<sub>x</sub> species in the plasma are either non-reactive, pumped away as a gaseous species, or decompose upon contact with the surface into atomic fluorine and sulphur, or a sulphony species that may subsequently attach to the CNTs. Irrespective of the mechanism, synchrotron radiation at much lower energy compared to that of lab-based X-rays was required just to observe the sulphur presence at all. This fact is strong evidence to indicate that the attachment of sulphur-based species to the CNT surface after exposure to SF<sub>6</sub> plasma was extremely unfavourable compared to that of the attachment of fluorine, to the point where for a majority of instruments its presence would most likely go completely undetected.

The amount of sulphur present on these surfaces unfortunately could not be quantified using these results since in XPS one requires a comparison to be made relative to other elements in the sample. As already noted, at this excitation energy the spectra from the core shells of other elements could not be obtained. However, as a general statement, the sensitivity of XPS to chemical species on a surface is at best 0.1% of the total atomic concentration (1000 ppm) for a standard system.<sup>191</sup> Given that when using an excitation of 1486.6 eV no sulphur was detected it could therefore be proposed that any sulphur presence on the surface was below the detection limits of the technique operating under somewhat standard conditions. This would then lead to the conclusion that sulphur species make up less than ~0.1% of the surface constituents.<sup>191</sup>

### 6.2.2. Fluorination Using Plasma in Mixtures of SF<sub>6</sub> and O<sub>2</sub>/H<sub>2</sub>O

Prior to the research detailed in this dissertation, an interesting observation was made whereby the fluorination of carbon surfaces appeared to be enhanced when performed with

**Table 6.2. Proposed chemical assignments for the fitted components in figure 6.1.**

	<b>Component 1</b> <b>2p<sub>3/2</sub> = 163.7 eV</b>	<b>Component 2</b> <b>2p<sub>3/2</sub> = 166.9 eV</b>	<b>Component 3</b> <b>2p<sub>3/2</sub> = 168.5 eV</b>
<b>Proposed Chemical Assignments</b>	Organic Sulphides -C-S -C-S-C-	(poly)Sulphoxy -RSOR- -RS(O)SR-	Sulphoxones, Sulphonyl -SO <sub>2</sub> , -SO <sub>2</sub> - Inorganic Sulphates FeSO <sub>4</sub> , Fe <sub>2</sub> (SO <sub>4</sub> ) <sub>3</sub>

oxygen mixed into the SF<sub>6</sub>.<sup>192</sup> As part of the proposal outlined in this chapter a small component of the research was dedicated to briefly investigating this phenomenon. Three samples were created under identical conditions with the only difference being the composition of the gaseous environment that was ignited into the plasma state; pure SF<sub>6</sub>, SF<sub>6</sub>/O<sub>2</sub> and SF<sub>6</sub>/H<sub>2</sub>O with mixtures taken at pressure ratios of 2.5:1.

XPS survey spectra of the three samples taken using synchrotron radiation at 1486.6 eV are presented in figure 6.3, with all spectra normalised to the intensity of the C1s peak to emphasise relative changes in the abundance of other elements. The bottom spectrum is for the sample exposed to SF<sub>6</sub> plasma at 10 W rf power (2.5 mTorr). There was a notable presence of fluorine on the surface indicated by the F1s peak at 688 eV, along with the expected O1s and C1s peaks that are present at 533 eV and 284.6 eV respectively. There is also an iron presence detected, attributed to the residual catalyst particles, and a minor nitrogen impurity ~399 eV from the dispersant used to deposit the sample (DMF). Overall this spectrum appears much the same as that already detailed, with the amount of fluorine being 15% of the total atomic concentration.

The addition of 1 mTorr of O<sub>2</sub> to the SF<sub>6</sub> reactant generated a substantial increase in the fluorine content on the surface, as evidenced by the top spectrum in figure 6.3 where the F1s peak is seen to be significantly more intense than that of the sample exposed to the pure SF<sub>6</sub> plasma. It is also worthwhile noting that for the first time, when using X-rays equivalent in energy to a lab-based system, a detectable sulphur presence was observed suggesting not only an enhanced addition of fluorine to the surface, but also of sulphur or sulphur containing species. The oxygen content of the surface was also significantly greater in comparison with the standard sample, suggesting also heavy oxidation of the CNT surface. The total fluorine content rose to 20% for this sample, an increase that was limited by the likewise increase of oxygen content. When compared to the C1s peak directly however, the amount of fluorine relative to carbon doubled over that of the

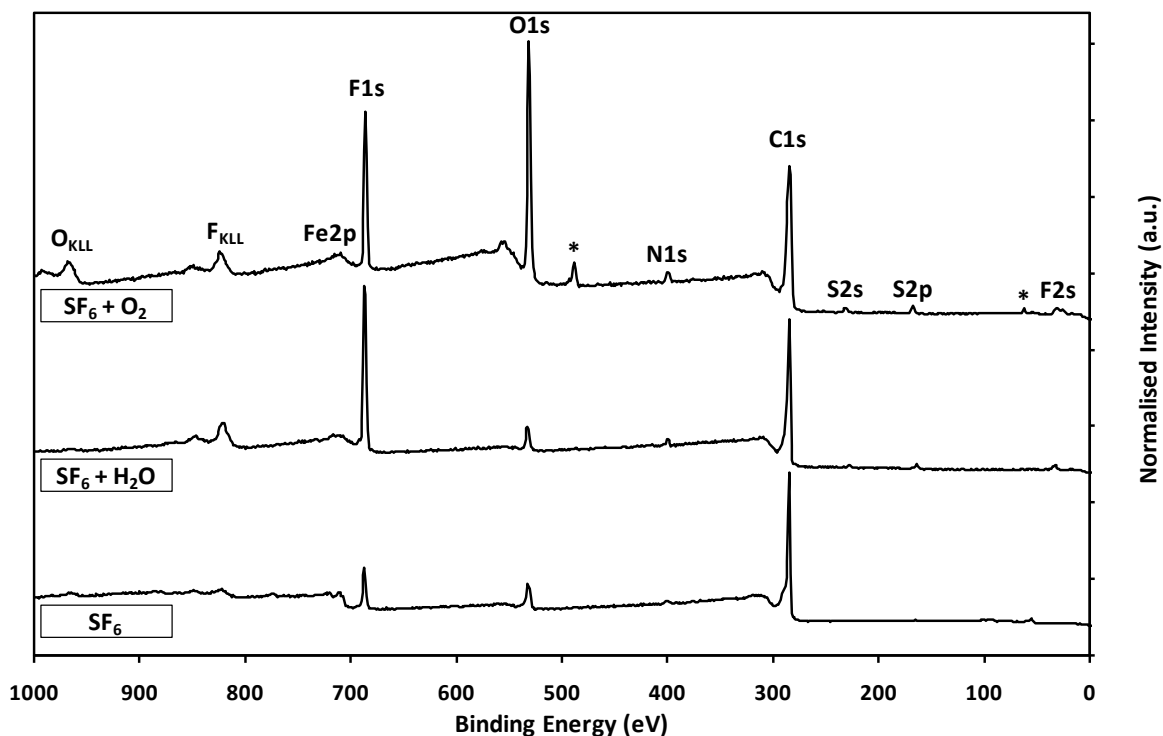


**Figure 6.3.** XPS survey spectra of samples exposed to SF<sub>6</sub> plasma pure (bottom), mixed with H<sub>2</sub>O (middle) and mixed with O<sub>2</sub> (top). Spectra recorded using synchrotron radiation at 1486.6 eV with 50 eV pass energy.

standard SF<sub>6</sub> exposure. Marked by an asterisk (\*) in this spectrum are also sodium peaks at 493 and 64 eV for the KLL Auger and 2s peaks respectively. As has been noted previously this was an unavoidable contaminant from the preparation process.

Something observed from this figure that was particularly interesting was what happened when water vapour was used in place of gaseous oxygen. As seen in the middle spectrum, the fluorine content was enriched, but the oxygen content remained essentially unchanged. This sample was exposed to plasma of 2.5 mTorr SF<sub>6</sub> doped with 1 mTorr of water vapour. Upon quantification it was found that fluorine was now 35% the total atomic content at the surface with the ratio of carbon to fluorine also increased to nearly three times that of the standard sample. Again in this sample S2s and S2p peaks were observed, suggesting also the enhancement of sulphur deposition.

Table 6.3 summarises the total atomic percentages determined from the spectra and also makes note of stoichiometric quantities on the surface from the ratio of the carbon and fluorine. The literature notes that when fluorinating CNTs the maximum stoichiometry achievable is C<sub>2</sub>F (or alternatively, CF<sub>0.5</sub>), i.e. two carbon atoms for every added fluorine atom.<sup>51</sup> At this point and beyond, the integrity of the nanotube structure comes into doubt

**Table 6.3. A summary of the quantified results from figure 6.3.**

Plasma Treatment	%C	%O	%F	CF Ratio	Stoichiometry
Pure SF <sub>6</sub>	70.0	14.1	15.9	0.2	CF <sub>0.2</sub>
SF <sub>6</sub> :O <sub>2</sub> 2.5:1	46.2	34.1	19.7	0.4	CF <sub>0.4</sub>
SF <sub>6</sub> :H <sub>2</sub> O 2.5:1	58.2	6.8	35.0	0.6	CF <sub>0.6</sub>

because the addition of fluorine to two neighbouring carbon atoms must necessarily result in a bond breaking within the hexagonal structure. From the ratios determined here, the standard treatment was well below this level yet the oxygen doped treatments each produced stoichiometries around this level, essentially reaching the maximum level of fluorination simply by adding oxygen to the plasma.

Figure 6.4 presents the high resolution C1s spectra from an untreated HiPCO sample, as well as the three samples exposed to the pure SF<sub>6</sub>, SF<sub>6</sub>/O<sub>2</sub> and SF<sub>6</sub>/H<sub>2</sub>O plasma treatments. The spectra presented were obtained using an excitation of 771 eV, and had a background subtraction performed prior to peak fitting (thus no background curve is shown here). The curves were fitted with a total of 8 discrete peaks, the positions and assignments for which are summarised in table 6.4. In the figure however, the peaks of particular importance have been labelled; the peak associated with sp<sup>2</sup> hybridised C-C bonding, and the three fluoro-carbon peaks CF, CF<sub>2</sub> and CF<sub>3</sub>.

After fluorination using the standard SF<sub>6</sub>-only treatment, given in (b), the most prominent change in the C1s spectrum was the small feature at 287.5 eV attributed to CF functionality. For completeness, peaks were also added to the CF<sub>2</sub> and CF<sub>3</sub> positions in this spectrum although only the CF<sub>2</sub> peak showed any significant intensity after the fitting procedure was performed with little to no CF<sub>3</sub> functionality detectable after the pure SF<sub>6</sub> treatment. Even the accuracy of the fitted CF<sub>2</sub> peak could be questioned since upon comparison with the C1s spectrum of the raw HiPCO sample in (a) the π-π\* shake-up satellite is seen to also reside near to this position. Thus it could be concluded that the greatest fluorine functionality detectable in these samples was CF.

The spectra in figure 6.4(c) and (d) emphasise how the level of resultant functionality is influenced by the addition of oxygen to the SF<sub>6</sub> plasma. In both cases, higher order

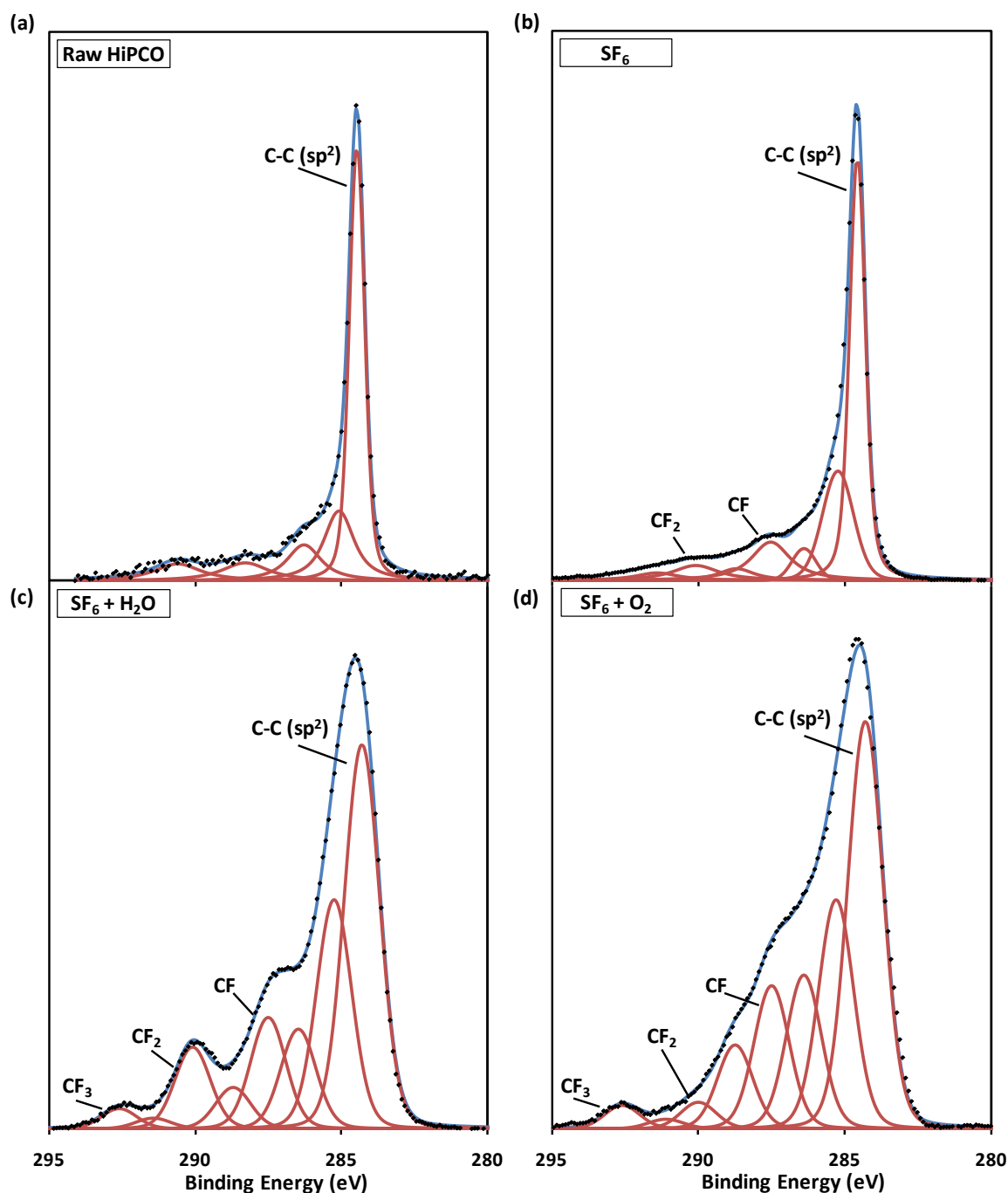


**Figure 6.4.** C1s spectra from HiPCO CNTs (a) untreated, and exposed to (b) pure SF<sub>6</sub> plasma, (c) SF<sub>6</sub>/H<sub>2</sub>O plasma and (d) SF<sub>6</sub>/O<sub>2</sub> plasma.

functionality in the form of CF<sub>2</sub> and CF<sub>3</sub> components is easily observable and particularly well-pronounced in the C1s photopeak. This was most evident for the sample exposed to the SF<sub>6</sub>/H<sub>2</sub>O plasma, which resulted in enhanced fluorine content without a corresponding increase in oxygen content. The three fluorine functionalities stood well-apart from the main C1s peak for this sample with the three components at 287.5, 290 and 292.5 eV attributed to CF<sub>x</sub> where x = 1, 2 and 3 respectively. This greater functionality was evident

**Table 6.4. The peak positions and assignments for the C1s spectra in figure 6.4.**

	292.5 eV	291.2 eV	289.9 eV	288.5 eV	287.5 eV	286.3 eV	285.2 eV	284.6 eV
<b>Proposed Chemical Assignment</b>	CF <sub>3</sub>	$\pi-\pi^*$	CF <sub>2</sub>	COOR	CF	C=O	C-C (sp <sup>3</sup> ) COR	C-C (sp <sup>2</sup> )

for the sample exposed to the SF<sub>6</sub>/O<sub>2</sub> plasma although fine structure was masked by the also increased components due to oxidised carbon. Nevertheless the CF<sub>3</sub> peak at 292.5 eV was again particularly pronounced, indicating much greater levels of fluorine functionality in this sample. When comparison is made between the spectra in (c) and (d) similar amounts of CF and CF<sub>3</sub> functionality are observed, however the CF<sub>2</sub> component appears to be limited in the sample exposed to the gaseous oxygen mixture, perhaps suggesting hindrance of the formation of this moiety when O<sub>2</sub> is used as a dopant.

To attempt to understand the observed behaviour, and to elucidate the root cause of the enhanced fluorination when oxygen containing species are added to SF<sub>6</sub> plasma, the various reaction pathways in the plasma that would produce atomic F were investigated.

If plasma is ignited within pure SF<sub>6</sub> and assuming no outside influences, the only possible mechanism to produce atomic fluorine is through the stepwise breakdown of the parent molecule into smaller fragments. This is depicted in figure 6.5 as the left-hand pathway. In the figure each value given is the total change in enthalpy from the reaction that would describe a transformation between two given species (in kJmol<sup>-1</sup>). At each step, with the SF<sub>6</sub> molecule dissociating into successively smaller species, a single fluorine atom is liberated. Herron originally published the enthalpies given in the figure, where they were also defined as the strength of the SF<sub>x</sub>-F bond, where x = 0, 1, 2 ... 5.<sup>193</sup> After its initial formation from SF<sub>6</sub>, and in the absence of other species, an SF<sub>5</sub> molecule has two possible reaction pathways; the recombination with a fluorine atom to produce SF<sub>6</sub>, or the dissociation to SF<sub>4</sub> with the subsequent liberation of a further fluorine atom. From the enthalpies given it can be seen that it is energetically more favourable for the latter process to occur, as it requires less energy to be expended. This does not mean that the former process will not occur however; merely that the probability of recombination to SF<sub>6</sub> would be less than the dissociation to SF<sub>4</sub>. This analysis can be continued for the entire left hand side describing the continued dissociation of SF<sub>6</sub>. Importantly, the recombination of F and SF<sub>4</sub> to produce SF<sub>5</sub> is more favourable than breakdown into SF<sub>3</sub>, and similarly for SF<sub>2</sub>, suggesting that at these smaller fragments further decomposition becomes less likely.

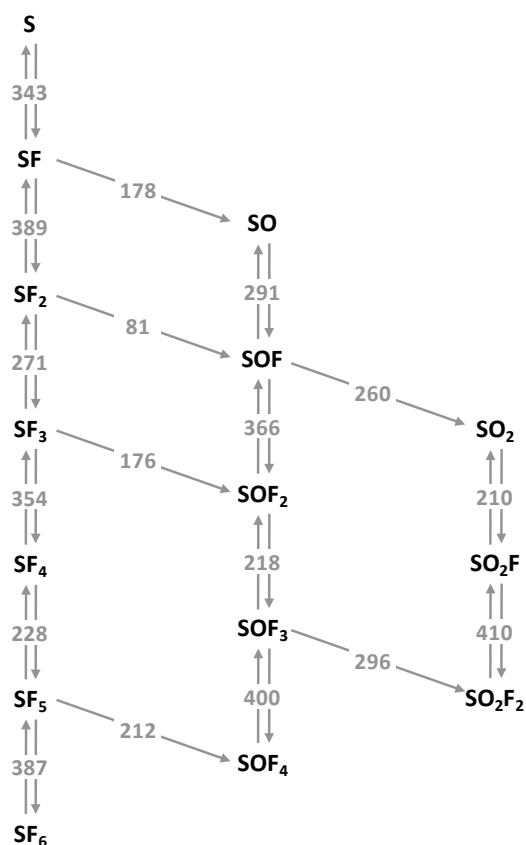


**Figure 6.5. Possible breakdown pathways for plasma in mixtures of SF<sub>6</sub> and O<sub>2</sub>. Values given are the enthalpies for the processes in kJmol<sup>-1</sup>. Modified from Ryan and Plumb.<sup>187</sup>**

Studying the reaction products in plasma generated from mixtures of SF<sub>6</sub> and O<sub>2</sub> with the intent to further understand the reactants responsible for etching of SiO<sub>2</sub> in these environments, Ryan and Plumb described further breakdown reactions present when oxygen is added to the system.<sup>187</sup> These are given as the middle and right-hand side pathways in figure 6.5 for the SOF<sub>x</sub> and SO<sub>2</sub>F<sub>x</sub> series respectively. Previously, it was found that it was most favourable for the SF<sub>5</sub> molecule to dissociate to SF<sub>4</sub>. Upon the addition of oxygen into the reaction however, a third mechanism becomes available whereby an oxygen atom can displace a fluorine atom. From the enthalpies given, it can be seen that this then becomes the energetically most favourable of the three available reaction pathways. A similar observation can be made for SF<sub>3</sub>, where the energy required to create the species SOF<sub>2</sub> is less than that required to break the SF<sub>2</sub>-F bond and form SF<sub>2</sub>. With these extra pathways available when oxygen is present, more atomic fluorine can be liberated than from the SF<sub>6</sub> molecule alone. Ultimately, this can result in two other final products being created; SO and SO<sub>2</sub>, with each product requiring less total energy than the complete decomposition into atomic sulphur from SF<sub>6</sub>.

The addition of oxygen into SF<sub>6</sub> plasma more than doubles the number of possible breakdown products, with each possible reaction mechanism resulting in the production of atomic fluorine. With so many more pathways available it could be speculated that the concentration of atomic fluorine, the species most expected to be responsible for the functionalisation of the CNTs, would be greatly increased, thus giving rise to the observed enhancement of fluorine at the surface. Ryan noted that this concentration in fact peaked with certain levels of oxygen content, suggesting that the process could in fact be controllable, and that a study of the reaction kinetics with varying oxygen content would be a worthwhile endeavour.

### 6.2.3. The Influence of rf Power on the Plasma Fluorination of CNTs

The main objective for this work is to study the effect of increasing the rf power on the fluorination of CNTs in SF<sub>6</sub> plasma using high resolution synchrotron radiation XPS. As such, a series of samples were created and exposed to plasma of systematically increasing power. The level of functionality was characterised from survey spectra using synchrotron radiation at 1486.6 eV, and from high resolution narrow scans obtained with a photon energy of 771 eV. It was found however that the identification of the relationship between rf power and fluorine content was marred by an unforeseen property of the surfaces, influencing the ultimate level of functionalisation. Also, due to constraints related to the allocated beamtime, not all samples were able to be studied and thus some gaps in the data were present.

Figure 6.6 gives the atomic percentages of the detected surface constituents; (a) iron, (b) oxygen, (c) fluorine and (d) carbon, determined through quantification of survey spectra. The measured iron content from the catalyst was consistent throughout the samples, with minimal deviation ( $\pm 0.1$ ) from an average of 1.4% of the total surface species. The oxygen content was found to be relatively constant across all measured samples with an average of  $9.3 \pm 1.1\%$ , although a greater level of deviation was notable.

Quantification of the fluorine content is shown in figure 6.6(c). The amount of total fluorine was seen to rise somewhat linearly with increasing absorbed power, indicating greater levels of functionality as a result of more intense plasma environments. As a result the measured carbon percentage was seen to decrease slightly over the course of the experiment, evidenced by the plot in (d). Intuitively this would be expected since the

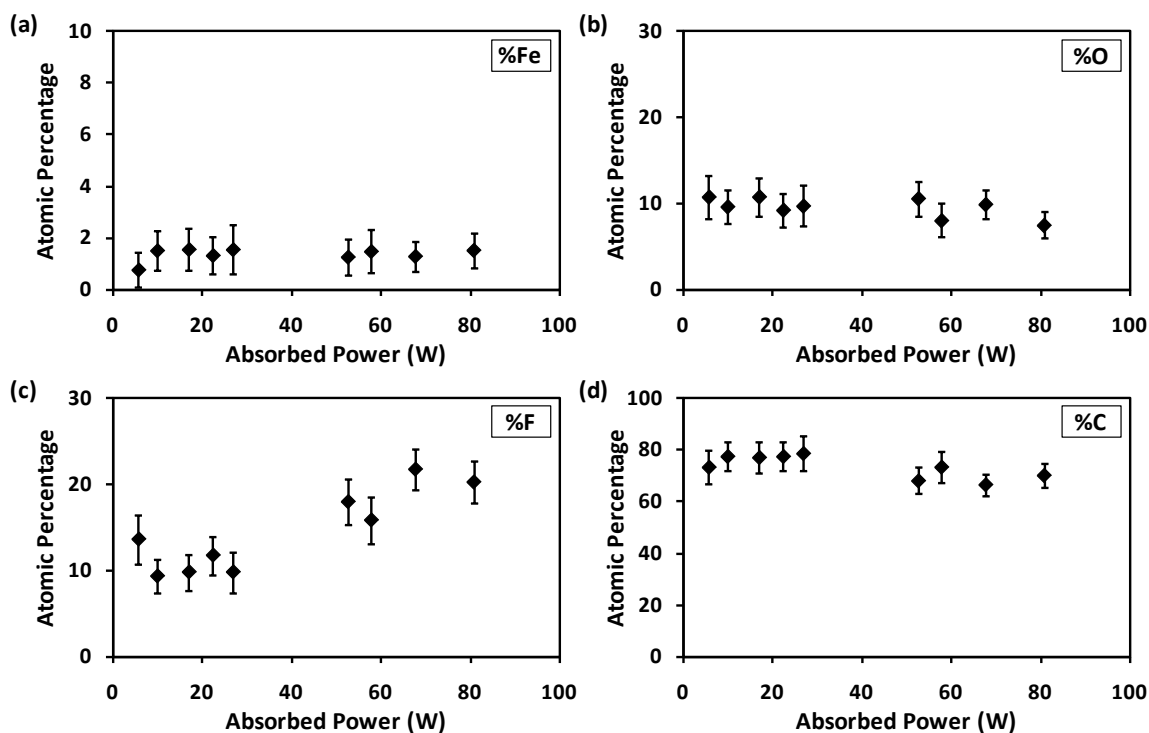


**Figure 6.6. Total atomic percentages of (a) iron, (b) oxygen, (c) fluorine and (d) carbon in samples exposed to SF<sub>6</sub> plasma of increasing absorbed rf power.**

percentage values were determined from the total peak area in the spectra. As the F1s area is increased, the total C1s area must decrease, assuming that all other peaks remain near to constant in intensity. The change in carbon percentage however was not observed to be equal in magnitude to the change in fluorine content.

The plot of the fluorine content with absorbed power was observed to display significant scatter between each of the points. Aside from an observed initial decrease in fluorine content overall an increasing trend was clear. The application of a linear fit to this data returns with a determination coefficient of  $\sim 0.9$ , suggesting the goodness of the fit could be improved upon. This could therefore lead to the conclusion that either a linear fit is not appropriate to describe the relationship between absorbed rf power and the resultant fluorine content, or that there was a significant amount of variability in the data.

Upon analysis of the high resolution O1s and F1s spectra from the studied samples, the source of this variability was potentially illuminated. The spectra are given in figure 6.7(a) and (b) and have been background-subtracted such that the low binding energy background signal was set to essentially zero. No other data manipulation was performed. Examination of the O1s spectra immediately revealed two crucial details; there were multiple chemical states of oxygen, and the relative presence of each of these states was not constant across

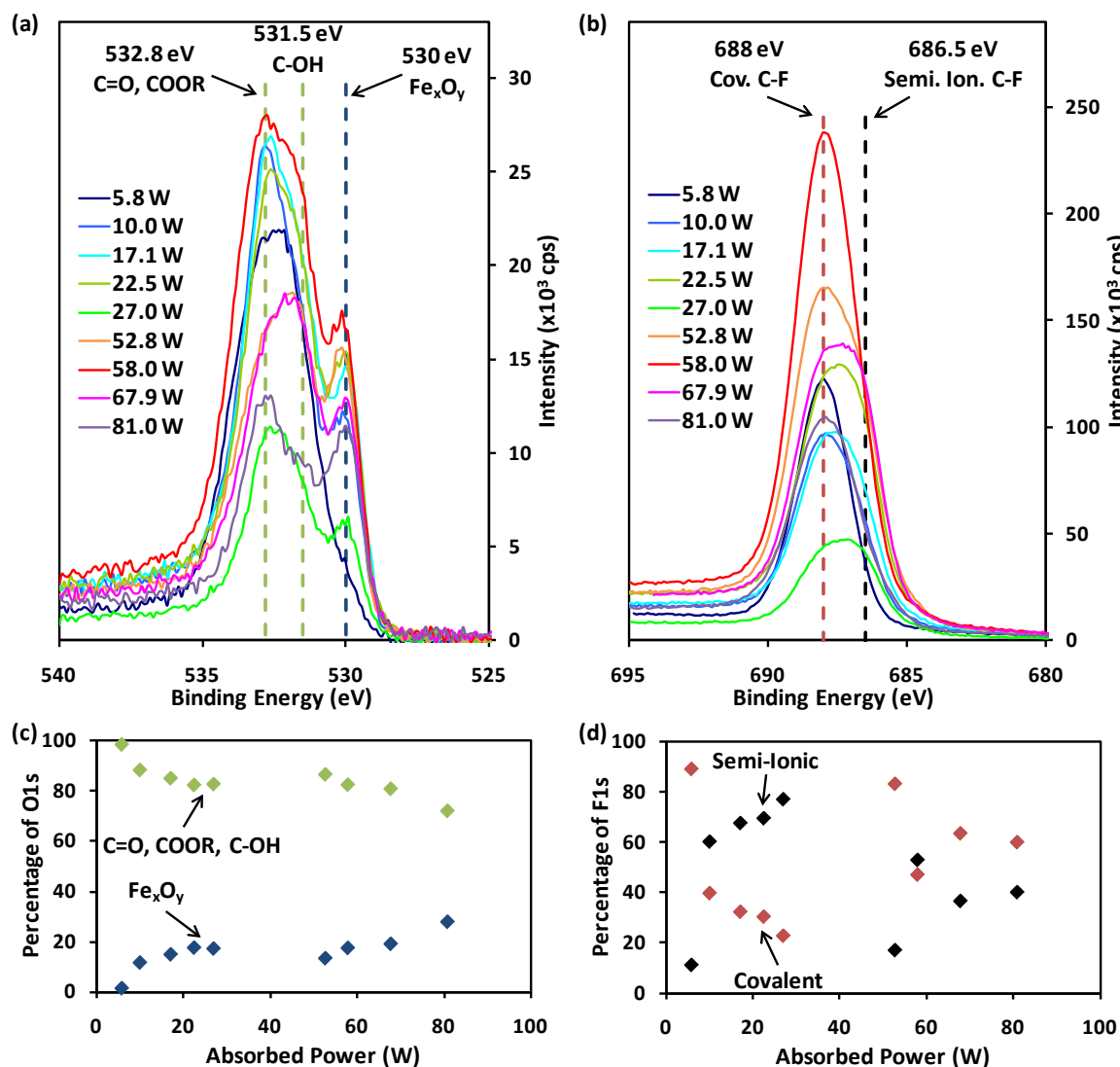


**Figure 6.7.** High resolution spectra from the (a) O1s and (b) F1s region with quantification of component percentages in (c) and (d) for O1s and F1s respectively.

the samples. A cursory study of the data would suggest that there were three distinct chemical states present in the O1s peaks observed. Considering what was known about the samples three dashed lines were overlaid onto the data for components that would be present from oxidised iron at 530 eV ( $\text{Fe}_2\text{O}_3$  and  $\text{Fe}_3\text{O}_4$ , denoted  $\text{Fe}_x\text{O}_y$ ) given by the blue line, and forms of oxidised carbon at 531.5 eV (C-OH) and 532.8 eV (C=O and COOR) given by the green lines. The agreement between the positions of these species and the data presented was particularly striking, especially for the iron oxide component. What is most important is that the relative amount of these states was not consistent between each sample. At a glance this is evident in the spectra. For example the 5.8 W sample (dark blue trace) shows little to no iron oxide presence but a strong C=O and COOR signal. This is in stark contrast with the sample exposed to the 81.0 W plasma (purple trace) showing nearly

equal amounts of the iron oxide and carbonaceous oxide. These differences continue throughout the set to various extremes.

It is worthwhile to stress that the component at 530 eV is not from fluorine attachment to oxygen species. Considering that the low-power plasma, and presumably then the ‘weakest’ exposure, did not present with a significant feature at 530 eV, and the high-power plasma presented with a strong feature around this energy, this thought could reasonably occur. However, components of the O1s peak from fluorine-oxygen bonded species are generally found at energies above 532 eV, discrediting it as a possibility.<sup>181</sup>

Similar inconsistencies were observable in the F1s spectra, shown in figure 6.7(b). Across the sample set the F1s peak was seen to display varied widths, suggesting the intermittent presence of multiple states. The covalent C-F bond is usually accepted to be at 688 eV. A second type of C-F bonding has also been observed in the fluorination of CNTs, known as semi-ionic bonding, and is found at 686.5 eV. This bond is essentially covalent in nature, but has a longer bond length resulting in weaker bond strength and thus presents at a binding energy 1 – 2 eV lower than the covalent bond.<sup>166</sup> Two dashed lines are overlaid onto the data marking these positions; the red line for the covalent C-F bond at 688 eV and the black line for the semi-ionic C-F bond at 686.5 eV. Similar to what was observed for the O1s region there is compelling agreement between the positions of these two bond types (semi-ionic and covalent C-F) and the shape of the peaks in the data, indicating the high likelihood that these states were present in the samples and that again the relative amount of these states was inconsistent. Taking the two extreme cases of low and high power (dark blue and purple traces respectively) it is seen that for the low power case, the F1s peak seemed almost purely covalent with only a minimal shoulder on the low binding energy side of the F1s peak. For the high power end of the data set however, the peak shape shows a considerable presence of the component associated with semi-ionic bound species.

Taking the prescribed chemical states within the O1s and F1s regions (and fitting the data accordingly) allowed the relative amount of each species to be quantified. Presented in figures 6.7(c) and (d) are the relative amounts of carbonaceous and iron oxides from in (c) and semi-ionic and covalent C-F bonds in (d), where the ordinate is the percentage of the total peak area that was attributed to each of the species.

The O1s region was fitted with three peaks, one of which was from metallic oxides (specifically iron oxides), and the remaining two from oxidised forms of carbon. If it were assumed that the oxidised carbon is predominantly present on the nanotubes and the iron oxide is from the catalyst particles (either internal or external to the CNT) then the components can be split into two groups; namely organic and inorganic oxides. In the spectra in (a) these are the green and blue dashed lines respectively. The plot in (c) gives the relative amounts of these oxides, again where the green trend relates to the organic oxides and the blue trace to the inorganic oxides. The significant variability of the two types of oxides in the samples is immediately apparent. Given the inter-dependency of the calculated percentages there is no surprise that one oxide increased in dominance while the other declined. However, this variability also appeared to affect the fluorination.

The plot in (d) gives the relative amounts of covalent and semi-ionic C-F bonding in the samples. The colour of the data points are again matched to the dashed lines in the F1s spectra where red is covalent and black is semi-ionic C-F bonding. The dominant C-F bonding type appeared to be extremely variable within this data, but once again the dependency between each species makes meaningful conclusions difficult to reach. However, a remarkable similarity becomes apparent when the plots in (c) and (d) are compared. It would appear that, with the exception of the point ~60 W, the trend defining the relative amount of organic oxide in (c) matched closely with that defining the level of covalent C-F bonding in (d). That is, as the level of organic oxides in the sample decreased, so too did the relative covalency of the F1s peak, and the semi-ionic component increased in dominance. The same observation could be made for the inorganic oxide trend, where the iron oxide content increased the semi-ionic nature of the C-F bonds.

It must be noted that all of the spectra presented here from fluorinated CNTs have been obtained after the exposure, with no analysis prior to the functionalisation. It seems clear that the fluorination mechanism has some level of dependence on surface oxygen species that is present in the samples. Given that in Section 6.2.2 it was shown that oxygen added to the SF<sub>6</sub> plasma could have a marked impact on the fluorination mechanism this may not come as a surprise. However, it is unclear from this work as to whether oxygen at the *surface* could also impact the fluorination and since no analysis was performed prior to the exposure, comparison with O1s percentages after fluorination may not be indicative of such a mechanism. Thus, after this work a question remained; does surface oxygen content

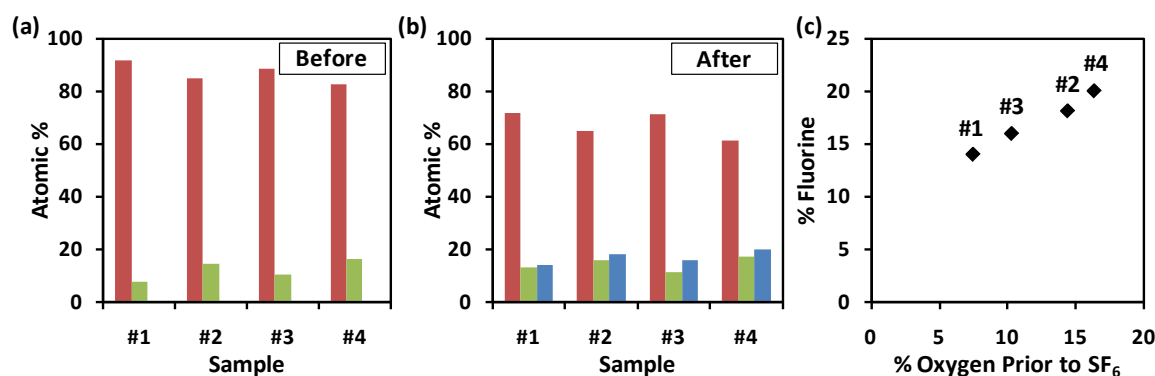


**Figure 6.8.** Quantification of four HiPCO CNT samples (a) before and (b) after exposure to an SF<sub>6</sub> plasma where red = carbon, green = oxygen and blue = fluorine percentages. The total fluorine percentage after exposure is plotted in (c) against the oxygen content beforehand.

prior to exposure to SF<sub>6</sub> plasma influence the fluorination process, and could this cause the undesired effects observed in the resultant quantification? To answer part of this question, during a period where the LHS system was partially operational, a supplementary experiment was performed at Flinders after the synchrotron experiments had concluded.

Four surfaces of HiPCO CNTs were created in an identical fashion to those used in the synchrotron work. In contrast to the aforementioned work however, the surfaces were characterised using XPS before and after exposure to SF<sub>6</sub> plasma simultaneously, with results given in figure 6.8. Relative percentages of carbon (red) and oxygen (green) for each of the four samples before exposure are given in (a) and as anticipated the oxygen levels at the surface were found to be far from constant. After exposure to SF<sub>6</sub> plasma in one batch (2.5 mTorr, 10 W, 60 seconds) the samples were again characterised, with the results presented in (b). As previously, percentages of carbon and oxygen are represented by the red and green columns respectively, while fluorine is now presented as the blue columns. Despite being exposed to an identical plasma environment at the same time the resultant level of fluorination was seen to vary considerably throughout the set, with the extrema separated by as much as 6%. When the total fluorine percentage is plotted against the oxygen content prior to fluorination exposure as is presented in (c), it becomes immediately clear that as the amount of surface oxygen increased, so too did the amount of fluorine that attached after exposure, indicating a direct link between the two. This effect warranted further investigation since multiple questions arose from the research. Foremost, if oxygen has such a significant impact on the fluorination mechanism, this effect could potentially be another level of control over not only the *amount* of fluorine that attaches to CNTs, but also the *type* of C-F bonding that occurs upon fluorination.

### 6.3. Summary of Synchrotron Studies I

To gain a deeper level of insight into the bonding mechanism responsible for the fluorination of CNTs, research was undertaken utilising the very high brilliance and energy resolution of the soft X-ray beamline at the Australian Synchrotron. Some key results were obtained as a result of this research.

It was previously concluded that fluorination from SF<sub>6</sub> plasma exposure occurred without contamination by sulphur, as evidenced by the lack of any significant peak in XPS spectra pertaining to sulphur. Using the continuously tuneable nature of the photon energies available at the synchrotron, this conclusion was further clarified; sulphur *is* present in samples after fluorination, albeit in very small concentrations well below the detection limits of a traditional lab-based XPS.

It was found during this study that the addition of oxygen containing species, such as O<sub>2</sub> and H<sub>2</sub>O, into the SF<sub>6</sub> plasma greatly enhanced the extent of fluorination of the CNT surfaces. In the case of O<sub>2</sub> this occurs with a likewise increase in the oxygen functionality, effectively oxidising and fluorinating the CNTs simultaneously. When water vapour is used however the fluorine content is greatly increase while the oxygen content remains relatively unaffected. Each of these processes was found to also increase the relative amounts of higher order C-F<sub>x</sub> functionality, such as CF<sub>2</sub> and CF<sub>3</sub> groups. This effect is a result of the enhanced breakdown of the parent SF<sub>6</sub> molecule in the presence of oxygen through further reaction pathways leading to SO<sub>x</sub>F<sub>y</sub> species. This mechanism was also observed to have an effect at the surface. The oxygen content of the surfaces prior to exposure directly influences the level of fluorination that would result, with greater oxygen content resulting in greater fluorination.



---

## **Chapter 7.**

# **SYNCHROTRON STUDIES OF FLUORINATED NANOTUBES II - FI2751: ROUND 2 2010**

### **7.1. Introduction**

The previous synchrotron work answered some key questions regarding the fluorination of SWCNTs in SF<sub>6</sub> plasma. One of great significance was the determination that sulphur was in fact present after an exposure, albeit in sufficiently small amounts as to remain essentially undetectable on a lab-based XPS instrument. This emphasised the value of very high resolution XPS measurements, and the great advantage of the continuously tunable synchrotron source. The work also identified some new research questions. Specifically, could the fluorination mechanism be controlled by the presence of oxygen both in terms of the total fluorine content and the type of bonding that would result?

#### **7.1.1. FI2751: Investigating the Effect of Oxygen on Fluorination**

Leading from the research performed during SXR187, the aim of this research was to solely investigate the effect that oxygen plays in the fluorination mechanism. This was to be investigated in two ways. The first would involve the doping of SF<sub>6</sub> plasma with gaseous oxygen. Despite the observed advantages of water vapour over oxygen, the latter

was to be used as experimentally it was far more controllable. That is, maintaining a constant pressure of O<sub>2</sub> in the plasma chamber was much easier than maintaining a constant pressure of H<sub>2</sub>O vapour. The second method was to modify the surfaces with oxidising treatments before an exposure to pure SF<sub>6</sub> plasma. Two research aims were to be addressed from this research;

- To determine the effect of changing the level of oxygen doping on the fluorination mechanism in a mixed SF<sub>6</sub>/O<sub>2</sub> plasma environment, and
- To determine the method that produces better fluorine attachment; a mixed gas SF<sub>6</sub>/O<sub>2</sub> plasma treatment or a two-step O<sub>2</sub> then SF<sub>6</sub> treatment?

The samples would be characterised using synchrotron radiation photoemission to elucidate changes in the 1s spectra of carbon, oxygen and fluorine. Analysis would elucidate changes in the total fluorine content on each of the surfaces, as well as detailed chemical shifts within each of the 1s shell spectra to further understand the bonding involved.

### 7.1.2. Experimental Design

Samples in the previous round of synchrotron experiments were raw HiPCO type, with residual catalyst particles contributing undesirable iron signal in the photoelectron spectra. This was also found to contribute a source of variability to the surface oxygen content, which in turn influenced the extent of functionalisation after a given plasma treatment. The surfaces were created on steel pucks with a thickness of ~1 mm. While performing alignment between the sample and the X-ray beam this thickness would introduce a systematic error. This was caused by the sampling area of the electron energy analyser on the surface and the position of the X-ray beam being potentially misaligned. The size of the substrates upon which samples were deposited (~1 cm diameter pucks) was also significantly larger than necessary given the size of the beam (0.15 × 0.015 mm<sup>2</sup>). Ultimately this lack of knowledge regarding the sample requirements reduced productivity, as it limited the number of samples that could be mounted for analysis on the sample stage.

In the second (2010) synchrotron beamtime allocation, all of these issues were addressed and alleviated. Purified arc discharge type CNTs (P2, low functionality) were deposited onto tantalum foil (using the same deposition technique previously described). Using purified CNTs removed any catalyst presence from the sample (and resulting spectra), while deposition onto thin tantalum foil allowed for accurate alignment of the sample,

X-ray beam and analyser. While the change in CNT type meant that direct comparison between the sample sets would be complicated by the different nature of the nanotubes, the effect under study was that of changing oxygen content and thus the aims could be better addressed. Sample size was also reduced considerably to increase the number of samples that could be mounted at any one time, thereby minimising pumping times and increasing throughput.

Three CNT sample sets were prepared for three parallel studies. Two sets would investigate the addition of gaseous O<sub>2</sub> to SF<sub>6</sub> plasma. The first set held the SF<sub>6</sub> partial pressure constant while the O<sub>2</sub> partial pressure was increased in regular controlled steps. Overall this meant a likewise increase in the total gas pressure. Experimentally this had the effect of also shrinking the plasma density around the antenna, a result of the reduced mean-free-path of electrons and atomic species at increased pressures. Table 7.1(a) details the partial pressures used in this experiment and their relative percentages. The second set followed a similar line of investigation, however in contrast to the previous samples this set would hold the *total* pressure constant. This meant that both the SF<sub>6</sub> and O<sub>2</sub> partial pressures were varied simultaneously from 0 – 10 mTorr (and thus 10 – 0 mTorr for the other constituent). Table 7.1(b) details this sample set. This experiment allowed the characterisation of the effect of going from pure SF<sub>6</sub> to pure O<sub>2</sub> plasma without a significant change in the plasma density as would be observed for the previous set. These two experiments also provided other in-built comparisons. Since two samples would be exposed to pure SF<sub>6</sub> plasma at 2.5 and 10 mTorr, an examination of pressure effects could be performed. Similarly, a mixing ratio of 1:1 was provided by two samples with total pressure of 5 and 10 mTorr, again allowing comparison. Also, two samples would be exposed to supposedly identical conditions, allowing an analysis of the reproducibility.

The third set of samples was designed to investigate the effect of surface pretreatments prior to exposure. One surface was exposed to 5 mTorr O<sub>2</sub> plasma at 10 W thus oxidising the CNTs. Two other surfaces were created from P2 CNTs that underwent two unique chemical oxidation treatments. The first treatment, dubbed the ‘oxidation’ treatment, exposed the CNTs to a 3 M nitric acid solution and refluxed overnight. The second treatment was based on that published by Smalley’s group and involved sonication of the P2 CNT material in a mixture of 98% sulphuric and 70% nitric acid in a ratio of 3:1 (v/v) at 0°C for a period of 8 hours.<sup>194</sup> The nitric acid treatment was expected to result in the

**Table 7.1. Partial and total pressures for the SF<sub>6</sub> and O<sub>2</sub> mixture experiments where in (a) the SF<sub>6</sub> partial pressure is held constant and (b) the total pressure is held constant. Relative percentages of each constituent are also given.**

(a)	P <sub>SF<sub>6</sub>=C</sub> Mixtures	Partial Pressures (mTorr)		Total (mTorr)	%SF <sub>6</sub>	%O <sub>2</sub>
		SF <sub>6</sub>	O <sub>2</sub>			
	<b>2.5:0</b>	2.5	0	2.5	100	0
	<b>2.5:1</b>	2.5	1	3.5	71.4	28.6
	<b>1:1</b>	2.5	2.5	5	50	50
	<b>1:2</b>	2.5	5	7.5	33.3	66.7
	<b>1:3</b>	2.5	7.5	10	25	75

(b)	P <sub>tot=C</sub> Mixtures	Partial Pressures (mTorr)		Total (mTorr)	%SF <sub>6</sub>	%O <sub>2</sub>
		SF <sub>6</sub>	O <sub>2</sub>			
	<b>10:0</b>	10	0	10	100	0
	<b>3:1</b>	7.5	2.5	10	75	25
	<b>1:1</b>	5	5	10	50	50
	<b>1:3</b>	2.5	7.5	10	25	75
	<b>0:10</b>	0	10	10	0	100

addition of carboxylic acid groups to the CNTs but no extensive shortening of the structures, while the mixed nitric/sulphuric treatment would cut, as well as heavily oxidise the nanotubes. The latter was dubbed a ‘cutting’ treatment. These samples provided a direct comparison between wet-chemical and plasma based oxidation methods.

The previous work saw the analysis of samples using multiple excitation energies to provide both a comparison between lab-based and synchrotron excitation, and also enhance the surface sensitivity and as well as the ionisation cross-section of the carbon, oxygen and fluorine. This significantly decreased sample throughput. In this work, wide spectra would be obtained using only an excitation of 760 eV. Narrow scans were also performed for the C1s, O1s and F1s regions at this energy.

## 7.2. Quantification of PES Results at Varying Excitation Energy

The varied sensitivity of elements to energetic photons is well known and as such databases of relative sensitivity factors exist for each of the core shells of the elements. The most common X-ray sources have energies of 1253.6 and 1486.6 eV and thus factors are either calculated theoretically or determined experimentally almost exclusively for these excitations.<sup>146,195,196</sup> Using any other photon energy would mean that consequently the documented sensitivity factors cannot be correctly applied. Since in this work wide-scan spectra were obtained using 760 eV photons, and that this data was to be used for quantification of total atomic percentages, determination of a new set of relative sensitivity factors was needed.

### 7.2.1. Calculation of Sensitivity Factors

The photoelectron intensity per photon of energy  $h\nu$  is given by

$$I_{AX_i}^{\infty}(h\nu) = n_{AX_i} \sigma_{AX_i}(h\nu) \sec \alpha N_A Q_A(E_{AX_i}) \lambda_A(E_{AX_i}) \quad (7-1)$$

for a homogeneous system where  $n_{AX_i}$  is the electron population in subshell  $i$  of core level  $X$  of element  $A$ ,  $\sigma_{AX_i}(h\nu)$  is the ionisation cross-section of that shell for photons of energy  $h\nu$ ,  $\alpha$  is the incidence angle of the photon beam relative to the surface normal,  $N_A$  is the atomic density of the element  $A$ ,  $Q_A(E_{AX_i})$  is the overall intensity reduction of electrons of energy  $E_{AX_i}$  due to inelastic scattering and  $\lambda_A(E_{AX_i})$  is the IMFP for those electrons.<sup>180</sup> This equation can be simplified by relating the intensity to the atomic density multiplied by some factor  $S_{AX_i}$  such that

$$I_{AX_i}^{\infty}(h\nu) = N_A S_{AX_i}$$

where

$$S_{AX_i} = n_{AX_i} \sigma_{AX_i}(h\nu) \sec \alpha Q_A(E_{AX_i}) \lambda_A(E_{AX_i}). \quad (7-2)$$

Since most experiments are performed at a fixed geometry  $\alpha$  becomes constant. Sensitivity factors are also generally presented relative to a particular element where that factor is set to unity (commonly the fluorine 1s shell). Thus the factor  $\sec \alpha$  can be dropped and

$$S_{AX_i} = n_{AX_i} \sigma_{AX_i}(h\nu) Q_A(E_{AX_i}) \lambda_A(E_{AX_i}). \quad (7-3)$$

This defines the atomic sensitivity factor (ASF) for subshell  $i$  of core level  $X$  from element  $A$  when irradiated by a photon of energy  $h\nu$ . The calculations regarding each of the terms in (7-3) are given in greater detail in Appendix C, including the sources from of the values, and as such only the results are reproduced here.

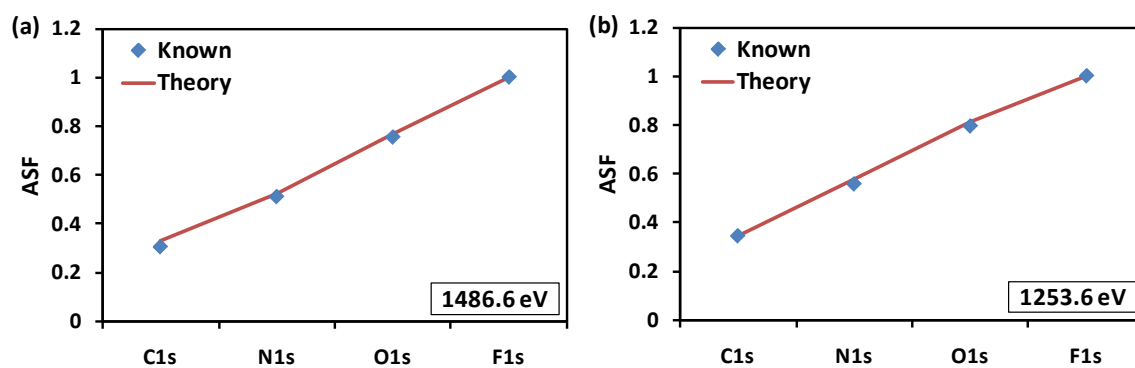


Figure 7.1. Comparison between known ASF values (blue diamonds) and those calculated here (red lines) for (a) Al  $K\alpha$  and (b) Mg  $K\alpha$  X-ray sources. Known values taken from work based on Seah.<sup>237</sup>

Table 7.2. Calculated Atomic Sensitivity Factors (ASFs) for the 1s shells of C, N, O and F irradiated by photons of energy 1486.6 eV, 1253.6 eV and 760 eV.

	$h\nu = 1486.6 \text{ eV}$		$h\nu = 1253.6 \text{ eV}$		$h\nu = 760 \text{ eV}$
	Theory	Known	Theory	Known	Theory
<b>C1s</b>	0.328	0.306	0.345	0.347	0.636
<b>N1s</b>	0.525	0.511	0.581	0.559	0.888
<b>O1s</b>	0.767	0.755	0.813	0.795	1.014
<b>F1s</b>	1.000	1.000	1.000	1.000	1.000

Prior to the calculation of the sensitivity factors for 760 eV photons, values were first calculated for the common excitation sources of Mg  $K\alpha$  and Al  $K\alpha$  to enable the direct comparison with known databases. Figure 7.1(a) and (b) makes this comparison for 1486.6 and 1253.6 eV photons respectively where the known values are given as the blue diamonds and the values calculated from the theory presented here are given by the red lines. The figure shows excellent agreement between the known and calculated ASF values which demonstrates the correct application of the theory.

With knowledge that the calculations could be appropriately performed, adjustments were then made to accommodate 760 eV photons. The change in excitation energy affects the total ionisation cross-section and IMFP terms in equation (7-3). Table 7.2 gives the ASFs that resulted from the calculations, and are presented relative to the F1s shell which was set to unity as is common among databases of these values.<sup>146,195</sup> With an appropriate set of sensitivity factors tailored for use at 760 eV the quantification of photoelectron spectra taken at this energy could now be correctly performed.

### 7.3. Fluorination in the Presence of Oxygen

#### 7.3.1. The Systematic Doping of SF<sub>6</sub> Plasma with O<sub>2</sub>

The first experiment considered was that of constant SF<sub>6</sub> partial pressure. Intuitively it was expected that for each treatment the samples would be exposed to a plasma environment containing a similar number of SF<sub>6</sub> molecules, regardless of oxygen content, because of the way in which the pressures were monitored and controlled. A variation in the amount of oxygen in the system should only affect the extent of the breakdown of the parent SF<sub>6</sub> molecule, and thus the amount of atomic fluorine that is liberated, and not the total amount of SF<sub>6</sub>.

Atomic percentages determined from 760 eV wide scan spectra are given in figure 7.2. Each plot is presented with primary and secondary abscissae showing the relative percentages of sulphur hexafluoride (primary) and oxygen (secondary) in the gas mixture. As previously, the CNTs were deposited from a DMF solution and thus contained a small amount of residual solvent. The relative percentage of nitrogen from the N1s peak attributed to this contamination is given in (a) and is seen to be quite consistent throughout the samples, showing only minor deviation from an average of 0.8% of the total peak area.

The oxygen content for the mixed plasma exposure is given in (b). As expected the oxygen content in the samples was observed to increase as the SF<sub>6</sub> plasma was doped with greater amounts of O<sub>2</sub>. The overall increase in relative O1s content was significantly lower than might have been expected, increasing from  $8.6 \pm 2.2\%$  to only  $14.3 \pm 2.7\%$ . It is understandable that the sample exposed to the plasma containing the greatest amount of O<sub>2</sub> would also have the highest O1s percentage. However this plasma consisted of 75% oxygen, an environment that was expected to significantly oxidise the CNT surfaces. Fortunately this could potentially be explained by what is already known about mixtures of SF<sub>6</sub> and O<sub>2</sub>; the oxygen aids in the breakdown of SF<sub>6</sub> into smaller, oxygen containing constituents. Perhaps then rather than greatly promoting the oxidation of the CNT structures, a majority of the O<sub>2</sub> was used to assist the formation of other gaseous species, such as SO<sub>2</sub>, that were pumped away rather than being re-ionised in the plasma or reacted with the CNT surface. If this proposed explanation is indeed correct then it should be expected that when exposed to pure O<sub>2</sub> plasma CNT surfaces should be greatly oxidised since SF<sub>6</sub> will not present to deplete the O<sub>2</sub>.

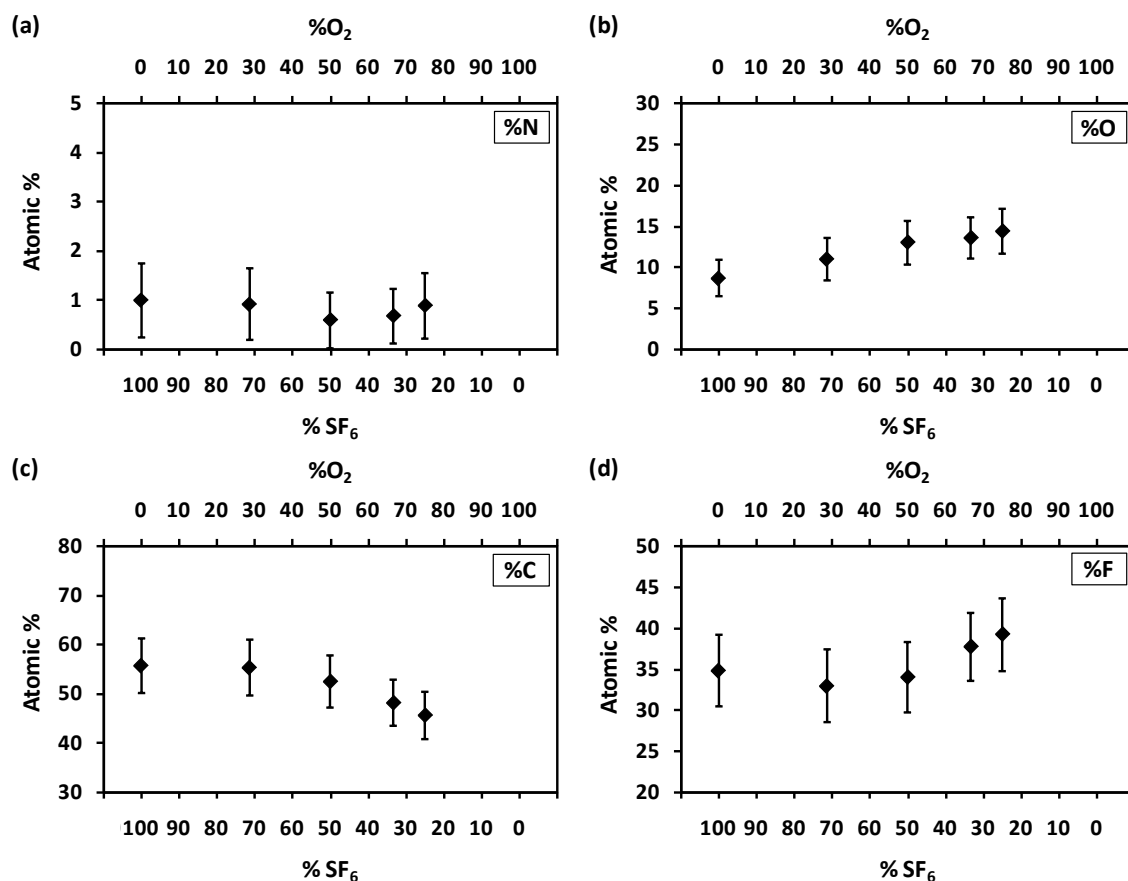


**Figure 7.2. Atomic percentage of (a) nitrogen, (b) oxygen, (c) carbon and (d) fluorine on the CNT surfaces for increasing oxygen content in the  $\text{SF}_6/\text{O}_2$  mixed plasma with the  $\text{SF}_6$  partial pressure held constant.**

Increasing oxygen content in the plasma caused an observable decrease in C1s peak area as seen in (c), an effect directly attributable to the increasing O1s peak area, as well as the increasing F1s peak area seen in (d). There is a noticeable decrease in fluorine percentage with the initial addition of oxygen, although within the error bars presented this may not be considered too significant. If it was a true decrease however, it could be attributed to a greater etching rate initiated by the addition of oxygen species. Nevertheless, after the initial addition, increased oxygen percentage in the plasma was observed to result in a likewise increase in fluorine attachment despite there being a constant  $\text{SF}_6$  partial pressure in the system. Therefore the addition of oxygen resulted in increased fluorine content at the surface. This further implies that oxygen aided in increasing the concentration of fluorine ions in the plasma that could then be reacted with the CNTs. Furthermore, increasing the amount of oxygen available acted to enhance this effect, a result of the mechanism producing a greater amount of reactive fluorine species.

The second series focused on maintaining a constant total pressure by varying the partial pressure of both the SF<sub>6</sub> and O<sub>2</sub> simultaneously. Figure 7.3 presents atomic percentages again determined from 760 eV wide spectra for the detected elements. Overall it would appear as though little observable change occurred across the samples until the ‘pure’ oxygen treatment, where the oxygen content was seen to spike, and conversely the fluorine content dropped to near zero. The small amount of fluorine presence (~3 %) despite no SF<sub>6</sub> being added to the plasma can be attributed to the sputtering of fluorine moieties attached to carbonaceous deposits on the chamber walls. This effect was also observed by Deslandes who found that treatment of HOPG with non-SF<sub>6</sub> plasma would result in fluorine contamination if SF<sub>6</sub> plasma had been ignited prior to the treatment.<sup>108</sup> There was also an apparent increase in nitrogen content at the surface for this sample. This effect may merely be an artefact of the atomic percentage calculation, but it is entirely possible that the plasma may have been contaminated with a small amount of nitrogen, or that an excess of solvent remained intercalated within this sample surface, producing the anomalous result observed.

The pure O<sub>2</sub> plasma resulted in a significant increase in oxygen content at the surface, attributed to the direct oxidation of the CNTs. This result would appear to affirm the theory proposed for the previous experiment whereby the oxygen in the plasma was utilised for the decomposition of SF<sub>6</sub> rather than for surface oxidation. It was proposed that if this were the case then for O<sub>2</sub> plasma in the absence of SF<sub>6</sub> the oxygen content should increase dramatically, which is the phenomenon observed here. Upon removal of SF<sub>6</sub> the oxygen species are no longer depleted and begin reacting strongly with the surface, ultimately producing the observed spike in oxygen content.

The determined carbon percentage was not seen to change significantly across the range of SF<sub>6</sub>:O<sub>2</sub> mixtures studied. This may be expected from this type of analysis, especially since the relative increase in O1s peak area is counteracted by the relative decrease in F1s area. From the F1s percentage area however a decreasing trend is perceivable as the relative amount of SF<sub>6</sub> in the plasma was reduced until ultimately the SF<sub>6</sub> was removed completely from the system and further attachment was hindered other than from sputtered chamber deposits. The lack of significant increase in fluorine content implies that the functionalisation process is not enhanced by the addition of oxygen to SF<sub>6</sub> in the way described. Perhaps then the improved breakdown of SF<sub>6</sub> is opposed by the simultaneous

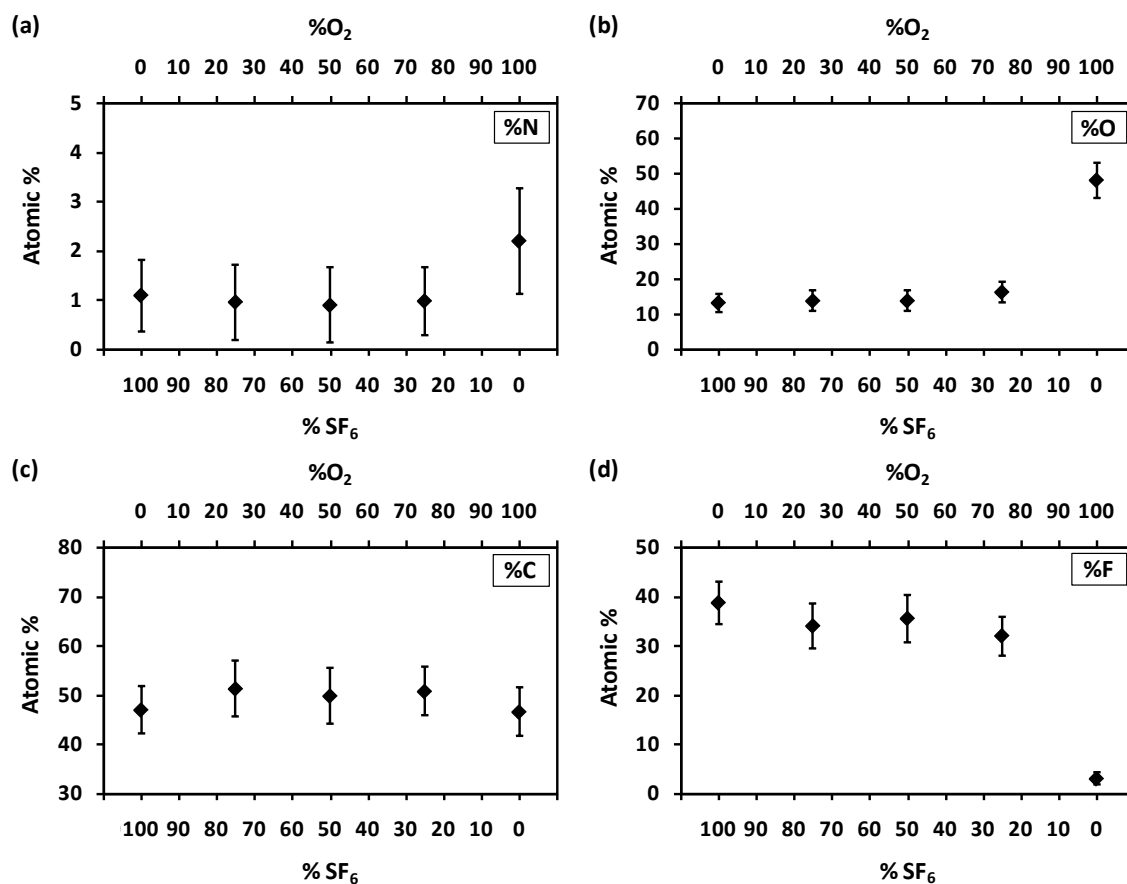


**Figure 7.3. Atomic percentage of (a) nitrogen, (b) oxygen, (c) carbon and (d) fluorine on the CNT surfaces for increasing oxygen content in the  $\text{SF}_6/\text{O}_2$  mixed plasma with the total pressure held constant.**

decrease in total  $\text{SF}_6$  molecules present in the source gas, thus leading to no net increase in reactive fluorine species. This would suggest that a greater level of control would come from maintaining a constant  $\text{SF}_6$  partial pressure, and adding to this gas controlled amounts of oxygen as was investigated in the previous experiment. However, changes in the chemical nature of the different bonding surface states has not yet been discussed, and is likely to be the most important factor in the study of these gas mixtures.

High resolution C1s, O1s and F1s spectra were obtained at a photon energy of 760 eV to elucidate detailed variations in the chemical nature of the surface species. These variations were then quantified against the peak area for that element, resulting in the relative percentages plotted in figure 7.4 for each of the key chemical species. Features of C1s peaks related to carbon-oxygen and carbon-fluorine bonds have already been shown to occupy similar binding energy positions in C1s peaks, resulting in strong convolution of the features. In this experiment, where the CNTs were exposed to plasma that resulted in the formation of both groups of functionalities, deconvolution of C1s peaks was found to

be difficult, resulting in some influence on the relative amount of fluorine functionality by oxygen functionality. This was particularly true for the CF and CF<sub>2</sub> groups, which were convoluted with COOR and C-CO features. Despite this, plots of the relative amounts of CF and CF<sub>2</sub> are given in figure 7.4(a) and (b) for the constant SF<sub>6</sub> and constant total pressure experiments respectively. Overall, from these plots it can be inferred that the CF functionality remained the most prevalent regardless of the SF<sub>6</sub>/O<sub>2</sub> ratio. In both experiments the samples exposed to plasma of highest oxygen content resulted in the greatest levels of CF compared to CF<sub>2</sub>. For the set of samples in (a) this correlated to a mixture of 2.5 and 7.5 mTorr of SF<sub>6</sub> and O<sub>2</sub>. By comparison, the equivalent sample in the constant pressure set in (b) was determined to have a different relative amount of the two species, despite being exposed to a similar plasma environment.

The O1s region was fitted with two components, as per the spectra in Chapter 6, for C-OH, C=O and COOR where the latter two species were combined into one fitted peak. Figures 7.4(c) and (d) show the evolution of these fitted peaks, and thus the species they represent, for the various mixtures of SF<sub>6</sub> and O<sub>2</sub>. For reference, the untreated P2 CNTs used in this study were found to have a 50:50 mix of C-O and C=O components, which is expected considering the purification process results in carboxylic functionality. The plots suggest that the addition of O<sub>2</sub> to the SF<sub>6</sub> has an impact on the type of oxygen species on the surface after the treatment, since the ratio of these components shifted to favour the singly bonded oxygen species. Furthermore, the *amount* of oxygen added influenced the type of oxygen species on the surface. Ultimately it would appear as though after a plasma treatment the majority of the oxygen species on the surface relate to C-OR moieties, such as hydroxyls. This is particularly evident in (d) where it is observed that as the ratio of O<sub>2</sub> to SF<sub>6</sub> is increased, the O1s components show an increased dominance of the C-OR functionality.

The F1s region was fitted with two peaks representing the semi-ionic and covalent C-F bond types. The relative percentages of the F1s region for these species are given in figure 7.4(e) and (f) in black and red respectively. With the SF<sub>6</sub> pressure held constant the ratio of the C-F bonding remained distinctly in favour of the semi-ionic type, regardless of the amount of oxygen added, with little change in the ratio across the sample set. In contrast, the sample set exposed to plasma with a controlled total pressure showed strong linear variation in the relative amounts of each C-F bonding type with oxygen content.

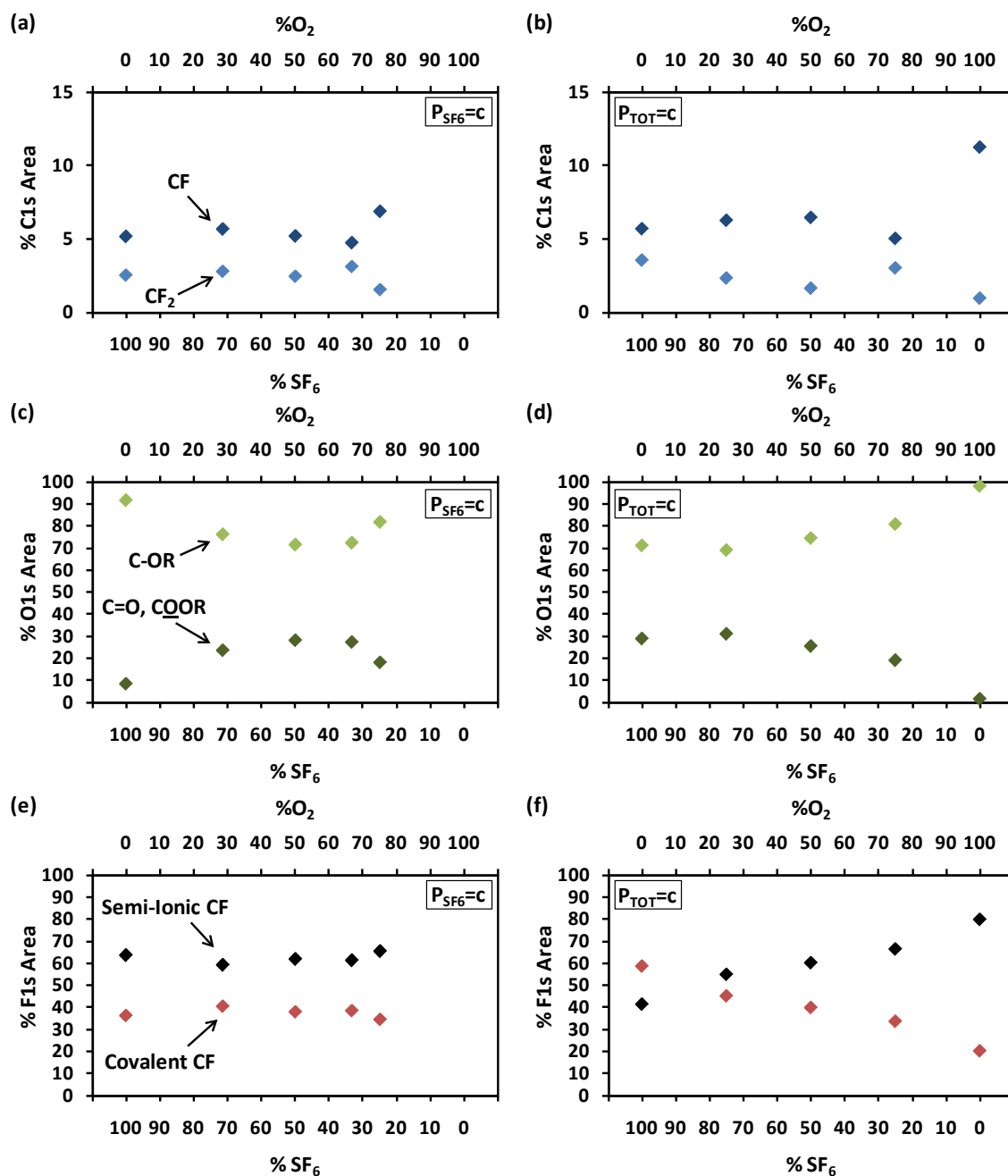


**Figure 7.4. Relative percentages of chemical species within the (a) and (b) C1s peaks, (c) and (d) the O1s peaks and (e) and (f) the F1s peaks.**

Importantly, the highest level of covalency,  $\sim 60\%$ , was found for the pure  $SF_6$  treatment. The addition of oxygen was found to be detrimental and promoted semi-ionic bonding preferentially. However, if pure  $SF_6$  gave the highest covalency in this experiment, then it should reasonably be expected to be same for the sample exposed to 100%  $SF_6$  in the experiment where its partial pressure was held constant. The difference between the two samples would appear to come from the nature of the exposure. While both samples were exposed to pure  $SF_6$  plasma, one was at a pressure of 2.5 mTorr with the other at 10 mTorr.

Thus the contrast between the two samples would come from the total amount of sulphur hexafluoride molecules present in the plasma environment. Upon the addition of oxygen in the constant total pressure experiment, the partial pressure of SF<sub>6</sub> was decreased simultaneously. Consequently the total number of sulphur hexafluoride molecules was reduced. With the constant SF<sub>6</sub> pressure experiment the number of sulphur hexafluoride molecules remained the same regardless of oxygen addition. From this it can be inferred that the number of fluorine species in the plasma has an impact on the covalency of the C-F bonds. In (e) the amount of SF<sub>6</sub> remained constant across the entire set, and the relative percentage of semi-ionic and covalent C-F bonds was also constant. In (f) the amount of SF<sub>6</sub> molecules decreased as oxygen was added (moving from left to right in the plot), and the percentage covalency decreased accordingly.

A similar observation has previously been made when comparing the functionalisation of CNTs in plasma generated within CF<sub>4</sub> and SF<sub>6</sub> environments.<sup>87</sup> Plank noted that F1s peaks from samples exposed to the CF<sub>4</sub> plasma required two peaks (at the semi-ionic and covalent positions) to achieve a suitable fit whereas when exposed to SF<sub>6</sub> plasma a single peak in the covalent position could be used. Using results from optical emission spectroscopy (OES) it was found that the atomic fluorine pressure was significantly greater for SF<sub>6</sub> plasma than CF<sub>4</sub> plasma and thus the conclusion was drawn that the increased number of fluorine species in the SF<sub>6</sub> case resulted in greater covalency.

The pure SF<sub>6</sub> exposure in the work by Plank resulted in largely covalent C-F bonding while in this work it resulted in both covalent and semi-ionic bonds. This could be explained by the strong experimental differences between the two pieces of work. The pressures used in the work by Plank were similar to that used here (~mTorr). However, the type of reactor was drastically different; a dc reactive ion etch (RIE) chamber in Plank's work versus an rf system here. RIE systems show strong directionality due to the high dc voltage, thus leading to significant ion bombardment. These systems also tend to have smaller plasma regions and thus higher densities at the sample surface compared to the 'diffusion' type plasma generated in the Flinders reactor. This could generate a greater fluorine concentration at the surface therefore giving the higher covalency observed. Here the sample is somewhat remote to the plasma density, meaning the concentration of fluorine species at the CNT surface could be significantly reduced, ultimately leading to the mixed semi-ionic and covalent C-F bonds.

### 7.3.2. Modification of the Surface Bound Oxygen Content

It would seem intuitive that adding oxygen into SF<sub>6</sub> would change the chemistry of the plasma leading to the formation of different molecular species and ultimately resulting in the enhanced breakdown of the parent molecule. Ryan and Plumb noted that the breakdown of sulphur hexafluoride could also be influenced by surface bound species. In their work this was used to explain how ions within the plasma could be lost to the chamber walls.<sup>186-188</sup> It has already been shown in the previous chapter that the amount of oxygen on the CNT surface prior to fluorination had some level of impact on the resultant functionalisation. Although that was a passive study, investigating the natural fluctuation of the oxygen content and its influence, it illuminated a possible avenue of research; to investigate how the fluorination mechanism would be affected if the surface oxygen content were to be *actively* modified.

To investigate this question a set of samples were created with three different pretreatments intended to oxidise the surface prior to exposure to SF<sub>6</sub> plasma; a pure O<sub>2</sub> plasma treatment, exposure to an acidic environment promoting the oxidation of the CNTs and the attachment of carboxylic moieties, and finally the exposure to a much stronger acid process designed to ‘cut’ the CNTs while also depositing carboxylic acid groups on the nanotube structure. A fourth control sample with no pretreatment was used as a comparison. All samples were exposed to the same plasma simultaneously. Each surface was also made in duplicate, allowing a before and after comparison to elucidate the effect of the pretreatment and the subsequent SF<sub>6</sub> exposure.

Figure 7.5(a) presents results from the characterisation of the control and pretreated surfaces using synchrotron radiation of 760 eV. The untreated P2 surfaces were found to have  $16.7 \pm 0.7\%$  oxygen and  $1.2 \pm 0.2\%$  nitrogen with the rest made up by carbon. As previously, residual nitrogen was concluded to be a result of the solvent used for deposition, which could also account for a small amount of the detected oxygen signal. After exposure to O<sub>2</sub> plasma (5 mTorr, 10 W) the atomic percentage related to oxygen increased to  $47.1 \pm 1.0\%$  of the total detected surface components. Each of the acid treatments also increased the oxygen content, although the increase was not as great as that observed for the plasma exposure. The ‘oxidative’ treatment resulted in  $34.1 \pm 0.9\%$  oxygen while the ‘cutting’ treatment gave  $28.0 \pm 0.9\%$ . This result was unexpected considering the latter process was expected to be a much stronger treatment. Both acid

treatments resulted in increased nitrogen content, an effect attributed to the usage of nitric acid in both of the treatments.

Total atomic percentages *after* the SF<sub>6</sub> exposure are given in figure 7.5(b) where the fluorine content is presented in purple. The P2 CNT surface with no pretreatment resulted in a total fluorine content of  $34.8 \pm 1.0\%$  after exposure, a result that was expected considering that already observed in the previous experiments. The sample that received the first pretreatment, an exposure to O<sub>2</sub> plasma prior to the SF<sub>6</sub> plasma, was found to have much greater total fluorine content after fluorination. The fluorine signal made up  $60.8 \pm 0.9\%$  of the total detected peak area, dominating the surface composition. This sample was exposed to O<sub>2</sub> plasma (5 mTorr, 10 W) prior to the 2.5 mTorr SF<sub>6</sub> plasma also at 10 W. A comparative sample from the previous experiment would be that exposed to the mixture of 2.5 mTorr SF<sub>6</sub> with 5 mTorr O<sub>2</sub> (again at 10 W), which resulted in  $\sim 38\%$  fluorine content. The contrast between the two lies with the former being exposed sequentially while the latter simultaneously. The sequential exposure clearly provided a much greater level of surface functionalisation despite the fact that the total amount of reactant was expected to be the same in each case.

Each of the acid pretreatments also resulted in an increase in fluorination after exposure, although not equally across the samples. The surface generated from CNTs that received the oxidative treatment ultimately gained  $\sim 2\%$  fluorine content over the control sample, with a total of  $36.7 \pm 0.8\%$ . The cutting procedure however resulted in a total fluorine content of  $60.0 \pm 0.9\%$  after SF<sub>6</sub> plasma exposure, which within the uncertainties determined was essentially equivalent to that observed for the O<sub>2</sub> plasma pretreatment.

As before, high resolution spectra were obtained to shed light on chemical changes occurring at the surface, the quantification of which is given in figures 7.5(c) and (d) before and after SF<sub>6</sub> plasma exposure respectively. The O1s region was again fitted with two components representing C-O groups (light green) and C=O/COOR groups (dark green). It has already been mentioned that the P2 CNTs used in this work are found to have essentially a 50:50 mix of the species on the surface, as seen in (c), and is suggestive of carboxylic functionality resultant from the purification process used by the supplier. Similar observations were made for each of the acid pretreated CNT samples, with nearly equal amounts of the two functional components. This is not surprising since the chemical oxidation method is known to leave behind carboxylic functionality and, in the case of the

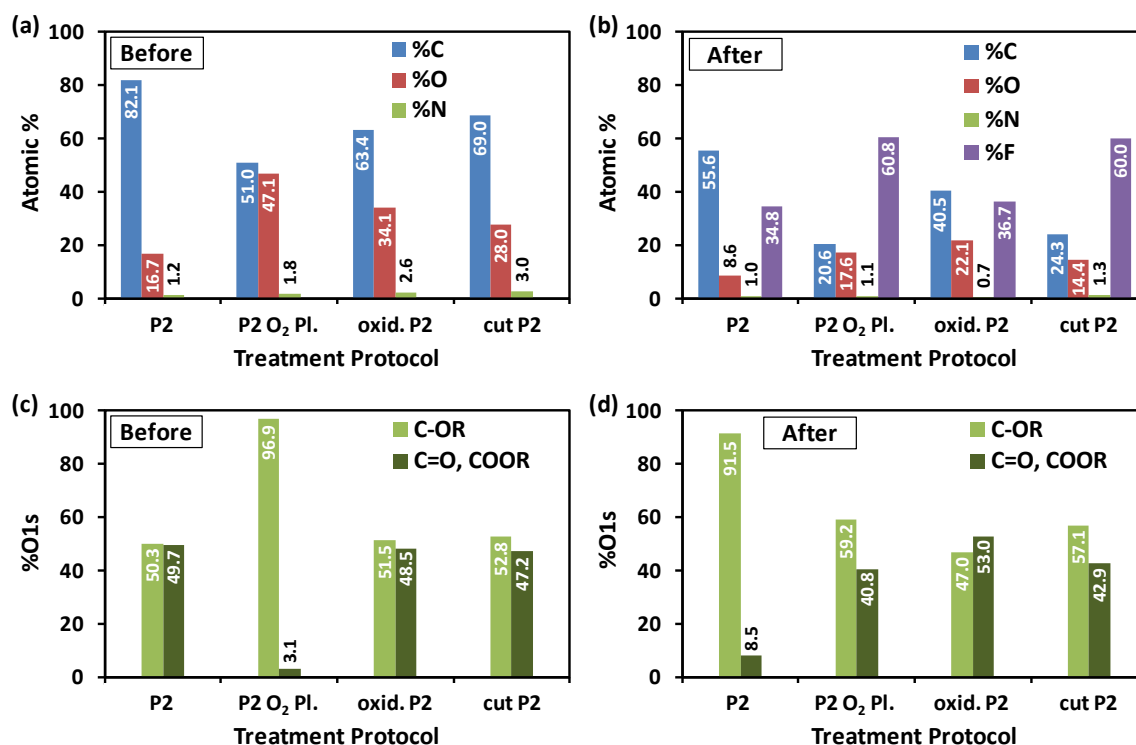


**Figure 7.5. Results from the characterisation of CNTs surfaces undergoing the pretreatment experiments; (a) and (b) the total atomic percentages before and after SF<sub>6</sub> plasma exposure, and (c) and (d) the relative amounts of each of the oxygen moieties from O1s spectra before and after SF<sub>6</sub> plasma exposure.**

cutting process, also reduce the length of the CNTs.<sup>194,197</sup> As a result, the ratio of the components in the O1s peaks remained largely the same, while the total oxygen content increased. The surface that underwent the plasma pretreatment was found to have an O1s spectrum that consisted of nearly 97% singly bonded oxygen to carbon. Therefore it would appear that this pretreatment not only greatly increased the oxygen content of the surface, but that it also modified the surface such that there was almost exclusively one type of carbon-oxygen bonding present.

After fluorination the O1s spectra were observed to be altered, as seen in figure 7.5(d). Each of the acid pretreated CNT samples had significant amounts of each of the oxygen species remaining after exposure, although some deviation is observable in the figure. Note here that the total oxygen content for these samples was also observed to decrease. The plasma pretreated sample showed a significant change, with a considerable amount of each of the species. This contrasts the chemical state prior to functionalisation greatly since this was the sample that showed predominantly one type of chemical bonding. Moreover the P2 sample (no pretreatment) also showed a considerable change, although in the case the

effect was opposite, with 91.5% of the O1s region found to be from C-OR groups. Again the total oxygen content for these surfaces was seen to decrease after plasma exposure.

These results show that the oxygen content at the surface is not the only factor that aids the fluorination mechanism. If this were true then the O<sub>2</sub> plasma pretreated sample would show the greatest total fluorine content after exposure by a significant amount. Instead it is essentially equivalent to that observed for the cut CNT sample, which was found to have 19% less oxygen at the surface prior to treatment. It also could not be the type of oxygen bonding at the surface that influences the functionalisation alone, since the two acid treated samples resulted in a nearly identical distribution of carbon-oxygen bond types yet gave vastly different fluorine percentages. Even if the total oxygen content was also taken into account here, the oxidised sample resulted in significantly less fluorine than the cut sample. Perhaps then a third effect is responsible for the variation in fluorine content observed after each of these pretreatments.

Both of the acid treatments are known to be particularly damaging to the CNTs. Overall these treatments induce significant defects throughout the CNT structure. Carbon that is sp<sup>2</sup> hybridised is particularly resistant to chemical attack. However, once defects are introduced then the lattice is disrupted and chemical functionalisation is made easier. Furthermore the cutting process is used to reduce the length distribution of the CNTs by literally shearing them about their circumference. This consequently results in the opening of the CNT end-caps and also the attachment of carboxylic moieties on the ends and sidewalls. Since the ends of the CNTs are most susceptible to attack this increases the number of sites available for fluorination significantly, thus improving the total content.

This argument can also be applied to the plasma treatment. Ion bombardment of the CNT surfaces will have inevitably created structural defects across the surface and also result in a significant amount of oxygen attachment. The process would likely have a sputtering effect on the CNTs, potentially attaching oxygen species to the structure which is subsequently removed upon further ion impacts, ultimately leaving behind a defect in the surface, as has been previously observed by Gu and Ziegler.<sup>56,57</sup> This improves the ability of the fluorine species to readily attach to the surface, resulting in the greatly improved fluorine content.

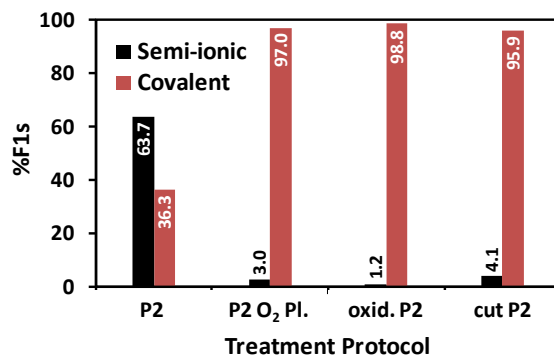


**Figure 7.6. Relative amounts of covalent and semi-ionic CF from F1s spectra after exposure.**

Figure 7.6 presents the relative amounts of semi-ionic and covalent C-F species from F1s spectra. As expected from previous results the exposure of the P2 surface resulted in a mixture of semi-ionic and covalent C-F bonding, with the weaker semi-ionic bond being the most dominant. However, each of the three pretreated samples showed a significant improvement over the untreated sample, with the relative covalency reaching 98.8 % for the oxidising acid pretreated sample. The lowest level was the sample consisting of cut CNTs, although this was found to be almost 96% covalent which was still a vast improvement. The plasma oxidised surface was found to have 97% covalency. From these results it could safely be concluded that the oxidising pretreatments detailed here vastly improved the quality of fluorine attachment to CNT surfaces. For the development of devices and surfaces that may be exposed to some form of chemical environment the ability to strengthen the bonding between the active species at the surface is paramount, since weaker bonds are likely to lead to enhanced surface (and thus device) degradation.

While the oxidised P2 sample ultimately provided the greatest level of covalency, no significant improvement in total fluorine was found over the standard pure SF<sub>6</sub> plasma treatment without additional oxidation. The cut CNT and the plasma oxidised CNT samples provided both high covalency and high total fluorine content. However, each of these processes produced such similar results that neither could really be distinguished as the superior method. Moreover, within error each of the percentages presented could be considered near enough to equivalent. The plasma oxidation technique however allowed for the pretreatment and fluorination to be performed within the same system and as such provided a ‘one-pot’ process where the CNTs would not need to be exposed to atmosphere between each step. Ultimately this may prove to be advantageous in device design, particularly in an industry where up-scalable techniques are often desired.

#### 7.4. Summary of Synchrotron Studies II

Following on from previous research at the Australian Synchrotron, the effect of tailoring the oxygen content both within SF<sub>6</sub> plasma and at the sample surface on the resultant fluorination of CNTs was investigated.

Two methods of systematically doping the SF<sub>6</sub> plasma with O<sub>2</sub> were investigated; maintaining a constant SF<sub>6</sub> partial pressure and maintaining a constant total pressure. The greatest level of control is observed when the SF<sub>6</sub> partial pressure is held constant and the amount of O<sub>2</sub> is steadily increased; as the percentage of O<sub>2</sub> in the plasma increase so too does the amount of fluorine attached to the surfaces. This change however was found to be relatively small compared to the errors associated with the measurement suggesting that it is not an ideal mechanism for controlling the *extent* of fluorination. The significant advantage of the doping of SF<sub>6</sub> plasma with O<sub>2</sub> was observed when the covalency of the C-F bonds was characterised. When the SF<sub>6</sub> pressure is held constant, the relative covalency of the C-F bond also remains constant at ~40%, irrespective of the amount of O<sub>2</sub> added. However, when the partial pressures of both the SF<sub>6</sub> and the O<sub>2</sub> are varied simultaneously, i.e. maintaining a constant total pressure, the relative covalency of the C-F was controlled from ~60% – 20% with striking linearity.

The covalency of the C-F bonding at the CNT surface could also be controlled by tailoring the oxygen content prior to SF<sub>6</sub> plasma exposure. This was achieved through wet-chemical oxidation of the CNTs in acid, and the exposure of a CNT surface to O<sub>2</sub> plasma. In all three cases the amount of fluorine that attaches to the surface is increased. Most remarkably however, the covalency of the attachment in all three cases is greatly increased, with a maximum covalency reaching 98.8%. This emphasises the high level of control that can be achieved with plasma based processing methods.



---

## Chapter 8.

# PECVD GROWTH OF CARBON NANOTUBES

### 8.1. Introduction

The applicability of carbon nanotubes to device integration in their as-prepared form is limited by their relative inertness and substantial difficulty inherent with the handling of the raw material. These limitations are generally circumvented through covalent functionalisation of nanotube sidewalls and ends. This chemical attachment expands the capabilities of the raw material allowing the experimentalist to purify and selectively separate nanotubes according to type and also controllably attach and subsequently align nanotubes onto surfaces. The attachment and alignment of nanotubes is of particular interest for chemical sensing applications, as well as for photovoltaics, where vertically aligned structures across a surface forming an array of collectors may be desired.<sup>98</sup>

Along with the work discussed in this thesis there has been much work performed in the area of covalent surface chemistry of carbon nanotubes.<sup>2,198</sup> However, it is often desirable to keep the nanotube as unaltered from its pristine state as possible. This desire is paramount for the application of nanotubes to chemical sensing and photovoltaics, where any covalent attachment is likely to not only disrupt the physical structure of the nanotube

but also the electronic structure, with potentially detrimental results. To avoid this issue many groups investigate the growth of carbon nanotubes directly onto a desired substrate using chemical vapour deposition (CVD), via a deposited transition metal catalyst layer. Upon growth the structures are physically tethered to the surface through the catalyst layer, and vertical growth tends to naturally occur through van der Waals interactions with the nanotube sidewalls. This removes the need to covalently modify the nanotubes to perform surface attachment and thus avoids affecting the electronic properties of the material. It also allows the growth of carbon nanostructures into defined patterns, which is particularly desirable for device applications.

Thermal CVD (TCVD) has proven to be a viable method for the homogeneous synthesis of carbon nanotubes in high yields, with some researchers demonstrating millimetre scale growth of CNT forests.<sup>199</sup> Although these forests grow vertically, the alignment is far from ideal at the nanotube level with much of the material forming the often described nanotube ‘spaghetti’. Furthermore, these processes rely on the thermal decomposition of a carbon containing source gas, or ‘feedstock’, to initiate growth and as such the substrate and gas temperatures are generally greater than 800°C. This limits the generality of the TCVD process to only those substrate materials capable of withstanding such high temperatures. Often this is a reasonable limitation as many groups focus on the growth of nanotubes onto silicon wafers. However, when studying photovoltaic systems the desire is to have transparent electrodes to maximise the light incident on the photo-responsive component such as a carbon nanotube array. Commonly soft glasses such as fluorine- or indium-doped tin oxide (FTO or ITO) are used. These materials lack the thermal stability of silicon wafers and as such cannot be applied to typical TCVD growth of CNTs.

Plasma-enhanced CVD (PECVD) is a variant of the typical thermal CVD process that makes use of the plasma state to facilitate the decomposition of the feedstock gas during nanotube growth. Having part of the work done therefore allows the process to be performed at lower substrate temperatures. Using PECVD SWCNT growth has been reported at temperatures of 450 – 500 °C and MWCNT growth at temperatures as low as 25 °C. Note however that this extremely low temperature growth was performed at high plasma power (~200 W) and the effects of plasma heating have been shown to increase substrate temperatures up to as much as 700 °C at these powers for a dc PECVD reactor.<sup>99,200</sup> Regardless, these observations significantly increase the applicability of CNT

growth to surfaces that could not normally withstand the high temperatures of TCVD. Nanotube growth is however a catalysed process and there is downside to operating at reduced temperature. As the substrate temperature is decreased the reaction rate accordingly drops and thus nanotube growth rates are diminished.<sup>98,201</sup> The true advantage of PECVD over its thermal counterpart is the promotion of vertical alignment of each individual nanotube as it grows. This is a result of the sheath creating a potential difference between the plasma and the substrate and consequently, an electric field normal to the surface. As the nanotubes grow they naturally align with the electric field and form homogeneous vertically aligned arrays. Some experimental setups allow the application of an external bias, with potentials as large as several hundreds of volts having been used previously.<sup>100</sup> Others simply rely on the natural potential difference that will accrue on the substrate upon plasma ignition.<sup>100</sup>

As mentioned earlier nanotube growth occurs through catalytic mechanisms. Maex and co-workers demonstrated nanostructure growth using a wide range of elements spanning the s-, d- and p-blocks of the periodic table without significant change in experimental protocol between the application of each catalyst.<sup>202</sup> SWCNT growth has even been demonstrated using lanthanoid catalysts.<sup>203</sup> It is generally accepted however that the transition elements produce the greatest levels of catalytic activity during nanotube growth with the metals Fe, Co, and Ni and their alloys being the most often used.<sup>99</sup> The catalyst layer is often deposited directly onto the substrate. Some researchers have found that the addition of an alumina ( $\text{Al}_2\text{O}_3$ ) barrier layer between the catalyst and the substrate greatly aids the process, with some growth not occurring in the absence of this layer. This barrier can be deposited through the direct sputtering of  $\text{Al}_2\text{O}_3$  onto the substrate, or by sputtering aluminium metal onto the substrate which subsequently oxidises on contact with air.<sup>100,204</sup>

PECVD is most commonly performed at reduced pressures, usually in the range of 0.1 – 100 Torr. Thus it should be expected that PECVD growth is a cleaner process than TCVD since atmospheric contaminants would be severely reduced while under vacuum. Common carbon sources are acetylene ( $\text{C}_2\text{H}_2$ ), ethylene ( $\text{C}_2\text{H}_4$ ) and methane ( $\text{CH}_4$ ). The feedstock is usually accompanied by diluents which ultimately act to reduce the carbon concentration. This has been found to be necessary for CNT growth where an abundance of carbon in the feedstock leads to the deposition of amorphous carbon layers which eventually poison the catalyst and cease growth. Hydrogen and ammonia are often chosen

as suitable diluents as they provide the secondary function of generating a reducing atmosphere, aiding the formation of suitable catalyst particles.<sup>39</sup> Neutral species such as argon or nitrogen are also suitable diluents, and act to aid in the removal of amorphous carbon from catalytic sites, preventing the poisoning of these sites. Ultimately this promotes homogeneous nanotube growth.<sup>38</sup>

At Flinders University there is a significant amount of research performed towards the application of nanotubes as chemical sensors, water filters and photovoltaic devices.<sup>205-207</sup> SWCNTs are usually purchased from an external source, purified and finally dispersed in solution before being attached to (usually) a silicon wafer substrate to create the desired device. As mentioned, this involves procedures that covalently modify the nanotube structure, something that may not be desirable in all cases. Limited work has been performed on the growth of CNTs directly onto substrates at Flinders, with processes yielding mostly MWCNTs through high temperature CVD. It would be desirable to have a method of growing CNTs onto substrates, eliminating the need for any solution processing. Moreover, growth at reduced temperatures that produces single-walled CNTs is desirable.

Since the plasma system used in this research was capable of producing plasma densities at pressures where nanotube growth is viable, the possibility of growing CNTs within the chamber directly onto a desired surface was deemed an important research avenue to investigate. If possible this would offer many new opportunities towards the controlled growth and functionalisation of CNTs.

## 8.2. Experimental Design

### 8.2.1. Choice of Carbon Source

Thermal CVD growth of MWCNTs at Flinders has been performed using industrial acetylene (98 % purity) and exotic materials such as ferrocene, which provides the carbon source and the necessary catalyst.<sup>208</sup> Plasma with an acetylene atmosphere had not been investigated within the plasma system in this research however, and its behaviour was therefore unknown. In 2008 Deslandes *et al.* demonstrated the hydrogenation of carbon surfaces through CH<sub>4</sub> plasma exposure using the Flinders reactor.<sup>102,108,209</sup> In this work the behaviour of CH<sub>4</sub> plasma was well characterised. When in the plasma state, CH<sub>4</sub> has the potential to not only supply the carbon source, but also a reducing hydrogen-rich atmosphere through various dissociation pathways.<sup>210</sup> This is often desirable for nanotube

growth as it aids in the formation of suitable catalyst particles. It was therefore chosen that high purity methane (99.95 %, BOC Australia) be used as the feedstock. Since hydrogen was not deemed a necessary addition, the diluent chosen was high purity argon (99.99 %, BOC Australia). The strong sputtering action of argon plasma was anticipated to assist in minimising amorphous carbon deposition on the catalyst layer.

### 8.2.2. Substrate Choice and Deposition of Catalyst Layer

Most CNT growth is performed on silicon wafers since this is often the desired substrate for application to electronic devices, as well as for performing electrochemical experiments such as cyclic voltammetry. Therefore silicon was chosen as the growth substrate in this work. The wafers were boron doped, p-type silicon ( $\{100\}$ , Siltronix France). The wafers had a native oxide layer ( $\text{SiO}_2$ ) of  $\sim 1 - 2$  nm thickness. This layer acted as a diffusion barrier between the catalyst and the substrate, reducing the intercalation of catalyst particles within the silicon.<sup>211</sup>

An iron catalyst layer (99.995 %, Koch-Light) was deposited onto the substrate via sputter coating (Quorumtech K575X, Quorum Technologies UK). Deposition thickness was determined via an *in situ* film thickness monitor (FTM, a quartz crystal microbalance) and maintained at 5 nm unless otherwise specified. Prior to catalyst deposition the sputter target underwent plasma cleaning to remove adventitious carbon and oxidized surface iron.

### 8.2.3. Sample Heating

As mentioned in Section 2.1.2, the sample table in the plasma chamber has three resistively heated elements and a thermocouple embedded within it to allow for samples to be heated. Initially it was thought that perhaps the table would be capable of reaching the temperatures required to catalyse growth as the chamber was designed for nitriding steel, but this had not been tested in the time that the apparatus had resided at Flinders. However, due to its geometry there was significant loss in heat conduction from the elements to the sample surface, and thus the temperature at the surface was routinely measured to be half of what the embedded thermocouple would read. This resulted in a maximum achievable surface temperature of only 400 °C. The radiant heat from the table also acted to heat the entire chamber to temperatures  $>70$  °C. Therefore another more localised heating system capable of greater temperatures was required.

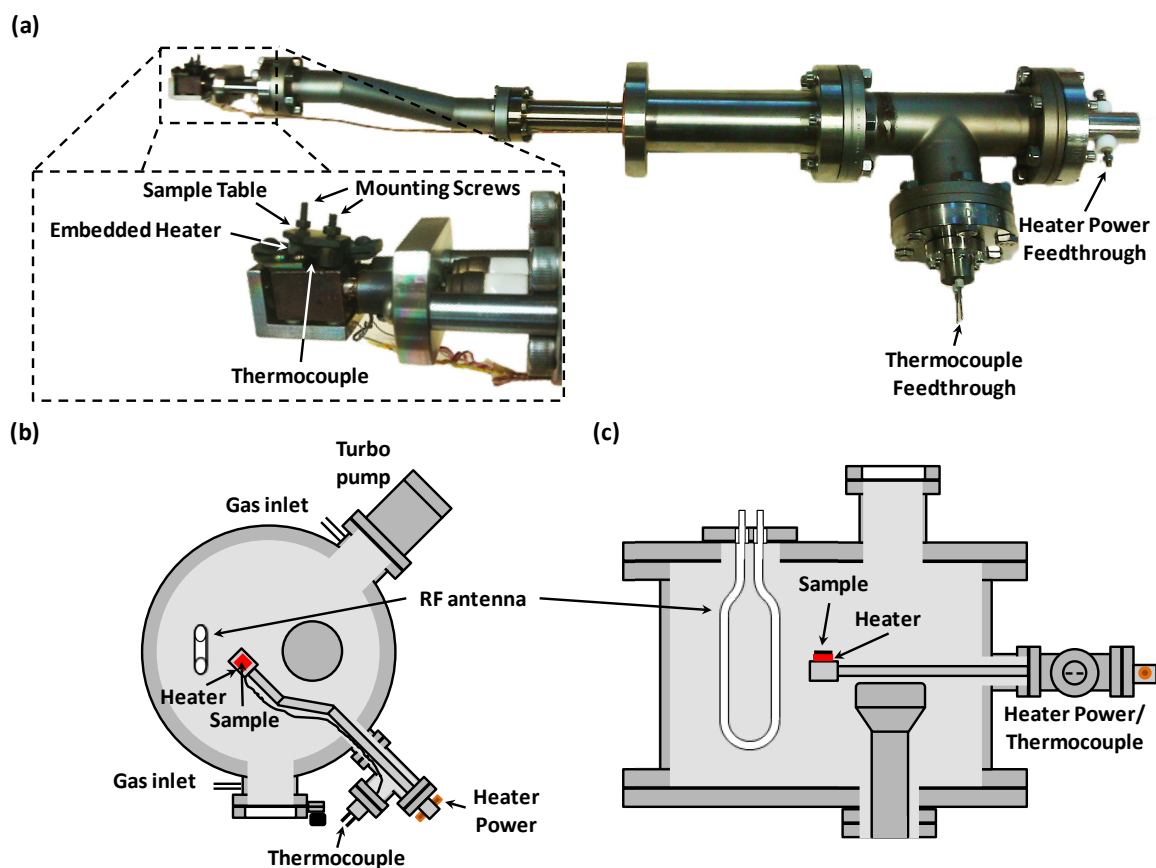


**Figure 8.1. (a) A photo of the sample heating arm with close-up of the heating mount and the position of the arm within the chamber as viewed from (b) the top and (c) the side.**

Pictured in figure 8.1(a) is the conceived heating arm to fulfil the heating requirements. The close-up in the figure shows the heating mount that was originally designed to be mounted within the LHS-10 being used here as the sample mount for growth. Heat was generated via a thoriated tungsten filament passed three times in series through an alumina ceramic cylinder that was embedded within the stainless steel table. When a current ( $\sim 5$  A) was applied to the filament it generated significant heat, in turn heating the table. The temperature was monitored via a K-type thermocouple that was in contact with the underside of the table. Initial tests under vacuum found that the surface of the table reached temperatures as high as  $720$  °C in a few minutes, with no adverse heating of any other surfaces within the chamber other than those in direct contact with the mount. Samples were mounted on top of the table and mechanically held in place by two nuts on threaded stud bolts that were attached to the table. Current was delivered to the filament through banana plugs that also served as the mounting point for the sample heater assembly. The position of the arm within the chamber is depicted in figures 8.1(b) and (c) as viewed from the top and side respectively. When in position the sample was approximately 5 cm from the antenna, well within the density while the plasma was ignited.

### 8.3. PECVD Growth of Carbon Nanotubes

#### 8.3.1. Preliminary Results and Proof of Principle

The stepwise preparation of the growth substrate was characterised with XPS. Survey spectra of the bare (top) and coated (bottom) silicon surface are presented in figure 8.2(a). As should be expected the bare silicon surface showed only the presence of Si, O and C signals in the XPS spectrum. The detected carbon is speculated to be adventitious, a result of the usage of ethanol and acetone to clean the surface of dust and oils after handling and cutting of the silicon wafer. The oxygen detected in the XPS spectrum is attribute to the native SiO<sub>2</sub> layer. This is further evidenced by the high resolution spectra given in figure 8.2(b) and (c). The Si2p spectrum shows two distinct features at 99.3 and 103.7 eV. These are consistent with the detection of the underlying bulk silicon signal and the silicon dioxide layer respectively.<sup>146</sup> The O1s spectrum gives a peak maximum at 532.5 eV, again consistent with the detection of silicon dioxide.<sup>146</sup> Using the TPP2M formula of Tanuma *et al.*, with an electron kinetic energy from the bulk Si2p orbital of ~1387 eV (note Al K $\alpha$  excitation) an electron IMFP of 30.9 Å was calculated.<sup>180</sup> Thus the fact that the bulk silicon was still detectable even through the native oxide affirms that the thickness of the SiO<sub>2</sub> layer was less than 3 nm.

Upon coating with 5 nm of iron, as determined by the *in situ* FTM during sputter deposition, the silicon signal in the survey spectrum was reduced to near undetectable levels. A very small feature at ~150 eV could possibly be attributed to a small amount of detectable silicon from the Si2s peak, and it is speculated that this be due to an incomplete coating rather than a layer that was thinner than expected. It has been shown previously that plasma sputtering of metals tends to naturally deposit nano-sized particles at these thicknesses rather than complete films.<sup>212,213</sup> The spectrum again indicates the presence of oxygen although in this case it is concluded to be due to the iron nano-particles being oxidised. This argument is strengthened by the high resolution O1s spectrum in figure 8.2(d) where it is seen that the peak energy is at significantly lower binding energy than the underlying SiO<sub>2</sub> layer, now appearing at 529.6 eV. This is indicative of a metal oxide and agrees well with the binding energy of iron oxide, specifically Fe<sub>2</sub>O<sub>3</sub>.<sup>146</sup> From the survey scan the peak energy of the Fe2p region was found to be 711 eV, again suggesting a majority of the iron layer was in the form of Fe<sub>2</sub>O<sub>3</sub>.<sup>146</sup> The O1s peak in figure 8.2(d) was found to be asymmetric, with a noticeable shoulder towards higher binding energies. This

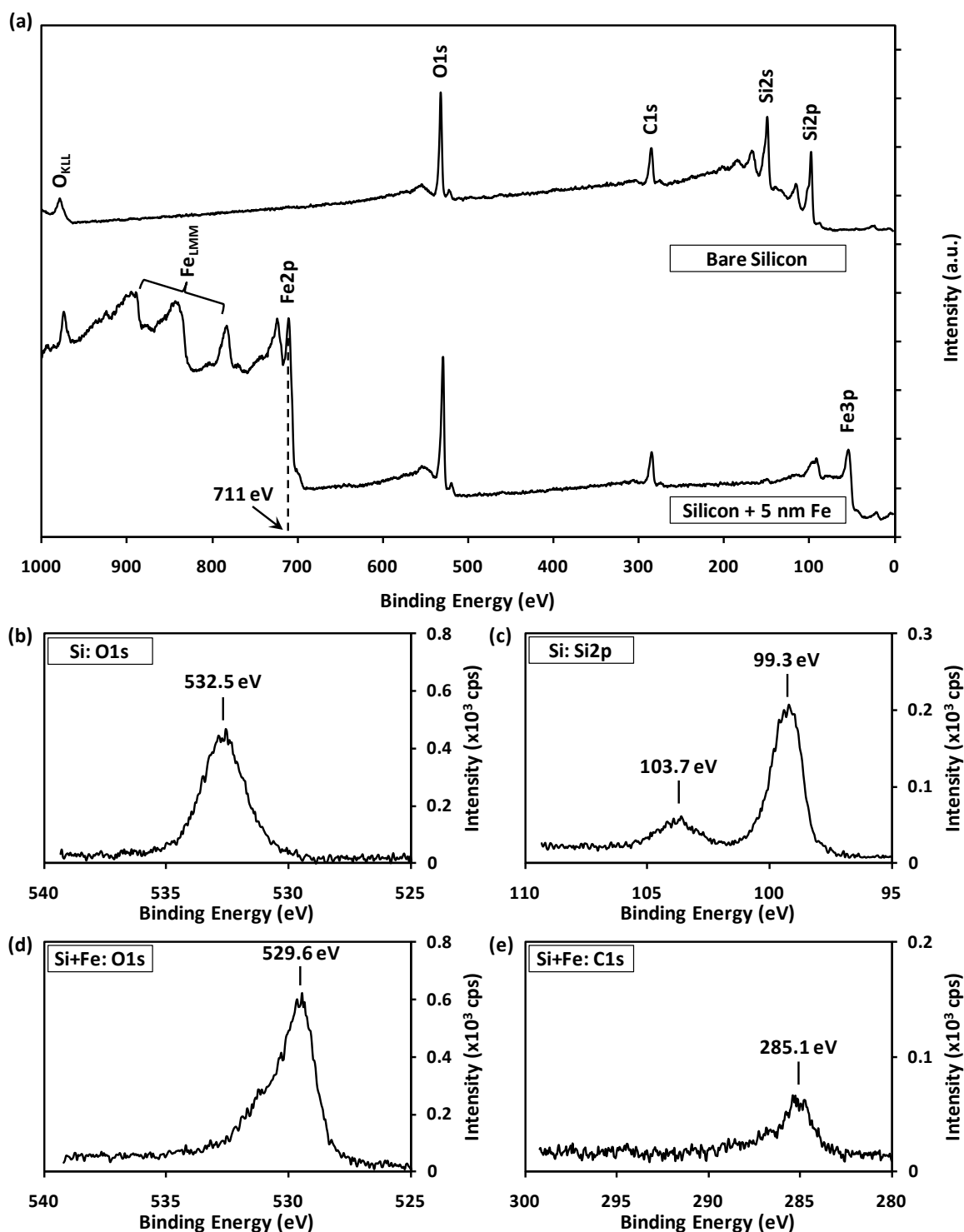


**Figure 8.2.** XPS spectra taken from bare and iron coated silicon; (a) survey spectra, (b) and (c) O<sub>1s</sub> and Si<sub>2p</sub> scans of the bare silicon, (d) and (e) O<sub>1s</sub> and C<sub>1s</sub> scans of the iron coated silicon. All spectra obtained using Al K $\alpha$  excitation with narrow scans at 20 eV pass energy.

could be due to other oxides of iron, such as FeO or FeOOH, in lesser concentrations. The remaining presence of carbon suggests that it could also be due to oxidised carbonaceous contaminants resultant from the deposition process and thus adventitious in nature.

To initiate growth the prepared substrate was placed under vacuum ( $\sim 1 \times 10^{-5}$  Torr) and heated to 650 °C within 3 minutes. The surface was held at this temperature for a further 7 minutes to ensure the catalyst layer formed nano-particles of metallic iron. This process also allowed for the sample to reach thermal equilibrium with the heater. Once the heating cycle was complete argon was released into the chamber up to a pressure of 80 mTorr, followed by the addition of 20 mTorr of methane, resulting in a total pressure of 100 mTorr. Equilibration of the feedstock pressure was achieved within 2 minutes. Once stable, plasma was ignited within the chamber at an rf power of 10 W and maintained for a 10 minute growth cycle. After this the plasma was extinguished, the flow of feedstock was ceased and the heater switched off. The sample was then allowed to cool to below 50 °C under vacuum before the chamber was vented and the sample was removed.

XPS results from the surface after the growth procedure are presented in figure 8.3. The survey spectrum is given in (a) and indicates a significant presence of carbon, as well as remaining iron catalyst and the underlying Si/SiO<sub>2</sub> substrate. The O1s and Si2p spectra are given in (b) and (c) respectively. The positions of these peaks are again characteristic of SiO<sub>2</sub>, although the ratio of the oxide to bulk silicon was observed to have increased, indicating the growth of the oxide layer. This is strengthened by the increased level of oxygen observed in the survey spectrum relative to the other detectable elements. However, it is not immediately clear as to what would facilitate the thickening of the oxide layer on the substrate. The surface was heated to temperatures that would be favourable for oxide growth and is thus a possible source of the increased SiO<sub>2</sub> signal. It has already been discussed that the deposited iron layer mostly consisted of iron oxide in the form of Fe<sub>2</sub>O<sub>3</sub>, as evidenced by the O1s peak at 529.6 eV and the Fe2p peak at 711 eV in figure 8.2. After growth the O1s peak was found at 532.6 eV with no significant feature below 530 eV that would be present from metal oxides on the surface. Also, the Fe2p peak was found to have shifted lower in binding energy, to 707 eV, indicative of metallic iron.<sup>146</sup> Thus as expected when heated under vacuum the iron catalyst was reduced to metallic iron. Such behaviour has been reported before. Jain and co-workers investigated the interface properties of iron oxide films on silicon substrates via electron beam deposition. It was found that upon contact with the beam (and therefore upon heating), Fe<sub>2</sub>O<sub>3</sub> would decompose to metallic iron and free oxygen. Since the enthalpy of formation of silicon(IV) oxide is much lower than that of the iron(III) oxide, Jain posited that the free oxygen would readily react with the silicon at the interface to grow the SiO<sub>2</sub> layer.<sup>214</sup> It is proposed that a similar

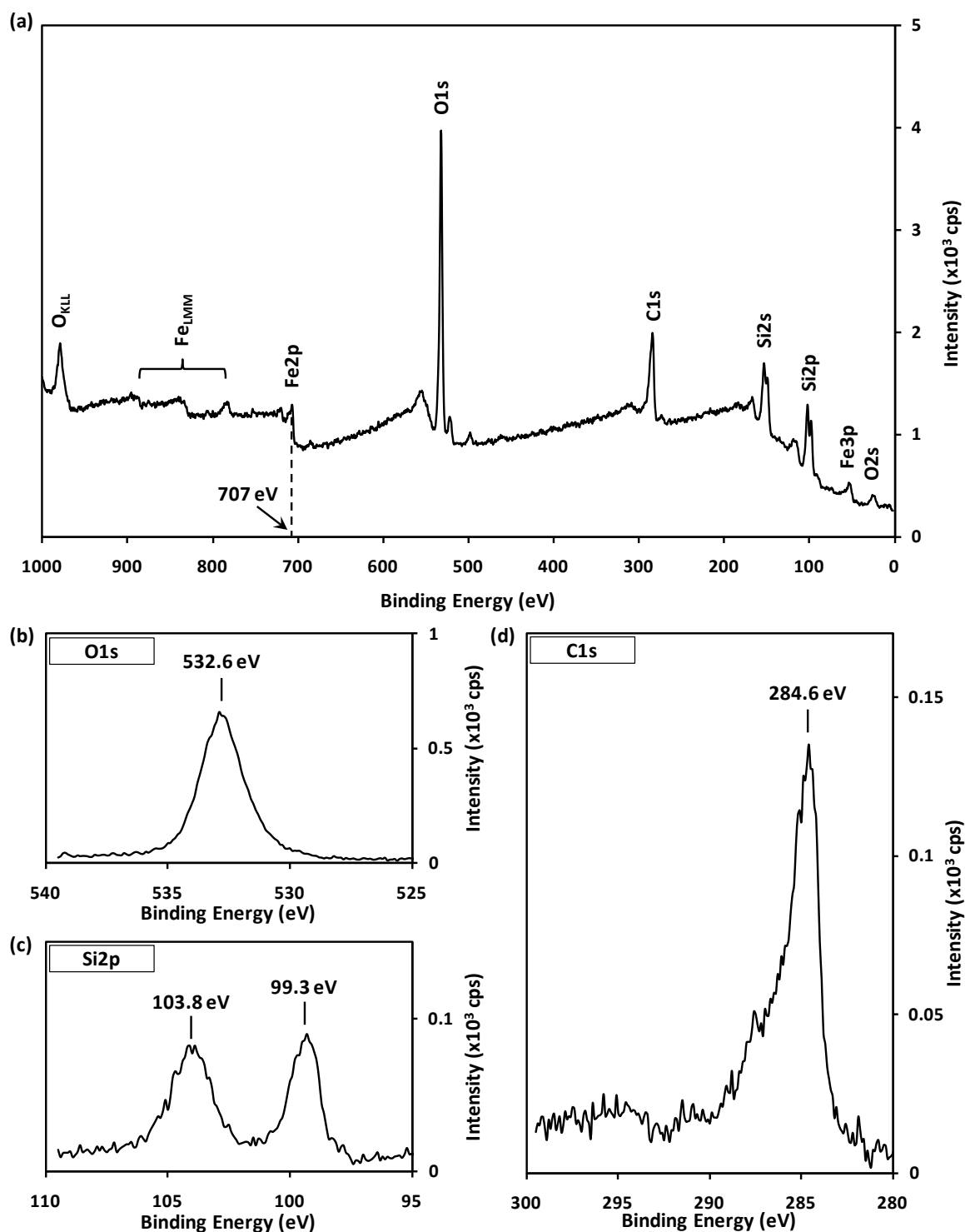


**Figure 8.3.** XPS spectra of the sample exposed to the growth procedure; (a) survey spectrum, (b)  $O_{1s}$  region, (c)  $Si_{2p}$  region and (d) the  $C_{1s}$  region. All spectra obtained using  $Al K\alpha$  excitation with narrow scans at 20 eV pass energy.

mechanism may be occurring here, whereby upon the heating and subsequent reduction of the iron oxide nanoparticles to metallic iron, the liberated oxygen has acted to grow the oxide. The bulk silicon signal was still detectable however indicating that the oxide remained less than 3 nm in thickness on average.

Figure 8.3(d) shows the high resolution C1s spectrum obtained from the surface after the growth treatment. Aside from the noticeable increase in intensity of the C1s signal over that of the iron coated silicon, the peak was also observed to have shifted to a lower binding energy, now observed at 284.6 eV. Often in XPS such small differences in peak positions could be attributed to minor levels of surface charging, due to either improper sample mounting or the nature of the sample itself. If this were the case here however, it is reasonable to expect that *all* peaks in the spectra exhibit the same shift. Since it is clear, particularly from the constant position of the Si/SiO<sub>2</sub> peaks, that this shift was not present for all peaks in the spectra then it can be reasonably concluded that the shift in the C1s peak is due to the detected carbon having a different chemical state to that observed prior to the treatment. The C1s region has a peak position of 284.6 eV which is characteristic of sp<sup>2</sup> hybridised carbon, i.e. graphitic carbon.<sup>145</sup> It has been suggested in the literature that the various forms of sp<sup>2</sup> carbon have slightly different C1s positions with HOPG generally found at 284.5 eV while the fullerenes such as CNTs are found at 284.6 eV. It could be concluded from these XPS results that the procedure has therefore resulted in carbon nanotube growth. However, such a statement must be made with care since a small difference in energy is well below the spectral resolution of the LHS-10 instrument. What can be concluded with confidence is that the growth procedure has deposited carbonaceous material onto the surface which appears to be graphitic in nature. Whether this carbonaceous material is in CNT form must be determined through other means.

The ability of Raman spectroscopy to definitively characterise carbon nanotubes has already been established and was used here to determine whether CNT growth had in fact been achieved. Figure 8.4(a) presents the wide Raman spectra for the bare p-type silicon and the catalyst coated silicon exposed to the aforementioned plasma treatment, obtained using 532 nm excitation. The bare silicon showed three features characteristic of crystalline silicon; the first order TO mode at 522 cm<sup>-1</sup> which was also the strongest phonon mode observed, and the 2TA and 2TO modes at 305 cm<sup>-1</sup> and 968 cm<sup>-1</sup> representing overtones of the transverse acoustic and optical modes respectively.<sup>123</sup> Upon exposure to PECVD treatment new features arose in the spectrum at 1351 cm<sup>-1</sup>, 1592 cm<sup>-1</sup> and 2670 cm<sup>-1</sup>. These can be attributed to the D, G and G' bands of graphitic carbon respectively. Note however, that the shape of the G band exhibits a prominent shoulder on the lower wavenumber side, an effect that has already been discussed in Section 5.3.1 relating curved forms of graphite. There is also a strong feature at low energies (i.e.

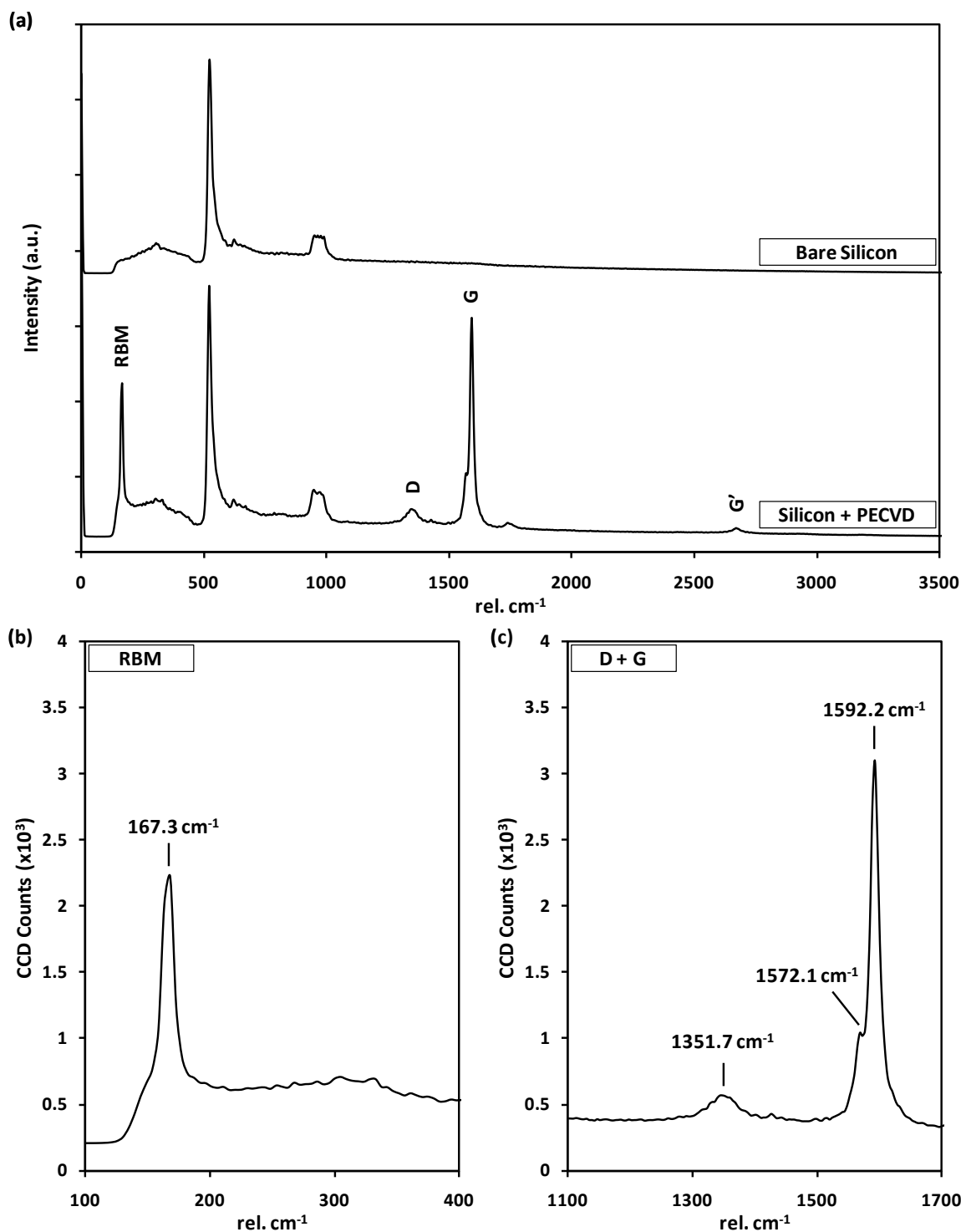


**Figure 8.4. Raman spectra of the PECVD samples; (a) the full Raman spectra of bare and PECVD treated silicon, (b) the RBM of the grown CNTs and (c) the D + G band. The spectra were obtained using 532 nm (2.33 eV) excitation.**

wavenumber values), around 167 cm<sup>-1</sup>, that can be attributed to the radial breathing mode. This feature is not seen in any of the graphitic forms of carbon other than nanotubes. Moreover, Dresselhaus states that the presence of an RBM in a sample is direct evidence of the presence of *single-walled* carbon nanotubes.<sup>123</sup> Figure 8.4(a) and (b) show the RBM

and D + G regions of the PECVD spectrum. The RBM presented as a single peak with maximum at  $167.3\text{ cm}^{-1}$ . The G band was observed to consist of two components; the  $G^-$  and  $G^+$  features at  $1572.1\text{ cm}^{-1}$  and  $1592.2\text{ cm}^{-1}$ . Again this is typically accepted to be a ‘nanotube only’ feature if present in Raman spectra as it is the result of curvature of the nanotube ultimately creating a dispersion in phonon speed (in those that travel along the tube versus those that travel around it).<sup>123</sup> The G band is observed to be quite narrow, with each of the components appearing to have a Lorentzian shape. As detailed earlier in Section 5.3.1, such a peak profile indicates that the resonant nanotubes are dominated by those that have semiconducting band structures.<sup>123</sup> The D band is small compared to the RBM and G bands, which is suggestive of high levels of homogeneity not only within the nanotube structure, but also across the sample (i.e. the nanotube growth has occurred with low levels of amorphous carbon deposition). From average spectra taken from random points across a wide area of the sample the RBM peaks yielded an average nanotube diameter of  $1.54 \pm 0.04\text{ nm}$ . Applying this same analysis to the  $I_D/I_G$  ratio gave an average value of  $0.14 \pm 0.04$ . Considering that in Section 5.3.1 the average  $I_D/I_G$  was found to be  $\sim 0.08$  for the commercial CNTs, this process appears to have produced very high quality CNTs.

From XPS analysis it was concluded that the PECVD growth resulted in incomplete coverage as indicated by the detection of the substrate and catalyst layers, with a less than dominant carbon signal. Pictured in figures 8.5(a) and (b) are  $50 \times 50\ \mu\text{m}^2$  optical images ( $\times 100$ ) of the surface before and after growth respectively. As should be expected before growth the surface appeared featureless in (a). After PECVD treatment was performed the surface in (b) appears to be covered with small islands of nanotube growth that is well dispersed across a large area. The Raman instrument used in this research has the capability of generating spatial images using spectral features, a so-called ‘spectro-microscopic’ technique. Presented in figure 8.5(c) and (d) are spectromicrographs generated by taking Raman spectra at regular intervals across a  $10 \times 10\ \mu\text{m}^2$  area (50 lines per image and 50 spectra per line). Through analysis of the spectra the intensity of a peak of choice can be plotted spatially in 2 dimensions to generate the images shown. The intensity of the RBM from  $120 - 200\text{ cm}^{-1}$  across the  $10 \times 10\ \mu\text{m}^2$  is presented in figure (c) while the G band intensity from  $1510 - 1670\text{ cm}^{-1}$  for the same region is presented in figure (d). Both of these features are marked by the red boxes in (e), which emphasises the

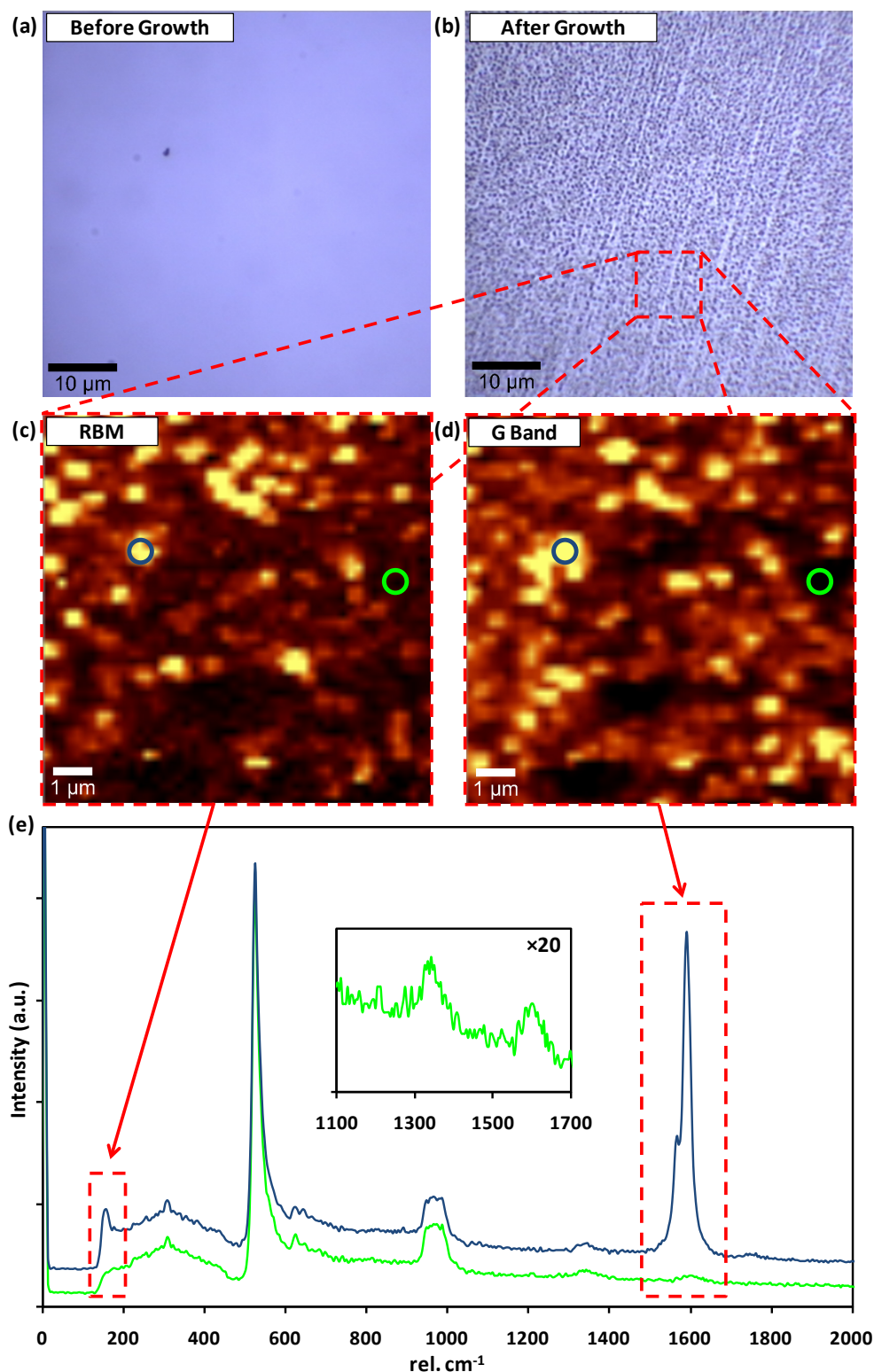


**Figure 8.5.** (a) and (b) Optical images ( $\times 100$  objective) of the silicon surface before and after PECVD growth, (c) and (d) Raman spectral images of the RBM and G band intensities as indicated by the spectral ranges marked by red boxes, and (e) Spectra from the circled regions in the images with the blue spectrum corresponding to a region of high RBM and G intensity and the green spectrum corresponding to a region of low RBM and G intensity. The inset gives the D+G region of the green trace at  $\times 20$  intensity.

relationship between the intensity in the images with that of the spectral peaks. The spectra are colour coded to the circles in the images indicating from where the data was obtained on the sample. The nanotube islands appear to have dimensions on the order of  $\sim 1 \mu\text{m}$ , and are randomly dispersed across the surface with incomplete coverage.

The inset shown within figure 8.5(e) is the D + G region of the green spectrum (from the indicated low intensity region of the images in (c) and (d)) magnified by  $\times 20$  in intensity to enhance the features present. This inset shows that even in the lowest intensity areas of the image there is still some form of graphitic growth present on the substrate surface. From the  $I_D/I_G$  ratio, which for the peaks presented was found to have a value of 1.10, it would appear to be either from nanotube growth that is either highly defective or more multi-walled in nature than the surrounding areas.

Since the surface features that were resultant of CNT growth were observed to be on the micron scale it was thus expected that the nanotubes could be imaged using scanning electron microscopy (SEM). Surprisingly though, when this was attempted no fine detail could be obtained. It was apparent that the morphology of the surface had changed, since there was contrast between bare silicon and the PECVD growth which showed sporadic islands of growth similar to that shown in figure 8.5. Beyond that no discernable features could be observed on the nano-scale (see figure 8.10). This suggested that the nanotubes grown here were either very short in length, or the density of the films was too low for the SEM to achieve sufficient contrast between the carbon nanotube islands and the underlying silicon substrate.

The PECVD experiment detailed here was repeated multiple times across a number of weeks. In each case much the same result was obtained with single-walled nanotube growth occurring with high levels of purity across the entire growth substrate. The efficacy of methane plasma to deposit carbonaceous films is well established however, so as a measure of control the critical elements required specifically for CNT growth were removed individually to test their individual effects. Figure 8.6 gives the average Raman spectra for three experiments removing

- i) the ignition of the feedstock into the plasma state (top),
- ii) the heating of the surface (middle) and
- iii) the presence of the catalyst particles on the surface (bottom).

In each case removal of a critical element resulted in a complete cessation of graphitic

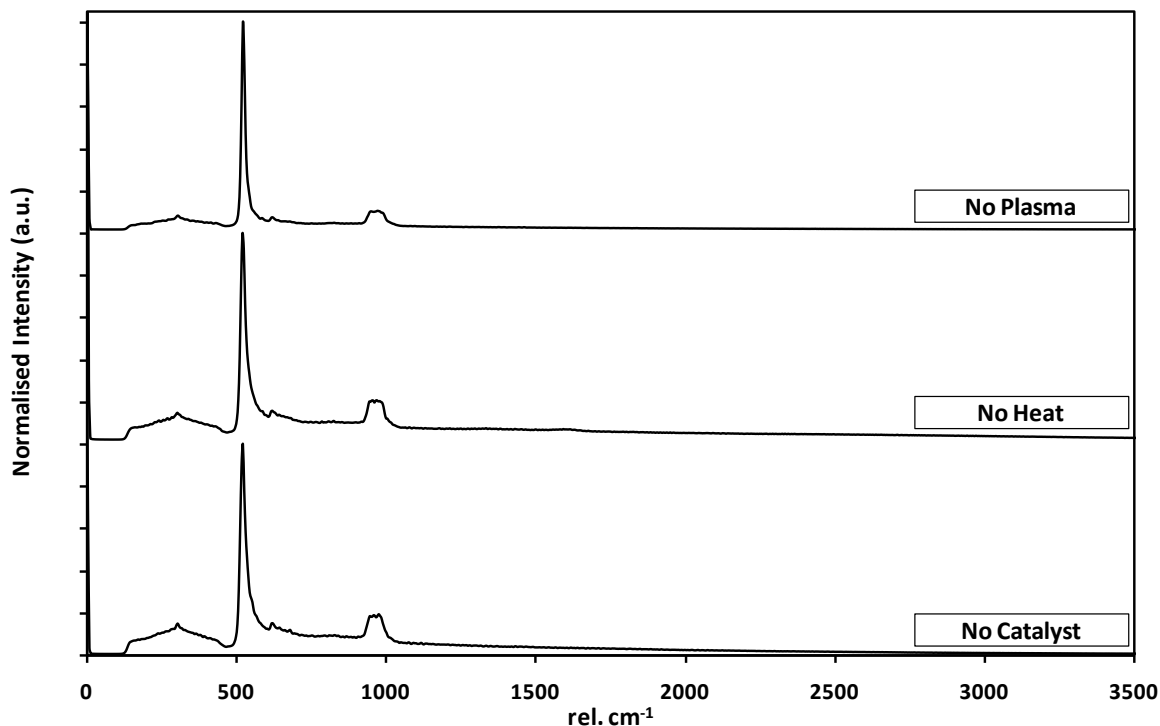


**Figure 8.6. Raman spectra from control experiments that removed critical elements from the CNT growth mechanism; ignition of the feedstock into the plasma state (top), the heating of the surface (middle) and the catalyst (bottom).**

growth, demonstrated by the distinct lack of any meaningful features  $\sim 1350$  and  $1600\text{ cm}^{-1}$  in the Raman spectra.

### 8.3.2. Variation of Growth Parameters

Particularly desirable in the field of nanotechnology is the ability to grow structures with properties tailored to suit a specific application. When studying the application of PECVD toward the growth of CNTs there are three main sources of variability expected to directly affect the properties of the resultant nanotubes; the catalyst, growth temperature and growth time. Upon establishment of a suitable experimental protocol that would reliably produce CNT growth, experiments were then performed to examine the influence of various experimental parameters on the growth and properties of the resultant nanotubes.

#### *Catalyst*

The type of catalyst, along with the thickness and design of the layer, has a marked impact on the way in which CNTs grow in both thermal and plasma-enhanced CVD.<sup>201</sup> As already stated, the catalyst is generally chosen from the group VIIIA transition metal elements; for instance Fe, Co, Ni, and their alloys. The thickness of these layers is found to have a direct

impact on the size of the nanoparticles and subsequent diameter of nanotubes grown from them.<sup>201,215</sup>

Due to its availability, Fe layers were used in this work to establish nanotube growth, with the catalyst deposited directly onto the silicon substrate. The wafers used here were not processed in any way prior to the addition of the catalyst layer and thus a native SiO<sub>2</sub> layer of around 1 – 2 nm thickness was present on the surface and expected to behave as a diffusion barrier, preventing the intercalation of iron into the bulk silicon. Figure 8.7(a) presents Raman spectra of CNT growth from three catalyst thicknesses (normalised to the G band); 1 nm (top), 5 nm (middle) and 10 nm (bottom). All three catalyst layers resulted in single-walled CNT growth evidenced by the strong RBM, D and G bands. Average I<sub>D</sub>/I<sub>G</sub> ratios were found to be  $0.08 \pm 0.02$ ,  $0.06 \pm 0.03$  and  $0.07 \pm 0.05$  for these three catalyst thicknesses respectively, suggesting that while the homogeneity within the areas of CNT growth remained somewhat consistent on average, deviation from this average tended to increase as more catalyst was deposited. This could be explained by an observed increase in the coverage at 10 nm of catalyst. The inset for each of the spectra in figure 8.7(a) are optical images of the surfaces prior to Raman analysis where the surface coverage on the sample with 10 nm of catalyst is visibly different from that of the 1 and 5 nm samples, having much denser CNT growth. This can also be observed in the Raman spectrum for the 10 nm sample where the intensity ratio between the CNT G band ( $\sim 1590 \text{ cm}^{-1}$ ) and the silicon TO mode at  $\sim 530 \text{ cm}^{-1}$  is noticeably different, indicating less interaction between the laser and the substrate, an effect that could be attributed to an increased coverage.

It was expected that a systematic variation in the catalyst thickness would result in a similarly controlled change in the diameter of the CNT growth. Upon analysis however the average diameters were found to be  $1.58 \pm 0.04$ ,  $1.54 \pm 0.04$  and  $1.60 \pm 0.05$  nm for the 1, 5 and 10 nm layers respectively. Despite expectations, the variation in these values is not considered to be significant enough to suggest that a strong dependence existed for these samples under the prescribed conditions. This conclusion assumes that the FTM within the sputter coater was accurate in its determination of the thickness of the deposited film.

Figure 8.7(b) compares three catalyst layers of different composition exposed to the same growth conditions; the standard 5 nm Fe catalyst layer already discussed (bottom), 5 nm of Fe with a 5 nm oxidised Al supporting layer (middle) and a 5 nm Ni layer (top). Graphitic growth was observed to occur for all catalyst types, although the simple 5 nm Fe layer was

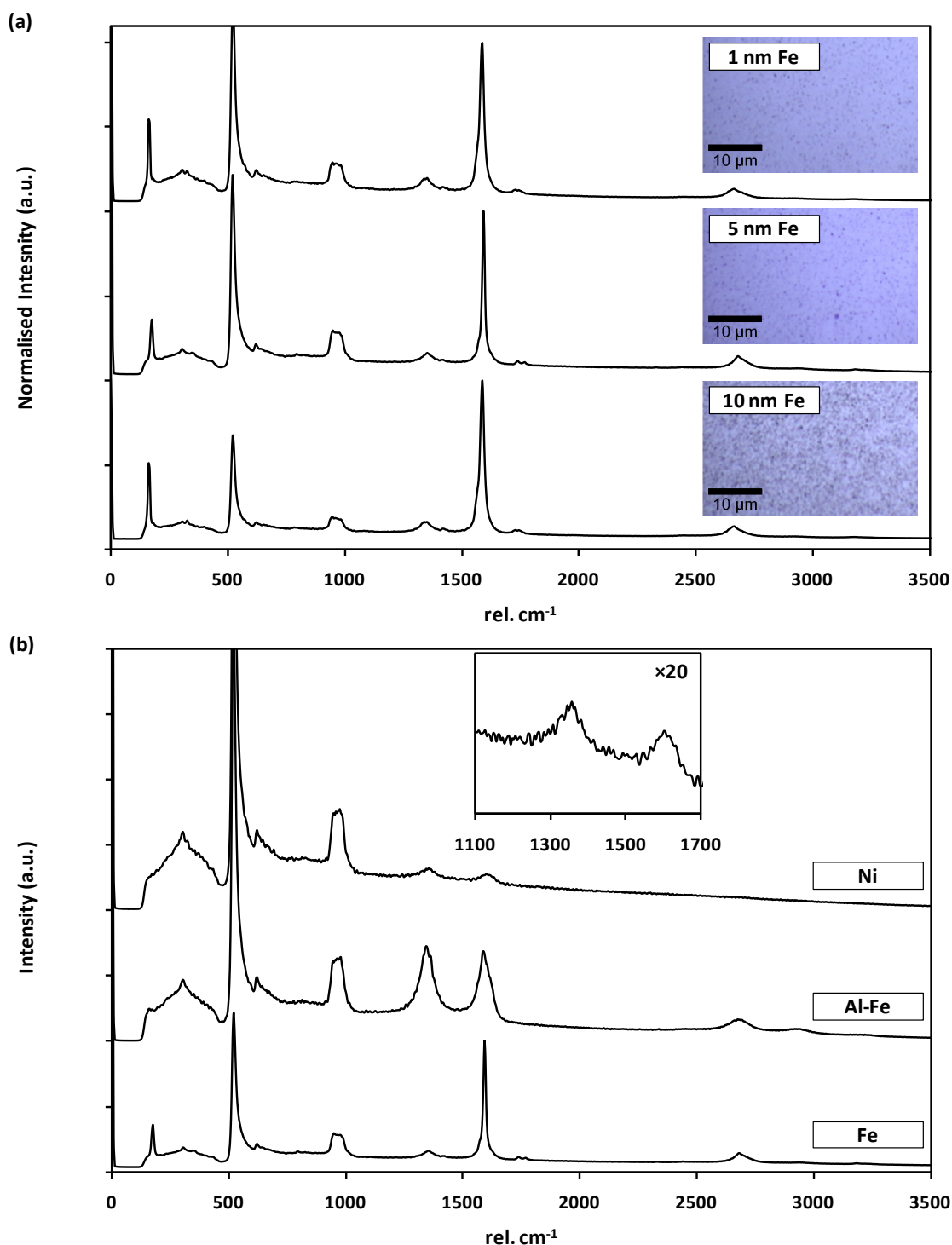


**Figure 8.7. (a) Raman spectra and optical images of 1, 5 and 10 nm Fe catalyst layers on silicon and (b) Raman spectra of catalyst layers consisting of 5 nm Fe (bottom), 5 nm Fe with an oxidized Al supporting layer (middle) and 5 nm of Ni (top).**

the only one to result in SWCNT growth under these conditions. The addition of the oxidised Al layer beneath the Fe did not appear to aid growth. The ratio of the D and G bands was drastically different to that of the pure Fe layer, found to be  $\sim 1.1$ , which is suggestive of the preferential growth of CNTs with multiple walls. A similar result was

observed when a Ni catalyst was used in place of Fe. Minimal growth occurred under a range of conditions with  $I_D/I_G$  again found to be greater than unity on average.

There is research to suggest that an oxidised aluminium layer separating the catalyst from the silicon substrate enhances the growth rate and also causes the preferential growth of SWCNT when MWCNT would grow in the absence of the layer.<sup>36,204,216,217</sup> As it would appear to be here, this is not always found to be the case. Mathur *et al.* studied the effect of an aluminium inter-layer on the growth of CNTs using microwave PECVD. The growth rate and thus overall nanotube length was observed to decrease as the barrier layer thickened and it was found that after a pretreatment the catalyst particle size was greater in the presence of a 6 nm aluminium oxide layer.<sup>218</sup> The CNTs grown in that work were also multi-walled as determined by Raman analysis. It is proposed that a similar effect has occurred here. Upon the heating of the substrate the catalyst layer forms nanoparticles. In the presence of an aluminium oxide layer, larger particles may be formed in comparison with the *absence* of the layer. If these particles are sufficiently large then the preferential growth of MWCNTs rather than SWCNTs may occur, even when treated to the same growth conditions.

#### *Growth Temperature*

The experimental setup allowed for the controlled heating of the surfaces to a given temperature within  $\pm 10^\circ\text{C}$ . Presented in figure 8.8(a) are the average Raman spectra for samples heated to  $450^\circ\text{C}$  (top),  $550^\circ\text{C}$  (middle) and  $650^\circ\text{C}$  (bottom) using otherwise identical growth conditions. Growth was achieved at all three temperatures however SWCNT growth was only achieved above  $550^\circ\text{C}$ , indicated by the presence of the RBM and splitting of the G band in the spectra. The coverage, and by implication the growth rate, was severely reduced at the lower temperatures, an effect that could be explained by either lack of dissolution of the feedstock at the catalyst surface or by improper nanoparticle formation from the Fe layer.

A plot of  $I_D/I_G$  versus growth temperature is presented in figure 8.8(b), with the values given in the inset table. As the temperature was reduced the ratio was seen to rapidly increase, particularly below  $550^\circ\text{C}$  where  $I_D/I_G$  approached unity. This suggested a transition from single-walled to predominantly multi-walled growth.<sup>219</sup> This is in agreement with research elsewhere where it is generally accepted that single-walled CNT growth requires greater substrate temperature than multi-walled growth, due to the high

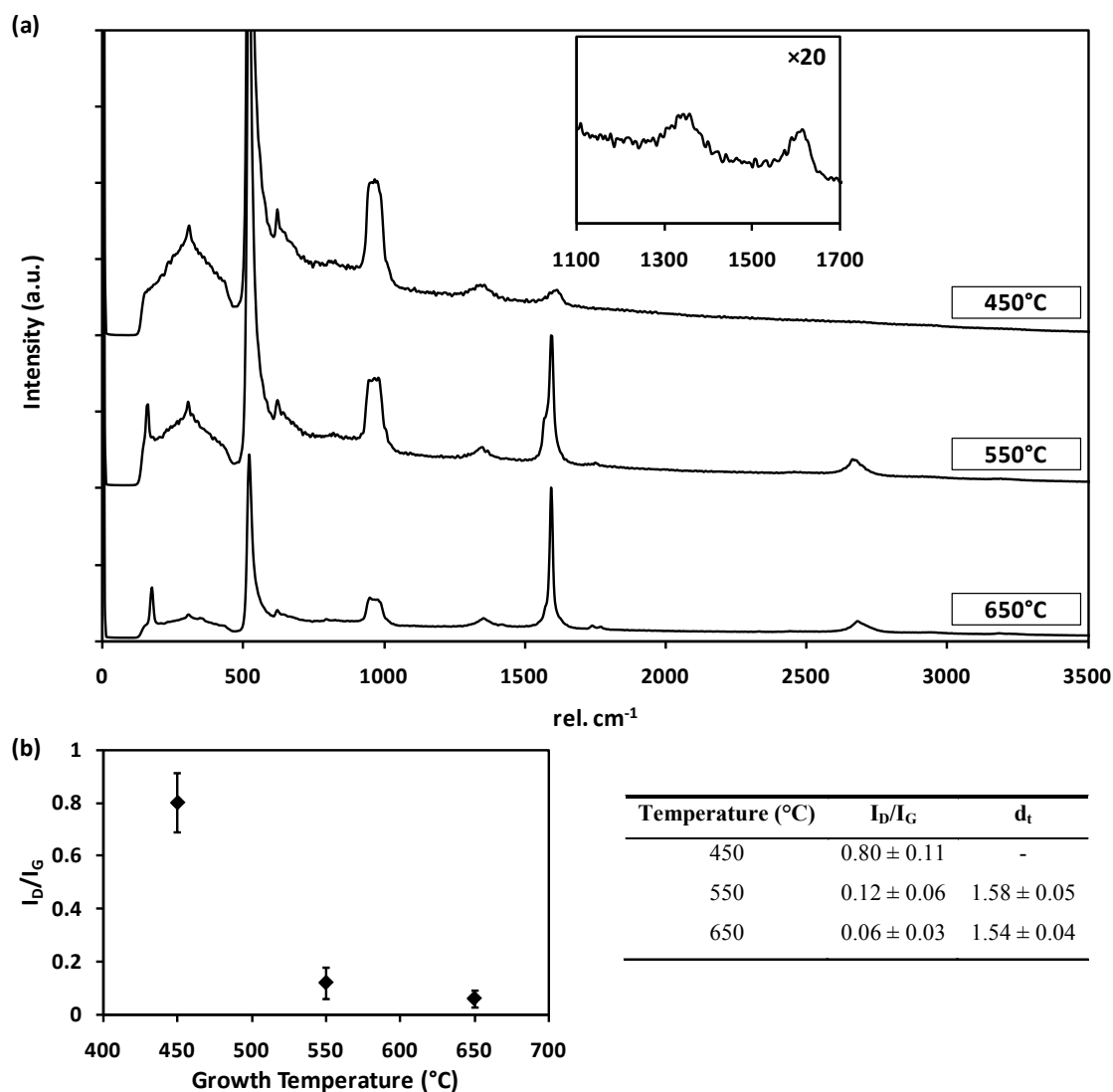


**Figure 8.8. (a) Raman spectra of CNT growth at 450°C (top), 550°C (middle) and 650°C (bottom). The inset shows the D+G region of the 450°C sample with the intensity at  $\times 20$ . (b)  $I_D/I_G$  versus temperature and inset the values of the ratio and the tube diameter.**

energy requirements for the formation of a closed ‘bucky-ball’ cap on the nanotube.<sup>100</sup> If the kinetic energy is not available at the surface then MWCNT growth would tend to occur more readily.

The RBM was only observed for CNTs grown at 550°C and 650°C, providing further evidence suggesting that SWCNT growth only occurred for these temperatures. Calculated diameters are given in the inset table in figure 8.8(b). The average diameter of the CNTs appeared to increase slightly upon reduction of the growth temperature. However within the deviations observed the change was not particularly significant. What is important however is the fact that no RBM was observed for the growth at 450°C. This agrees with the proposition that a change from single- to multi-walled growth has occurred, although

the spectral filter within the Raman instrument designed to attenuate Rayleigh scattering truncates the spectra below  $\sim 140\text{ cm}^{-1}$ , so if an RBM was present below this value it would not be detectable. Additionally, such low energies correspond to large diameter nanotubes with RBMs that are weak and therefore difficult to observe.<sup>123</sup>

### *Growth Time*

Since the nanotubes being grown via the established PECVD method could not be observed under SEM it was proposed that they were very short, therefore making contrast difficult to achieve. Increasing the administered growth time was therefore investigated to attempt to lengthen the CNTs and enhance the likelihood that the structures would be observable by electron microscopy.

Figure 8.9 shows the average Raman spectra for samples grown for 10, 30 and 60 minutes under otherwise identical conditions. Each of the spectra are normalised to the G band. In contrast to what was expected coverage appeared to decrease with longer growth times. An increased growth time of course meant a greater length of exposure to the plasma. The composition of the feedstock was 80% argon, which in the plasma state is often used to physically sputter surfaces. Greater exposure to this feedstock may have resulted in greater levels of sputtering, not only removing the carbonaceous material as it grew but also the catalyst layer, preventing further growth.

An analysis of  $I_D/I_G$  versus growth time is given in figure 8.9(b). Similar to the trend observed when the growth temperature was varied, the ratio rapidly increased the longer that growth was performed. A rough estimate would suggest that SWCNT growth occurred for times less than 30 minutes, while a transition to MWCNT growth occurred beyond this time. Gohier *et al.* discussed a similarly non-linear mechanism observed in the PECVD growth process as time was increased.<sup>220</sup> In that work two mechanisms were proposed that would compete against the growth of CNTs. The first relates to the poisoning of the catalyst. As time increases the catalyst particles still exposed to the plasma can become encased in non-nanotube carbonaceous material. This acts as a diffusion barrier to the feedstock and thus removes the particles as possible growth sites.<sup>220</sup> The second mechanism results from etching of the nanotubes by the plasma as they grow. Nanotubes consisting of few walls (i.e. single- or double-walled) were deemed to be more fragile when exposed to the plasma species than nanotubes with multiple walls.<sup>220</sup> This results in the preferential etching of SWCNTs over time. Assuming that these two processes are

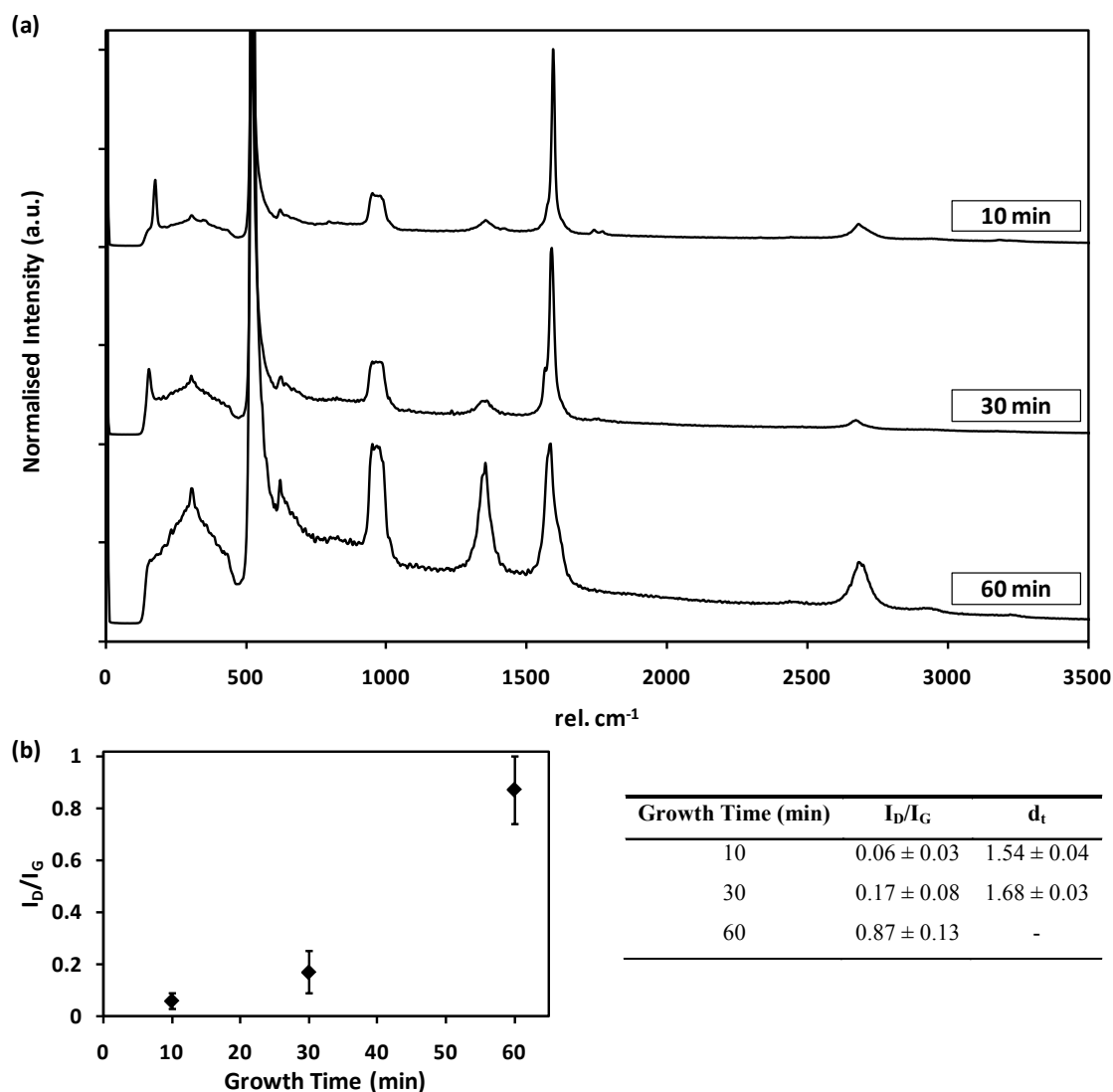


**Figure 8.9. (a) Raman spectra of CNT growth for 10 (top), 30 (middle) and 60 minutes (bottom) and (b)  $I_D/I_G$  versus growth time and inset the values of the ratio and the calculated tube diameters for each of these growth times.**

active during PECVD, then as the catalyst particles are poisoned less sites are available for new SWCNT growth and as time progresses the SWCNTs already present are etched at a greater rate compared to the MWCNTs. This ultimately results in a transition of predominantly SWCNTs to MWCNTs on the surface, while also reducing the overall nanotube coverage.

SWCNT growth was observed at 10 and 30 minutes, evidenced by the significant RBM presence. The table inset in figure 8.9(b) gives calculated values of the nanotube diameter for these growth times. A noticeable increase in the average diameter was found when the growth time was increased to 30 minutes over the established 10 minute growth time. When growth was performed for 60 minutes no RBM was found. These observations agree

with the hypothesis already discussed, whereby the increased growth time reduced overall SWCNT content through a combination of preferential etching and catalyst poisoning. That the average nanotube diameter was found to increase suggests that the smallest CNTs were also etched at a greater rate compared to the larger single- and multi-walled CNTs, and over time the average diameter increased as only the largest nanotubes remained.

#### **8.4. Patterned Growth of SWCNTs**

The implementation of carbon nanotubes in device fabrication requires some level of control over the sites at which either chemical attachment or direct CNT growth occurs. This allows for precise control over the active surface area in a given application, such as chemical sensing, photovoltaics or nanoscale electronic devices where a strong knowledge of the active surface area is desirable.

A simple method for producing patterned nanotube growth in CVD is the physical masking of the catalyst. This can be achieved either during deposition, resulting in the growth template being formed from the catalyst, or by masking during growth, preventing the feedstock from reaching the catalytic material in areas covered by the template. The latter case can be problematic since the mask could easily move during the growth cycle causing the pattern to lose definition. However, patterning during catalyst deposition has been successfully performed using multiple methods. Very high resolution growth features have been achieved using lithographic techniques, such as in the work by Teo *et al.* where the group was able to grow single nanotubes from nickel catalyst sites deposited in a sub-micron scale array.<sup>221</sup> In the absence of advanced lithography some researchers use physical masks that have features already defined, such as sample support grids used for transmission electron microscopy (TEM), where the holes in the mesh generally have dimensions in the order of tens of microns.<sup>36,222</sup>

In this research a physical mask was placed onto the silicon substrate during catalyst deposition. The mask used was a circular TEM grid (300 mesh Cu grid with lacey carbon support, ProSciTech Australia) with squares of 50  $\mu\text{m}$  sides. The result was a negative template with square islands of iron catalyst. Prior to masking the grid was cleaned in chloroform to remove the lacey carbon support and expose more of the underlying grid, however it was expected that some would still remain, potentially affecting the quality of the template. After catalyst deposition the surface was treated to the standard growth

procedure (650°C, 10 mins heating, 10 mins growth at 10 W, 80:20 Ar:CH<sub>4</sub>) and characterised using SEM and Raman.

Figure 8.10 shows SEM images of the patterned surface after growth; (a) the entire patterned surface, (b) a magnified view of the patterned CNT grid, (c) a single patterned square and (d) a high magnification image of the grown CNT surface. Each of the dashed squares indicates the region of the sample that was magnified to produce the following image. A drawback to the simplicity of this masking technique is highlighted in (a) by arrows. The mask was not sitting flat on the surface during catalyst deposition and consequently there was significant ‘bleed-through’, resulting in a malformed template, as observed in the top left corner of the circular pattern. The effect of the residual lacey carbon support was observable in (b) where the holes in the support resulted in patchy coverage within each of the squares. A single patterned square is imaged in (c) with the dimensions measured as 60×60 μm<sup>2</sup>. The extra area is likely to be from ill-defined catalyst deposition due to the mask not sitting flat on the surface. The CNT growth is pictured in (d). The definition of fine nanotube structure was not achievable due in part to the resolution limits of the SEM used in this work, and the difficulty in gaining contrast between the CNTs and the surface at high magnification.

Results from the Raman characterisation of the patterned surface are given in figure 8.11. Spectrographic images were obtained across the patterned region with an example shown as the inset within (a), generated by the intensity of the G band taken over a 50×50 μm<sup>2</sup> area. The yellow areas represent the regions of highest G band intensity and thus where nanotube growth has occurred. In contrast, the dark areas represent the masked silicon, where no growth was produced and only the background signal was detected. The blue and green spectra given are averages obtained from the patterned and masked areas in the image respectively. The highest intensity regions within the patterned area produce Raman spectra showing SWCNT growth with, on average, an I<sub>D</sub>/I<sub>G</sub> of 0.17 ± 0.03, and an average diameter of 1.58 ± 0.07 nm. The spectra within the features were found to be reasonably regular suggesting consistent growth throughout each patterned feature, although as stated previously the remaining lacey carbon support on the grid resulted in a somewhat inhomogeneous catalyst deposition in some patterned areas resulting in incomplete coverage.

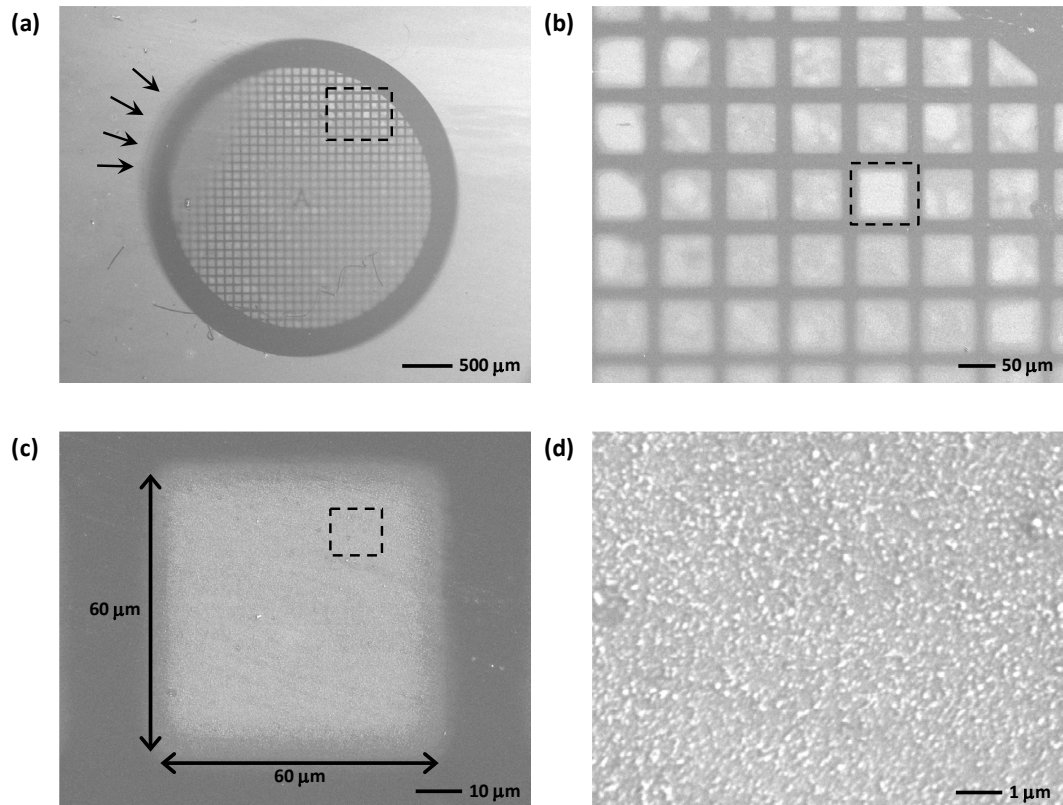


**Figure 8.10. SEM images of patterned SWCNT growth on silicon via the use of a TEM grid as a mask during catalyst deposition. Each image shows the progressive magnification of the dashed area in the previous image.**

Presented in figure 8.11(b) is a cross-sectional analysis of a patterned region allowing the generation of a plot of the G band intensity as a function of distance across the feature. The red line on the image represents the cross section taken, with the resultant intensity plot given on the right hand side. The distance across the highest intensity section of the plot was found to be  $\sim 50 \mu\text{m}$ , in good agreement with the known dimensions of the holes in the TEM grid used to produce the pattern. The G band intensity does not immediately fall to zero at the edges. Rather, a steady decrease in intensity was observed over a distance of  $\sim 5 \mu\text{m}$ . This observation is consistent with that observed from SEM analysis, where it was seen that as a result of the grid not sitting flat on the surface the catalyst deposition and thus growth was imperfect, producing features with widths of  $\sim 60 \mu\text{m}$ .

Spectra were extracted from regular intervals (0 – 21  $\mu\text{m}$ , separated by 3  $\mu\text{m}$ ) along the cross section and are given in figure 8.11(c). The position that each spectrum was retrieved from is indicated by the markers on the plot in (b). Not only was the gradual increase in intensity of the G band observable here, but also an interesting side effect of the imperfect

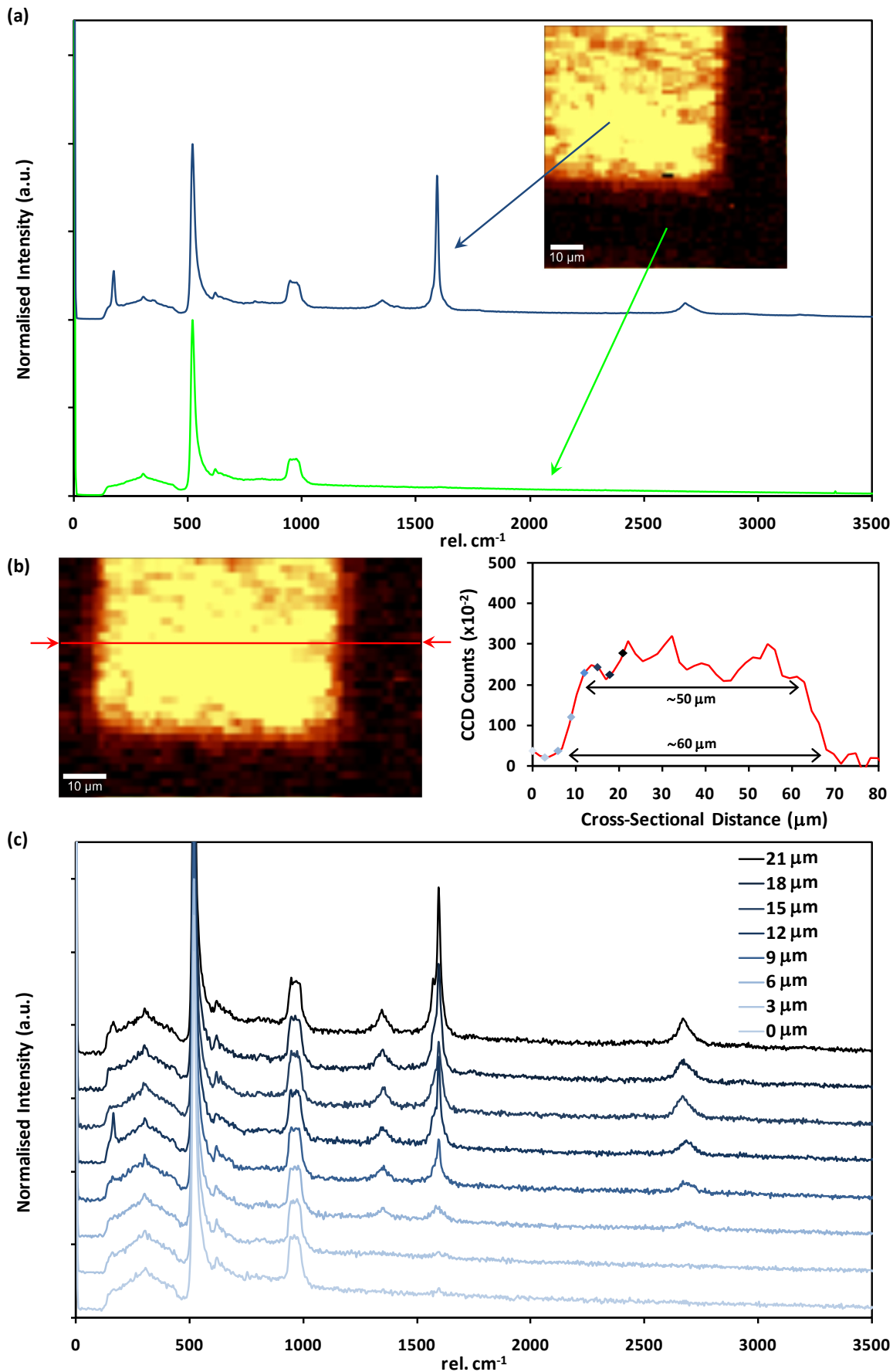


Figure 8.11. Raman characterisation of the patterned SWCNT growth on silicon; (a) spectra from the patterned and masked region, (b) and (c) cross-sectional analysis of the feature.

deposition process. At the onset of the feature,  $\sim 6 \mu\text{m}$  along the cross section, both D and G band phonons were observable in the spectra, with a ratio close to unity. This is suggestive of either highly disordered growth, or the presence of multi-walled CNTs. As one moves further into the feature the ratio quickly decreases, producing spectra familiar to SWCNT growth, with an RBM present in some spectra. This analysis suggests that there may be a higher level of multi-walled growth at the edges of the patterns compared to the centre, perhaps indicating poor nanoparticle formation on the periphery of the features.

### **8.5. Summary of PECVD Nanotube Growth Studies**

Carbon nanotube research at Flinders is extensive, with a significant focus within the field of photovoltaics. The CNTs are generally purchased from external sources, and arrive in a form that requires significant chemical treatment prior to their incorporation into devices. This can be likened to Nessim's 'grow-then-place' methodology, a drawback of which is less than optimal control over placement of nanotubes on a device substrate.<sup>39</sup> As a result there was a desire to develop methods towards the growth of CNTs directly onto a desired substrate. Some research into thermal CVD had been performed at Flinders, although the process was typically performed at temperatures in excess of  $900 \text{ }^\circ\text{C}$ , and would generally result in multi-walled growth. For photovoltaics, where the substrate would typically be a transparent soft glass, such elevated temperatures are unacceptable. To remedy this, the technique of plasma-enhanced CVD was investigated using the already established rf plasma system at Flinders in an attempt to establish a proof-of-principle for the growth of single-walled CNTs directly onto a given substrate at significantly reduced temperatures.

SWCNT growth was achieved by heating silicon substrates coated with iron catalyst to temperatures ranging from  $450$  to  $650 \text{ }^\circ\text{C}$  in the presence of plasma ignited within an argon/methane mixture at a ratio of 80:20. Raman spectroscopy revealed high quality single-walled CNT growth with  $I_D/I_G$  found to be far less than 1 on average. Using either nickel as the catalyst, or an alumina layer underneath the iron resulted in poor quality growth. Using iron however, the greatest quality sample achieved a ratio of  $0.06 \pm 0.03$ , indicating extremely high levels of homogeneity, comparable to that obtained from purchased CNTs. Nanotube diameters were found to be between  $1.5$  and  $1.7 \text{ nm}$ . An observed transition from single- to multi-walled growth occurred with decreasing growth temperature and increasing growth time.

Patterned CNT growth was also demonstrated. This was achieved through the masked deposition of the catalyst using a TEM grid as a template. An array of  $50 \times 50 \mu\text{m}^2$  squares of CNTs resulted after growth, again with high levels of homogeneity. The masking technique used did not produce perfect islands of catalyst. Instead, some edge effects were present which resulted in the features having dimensions  $10 \mu\text{m}$  larger than the template. These effects also resulted in the outer edge of the features having significant multi-walled content compared to the centre which largely consisted of single-walled CNTs.

---

## Chapter 9.

# CONCLUSION

### 9.1. Key Outcomes

This dissertation has focussed on applied rf plasma processing techniques to the fluorination, and also the growth, of single-walled carbon nanotubes. This involved the use of varied plasma environments; sulphur hexafluoride plasma provided an environment that resulted in fluorine functionalised CNTs, while the application of methane-argon mixed plasma to heated catalytic substrates generated CNT growth. The various aspects of the experiments were characterised, including the physics of the plasma state, as well as the resultant functionalisation and growth of the structures.

The plasma state was characterised using a Langmuir probe apparatus. Upon application to SF<sub>6</sub> plasma it was found that the plasma density displayed a curious oscillation that was the result of instability within the SF<sub>6</sub> plasma. This created difficulty in elucidating trends in the plasma properties with variation in experimental parameters. The instability created periodic fluctuations in measured probe current at constant bias voltage and were most prominent in the electron current, i.e. at high positive probe bias. The fluctuations occurred within a discrete range of pressure and power parameters, outside of which the plasma was quiescent. They were observed to occur with a frequency of tens of Hertz, with the lowest

measured at  $\sim 10$  Hz and the greatest at  $\sim 80$  Hz. Due to the low frequency at which the instability was presented, it was visible to the naked eye as a fluctuation of the main plasma density radially outward from the antenna. With this observation the instability was hypothesised to manifest as a radially expanding wave throughout the plasma chamber. By moving the Langmuir probe radially outward from centre of the chamber, the speed at which the ‘instability wave’ travels was determined to be  $16.3 \pm 1.0 \text{ ms}^{-1}$ .

Knowledge of the nature of the instability allowed modifications to be made to the Langmuir probe experiment which in turn enabled the characterisation of  $\text{SF}_6$  plasma. This was achieved by sampling at shorter time intervals than a single instability cycle, thus ensuring the plasma was essentially steady-state for each Langmuir probe measurement. Upon characterisation, the self-bias voltage on the source was found to increase linearly with absorbed rf power, and the rate of increase was greater for lower pressures. Overall the greatest bias voltage was found to be  $-430 \text{ V}$  for  $2.5 \text{ mTorr SF}_6$  plasma at  $80 \text{ W}$ , while the lowest was found to be  $-70 \text{ V}$  for  $\text{SF}_6$  plasma at  $11 \text{ W}$ , regardless of pressure. Ion and electron densities were found to also depend on absorbed rf power and gas pressure. Electron densities increased with power and also with decreasing pressure although the effect was most prominent with variation in power. A maximum experimentally determined electron density of  $1.7 \times 10^8 \text{ cm}^{-3}$  was achieved. Ion density was observed to decrease with pressure. For plasma at pressures of  $2.5$  and  $5 \text{ mTorr}$  the electrons could be described by a single distribution of temperatures that were independent of absorbed rf power and had an average of  $\sim 7 \text{ eV}$ . At  $10 \text{ mTorr}$  however, the presence of a secondary distribution of ‘hot’ electrons was detected that reached a temperature of  $\sim 21 \text{ eV}$ .

Exposure of carbon nanotube surfaces to  $\text{SF}_6$  plasma resulted in fluorine functionalised structures that were characterised using primarily photoemission techniques. It was found that an exposure of only  $1$  minute at low rf power resulted in significant initial fluorine attachment, although the surfaces quickly degraded over a period of days to a level around half that of the initial value. Smaller diameter CNTs, as well as those that had metallic electronic structure, were found to be more susceptible to functionalisation. From initial XPS studies it was thought that the fluorination process occurred with no contamination by sulphur despite its inevitable presence in the plasma. However synchrotron radiation XPS clarified that there *was* a sulphur presence on the samples, although it was in such small concentration as to make it undetectable using conventional instrumentation.

It was found that oxygen species, either within the plasma environment or bound to the CNT surfaces, greatly influenced the amount and type of functionalisation present. This occurred through an increased breakdown of the SF<sub>6</sub> molecule. Plasma was ignited in mixtures of SF<sub>6</sub> and O<sub>2</sub> where the ratio of each component could be varied. After the initial doping of the SF<sub>6</sub> plasma and the accompanied increase in total fluorine attachment, no strong dependence was observed between oxygen content and fluorine concentration at the surface. The *type* of C-F bonding present at the surface however was significantly influenced by the amount of oxygen added to the SF<sub>6</sub>, and the relative covalency of the F1s peaks was found to decrease as oxygen was added. This was attributed to a decreasing fluorine concentration as the ratio shifted from pure SF<sub>6</sub> to pure O<sub>2</sub>. When the oxygen content at the CNT surface was modified, through either plasma or wet-chemical oxidation, the amount of fluorine attachment was found to be far superior to that of both the pure SF<sub>6</sub> and mixed SF<sub>6</sub>-O<sub>2</sub> plasma. Furthermore, the oxidative surface pretreatments resultant in C-F covalency as high as ~99% compared to only ~36% for an equivalent SF<sub>6</sub> exposure to CNTs with no pretreatment. No single pretreatment was found to stand out as having superiority, although the plasma oxidation allowed for a ‘one-pot’ process whereas each of the wet-chemical techniques required significant sample processing prior to fluorination.

Motivated by the desire to develop a method for the growth of single-walled CNTs at lower temperatures than typical thermal CVD growth methods, the technique of plasma-enhanced CVD was developed using the rf plasma system. Growth was achieved through the deposition of 5 nm of iron catalyst onto silicon which was subsequently heated to temperatures of 450 – 650 °C, and exposed to plasma of argon and methane. XPS results indicated that the catalyst was deposited as Fe<sub>2</sub>O<sub>3</sub> and formed into metallic iron after growth. Raman spectroscopy revealed high quality single-walled CNT growth on iron catalysts with ratios of I<sub>D</sub>/I<sub>G</sub> found on average to be far less than 1 with the greatest quality sample achieving a ratio of 0.06 ± 0.03 indicating extremely high levels of homogeneity. Nanotube diameters were found to be between 1.5 and 1.7 nm. Variations in experimental parameters resulted in a transition from single- to multi-walled growth with decreasing growth temperature and increasing growth time. Patterned CNT growth was demonstrated via the masked deposition of the catalyst using a TEM grid as a template. An array of 50×50 μm<sup>2</sup> squares of CNTs growth was achieved, again with high levels of homogeneity.

## 9.2. Future Work and Recommendations

The research in this dissertation investigated some specific plasma processes with an aim to develop a greater fundamental understanding of their impact on, and application towards, nanotechnology. This work however is far from a complete study, with many questions remaining to be answered, and research avenues yet to be explored.

The sulphur hexafluoride plasma environment within the rf plasma chamber was characterised using an in-house built Langmuir probe apparatus. This technique provides key *physical* information, yet falls short when it comes to detailed *chemical* properties of the plasma. To fill this void, Langmuir probes are often accompanied by other diagnostic instruments such as mass spectrometry and optical emission spectroscopy. In this work, while an understanding of the physical behaviour of the plasma under different experimental conditions was useful, a thorough understanding of the gas-phase chemistry would provide a complementary level of insight into the functionalisation of CNT surfaces in sulphur hexafluoride plasma. For example, consider the experiments studying the addition of O<sub>2</sub> to SF<sub>6</sub>. It was concluded from previous work that the addition of oxygen enabled a greater level of breakdown of the hexafluoride molecule, which lead to greater atomic fluorine concentration. By monitoring the light intensity of a specific wavelength such as the fluorine line at 703.7 nm using an optical spectrometer, changes in fluorine concentration could be quantified. Furthermore, another level of characterisation would provide a greater understanding of the nature of the density oscillation observed in SF<sub>6</sub> plasma and whether it influenced the total number of reactive fluorine species. Many small-scale optical spectrometers are available that can be interfaced with programming environments such as LabVIEW, and routinely achieve spectral resolution down to 200 nm, which would cover a majority of the desirable emission lines in SF<sub>6</sub> plasma.

Further insight into the nature of the instability could also be achieved through controlled timing of the Langmuir probe apparatus. For example, if the experiment was controlled in such a way as to only obtain the I-V characteristic when the SF<sub>6</sub> plasma was in a single state, i.e. the low or high density state, then a more detailed understanding of the plasma in each of these limiting cases could be elucidated. Such an experiment would however require very careful experimental design, while also presenting a multitude of problems due largely to the observation that very few experimental domains of rf power and gas pressure were amenable to very regular oscillations.

Carbon nanotube surfaces were exposed to sulphur hexafluoride plasma. This was shown to be an effective way of introducing fluorine-rich functionality to these otherwise generally inert structures. While some intriguing aspects of this fluorination mechanism were investigated a great level of optimisation still remains to be elucidated. Specifically, the effect of gas pressure on the extent of functionalisation was not investigated in this work, largely due to instrumental setbacks. Since it was concluded that fluorine concentration has an impact on the level of covalency in C-F bonds, adjustment of the gas pressure in the plasma environment would provide another level of control of the bond structure found at the CNT surface. Additionally, lower gas pressures tend to aid the dispersion of the plasma thus providing a greater level of homogeneity throughout the chamber and possibly improving reproducibility.

Many researchers wanting to functionalise carbon surfaces with fluorine species opt for an elevated temperature gas flow reaction, often using  $F_2$  gas. Due to the reactivity of elemental fluorine, functionality has been observed at as low as room temperature, however very high levels of functionality are generally achieved at temperatures around 400 °C. With the addition of the heating apparatus used to grow single-walled CNTs in the chamber, a study investigating the controlled heating of nanotube surfaces within  $SF_6$  plasma may uncover yet another level of control, and perhaps a method for further improving the quality of the fluorine attachment to CNTs.

It was thought that some amount of the observed fluorine functionality may be from weakly bound species. It was found that the C-F bonding present on the fluorinated CNTs could be attributed to a mixture of covalent and semi-ionic attachment. To further investigate this, an experiment that could controllably promote and measure the desorption of fluorine species from the surface would be desired. Such an experiment could be achieved using a technique known as temperature programmed desorption (or alternatively, thermal desorption spectroscopy). Under a vacuum environment the samples could be heated in a controlled manner and using a mass spectrometer the mass of the desorbed species, as well as the amount desorbed, could be measured. This would provide great insight into the type of bonding present at the surface, and help to monitor any improvements made towards C-F bond strength.

Single-walled carbon nanotubes were grown directly onto silicon substrates via the modification of the plasma chamber, and the development of a PECVD protocol. As with

many nanotube growth mechanisms the process was found to be highly sensitive to experimental parameters and as such in this work only a very narrow experimental regime was found that would reliably produce SWCNT growth. Even when growth was reliably achieved, the CNTs were found to be so short that they could not be imaged using the SEM instrument at Flinders, despite seemingly complete coverage of the substrate. Thus the yield of the PECVD process was very low, and not particularly applicable to much of the device applications investigated at Flinders. Through a thorough investigation of all the experimental parameters that govern the growth mechanism this process could no doubt be further optimised. This would require one of two avenues to be followed; either the established reaction system would need to be further modified, or a stand-alone system dedicated to the growth of carbon films could be commissioned. In each case some requirements would need to be addressed. Plasma density around the sample would need to be greatly improved, with the sample ideally situated within the main plasma density rather than remote as it was in this work. Very precise control over the gaseous environment would also be a necessity, preferably through the use of an automatic flow controller capable of delivering up to 4 individual reactants. A greater level of control over the substrate temperature would also be desired, as well as the ability to reliably heat well beyond 700 °C. Finally, the design of the substrate itself, including the catalyst layer would likely prove to be an extremely important factor in achieving high yield, homogeneous single-walled CNT growth.

Doping of carbon nanotubes during PECVD growth was not investigated in this thesis but would be a fascinating way of controlling the chemical and electrical properties of the resultant structures. The addition of sulphur hexafluoride into the plasma either during or after growth may be a method for the *in-situ* growth and subsequent functionalisation of single-walled CNTs with fluorine species. It is also known that sulphur promotes the growth of CNTs<sup>223</sup> and is used in some industrial scale processes to increase yield. Thus the added benefit of having a sulphur containing species within the plasma may also provide an increased yield.

---

## REFERENCES

1. Lieberman, M. A.; Lichtenberg, A. J., *Principles of Plasma Discharges and Materials Processing*. Second ed.; John Wiley & Sons: New Jersey, 2005.
2. Banerjee, S.; Hemraj-Benny, T.; Wong, S. S., Covalent Surface Chemistry of Single-Walled Carbon Nanotubes. *Adv. Mater.* **2005**, *17* (1).
3. Kruger, D. H.; Schneck, P.; Gelderblom, H. R., Helmut Ruska and the visualisation of viruses. *The Lancet* **2000**, *355* (9216), 1713-1717.
4. Feynman, R., There's Plenty of Room at the Bottom. *Engineering and Science* **1960**, *23* (5).
5. *Nobel Lectures in Physics 1981-1990*. World Scientific Publishing Company, Incorporated: 1993.
6. Norwegian Academy of Science and Letters, Kavli Prize in Nanoscience 2010. <http://www.kavliprize.no/binfil/download.php?tid=47205> (accessed 13/9/2011).
7. *Nobel Lectures in Chemistry 1996-2000*. World Scientific Publishing Company, Incorporated: 2003.
8. Bethune, D. S.; Klang, C. H.; de Vries, M. S.; Gorman, G.; Savoy, R.; Vazquez, J.; Beyers, R., Cobalt-catalysed growth of carbon nanotubes with single-atomic-layer walls. *Nature* **1993**, *363* (6430), 605-607.
9. Iijima, S., Helical Microtubules of Graphitic Carbon. *Nature* **1991**, *354*, 56-58.
10. Iijima, S.; Ichihashi, T., Single-shell carbon nanotubes of 1-nm diameter. *Nature* **1993**, *363* (6430), 603-605.
11. Monthieux, M.; Kuznetsov, V. L., Who should be given the credit for the discovery of carbon nanotubes? *Carbon* **2006**, *44* (9), 1621-1623.
12. Radushkevich, L. V.; Lukyanovich, V. M., O strukture ugleroda, obrazujucesja pri termiceskom razlozenii okisi ugleroda na zeleznom kotakte. *Zurn Fisic Chim* **1952**, *26*, 88-95.

13. Hamada, N.; Sawada, S.-i.; Oshiyama, A., New One-Dimensional Conductors: Graphitic Microtubules. *Phys. Rev. Lett.* **1992**, *68* (10), 1579-1581.
14. Radosavljevic, M.; Lefebvre, J.; Johnson, A. T., High-field electrical transport and breakdown in bundles of single-wall carbon nanotubes. *Physical Review B* **2001**, *64* (24), 241307.
15. Yao, Z.; Kane, C. L.; Dekker, C., High-Field Electrical Transport in Single-Wall Carbon Nanotubes. *Physical Review Letters* **2000**, *84* (13), 2941.
16. Treacy, M. M. J.; Ebbesen, T. W.; Gibson, J. M., Exceptionally high Young's modulus observed for individual carbon nanotubes. *Nature* **1996**, *381* (6584), 678-680.
17. Falvo, M. R.; Clary, G. J.; Taylor, R. M.; Chi, V.; Brooks, F. P.; Washburn, S.; Superfine, R., Bending and buckling of carbon nanotubes under large strain. *Nature* **1997**, *389* (6651), 582-584.
18. Kinoshita, K., *Carbon: Electrochemical and Physicochemical Properties*. Wiley: New York, 1988.
19. Bruhwiler, P. A., Synchrotron studies of carbon surfaces. *J. Phys.: Condens. Matt.* **2001**, *13* (49), 11229-11248.
20. Dresselhaus, M. S.; Dresselhaus, G.; Saito, R., Physics of Carbon Nanotubes. *Carbon* **1995**, *33* (7), 883-891.
21. Saito, R.; Dresselhaus, G.; Dresselhaus, M. S., *Physical Properties of Carbon Nanotubes*. Imperial College Press: London, 1998.
22. Belin, T.; Epron, F., Characterization methods of carbon nanotubes: a review. *Materials Science and Engineering B* **2005**, *119* (2), 105-118.
23. Dresselhaus, M. S.; Dresselhaus, G.; Jorio, A., Unusual properties and structure of carbon nanotubes. *Annual Review of Materials Research* **2004**, *34* (1), 247-278.
24. Banerjee, S.; Hemraj-Benny, T.; Wong, S. S., Routes Towards Separating Metallic and Semiconducting Nanotubes. *J. Nanosci. Nanotech.* **2005**, *5*, 841-855.
25. Kuzmany, H.; Kukovecz, A.; Simon, F.; Holzweber, M.; Kramberger, C.; Pichler, T., Functionalization of carbon nanotubes. *Synthetic Metals* **2004**, *141* (1-2), 113-122.
26. Bahr, J. L.; Tour, J. M., Covalent chemistry of single-wall carbon nanotubes. *J. Mater. Chem.* **2002**, *12*, 1952-1958.
27. Hirsch, A., Functionalisation of Single-Walled Carbon Nanotubes. *Angew. Chem. Int. Ed.* **2002**, *41* (11), 1853-1859.
28. Hirsch, A.; Vostrowsky, O., Functionalization of Carbon Nanotubes. *Top Curr. Chem.* **2005**, *245*, 193-237.
29. Liu, M.; Yang, Y.; Zhu, T.; Liu, Z., Chemical modification of single-walled carbon nanotubes with peroxytrifluoroacetic acid. *Carbon* **2005**, *43*, 1470-1478.
30. Niyogi, S.; Hamon, M. A.; Hu, H.; B. Zhao; Bhowmik, P.; Sen, R.; Itkis, M. E.; Haddon, R. C., Chemistry of Single-Walled Carbon Nanotubes. *Acc. Chem. Res.* **2002**, *35*, 1105-1113.
31. Lu, X.; Chen, Z., Curved Pi-Conjugation, Aromaticity, and the Related Chemistry of Small Fullerenes (<C60) and Single-Walled Carbon Nanotubes. *Chem. Rev.* **2005**, *105*, 3643-3696.
32. Lu, X.; Chen, Z.; Schleyer, P. v. R., Are Stone-Wales Defect Sites Always More Reactive Than Perfect Sites in the Sidewalls of Single-Wall Carbon Nanotubes? *J. Am. Chem. Soc.* **2005**, *127* (1), 20-21.
33. Terrones, M., Science and Technology of the Twenty-First Century: Synthesis, Properties, and Applications of Carbon Nanotubes. *Annual Review of Materials Research* **2003**, *33* (1), 419-501.

34. Guo, T.; Nikolaev, P.; Thess, A.; Colbert, D. T.; Smalley, R. E., Catalytic growth of single-walled nanotubes by laser vaporization. *Chem. Phys. Lett.* **1995**, *243* (1-2), 49-54.
35. Dai, H., Carbon nanotubes: opportunities and challenges. *Surface Science* **2002**, *500* (1-3), 218-241.
36. Delzeit, L.; Nguyen, C. V.; Stevens, R. M.; Han, J.; Meyyappan, M., Growth of carbon nanotubes by thermal and plasma chemical vapour deposition processes and applications in microscopy. *Nanotechnology* **2002**, *13* (3), 280.
37. Journet, C.; Maser, W. K.; Bernier, P.; Loiseau, A.; de la Chapelle, M. L.; Lefrant, S.; Deniard, P.; Lee, R.; Fischer, J. E., Large-scale production of single-walled carbon nanotubes by the electric-arc technique. *Nature* **1997**, *388* (6644), 756-758.
38. Meyyappan, M., A review of plasma enhanced chemical vapour deposition of carbon nanotubes. *Journal of Physics D: Applied Physics* **2009**, *42* (21), 213001.
39. Nessim, G. D., Properties, synthesis, and growth mechanisms of carbon nanotubes with special focus on thermal chemical vapor deposition. *Nanoscale* **2010**, *2* (8), 1306-1323.
40. Nikolaev, P.; Bronikowski, M. J.; Bradley, R. K.; Rohmund, F.; Colbert, D. T.; Smith, K. A.; Smalley, R. E., Gas-phase catalytic growth of single-walled carbon nanotubes from carbon monoxide. *Chem. Phys. Lett.* **1999**, *313* (1-2), 91-97.
41. Bronikowski, M. J.; Willis, P. A.; Colbert, D. T.; Smith, K. A.; Smalley, R. E., Gas-phase production of carbon single-walled nanotubes from carbon monoxide via the HiPco process: A parametric study. *journal article* **2001**, *19*, 1800-1805.
42. Vargas-Garcia, J. R.; Goto, T., Catalytic materials prepared by chemical vapor deposition. *IOP Conference Series: Materials Science and Engineering* **2011**, *20* (1), 012001.
43. Harsha, K. S. S., *Principles of Vapor Deposition of Thin Films*. Elsevier: 2006.
44. Gracio, J. J.; et al., Diamond growth by chemical vapour deposition. *Journal of Physics D: Applied Physics* **2010**, *43* (37), 374017.
45. Page, A. J.; Ohta, Y.; Irle, S.; Morokuma, K., Mechanisms of Single-Walled Carbon Nanotube Nucleation, Growth, and Healing Determined Using QM/MD Methods. *Accounts of Chemical Research* **2010**, *43* (10), 1375-1385.
46. Sinnott, S. B.; Andrews, R.; Qian, D.; Rao, A. M.; Mao, Z.; Dickey, E. C.; Derbyshire, F., Model of carbon nanotube growth through chemical vapor deposition. *Chem. Phys. Lett.* **1999**, *315* (1-2), 25-30.
47. Valentini, L.; Puglia, D.; Carniato, F.; Boccaleri, E.; Marchese, L.; Kenny, J. M., Use of plasma fluorinated single-walled carbon nanotubes for the preparation of nanocomposites with epoxy matrix. *Composites Science and Technology* **2008**, *68* (3-4), 1008-1014.
48. Khabashesku, V. N.; Billups, W. E.; Margrave, J. L., Fluorination of Single-Wall Carbon Nanotubes and Subsequent Derivatization Reactions. *Acc. Chem. Res.* **2002**, *35* (12), 1087-1095.
49. Taylor, R., Progress in fullerene fluorination. *Russian Chemical Bulletin* **1998**, *47* (5), 823-832.
50. Dunlap, B. I.; Brenner, D. W.; Mintmire, J. W.; Mowrey, R. C.; White, C. T., Geometric and electronic structures of C<sub>60</sub>H<sub>60</sub>, C<sub>60</sub>F<sub>60</sub>, and C<sub>60</sub>H<sub>36</sub>. *The Journal of Physical Chemistry* **1991**, *95* (15), 5763-5768.
51. Mickelson, E. T.; Huffman, C. B.; Rinzler, A. G.; Smalley, R. E.; Hauge, R. H.; Margrave, J. L., Fluorination of single-walled carbon nanotubes. *Chem. Phys. Lett.* **1998**, *296*, 188-194.

52. Mickelson, E. T.; Chiang, I. W.; Zimmerman, J. L.; Boul, P. J.; Lozano, J.; Liu, J.; Smalley, R. E.; Hauge, R. H.; Margrave, J. L., Solvation of Fluorinated Single-Wall Carbon Nanotubes in Alcohol Solvents. *J. Phys. Chem. B* **1999**, *103*, 4318-4322.
53. Cranford, S.; Yao, H.; Ortiz, C.; Buehler, M. J., A single degree of freedom 'lollipop' model for carbon nanotube bundle formation. *Journal of the Mechanics and Physics of Solids* **2010**, *58* (3), 409-427.
54. Kelly, K. F.; Chiang, I. W.; Mickelson, E. T.; Hauge, R. H.; Margrave, J. L.; Wang, X.; Scuseria, G. E.; Radloff, C.; Halas, N. J., Insight into the Mechanism of Sidewall Functionalization of Single-Walled Nanotubes: an STM Study. *Chem. Phys. Lett.* **1999**, *313*, 445-450.
55. Van Lier, G.; Ewels, C. P.; Zuliani, F.; De Vita, A.; Charlier, J.-C., Theoretical Analysis of Fluorine Addition to Single-Walled Carbon Nanotubes: Functionalization Routes and Addition Patterns. *The Journal of Physical Chemistry B* **2005**, *109* (13), 6153-6158.
56. Gu, Z.; Peng, H.; Hauge, R. H.; Smalley, R. E.; Margrave, J. L., Cutting Single Walled Carbon Nanotubes through Fluorination. *Nano Lett.* **2002**, *2* (9), 1009-1013.
57. Ziegler, K. J.; Gu, Z.; Shaver, J.; Chen, Z.; Flor, E. L.; Schmidt, D. J.; Chan, C.; Hauge, R. H.; Smalley, R. E., Cutting single-walled carbon nanotubes. *Nanotechnology* **2005**, *16*, S539-S544.
58. An, K. H.; Heo, J. G.; Jeon, K. G.; Bae, D. J.; Jo, C.; Yang, C. W.; Park, C.-Y.; Lee, Y. H.; Lee, Y. S.; Chung, Y. S., X-ray photoemission spectroscopy study of fluorinated single-walled carbon nanotubes. *Applied Physics Letters* **2002**, *80* (22), 4235-4237.
59. Park, K. A.; Choi, Y. S.; Lee, Y. H., Atomic and Electronic Structures of Fluorinated Single-Walled Carbon Nanotubes. *Phys. Rev. B* **2003**, *68*.
60. Peng, H.; Gu, Z.; Yang, J.; Zimmerman, J. L.; Willis, P. A.; Bronikowski, M. J.; Smalley, R. E.; Hauge, R. H.; Margrave, J. L., Fluorotubes as Cathodes in Lithium Electrochemical Cells. *Nano Lett.* **2001**, *1* (11), 625-629.
61. Chen, F. F., *Introduction to Plasma Physics and Controlled Fusion*. Plenum Press: New York, 1984; Vol. 1: Plasma Physics.
62. Fridman, A., *Plasma Chemistry*. Cambridge University Press: Cambridge, 2008.
63. Laroussi, M.; Lu, X., Room-temperature atmospheric pressure plasma plume for biomedical applications. *Appl. Phys. Lett.* **2005**, *87*, 113902.
64. Laroussi, M.; Tendero, C.; Lu, X.; Alla, S.; Hynes, W. L., Inactivation of Bacteria by the Plasma Pencil. *Plasma Processes and Polymers* **2006**, *3* (6-7), 470-473.
65. Schneider, J.; Baumgärtner, K. M.; Feichtinger, J.; Kräger, J.; Muranyi, P.; Schulz, A.; Walker, M.; Wunderlich, J.; Schumacher, U., Investigation of the practicability of low-pressure microwave plasmas in the sterilisation of food packaging materials at industrial level. *Surface and Coatings Technology* **2005**, *200* (1-4), 962-966.
66. Aanesland, A.; et al., Electric propulsion using ion-ion plasmas. *Journal of Physics: Conference Series* **2009**, *162* (1), 012009.
67. Frisbee, R. H., Advanced Space Propulsion for the 21st Century. *Journal of Propulsion and Power* **2003**, *19* (6), 1129-1154.
68. Mitterauer, J., Micropropulsion for small spacecraft: a new challenge for field effect electric propulsion and microstructured liquid metal ion sources. *Surface and Interface Analysis* **2004**, *36* (5-6), 380-386.
69. Swift, J. D.; Schwar, M. J. R., *Electrical probes for Plasma Diagnostics*. Elsevier: New York, 1969.

70. Merlino, R. L., Understanding Langmuir probe current-voltage characteristics. *American Journal of Physics* **2007**, *75* (12), 1078-1085.
71. Langmuir, I.; Mott-Smith, H. M., Studies of electric discharges in gases at low pressure. *Gen. Electr. Rev.* **1924**, *27* (449).
72. Mott-Smith, H. M.; Langmuir, I., The Theory of Collectors in Gaseous Discharges. *Physical Review* **1926**, *28* (4), 727.
73. Hershkowitz, N., How Langmuir Probes Work. In *Plasma Diagnostics*, Auciello, O.; Flamm, D. L., Eds. Academic Press: Boston, 1989; Vol. 1.
74. Boyd, T. J. M.; Sanderson, J. J., *The Physics of Plasmas*. Cambridge University Press: Cambridge, 2003.
75. Chen, S.-L.; Sekiguchi, T., Instantaneous Direct-Display System of Plasma Parameters by Means of Triple Probe. *Journal of Applied Physics* **1965**, *36* (8), 2363-2375.
76. Kim, T. W.; Aydil, E. S., Spatial and temporal variation of ion flux in the presence of an instability in inductively coupled. *Plasma Sources Science and Technology* **2003**, *12* (2), 148.
77. Chen, F. F. In *Lecture Notes on Langmuir Probe Diagnostics*, Mini-Course on Plasma Diagnostics, IEEE-ICOPS (International Conference on Plasma Science) Meeting, Jeju, Korea, Jeju, Korea, 2003.
78. Hutchinson, I. M., Principles of Plasma Diagnostics. Cambridge Univ. Press: Cambridge, 1987.
79. Claves, D.; Li, H.; Dubois, M.; Ksari, Y., An unusual weak bonding mode of fluorine to single-walled carbon nanotubes. *Carbon* **2009**, *47* (11), 2557-2562.
80. Kawasaki, S.; Komatsu, K.; Okino, F.; Touhara, H.; Kataura, H., Fluorination of open- and closed-end single-walled carbon nanotubes. *Phys. Chem. Chem. Phys.* **2004**, *6* (8), 1769-1772.
81. Ricca, P. M., A Survey of the Acute Toxicity of Elemental Fluorine. *American Industrial Hygiene Association Journal* **1970**, *31* (1), 22-29.
82. Ho, K. K. C.; Lee, A. F.; Bismarck, A., Fluorination of carbon fibres in atmospheric plasma. *Carbon* **2007**, *45* (4), 775-784.
83. Tressaud, A.; Durand, E.; Labrugere, C., Surface modification of several carbon-based materials: comparison between CF<sub>4</sub> rf plasma and direct F<sub>2</sub>-gas fluorination routes. *Journal of Fluorine Chemistry* **2004**, *125* (11), 1639-1648.
84. Hou, Z.; Cai, B.; Liu, H.; Xu, D., Ar, O<sub>2</sub>, CHF<sub>3</sub>, and SF<sub>6</sub> plasma treatments of screen-printed carbon nanotube films for electrode applications. *Carbon* **2008**, *46* (3), 405-413.
85. Kalita, G.; Adhikari, S.; Aryal, H. R.; Ghimre, D. C.; Afre, R.; Soga, T.; Sharon, M.; Umeno, M., Fluorination of multi-walled carbon nanotubes (MWNTs) via surface wave microwave (SW-MW) plasma treatment. *Physica E: Low-dimensional Systems and Nanostructures* **2008**, *41* (2), 299-303.
86. Khare, B. N.; Wilhite, P.; Meyyappan, M., The Fluorination of Single-Wall Carbon Nanotubes using Microwave Plasma. *Nanotechnology* **2004**, *15*, 1650-1654.
87. Plank, N. O. V.; Cheung, R., Functionalisation of Carbon Nanotubes for Molecular Electronics. *Microelectron. Eng.* **2004**, *73-74*, 578-582.
88. Plank, N. O. V.; Forrest, G. A.; Cheung, R.; Alexander, A. J., Electronic Properties of n-type Carbon Nanotubes Prepared by CF<sub>4</sub> Plasma Fluorination and Amino Functionalisation. *J. Phys. Chem. Lett. B* **2005**, *109*, 22096-22101.
89. Plank, N. O. V.; Jiang, L.; Cheung, R., Fluorination of Carbon Nanotubes in CF<sub>4</sub> Plasma. *Appl. Phys. Lett.* **2003**, *83* (12), 2426-2428.

90. Shoda, K.; Kohno, H.; Kobayashi, Y.; Takagi, D.; Takeda, S., Feasibility study for sidewall fluorination of SWCNTs in CF<sub>4</sub> plasma. *Journal of Applied Physics* **2008**, *104* (11), 113529-6.
91. Shoda, K.; Takeda, S., Systematic characterization of carbon nanotubes functionalized in CF<sub>4</sub> plasma. *Japanese Journal of Applied Physics Part 1-Regular Papers Brief Communications & Review Papers* **2007**, *46* (12), 7977-7982.
92. Shoda, K.; Takeda, S., Transmission Electron Microscopy Study on the Surface Properties of CNTs and Fullerites Exposed to CF<sub>4</sub> Plasma. *Mater. Res. Soc. Symp. Proc.* **2007**, *1018*.
93. Valentini, L.; Puglia, D.; Armentano, I.; Kenny, J. M., Sidewall functionalization of single-walled carbon nanotubes through CF<sub>4</sub> plasma treatment and subsequent reaction with aliphatic amines. **2005**.
94. Malik, N. H.; Qureshi, A. H., A Review of Electrical Breakdown in Mixtures of SF<sub>6</sub> and Other Gases. *Electrical Insulation, IEEE Transactions on* **1979**, *EI-14* (1), 1-13.
95. Auciello, O.; Sumant, A. V., Status review of the science and technology of ultrananocrystalline diamond (UNCD(TM)) films and application to multifunctional devices. *Diamond and Related Materials* **2010**, *19* (7-9), 699-718.
96. Hamelmann, F.; Aschentrup, A.; Brechling, A.; Heinzmann, U.; Abrashev, M.; Szekeres, A.; Gesheva, K., Plasma-assisted deposition of thin carbon films from methane and the influence of the plasma parameters and additional gases. *Vacuum* **2004**, *76* (2-3), 139-142.
97. Patsalas, P., Optical properties of amorphous carbons and their applications and perspectives in photonics. *Thin Solid Films* **2011**, *519* (12), 3990-3996.
98. Meyyappan, M., Plasma nanotechnology: past, present and future. *Journal of Physics D: Applied Physics* **2011**, *44* (17), 174002.
99. Lim, S.; Luo, Z.; Shen, Z.; Lin, J., Plasma-Assisted Synthesis of Carbon Nanotubes. *Nanoscale Research Letters* **2010**, *5* (9), 1377 - 1386.
100. Meyyappan, M.; et al., Carbon nanotube growth by PECVD: a review. *Plasma Sources Science and Technology* **2003**, *12* (2), 205.
101. Ostrikov, K., Plasma nanoscience: setting directions, tackling grand challenges. *Journal of Physics D: Applied Physics* **2011**, *44* (17), 174001.
102. Deslandes, A.; Jasieniak, M.; Ionescu, M.; Shapter, J. G.; Quinton, J. S., Hydrogenation of sp<sup>2</sup>-bonded carbon surfaces using methane plasma. *Applied Surface Science* **2010**, *256* (6), 1888-1894.
103. Priest, J. M. Langmuir Probe Measurements in rf Nitriding Plasmas. University of New England, Armidale, NSW, 1996.
104. Kanai, Y.; Grossman, J. C., Role of Semiconducting and Metallic Tubes in P3HT/Carbon-Nanotube Photovoltaic Heterojunctions: Density Functional Theory Calculations. *Nano Letters* **2008**, *8* (3), 908-912.
105. Priest, J. M.; Baldwin, M. J.; Fewell, M. P., The action of hydrogen in low-pressure r.f.-plasma nitriding. *Surface and Coatings Technology* **2001**, *145* (1-3), 152-163.
106. Baldwin, M. J.; Short, K. T.; Tendys, J.; Collins, G. A.; Fewell, M. P.; Haydon, S. C.; Kumar, S., Rf-plasma nitriding of stainless steel. *Surface and Coatings Technology* **1998**, *98* (1-3), 1187-1191.
107. Priest, J. M.; Baldwin, M. J.; Fewell, M. P.; Haydon, S. C.; Collins, G. A.; Short, K. T.; Tendys, J., Low pressure r.f. nitriding of austenitic stainless steel in an industrial-style heat-treatment furnace. *Thin Solid Films* **1999**, *345*, 113-118.
108. Deslandes, A. RF-Plasma Hydrogenation of sp<sup>2</sup>-bonded Carbon Surfaces. Flinders University, Adelaide, SA, 2009.

109. Siegbahn, K., Electron spectroscopy for atoms, molecules, and condensed matter. *Reviews of Modern Physics* **1982**, *54* (3), 709.
110. Jenkin, J. G.; Leckey, R. C. G.; Liesegang, J., The development of x-ray photoelectron spectroscopy: 1900-1960. *Journal of electron spectroscopy and related phenomena* **1977**, *12* (1), 1-35.
111. Einstein, A., Über einen die Erzeugung und Verwandlung des Lichtes betreffenden heuristischen Gesichtspunkt. *Annalen der Physik* **1905**, *322* (6), 132-148.
112. *Nobel Lectures in Physics 1901-1921*. World Scientific Publishing Co. Pte Ltd: 1998.
113. Persson, L., Pierre Auger-A Life in the Service of Science. *Acta Oncologica* **1996**, *35* (7), 785-787.
114. Sime, R. L., *Lise Meitner: a Life in Physics*. University of California Press: 1996.
115. Kibel, M. H., X-ray Photoelectron Spectroscopy. In *Surface Analysis Methods in Materials Science*, O'Connor, D. J.; Sexton, B. A.; Smart, R. S. C., Eds. Springer-Verlag: Berlin, 1992.
116. Seah, M. P.; Dench, W. A., Quantitative electron spectroscopy of surfaces: A standard data base for electron inelastic mean free paths in solids. *Surface and Interface Analysis* **1979**, *1* (1), 2-11.
117. Sigle, W., Analytical Transmission Electron Microscopy. *Annual Review of Materials Research* **2005**, *35* (1), 239-314.
118. Wojdyr, M., Fityk: a general-purpose peak fitting program. *Journal of Applied Crystallography* **2010**, *43* (5 Part 1), 1126-1128.
119. Lilienfeld, P., A Blue Sky History. *Opt. Photon. News* **2004**, *15* (6), 32-39.
120. *Nobel Lectures in Physics 1922-1941*. World Scientific Publishing Co. Pte Ltd: 1998.
121. Smith, E.; Dent, G., *Modern Raman Spectroscopy A Practical Approach*. John Wiley & Sons: West Sussex, 2005.
122. Long, D. A., *The Raman Effect A Unified Treatment of the Theory of Raman Scattering by Molecules*. John Wiley & Sons: West Sussex, 2002.
123. Dresselhaus, M. S.; Dresselhaus, G.; Saito, R.; Jorio, A., Raman spectroscopy of carbon nanotubes. *Physics Reports* **2005**, *409* (2), 47-99.
124. Amelinckx, S.; Dyk, D. v.; Landuyt, J. v.; Tendeloo, G. v., *Electron Microscopy Principles and Fundamentals*. Verlag: Weinheim, 1997.
125. Australian Synchrotron, Soft X-ray Beamline Factsheet. <http://www.synchrotron.org.au/images/stories/beamline/factsheets/synchrotron-factsheet-softxray.pdf> (accessed 23/9/2011).
126. Cowie, B. C. C.; Tadich, A.; Thomsen, L., The Current Performance of the Wide Range (90--2500 eV) Soft X-ray Beamline at the Australian Synchrotron. *AIP Conference Proceedings* **2010**, *1234* (1), 307-310.
127. Aanesland, A.; Charles, C.; Boswell, R. W.; Lieberman, M. A., Grounded radio-frequency electrodes in contact with high density plasmas. *Phys. Plasmas* **2005**, *12* (10), 103505.
128. Park, J. H.; Lee, N. E.; Lee, J.; Park, J. S.; Park, H. D., Deep dry etching of borosilicate glass using SF<sub>6</sub> and SF<sub>6</sub>/Ar inductively coupled plasmas. *Microelectronic Engineering* **2005**, *82* (2), 119-128.
129. d'Agostino, R.; Flamm, D. L., Plasma etching of Si and SiO<sub>2</sub> in SF<sub>6</sub>-O<sub>2</sub> mixtures. *Journal of Applied Physics* **1981**, *52* (1), 162-167.
130. Fukutaro, H.; et al., Modeling of Deep Si Etching in Two-Frequency Capacitively Coupled Plasma in SF<sub>6</sub>/O<sub>2</sub>. *Journal of Physics: Conference Series* **2007**, *86* (1), 012018.

131. Jiang, L.; Plank, N. O. V.; Cheung, R.; Brown, R.; Mount, A., Surface characterization of inductively coupled plasma etched SiC in SF<sub>6</sub>/O<sub>2</sub>. *Microelectronic Engineering* **2003**, *67-68*, 369-375.
132. Knizikevicius, R., Simulations of Si and SiO<sub>2</sub> etching in SF<sub>6</sub>+O<sub>2</sub> plasma. *Vacuum* **2009**, *83* (6), 953-957.
133. Manenschijn, A.; Janssen, G. C. A. M.; van der Drift, E.; Radelaar, S., The etching mechanism of titanium polycide in a mixture of SF<sub>6</sub> and O<sub>2</sub>. *Journal of Applied Physics* **1989**, *65* (8), 3226-3235.
134. Sreenidhi, T.; Baskar, K.; DasGupta, A.; DasGupta, N., Reactive ion etching of GaN in SF<sub>6</sub>+Ar and SF<sub>6</sub>+N<sub>2</sub> plasma. *Semiconductor Science and Technology* **2008**, *23* (12), 125019.
135. Tuszewski, M., An electronegative inductive discharge instability. *Journal of Applied Physics* **1996**, *79* (12), 8967-8975.
136. Lieberman, M. A.; Lichtenberg, A. J.; Marakhtanov, A. M., Instabilities in low-pressure inductive discharges with attaching gases. *Applied Physics Letters* **1999**, *75* (23), 3617-3619.
137. Chabert, P.; Lichtenberg, A. J.; Lieberman, M. A.; Marakhtanov, A. M., Instabilities in low-pressure electronegative inductive discharges. *Plasma Sources Science and Technology* **2001**, *10* (3), 478-489.
138. Lieberman, M. A.; Boswell, R. W., Modeling the transitions from capacitive to inductive to wave-sustained rf discharges. *J. Phys. IV France* **1998**, *08* (PR7), Pr7-145-Pr7-164.
139. Miyoshi, Y.; Petrovic, Z. L.; Makabe, T., Transition between capacitive and inductive mode in inductively coupled plasma observed by emission computerized tomography. *IEEE Transactions on Plasma Science* **2002**, *30* (1), 130-131.
140. Tuszewski, M.; White, R. R.; Wurden, G. A., Relaxation oscillations of low-frequency Ar/SF<sub>6</sub> inductive plasma discharges. *Plasma Sources Science and Technology* **2003**, *12* (3), 396-402.
141. Tuszewski, M.; White, R. R., Instabilities of Ar/SF<sub>6</sub> inductive plasma discharges. *Journal of Applied Physics* **2003**, *94* (5), 2858-2863.
142. Tuszewski, M.; Scarborough, W. K.; White, R. R., Spectrometry of 0.46 and 13.56 MHz Ar/SF<sub>6</sub> inductive plasma discharges. *Journal of Applied Physics* **2004**, *96* (4), 1811-1818.
143. Tuszewski, M.; Gary, S. P., Downstream instabilities of electronegative plasma discharges. *Phys. Plasmas* **2003**, *10* (2), 539-545.
144. Yeh, J. J.; Lindau, I., Atomic subshell photoionization cross sections and asymmetry parameters: 1<Z<103. *Atomic Data and Nuclear Data Tables* **1985**, *32* (1), 1-155.
145. Xie, Y.; Sherwood, P. M. A., X-ray photoelectron-spectroscopic studies of carbon fiber surfaces. 11. Differences in the surface chemistry and bulk structure of different carbon fibers based on poly(acrylonitrile) and pitch and comparison with various graphite samples. *Chemistry of Materials* **1990**, *2* (3), 293-299.
146. Moulder, J. F.; Stickle, W. F.; Sobol, P. E.; Bomben, K. D., *Handbook of X-ray Photoelectron Spectroscopy*. Perkin-Elmer Corporation: 1992.
147. Alemany, L. B.; Zhang, L.; Zeng, L. L.; Edwards, C. L.; Barron, A. R., Solid-state NMR analysis of fluorinated single-walled carbon nanotubes: Assessing the extent of fluorination. *Chem. Phys. Lett.* **2007**, *19* (4), 735-744.
148. Banerjee, S.; Wong, S. S., Selective Metallic Tube Reactivity in the Solution-Phase Osmylation of Single-Walled Carbon Nanotubes. *J. Am. Chem. Soc.* **2004**, *126* (7), 2073-2081.

149. Lee, Y. S.; Cho, T. H.; Lee, B. K.; Rho, J. S.; An, K. H.; Lee, Y. H., Surface properties of fluorinated single-walled carbon nanotubes. *J. Fluorine Chem.* **2003**, *120* (2), 99-104.
150. Marcoux, P. R.; Schreiber, J.; Batail, P.; Lefrant, S.; Renouard, J.; Jacob, G.; Albertini, D.; Mevellec, J.-Y., A spectroscopic study of the fluorination and defluorination reactions on single-walled carbon nanotubes. *Phys. Chem. Chem. Phys.* **2002**, *4* (11), 2278-2285.
151. Pulikkathara, M. X.; Kuznetsov, O. V.; Khabashesku, V. N., Sidewall Covalent Functionalization of Single Wall Carbon Nanotubes Through Reactions of Fluoronanotubes with Urea, Guanidine, and Thiourea. *Chemistry of Materials* **2008**, *20* (8), 2685-2695.
152. Shofner, M. L.; Khabashesku, V. N.; Barrera, E. V., Processing and Mechanical Properties of Fluorinated Single-Wall Carbon Nanotube-Polyethylene Composites. *Chemistry of Materials* **2006**, *18* (4), 906-913.
153. Shulga, Y. M.; Tien, T.-C.; Huang, C.-C.; Lo, S.-C.; Muradyan, V. E.; Polyakova, N. V.; Ling, Y.-C.; Loutfy, R. O.; Moravsky, A. P., XPS study of fluorinated carbon multi-walled nanotubes. *Journal of Electron Spectroscopy and Related Phenomena* **2007**, *160* (1-3), 22-28.
154. Takahiro, K.; Terai, A.; Oizumi, S.; Kawatsura, K.; Yamamoto, S.; Naramoto, H., Amorphization of carbon materials studied by X-ray photoelectron spectroscopy. *Nuclear Instruments and Methods in Physics Research Section B: Beam Interactions with Materials and Atoms* **2006**, *242* (1-2), 445-447.
155. Wang, Y.-Q.; Sherwood, P. M. A., Studies of Carbon Nanotubes and Fluorinated Nanotubes by X-ray and Ultraviolet Photoelectron Spectroscopy. *Chem. Mater.* **2004**, *16*, 5427-5436.
156. Wagner, C. D.; Davis, L. E.; Zeller, M. V.; Taylor, J. A.; Raymond, R. H.; Gale, L. H., Empirical atomic sensitivity factors for quantitative analysis by electron spectroscopy for chemical analysis. *Surface and Interface Analysis* **1981**, *3* (5), 211-225.
157. Filho, A. G. S.; et al., Raman spectroscopy for probing chemically/physically induced phenomena in carbon nanotubes. *Nanotechnology* **2003**, *14* (10), 1130.
158. Dartois, E.; Caro, G. M. M.; Deboffle, D.; Montagnac, G.; d'Hendecourt, L., Ultraviolet photoproduction of ISM dust. *A&A* **2005**, *432* (3), 895-908.
159. Chattopadhyay, D.; Galeska, I.; Papadimitrakopoulos, F., A Route for Bulk Separation of Semiconducting from Metallic Single-Wall Carbon Nanotubes. *J. Am. Chem. Soc.* **2003**, *125* (11), 3370-3375.
160. Lu, J.; Lai, L.; Luo, G.; Zhou, J.; Qin, R.; Wang, D.; Wang, L.; Mei, W. N.; Li, G.; Gao, Z.; Nagase, S.; Maeda, Y.; Akasaka, T.; Yu, D., Why Semiconducting Single-Walled Carbon Nanotubes are Separated from their Metallic Counterparts. *Small* **2007**, *3* (9), 1566-1576.
161. Knight, D. S.; White, W. B., Characterization of diamond films by Raman spectroscopy. *J. Mater. Res.* **1989**, *4*, 385-393.
162. Tuinstra, F.; Koenig, J. L., Raman Spectrum of Graphite. *The Journal of Chemical Physics* **1970**, *53* (3), 1126-1130.
163. Huong, P. V.; Cavagnat, R.; Ajayan, P. M.; Stephan, O., Temperature-dependent vibrational spectra of carbon nanotubes. *Physical Review B* **1995**, *51* (15), 10048.
164. Huang, F.; Yue, K. T.; Tan, P.; Zhang, S.-L.; Shi, Z.; Zhou, X.; Gu, Z., Temperature dependence of the Raman spectra of carbon nanotubes. *Journal of Applied Physics* **1998**, *84* (7), 4022-4024.

165. Chamssedine, F.; Claves, D., Three different modes of fluorine chemisorption at the surface of single wall carbon nanotubes. *Chem. Phys. Lett.* **2007**, *443* (1-3), 102-106.
166. Sato, Y.; Itoh, K.; Hagiwara, R.; Fukunaga, T.; Ito, Y., On the so-called "semi-ionic" C-F bond character in fluorine-GIC. *Carbon* **2004**, *42* (15), 3243-3249.
167. Hassanien, A.; Tokumoto, M.; Umek, P.; Vrbancic, D.; MZozetic; DMihailovic; Venturini, P.; Pejovnik, S., Selective etching of metallic single-wall carbon nanotubes with hydrogen plasma. *Nanotechnology* **2005**, *16*, 278-281.
168. Zhang, G.; Qi, P.; Wang, X.; Lu, Y.; Li, X.; Tu, R.; Bangsaruntip, S.; Mann, D.; Zhang, L.; Dai, H., Selective Etching of Metallic Carbon Nanotubes by Gas-Phase Reaction. *Science* **2006**, *314*, 974-977.
169. Yang, C.-M.; An, K. H.; Park, J. S.; Park, K. A.; Lim, S. C.; Cho, S.-H.; Lee, Y. S.; Park, W.; Park, C. Y.; Lee, Y. H., Preferential etching of metallic single-walled carbon nanotubes with small diameter by fluorine gas. *Phys. Rev. B* **2006**, *73*, 075419.
170. Gerson, A. R.; Cookson, D. J.; Prince, K. C., Synchrotron-Based Techniques. In *Handbook of Surface and Interface Analysis*, Second ed.; Riviere, J. C.; Myrha, S., Eds. Taylor & Francis: Boca Raton, 2009.
171. Banerjee, S.; Hemraj-Benny, T.; Sambasivan, S.; Fischer, D. A.; Misewich, J. A.; Wong, S. S., Near-Edge X-ray Absorption Fine Structure Investigations of Order in Carbon Nanotube-Based Systems. *Journal of Physical Chemistry B* **2005**, *109* (17), 8489-8495.
172. Brzhezinskaya, M.; Vinogradov, N.; Zimina, A.; Muradyan, V.; Shul'ga, Y.; Vinogradov, A., Characterization of fluorinated multiwalled carbon nanotubes with X-ray absorption, photoelectron and emission spectroscopies. *Applied Physics A: Materials Science & Processing* **2009**, *94* (3), 445-448.
173. Brzhezinskaya, M. M.; Vinogradov, A. S.; Krestinin, A. V.; Zvereva, G. I.; Kharitonov, A. P., Electronic Structure of Fluorinated Single-Walled Carbon Nanotubes Studied by X-Ray Absorption and Photoelectron Spectroscopy. *Fullerenes, Nanotubes and Carbon Nanostructures* **2010**, *18* (4-6), 590-594.
174. Davies, R. J.; Riekel, C.; Koziol, K. K.; Vilatela, J. J.; Windle, A. H., Structural studies on carbon nanotube fibres by synchrotron radiation microdiffraction and microfluorescence. *Journal of Applied Crystallography* **2009**, *42* (6), 1122-1128.
175. Karmakar, S.; Sharma, S. M.; Sood, A. K., Studies on high pressure behavior of carbon nanotubes: X-ray diffraction measurements using synchrotron radiation. *Nucl. Instrum. Methods Phys. Res., Sect. B* **2005**, *238* (1-4), 281-284.
176. Kim, S. Y.; Lee, J. Y.; Park, J.; Park, C. J.; Lee, C. J.; Shin, H.-J., Synchrotron X-ray photoelectron spectroscopy and field emission of double-walled carbon nanotubes - Dependence on growth temperature. *Chem. Phys. Lett.* **2006**, *420* (4-6), 271-276.
177. Schiessling, J.; Kjeldgaard, L.; Rohmund, F.; Falk, L. K. L.; Campbell, E. E. B.; Nordgren, J.; Br; hwiler, P. A., Synchrotron radiation study of the electronic structure of multiwalled carbon nanotubes. *J. Phys.: Condens. Matt.* **2003**, *15* (38), 6563-6579.
178. Wang, W.; Murthy, N. S.; Chae, H. G.; Kumar, S., Small-angle X-ray scattering investigation of carbon nanotube-reinforced polyacrylonitrile fibers during deformation. *Journal of Polymer Science Part B: Polymer Physics* **2009**, *47* (23), 2394-2409.
179. Wu, Z. Y.; Davoli, I.; Terranova, M. L.; Orlanducci, S.; Sessa, V.; Abbas, M.; Ibrahim, K.; Zhong, J.; Botti, S., Electronic characterization of the single-wall carbon nanotubes: a XANES study. *Physica Scripta* **2005**, *T115*, 717-720.
180. Tanuma, S.; Powell, C. J.; Penn, D. R., Calculations of electron inelastic mean free paths. *Surface and Interface Analysis* **2005**, *37* (1), 1-14.

181. Lindberg, B. J.; et al., Molecular Spectroscopy by Means of ESCA II. Sulfur compounds. Correlation of electron binding energy with structure. *Physica Scripta* **1970**, *1* (5-6), 286.
182. Clark, D. T.; Thomas, H. R., Applications of ESCA to polymer chemistry. XVII. Systematic investigation of the core levels of simple homopolymers. *Journal of Polymer Science: Polymer Chemistry Edition* **1978**, *16* (4), 791-820.
183. Pratt, A. R.; Muir, I. J.; Nesbitt, H. W., X-ray photoelectron and Auger electron spectroscopic studies of pyrrhotite and mechanism of air oxidation. *Geochimica et Cosmochimica Acta* **1994**, *58* (2), 827-841.
184. Smart, R. S. C.; Skinner, W. M.; Gerson, A. R., XPS of sulphide mineral surfaces: metal-deficient, polysulphides, defects and elemental sulphur. *Surface and Interface Analysis* **1999**, *28* (1), 101-105.
185. Nakamura, T.; Ohana, T.; Ishihara, M.; Hasegawa, M.; Koga, Y., Chemical modification of single-walled carbon nanotubes with sulfur-containing functionalities. *Diamond and Related Materials* **2006**, *16* (4-7), 1091-1094.
186. Ryan, K. R., Aspects of the Chemistry of SF<sub>6</sub>/O<sub>2</sub> Plasmas. *Plasma Chemistry and Plasma Processing* **1989**, *9* (4), 483-496.
187. Ryan, K. R.; Plumb, I. C., Gas-phase reactions in plasmas of SF<sub>6</sub> with O<sub>2</sub> in He. *Plasma Chemistry and Plasma Processing* **1988**, *8* (3), 263-280.
188. Ryan, K. R.; Plumb, I. C., Gas-Phase Combination Reactions of SF<sub>4</sub> and SF<sub>5</sub> with F in Plasmas of SF<sub>6</sub>. *Plasma Chemistry and Plasma Processing* **1988**, *8* (3), 281-291.
189. McIntyre, N. S.; Chan, T. C., Uses of Auger Electron and Photoelectron Spectroscopies in Corrosion Science. In *Practical Surface Analysis Vol. 1: Auger and X-ray Photoelectron Spectroscopy*, Second ed.; Briggs, D.; Seah, M. P., Eds. John Wiley & Sons: West Sussex, 1994.
190. Iacona, F.; Marletta, G., XPS study of radiation-induced modification of poly(butene-1-sulfone): Dependence on the energy deposition mechanism. *Nuclear Instruments and Methods in Physics Research Section B: Beam Interactions with Materials and Atoms* **2000**, *166-167*, 676-681.
191. Riviere, J. C., Instrumentation. In *Practical Surface Analysis Vol. 1: Auger and X-ray Photoelectron Spectroscopy*, Second ed.; Briggs, D.; Seah, M. P., Eds. John Wiley & Sons: West Sussex, 1994.
192. Barlow, A. J.; Quinton, J. S. In *SF<sub>6</sub> Plasma Functionalisation of Carbon Surfaces*, AIP 17th National Congress, Brisbane, Queensland, Brisbane, Queensland, 2006.
193. Herron, J. T., Thermochemical Data on Gas Phase Compounds of Sulfur, Fluorine, Oxygen, and Hydrogen Related to Pyrolysis and Oxidation of Sulfur Hexafluoride. *J. Phys. Chem. Ref. Data* **1986**, *16* (1), 6.
194. Liu, J.; Rinzler, A. G.; Dai, H.; Hafner, J. H.; Bradley, R. K.; Boul, P. J.; Lu, A.; Iverson, T.; Shelimov, K.; Huffman, C. B.; Rodriguez-Macias, F.; Shon, Y.-S.; Lee, T. R.; Colbert, D. T.; Smalley, R. E., Fullerene Pipes. *Science* **1998**, *280* (5367), 1253-1256.
195. Briggs, D.; Seah, M. P., *Practical Surface Analysis Vol. 1: Auger and X-ray Photoelectron Spectroscopy*. Second ed.; John Wiley & Sons: 1990.
196. Scofield, J. H., Hartree-Slater subshell photoionization cross-sections at 1254 and 1487 eV. *Journal of electron spectroscopy and related phenomena* **1976**, *8* (2), 129-137.
197. Marshall, M. W.; Popa-Nita, S.; Shapter, J. G., Measurement of functionalised carbon nanotube carboxylic acid groups using a simple chemical process. *Carbon* **2006**, *44*, 1137-1141.

198. Banerjee, S.; Kahn, M. G. C.; Wong, S. S., Rational Chemical Strategies for Carbon Nanotube Functionalization. *Chem. Eur. J.* **2003**, *9*, 1898-1908.
199. Hata, K.; Futaba, D. N.; Mizuno, K.; Namai, T.; Yumura, M.; Iijima, S., Water-Assisted Highly Efficient Synthesis of Impurity-Free Single-Walled Carbon Nanotubes. *Science* **2004**, *306* (5700), 1362-1364.
200. Teo, K. B. K.; Hash, D. B.; Lacerda, R. G.; Rupesinghe, N. L.; Bell, M. S.; Dalal, S. H.; Bose, D.; Govindan, T. R.; Cruden, B. A.; Chhowalla, M.; Amaratunga, G. A. J.; Meyyappan, M.; Milne, W. I., The Significance of Plasma Heating in Carbon Nanotube and Nanofiber Growth. *Nano Letters* **2004**, *4* (5), 921-926.
201. Chhowalla, M.; Teo, K. B. K.; Ducati, C.; Rupesinghe, N. L.; Amaratunga, G. A. J.; Ferrari, A. C.; Roy, D.; Robertson, J.; Milne, W. I., Growth process conditions of vertically aligned carbon nanotubes using plasma enhanced chemical vapor deposition. *Journal of Applied Physics* **2001**, *90* (10), 5308-5317.
202. Esconjauregui, S.; Whelan, C. M.; Maex, K., The reasons why metals catalyze the nucleation and growth of carbon nanotubes and other carbon nanomorphologies. *Carbon* **2009**, *47* (3), 659-669.
203. Swierczewska, M.; Rusakova, I.; Sitharaman, B., Gadolinium and europium catalyzed growth of single-walled carbon nanotubes. *Carbon* **2009**, *47* (13), 3139-3142.
204. Delzeit, L.; Nguyen, C. V.; Chen, B.; Stevens, R.; Cassell, A.; Han, J.; Meyyappan, M., Multiwalled Carbon Nanotubes by Chemical Vapor Deposition Using Multilayered Metal Catalysts. *The Journal of Physical Chemistry B* **2002**, *106* (22), 5629-5635.
205. Bissett, M. A.; Shapter, J. G., Electrochemistry and Photocurrent Response from Vertically-Aligned Chemically-Functionalized Single-Walled Carbon Nanotube Arrays. *Journal of The Electrochemical Society* **2011**, *158* (3), K53-K57.
206. Shearer, C. J.; Ellis, A. V.; Shapter, J. G.; Voelcker, N. H., Chemically Grafted Carbon Nanotube Surface Coverage Gradients. *Langmuir* **2010**, *26* (23), 18468-18475.
207. Shearer, C. J.; Yu, J.; O'Donnell, K. M.; Thomsen, L.; Dastoor, P. C.; Quinton, J. S.; Shapter, J. G., Highly resilient field emission from aligned single-walled carbon nanotube arrays chemically attached to n-type silicon. *Journal of Materials Chemistry* **2008**, *18* (47), 5753-5760.
208. Lee, Y. T.; Kim, N. S.; Park, J.; Han, J. B.; Choi, Y. S.; Ryu, H.; Lee, H. J., Temperature-dependent growth of carbon nanotubes by pyrolysis of ferrocene and acetylene in the range between 700 and 1000 Å°C. *Chemical Physics Letters* **2003**, *372* (5-6), 853-859.
209. Deslandes, A.; Shapter, J.; Lawrance, E.; Quinton, J. In *Preparation of Carbon Surfaces for Sensing Applications via Plasma Hydrogenation*, International Conference on Nanoscience and Nanotechnology, Brisbane, Queensland, 3/07/2006; Brisbane, Queensland, 2006.
210. Mao, M.; Bogaerts, A., Investigating the plasma chemistry for the synthesis of carbon nanotubes/nanofibres in an inductively coupled plasma enhanced CVD system: the effect of different gas mixtures. *Journal of Physics D: Applied Physics* **2010**, *43* (20), 205201.
211. Jung, Y. J.; Wei, B.; Vajtai, R.; Ajayan, P. M.; Homma, Y.; Prabhakaran, K.; Ogino, T., Mechanism of Selective Growth of Carbon Nanotubes on SiO<sub>2</sub>/Si Patterns. *Nano Letters* **2003**, *3* (4), 561-564.
212. Hahn, H.; Averback, R. S., The production of nanocrystalline powders by magnetron sputtering. *J. Appl. Phys.* **1990**, *67*, 1113-1115.

- 
213. Nie, M.; Sun, K.; Meng, D. D., Formation of metal nanoparticles by short-distance sputter deposition in a reactive ion etching chamber. *J. Appl. Phys.* **2009**, *106*, 054314.
214. Jain, S.; et al., Interface properties of iron oxide films. *Journal of Physics D: Applied Physics* **2004**, *37* (19), 2720.
215. Kukovitsky, E. F.; L'Vov, S. G.; Sainov, N. A.; Shustov, V. A.; Chernozatonskii, L. A., Correlation between metal catalyst particle size and carbon nanotube growth. *Chemical Physics Letters* **2002**, *355* (5-6), 497-503.
216. Delzeit, L.; Chen, B.; Cassell, A.; Stevens, R.; Nguyen, C.; Meyyappan, M., Multilayered metal catalysts for controlling the density of single-walled carbon nanotube growth. *Chemical Physics Letters* **2001**, *348* (5-6), 368-374.
217. Delzeit, L.; McAninch, I.; Cruden, B. A.; Hash, D.; Chen, B.; Han, J.; Meyyappan, M., Growth of multiwall carbon nanotubes in an inductively coupled plasma reactor. *J. Appl. Phys.* **2002**, *91*, 6027-6033.
218. Mathur, A.; Roy, S. S.; Dickinson, C.; McLaughlin, J. A., Effect of thin aluminum interlayer on growth and microstructure of carbon nanotubes. *Current Applied Physics* **2010**, *10* (2), 407-410.
219. Bissett, M. A.; Barlow, A. J.; Shapter, J. G.; Quinton, J. S., Transition from single to multi-walled carbon nanotubes grown by inductively coupled plasma enhanced chemical vapor deposition. *J. Appl. Phys.* **2011**, *110* (3), 034301.
220. Gohier, A.; Minea, T. M.; Djouadi, A. M.; Granier, A.; Dubosc, M., Limits of the PECVD process for single wall carbon nanotubes growth. *Chemical Physics Letters* **2006**, *421* (1-3), 242-245.
221. Teo, K. B. K.; Chhowalla, M.; Amaratunga, G. A. J.; Milne, W. I.; Hasko, D. G.; Pirio, G.; Legagneux, P.; Wyczisk, F.; Pribat, D., Uniform patterned growth of carbon nanotubes without surface carbon. *Applied Physics Letters* **2001**, *79* (10), 1534-1536.
222. Yu, J.; Chen, Y., Patterned Growth of Carbon Nanotubes. In *30th Annual Condensed Matter and Materials Meeting*, Avdeev, M., Ed. AIP: Wagga Wagga, NSW, 2006.
223. Motta, M. S.; Moiala, A.; Kinloch, I. A.; Windle, A. H., The Role of Sulphur in the Synthesis of Carbon Nanotubes by Chemical Vapour Deposition at High Temperatures. *Journal of Nanoscience and Nanotechnology* **2008**, *8* (5), 2442-2449.
224. Shankar, R., *Principles of Quantum Mechanics*. Kluwer Academic: New Haven, Connecticut, 1994.
225. Langmuir, I., The Interaction of Electron and Positive Ion Space Charges in Cathode Sheaths. *Physical Review* **1929**, *33* (6), 954.
226. Sears, F. W.; Salinger, G. L., *Thermodynamics, Kinetic Theory, and Statistical Thermodynamics*. Addison-Wesley: 1986.
227. Seah, M. P., Charge Referencing Techniques for Insulators. In *Practical Surface Analysis Vol. 1: Auger and X-ray Photoelectron Spectroscopy*, Second ed.; Briggs, D.; Seah, M. P., Eds. John Wiley & Sons: West Sussex, 1994.
228. Giancoli, D. C., *Physics for Scientists and Engineers*. 3rd ed.; Prentice-Hall of Australia Pty. Ltd., Sydney: 2000.
229. Krause, M. O.; Oliver, J. H., Natural widths of atomic K and L levels, K alpha X-ray lines and several KLL Auger lines. *Journal of Physical and Chemical Reference Data* **1979**, *8* (2), 329-338.
230. Briggs, D.; Riviere, J. C., Spectral Interpretation. In *Practical Surface Analysis Vol. 1: Auger and X-ray Photoelectron Spectroscopy*, Second ed.; Briggs, D.; Seah, M. P., Eds. John Wiley & Sons: West Sussex, 1994.
-

231. Samson, J. A. R., Line Broadening in Photoelectron Spectroscopy. *Review of Scientific Instruments* **1969**, *40* (9), 1174-1177.
232. Sherwood, P. M. A., Data Analysis in XPS and AES. In *Practical Surface Analysis Vol. 1: Auger and X-ray Photoelectron Spectroscopy*, Second ed.; Briggs, D.; Seah, M. P., Eds. John Wiley & Sons: West Sussex, 1994.
233. Shirley, D. A., High-Resolution X-Ray Photoemission Spectrum of the Valence Bands of Gold. *Physical Review B* **1972**, *5* (12), 4709.
234. Tougaard, S., Quantitative analysis of the inelastic background in surface electron spectroscopy. *Surface and Interface Analysis* **1988**, *11* (9), 453-472.
235. Quinton, J. S. The Oscillatory Adsorption of Organofunctional Silanes on Metal Oxide Surfaces. University of Newcastle, Newcastle, 2000.
236. Krane, K. S., *Introductory Nuclear Physics*. John Wiley and Sons, Inc.: 1987.
237. Seah, M. P.; Gilmore, I. S.; Spencer, S. J., Quantitative XPS: I. Analysis of X-ray photoelectron intensities from elemental data in a digital photoelectron database. *Journal of electron spectroscopy and related phenomena* **2001**, *120* (1-3), 93-111.
238. Jablonski, A., Determination of Surface Composition by X-ray Photoelectron Spectroscopy Taking into Account Elastic Photoelectron Collisions. *Analytical Sciences* **2010**, *26*, 155-164.
239. Seah, M. P.; Gilmore, I. S., Simplified equations for correction parameters for elastic scattering effects in AES and XPS for  $Q$ ,  $\beta$  and attenuation lengths. *Surface and Interface Analysis* **2001**, *31* (9), 835-846.

---

## Appendix A.

# ANCILLARY INFORMATION FOR LANGMUIR PROBE STUDIES

### A.1. Derivation of Electrostatic Probe Theory

#### *The Space Potential and the Electron Density and Temperature*

When an electric probe is biased near to the plasma potential, much of the resultant current is due to the flow of electrons between the plasma and probe since the ion mass is much greater than the electron mass. To describe these electrons one uses a distribution function  $f(\vec{x}, \vec{v}, t)$  which gives the number of electrons per unit volume with velocities between  $\vec{v}$  and  $\vec{v} + d\vec{v}$ , at position  $\vec{x}$  and time  $t$ . It then follows that the electron density is given by

$$n_e(\vec{x}, t) = \int f(\vec{x}, \vec{v}, t) dv_x dv_y dv_z \quad (\text{A-1})$$

and the current density of electrons impinging upon the probe is given by

$$j = e \int f(\vec{v})(\vec{v} \cdot \hat{n}) d^3v \quad (\text{A-2})$$

where  $\hat{n}$  is normal to the probe surface.<sup>73,103</sup> At this point, some assumptions must be made relating to the probe surface and the distribution function,

- $\lambda_D \ll r \ll \lambda_e, \lambda_i$
- $T_e > T_i$
- $n_e = n_i$

where  $r$  is the radius of the probe,  $\lambda_D$  is the Debye length,  $\lambda_e$  and  $\lambda_i$  are the electron and ion mean free paths,  $T_e$  and  $T_i$  are the electron and ion temperatures and  $n_e$  and  $n_i$  are the electron and ion densities.<sup>69</sup>

The first assumption (or rather approximation) says that the radius of the probe must be much greater than the Debye length, but much less than the electron and ion mean free paths. For the first part this means that the sheath dimensions are sufficiently small compared to the probe dimensions to allow us to approximate the probe surface to be an infinite flat plane as depicted in figure A.1.

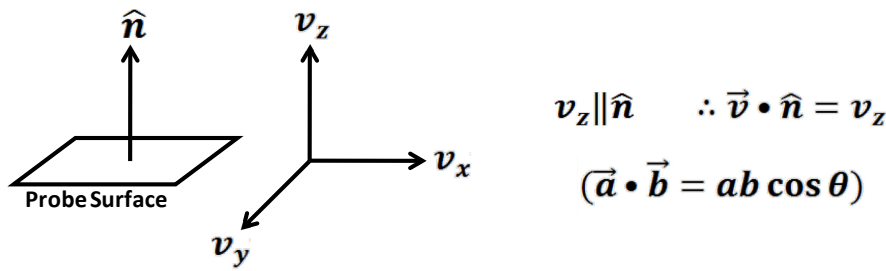


**Figure A.1. Orientation of the probe surface with respect to the coordinate system.**

The second part assumes that the probe does not become a drain on the plasma and adversely affect the density of any species local to the probe. Coupling this assumption with the last two, i.e. saying that the electron temperature must be greater than the ion temperature, and that both densities must be equal so that the plasma is charge neutral across a large enough length scale, allows one to use Maxwell-Boltzmann statistics to describe the distribution function as follows:

$$f(\vec{x}, \vec{v}, t) = n_e \left( \frac{m_e}{2\pi k_B T_e} \right)^{3/2} \exp \left( - \left( \frac{m_e v^2}{2k_B T_e} \right) \right) \quad (\text{A-3})$$

where  $m_e$  is the electron mass,  $k_B$  is the Boltzmann constant and  $v^2 = v_x^2 + v_y^2 + v_z^2$ .<sup>73</sup> It then follows that the probe current density can be written as

$$\begin{aligned} j &= e \int_{v_{min}}^{\infty} \int_{-\infty}^{\infty} \int_{-\infty}^{\infty} f(v_x, v_y, v_z) v_z dv_x dv_y dv_z \\ &= e n_e \left( \frac{m_e}{2\pi k_B T_e} \right)^{3/2} \int_{v_{min}}^{\infty} \int_{-\infty}^{\infty} \int_{-\infty}^{\infty} \exp \left( - \left( \frac{m_e (v_x^2 + v_y^2 + v_z^2)}{2k_B T_e} \right) \right) v_z dv_x dv_y dv_z \end{aligned}$$

where  $v_{min}$  is the minimum velocity required for an electron to overcome the potential difference between the space potential  $V_s$  and the probe voltage  $V_p$ ,

$$v_{min} = \left( \frac{2e(V_s - V_p)}{m_e} \right)^{1/2} \quad (\text{A-4})$$

To simplify the algebra, one can perform a simple change in constants by letting

$$a = \frac{m_e}{2k_B T_e} \quad (\text{A-5})$$

such that the current density now becomes

$$\begin{aligned} j &= en_e \left(\frac{a}{\pi}\right)^{3/2} \int_{v_{min}}^{\infty} \int_{-\infty}^{\infty} \int_{-\infty}^{\infty} \exp\left(-a(v_x^2 + v_y^2 + v_z^2)\right) v_z dv_x dv_y dv_z \\ &= en_e \left(\frac{a}{\pi}\right)^{3/2} \int_{-\infty}^{\infty} \exp(-av_x^2) dv_x \int_{-\infty}^{\infty} \exp(-av_y^2) dv_y \int_{v_{min}}^{\infty} \exp(-av_z^2) v_z dv_z \end{aligned}$$

Setting up the problem in this way allows one to make use of the known solution to the Gaussian integral<sup>224</sup>,

$$\int_{-\infty}^{\infty} e^{-ax^2} dx = \left(\frac{\pi}{a}\right)^{1/2} \quad \text{for } a > 0$$

which reduces the current density to a single integral

$$\begin{aligned} j &= en_e \left(\frac{a}{\pi}\right)^{3/2} \left(\frac{\pi}{a}\right)^{1/2} \left(\frac{\pi}{a}\right)^{1/2} \int_{v_{min}}^{\infty} \exp(-av_z^2) v_z dv_z \\ &= en_e \left(\frac{a}{\pi}\right)^{1/2} \int_{v_{min}}^{\infty} \exp(-av_z^2) v_z dv_z. \end{aligned}$$

The remaining integral also has a known solution,

$$\int x e^{-ax^2} dx = -\frac{1}{2a} e^{-ax^2}$$

allowing the current density to be solved as follows

$$\begin{aligned} j &= en_e \left(\frac{a}{\pi}\right)^{1/2} \left[-\frac{1}{2a} \exp(-av_z^2)\right]_{v_{min}}^{\infty} \\ &= en_e \left(\frac{a}{\pi}\right)^{1/2} \left(\frac{1}{2a}\right) \exp(-av_{min}^2) \\ &= en_e \left(\frac{1}{4\pi a}\right)^{1/2} \exp(-av_{min}^2) \end{aligned}$$

and substituting in (A-4) and (A-5)

$$\begin{aligned} j &= en_e \left(\frac{k_B T_e}{2\pi m_e}\right)^{1/2} \exp\left(-\frac{m_e}{2k_B T_e} \cdot \frac{2e(V_s - V_p)}{m_e}\right) \\ &= en_e \left(\frac{k_B T_e}{2\pi m_e}\right)^{1/2} \exp\left(\frac{-e(V_s - V_p)}{k_B T_e}\right). \end{aligned} \quad (\text{A-6})$$

Equation (A-6) describes the probe current density as a function of the probe bias  $V_p$ . Multiplication of (A-6) by the total probe collecting area  $A$  leads to the electron current  $I_e$  as a function of  $V_p$ ,

$$I_e(V_p) = Aen_e \left(\frac{k_B T_e}{2\pi m_e}\right)^{1/2} \exp\left(\frac{-e(V_s - V_p)}{k_B T_e}\right) \quad \text{for } V_p \leq V_s. \quad (\text{A-7})$$

When the probe voltage reaches the space potential (i.e. when  $V_p = V_s$ ), the exponential term in (A-7) goes to unity and the relationship for the electron saturation current is

$$I_{e,sat} = Aen_e \left( \frac{k_B T_e}{2\pi m_e} \right)^{1/2} \quad (\text{A-8})$$

allowing (A-7) to be re-written as

$$I_e(V_p) = I_{e,sat} \exp\left(\frac{-e(V_s - V_p)}{k_B T_e}\right). \quad (\text{A-9})$$

Taking the natural logarithm of both sides of (A-9) yields

$$\begin{aligned} \ln(I_e) &= \ln\left(I_{e,sat} \exp\left(\frac{-e(V_s - V_p)}{k_B T_e}\right)\right) \\ &= \ln(I_{e,sat}) + \left(\frac{-e(V_s - V_p)}{k_B T_e}\right) \\ &= \left\{ \ln(I_{e,sat}) - \frac{e}{k_B T_e} V_s \right\} + \frac{e}{k_B T_e} V_p \end{aligned}$$

and one can see that a semi-log plot of  $\ln(I_e)$  versus  $V_p$  in the region where the electrons can be described by the Maxwell distribution should indicate a straight line with slope of value  $\frac{e}{k_B T_e}$ , allowing for determination of the electron temperature.

It is important to note units at this stage. If one were to simply take the slope and invert it to determine the electron temperature the units would be in those of eV, since the Boltzmann constant has units of  $\text{JK}^{-1}$ , temperature of K and e is the electronic charge in J. It has become customary in plasma physics to discuss the temperature of a particular plasma species in terms of energy with units eV, and the conversion between eV and K can be given as

$$\begin{aligned} 1\text{eV} &= 1.602 \times 10^{-19}\text{J} \\ \frac{1.602 \times 10^{-19}\text{J}}{1.381 \times 10^{-23}\text{JK}^{-1}} &\approx 11,600\text{K} \\ \therefore 1\text{eV} &\approx 11,600\text{K} \end{aligned} \quad (\text{A-10})$$

From the semi-log plot of  $\ln(I_e)$  versus  $V_p$  one is able to deduce values for both  $I_{e,sat}$  and  $V_s$  by making linear fits in the electron saturation region and the transition region of the I-V characteristic. The point at which the linear fits intersect will be  $[V_s, I_{e,sat}]$ . However due to the exponential nature of the relationship between the electron current and the space potential, small errors in judgment regarding the linear fits can be magnified during the fitting procedure. It is therefore prudent to have a secondary measure of the space potential.

At a particular probe bias, a point is reached where the electron current is equivalent in magnitude, but opposite in sign, to the ion current, resulting in no net flow of current. This bias is called the floating potential,  $V_f$ , and can also be defined as the potential a floating surface (i.e. not Earthed) would take up on contact with the plasma. The ion current can be estimated from the Bohm current <sup>77</sup>

$$I_B = \frac{1}{2} n_e e A \left( \frac{k_B T_e}{m_i} \right)^{1/2}. \quad (\text{A-11})$$

Since the electron current has already been defined in (A-7), one can equate it to (A-11) and let  $V_p = V_f$

$$\begin{aligned} \frac{1}{2} n_e e A \left( \frac{k_B T_e}{m_i} \right)^{1/2} &= A e n_e \left( \frac{k_B T_e}{2\pi m_e} \right)^{1/2} \exp\left(\frac{-e(V_s - V_f)}{k_B T_e}\right) \\ \frac{1}{2} \left( \frac{1}{m_i} \right)^{1/2} &= \left( \frac{1}{2\pi m_e} \right)^{1/2} \exp\left(\frac{-e(V_s - V_f)}{k_B T_e}\right) \\ \ln\left(\left(\frac{\pi m_e}{2m_i}\right)^{1/2}\right) &= \frac{-e(V_s - V_f)}{k_B T_e} \\ -\frac{k_B T_e}{2e} \ln\left(\frac{\pi m_e}{2m_i}\right) &= V_s - V_f \\ \therefore V_f &= V_s + \frac{k_B T_e}{2e} \ln\left(\frac{\pi m_e}{2m_i}\right) \end{aligned}$$

or equivalently

$$V_f = V_s - \frac{k_B T_e}{2e} \ln\left(\frac{2m_i}{\pi m_e}\right). \quad (\text{A-12})$$

Thus, finding the electron temperature via the slope of the linear region for  $V_p \leq V_s$ , and the floating potential from the value of  $V_p$  at which  $I_e = 0$ , allows one to calculate a value for the space potential  $V_s$ .

Electron densities can also be calculated multiple ways. The first method would be to again take the intersection point  $[V_s, I_{e,sat}]$  along with the calculated  $T_e$  and apply these values to the relationship for the electron saturation current, (A-8). This method suffers the same drawbacks as those discussed for calculating the space potential. Another method is to take the natural logarithm of the electron current at the point when  $V_p = 0$

$$\begin{aligned} I_e(V_p) &= A e n_e \left( \frac{k_B T_e}{2\pi m_e} \right)^{1/2} \exp\left(\frac{-e(V_s - V_p)}{k_B T_e}\right) \\ I_e(V_p = 0) &= A e n_e \left( \frac{k_B T_e}{2\pi m_e} \right)^{1/2} \exp\left(\frac{-eV_s}{k_B T_e}\right) \end{aligned}$$

$$\begin{aligned}
 Aen_e \left( \frac{k_B T_e}{2\pi m_e} \right)^{1/2} \exp\left(\frac{-eV_s}{k_B T_e}\right) &= I_e(V_p = 0) \\
 Aen_e \left( \frac{k_B T_e}{2\pi m_e} \right)^{1/2} &= \frac{I_e(V_p=0)}{\exp\left(\frac{-eV_s}{k_B T_e}\right)} \\
 Aen_e \left( \frac{k_B T_e}{2\pi m_e} \right)^{1/2} &= I_e(V_p = 0) \cdot \exp\left(\frac{eV_s}{k_B T_e}\right) \\
 n_e &= \frac{I_e(V_p=0) \cdot \exp\left(\frac{eV_s}{k_B T_e}\right)}{Ae \left( \frac{k_B T_e}{2\pi m_e} \right)^{1/2}}.
 \end{aligned} \tag{A-13}$$

### *Orbital Motion Limit Theory*

So far the theoretical treatment presented has almost completely ignored the presence and influence of the positive ion contribution to the probe current. A simple theoretical approach towards analysis of this contribution was first discussed by Langmuir and Mott-Smith<sup>72</sup> and is named Orbital Motion Limit (OML) theory.

Consider figure A.2 depicting the trajectory of a single particle of elementary charge  $e$  and velocity  $v_0$  coming from infinity where the space potential is zero and negative everywhere else.<sup>77</sup> In the absence of the probe the particle would follow the path described by the line AB. If however a probe of significant sheath thickness were to be placed such that the sheath impinged on the line AB, then the path is varied by the force exerted on the particle and it instead follows the line AC. At some point during the trajectory there will be a minimum distance  $a$  at which point the particle will have a velocity  $v_a$  tangential to the probe surface. Conservation of angular momentum requires that

$$L_0 = L_a$$

where

$$\begin{aligned}
 L_0 &= I_0 \omega_0 \\
 &= (mp^2) \left( \frac{v_0}{p} \right) \quad \text{since } I = mR^2 \quad \text{and } v = \omega R \\
 &= mpv_0
 \end{aligned}$$

and similarly

$$L_a = mav_a$$

thus

$$pv_0 = av_a. \tag{A-14}$$

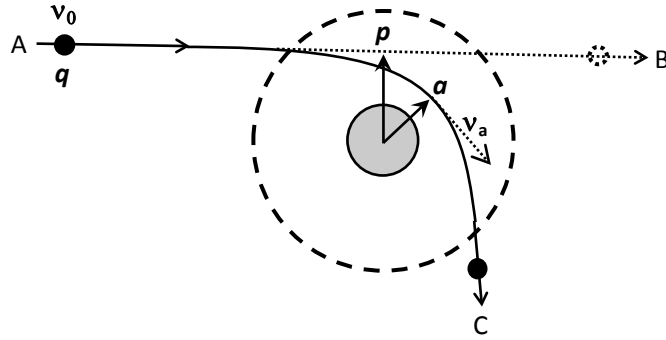


**Figure A.2. The trajectory of a particle with charge  $q$  passing through the sheath produced by a Langmuir probe. Modified from Priest<sup>103</sup> and Chen.<sup>77</sup>**

The initial kinetic energy of the particle can be described by

$$KE_i = \frac{1}{2}mv_0^2$$

or equivalently

$$KE_i = -eV_0$$

thus

$$\frac{1}{2}mv_0^2 \equiv -eV_0. \quad (\text{A-15})$$

The kinetic energy at  $a$  can similarly be described by

$$KE_a = \frac{1}{2}mv_a^2 + eV_a \quad (\text{A-16})$$

where the extra term  $eV_a$  accounts for energy gained by acceleration due to the potential  $V_a$  at  $a$ . Conservation of energy requires that

$$KE_i = KE_a$$

and thus

$$\frac{1}{2}mv_0^2 = \frac{1}{2}mv_a^2 + eV_a.$$

With substitution of (A-15)

$$\frac{1}{2}mv_a^2 + eV_a = -eV_0 \quad (\text{A-17})$$

which if re-arranged like so

$$\begin{aligned} \frac{1}{2}mv_a^2 &= -eV_0 - eV_a \\ &= -eV_0 \left(1 + \frac{V_a}{V_0}\right) \\ &= \frac{1}{2}mv_0^2 \left(1 + \frac{V_a}{V_0}\right) \\ \frac{\frac{1}{2}mv_a^2}{\frac{1}{2}mv_0^2} &= \left(1 + \frac{V_a}{V_0}\right) \end{aligned}$$

it is seen that

$$\frac{v_a}{v_0} = \left(1 + \frac{V_a}{V_0}\right)^{1/2}. \quad (\text{A-18})$$

Now, from (A-14)

$$p = a \frac{v_a}{v_0}$$

and upon substitution of (A-18) one finds

$$p = a \left(1 + \frac{V_a}{V_0}\right)^{1/2}.$$

Since the potential  $V_a$  is a result of the difference between the probe bias and the space potential at  $a$ , then  $V_a = V_p - V_s$  and

$$p = a \left(1 + \frac{V_p - V_s}{V_0}\right)^{1/2}.$$

If  $a$  is taken to be the probe radius  $r$  then any particle with

$$p \leq r \left(1 + \frac{V_p - V_s}{V_0}\right)^{1/2} \equiv p_r \quad (\text{A-19})$$

will be collected by the probe <sup>73</sup>.

From Hershkowitz <sup>73</sup> the probe current is given by

$$I = 2\pi j_r l p_r \quad (\text{A-20})$$

for particles approaching from infinity with the same energy and where  $j_r$  is the uni-directional random current density of particles passing through a unit area and  $l$  is the probe length. Upon substitution with (A-19) one obtains

$$I = 2\pi j_r l r \left(1 + \frac{V_p - V_s}{V_0}\right)^{1/2}. \quad (\text{A-21})$$

It must be noted that the expression in (A-21) is derived for the case of single, mono-energetic particles, which is not realistic for experimental plasma.

The problem was extended to Maxwellian distributions of velocities by Langmuir <sup>225</sup>. In this scenario, the probe current can be approximated by

$$I = \frac{A j_r}{\sqrt{\pi}} \left(\frac{eV_p}{k_B T_i} + 1\right)^{1/2}. \quad 103$$

By squaring the above equation one yields

$$I^2 = \frac{A^2 j_r^2}{\pi} \left(\frac{eV_p}{k_B T_i} + 1\right)$$

where it can be seen that a plot of  $I^2$  versus  $V_p$  will yield a straight line with slope

$$\frac{d}{dV_p}(I^2) = \frac{A^2 j_r^2 e}{\pi k_B T_i} \quad \text{for } V_p < V_f. \quad (\text{A-22})$$

The random current density can also be written in terms of the density of particles  $N_i^+$  and the average velocity  $\bar{v}$ <sup>61</sup>,

$$j_r = \frac{1}{4} N_i^+ \bar{v} e \quad (\text{A-23})$$

where the average velocity is taken from kinetic theory<sup>226</sup> to be

$$\bar{v} = \left( \frac{8k_B T_i}{\pi m_i} \right)^{1/2}. \quad (\text{A-24})$$

Substitution of (A-24) into (A-23) gives

$$\begin{aligned} j_r &= \frac{1}{4} N_i^+ e \left( \frac{8k_B T_i}{\pi m_i} \right)^{1/2} \\ j_r^2 &= \frac{1}{2} N_i^{+2} e^2 \left( \frac{k_B T_i}{\pi m_i} \right) \\ \text{and } \therefore N_i^{+2} &= \frac{2\pi m_i}{k_B T_i e^2} j_r^2. \end{aligned} \quad (\text{A-25})$$

Now from (A-22) it is seen that

$$j_r^2 = \frac{\pi k_B T_i}{A^2 e} \cdot \left. \frac{dI^2}{dV_p} \right|_{V_p < V_f}$$

and so (A-25) becomes

$$\begin{aligned} N_i^{+2} &= \frac{2\pi m_i}{k_B T_i e^2} \cdot \frac{\pi k_B T_i}{A^2 e} \cdot \left. \frac{dI^2}{dV_p} \right|_{V_p < V_f} \\ &= \frac{2\pi^2 m_i}{A^2 e^3} \cdot \left. \frac{dI^2}{dV_p} \right|_{V_p < V_f}. \end{aligned} \quad (\text{A-26})$$

Thus, from (A-26), a plot of  $I^2$  versus  $V_p$  for large values of  $V_p$  allows the calculation of the positive ion density.

## A.2. Mean Free Path Calculations and the Debye Length

### *Ion and Electron Mean Free Path*

For particles with a Maxwell distribution of velocities, the ion mean free path is given by

$$\lambda_i = \frac{1}{4\sqrt{2}\pi N_g r_g^2} \quad (\text{A-27})$$

where  $N_g$  = the number of molecules per unit volume and  $r_g$  = the hard sphere radius of the gas molecules<sup>69</sup>. Using the ideal gas law,

$$PV = Nk_B T$$

which for a unit volume can be written as,

$$P = N_g k_B T$$

equation (A-27) can therefore be re-written as,

$$\lambda_i = \frac{k_B T}{4\sqrt{2}\pi r_g^2 P} \tag{A-28}$$

where  $P$  = pressure ( $\text{Nm}^{-2}$ ) and  $T$  = temperature (K).

With knowledge of the radius of the species under investigation, the mean free path could therefore be calculated across the nominal experimental pressure range of 1 – 100 mTorr. It must be noted however that this is an approximation only, based on the hard sphere model of atoms and molecules. Still, it is sufficient to allow one to make educated decisions regarding Langmuir Probe design. From Swift and Schwar<sup>69</sup>, the ratio of the ion and electron mean free path is given by

$$\frac{\lambda_e}{\lambda_i} = 4\sqrt{2}$$

allowing one to also calculate an estimate of the electron mean free path once the ion mean free path is determined from (A-28).

#### *Debye Length*

Plasma is often referred to as quasi-neutral<sup>61</sup>. The charge carriers in the plasma mutually screen the electric fields of fellow charge carriers that are present on a microscopic scale resulting in the plasma only appearing neutral when viewed on a macroscopic scale. The scale over which the charge carriers can effectively screen out electric fields is known as the Debye length, denoted  $\lambda_D$ . Swift and Schwar define  $\lambda_D$  as

$$\lambda_D = \left[ \frac{k_B T_e}{4\pi e^2 n_e} \right]^{1/2} \tag{A-29}$$

When plasma contacts a boundary it forms a protective sheath across which neutrality no longer exists, and large potentials may develop. The thickness of this sheath is of particular interest when studying plasma, and so a measure is required. When appropriate analysis is performed one finds that the thickness is equivalent to that given in (A-29), and so it can be concluded that the length scale across which plasma no longer maintains neutrality is  $\lambda_D$ , the Debye length<sup>69</sup>. This is an important quantity as it requires that the dimensions of an ionised gas be much greater than that of  $\lambda_D$  for it to be rightly called plasma. It also has implications regarding the design of Langmuir probes; the probe radius must be sufficiently greater than  $\lambda_D$  to allow the analysis in A.1 to be performed.

### A.3. RF Compensation

Plasma generated from rf sources are not steady-state. The temporal nature of the space potential translates into distortions of the I-V characteristic when no measures are taken to remove the rf component. A simple yet effective technique to eliminate these distortions is rf compensation whereby a secondary electrode, as near to the probe as possible, senses the variations in potential and superimposes them onto the probe tip.

Figure A.3 shows an equivalent circuit of a self-compensating Langmuir probe<sup>103</sup>. The probe itself is connected to the plasma by an effective capacitance labelled  $C_{p1}$ , while the compensating electrode also has an effective capacitance to the plasma of  $C_{p2}$ . The probe and compensating electrode are connected via a capacitance  $C_e$ , which in the case of the Langmuir probe used in this research, is in the form of ceramic encasing the probe. The probe is biased externally by a variable dc potential  $V_p$ , at point A, inducing a current flow of  $I_p$  through the circuit. This current is a function of the potential difference between the probe voltage,  $V_p$ , and the space potential,  $V_s$ , given by  $(V_p - V_s)$ . Since the space potential has a time dependent nature, it may be represented by

$$V_s(t) = V_{s(dc)} + V_{s(rf)}(t) \quad (\text{A-30})$$

where  $V_{s(dc)}$  is the component of the space potential that is constant, and  $V_{s(rf)}(t)$  is the time-varying component.

If one now considers a point B in the circuit (see figure A.3), that has bias  $V_B$ , the current flowing at that point can be represented by

$$I_p = f[V_s(t) - V_B]. \quad (\text{A-31})$$

Now since the compensating electrode superimposes the time-varying space potential onto the probe tip,  $V_B$  can be represented by

$$V_B = V_p + V_{s(rf)}(t). \quad (\text{A-32})$$

Substituting (A-32) and (A-30) into (A-31), one arrives at a solution of

$$\begin{aligned} I_p &= f[V_{s(dc)} + V_{s(rf)}(t) - V_p - V_{s(rf)}(t)] \\ &= f[V_{s(dc)} - V_p] \end{aligned} \quad (\text{A-33})$$

which is constant for a given probe bias  $V_p$ , allowing the theory presented in A.1 to be used for analysis of I-V characteristics collected using this probe.

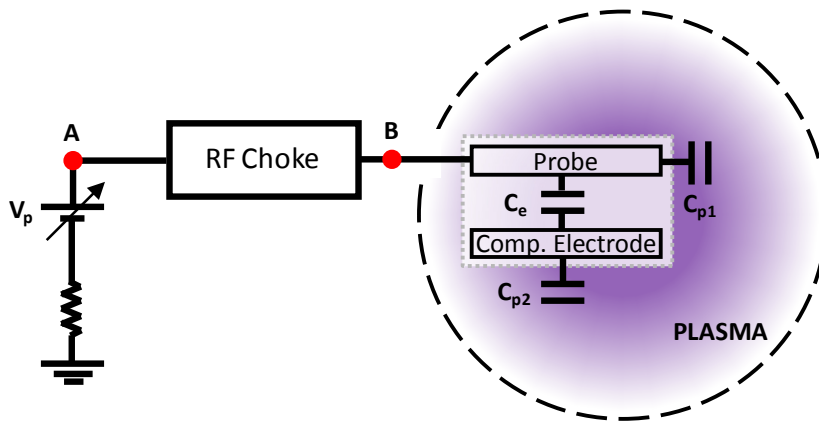


**Figure A.3. Equivalent circuit of a self-compensating Langmuir probe.**  
Modified from Priest.<sup>103</sup>

---

## Appendix B.

# ANCILLARY INFORMATION FOR XPS STUDIES

### B.1. Calibration of the Binding Energy Scale

In XPS the kinetic energy,  $E_k$ , of a detected electron depends on the energy of the incident photon,  $h\nu$ , the binding energy of the element from which the electron was ejected,  $E_b$ , and the work function of the surface,  $\Phi_s$ , according to the equation

$$E_k = h\nu - E_b - \Phi_s . \quad (\text{B-1})$$

Since the surface under study is electrically connected with the spectrometer the Fermi levels of both the spectrometer and the sample shift until they are in alignment, at which point the work function term in equation (B-1) becomes that of the spectrometer,  $\Phi_{\text{sp}}$ . This results in kinetic energy measurements that are offset by a few eV and in practice a spectral shift along the  $x$ -axis occurs. The spectrometer work function is sometimes considered a ‘catch-all’ term that can be convoluted with other inaccuracies within a given system, such as aging of components leading to incorrect voltage outputs on the lens or hemisphere system and subsequent incorrect electron kinetic energies being passed. It is because of this that rather than discussing a calibration in terms of the work function of the spectrometer analysts may refer to the calibration factor  $C$  such that

$$E_b = E'_b + C \quad (\text{B-2})$$

where  $E_b$  is the actual binding energy of the element and  $E'_b$  is the measured binding energy.<sup>227</sup> In XPS the analyst is often looking for small changes in relative peak positions and as such  $C$  must be accounted for during experiments to ensure confidence in collected data. On the LHS-10 at Flinders this is performed programmatically within XSpec, the data acquisition software designed and commissioned as part of this work.

Assuming a conductive sample is being studied, the simplest method of calibrating a given XPS spectrum is by referencing peak positions with that of known values. However, since the binding energy of an element is dependent upon its chemical state not just any sample can be used as a reference. The broad constraints for a suitable reference sample is that it must be conductive, and reasonably chemically inert to ensure that measured peak positions are coming from an element in the same chemical state as the known values. A third consideration is that the preferred element has measurable photo peaks across as wide a range of energies as is possible, to ensure the spectrometer is calibrated across the entire accessible energy scale.

An element that satisfies these criteria is gold. It is relatively inert, usually suffering only from surface contamination due to adsorbates, is conductive, and displays photo peaks across a range of more than 700 eV, from 54 eV up to 763 eV.<sup>146</sup> Considering the usual energy range analysed in XPS is from 0 – 1000 eV this covers nearly 75% of the energy scale. Shown in figure B.1 is an uncalibrated XPS spectrum of gold with its peaks labelled accordingly, collected with the spectrometer in FAT mode with a transmission energy of 50 eV. Note the minor presence of a carbon peak at ~280 eV. Prior to analysis a calibration sample would typically be cleaned through physical sputtering by an *in situ* ion gun, removing residual carbon signal. This technique was not available on the system in question and so methods were used to merely minimise contamination. One such method was to prepare calibration samples via the vacuum evaporation of gold onto conductive metal substrates just prior to analysis. The cleanliness of the vacuum environment helps to prevent unwanted contaminants from adsorbing onto the sample, and with minimal exposure to atmosphere between deposition and analysis a high quality calibration sample can be obtained. The level of carbon contamination observed in the gold spectrum presented was considered quite acceptable in the absence of any *in situ* cleaning processes.

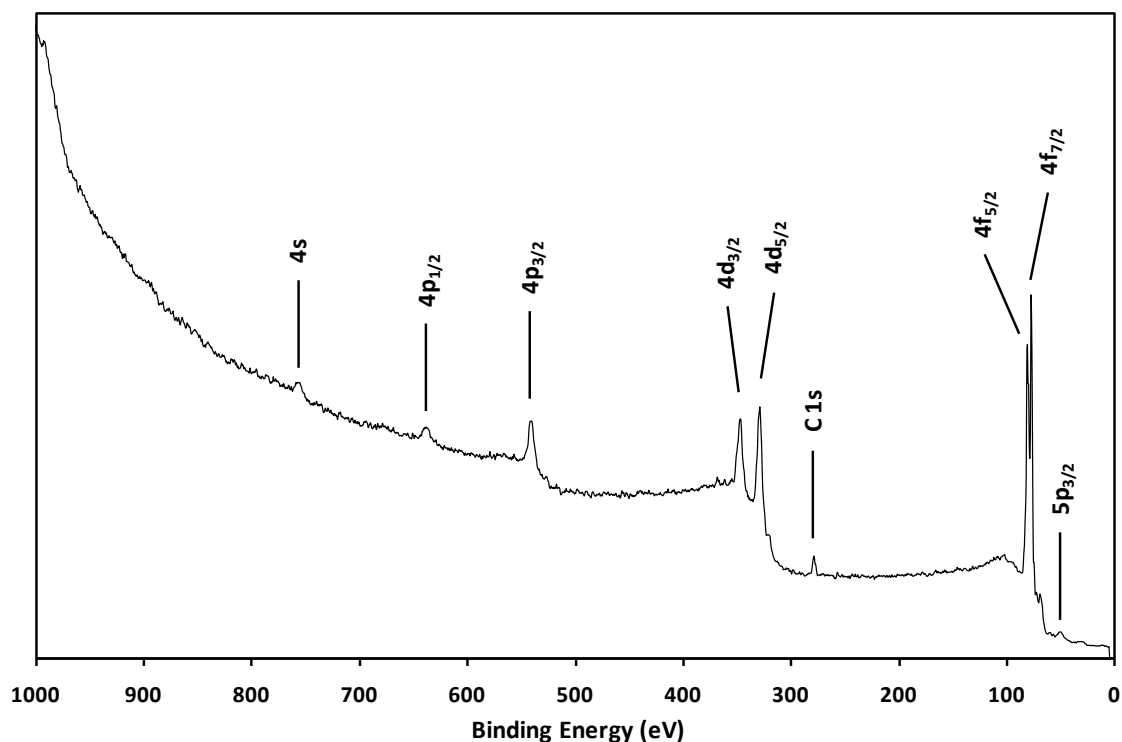


**Figure B.1.** An XPS spectrum of evaporated gold taken with the spectrometer in FAT mode with a transmission energy of 50 eV.

**Table B.1.** A summary of the known binding energies for the XPS peaks in gold compared to the measured values from the LHS-10 spectrometer.

Peak	Known Energy	Measured Energy
$5p_{3/2}$	57	50.9
$4f_{7/2}$	84	78.1
$4f_{5/2}$	87.7	81.6
$4d_{5/2}$	335	329.3
$4d_{3/2}$	353	347.4
$4p_{3/2}$	547	541.1
$4p_{1/2}$	643	637.4
$4s$	763	757.4

Table B.1 summarises the measured peak positions from figure B.1 along with the accepted peak positions from Moulder.<sup>146</sup> By plotting the measured values against the accepted values one obtains the calibration curve seen in figure B.2. By producing a linear fit through this data and obtaining the equation of the line the calibration factor can be obtained through the  $y$ -intercept. In this case the data should be shifted higher in binding energy by 6.04 eV to obtain an accurate spectrum. Note that the data collected here was in FAT mode, which maintains a constant energy resolution across the energy scale and thus

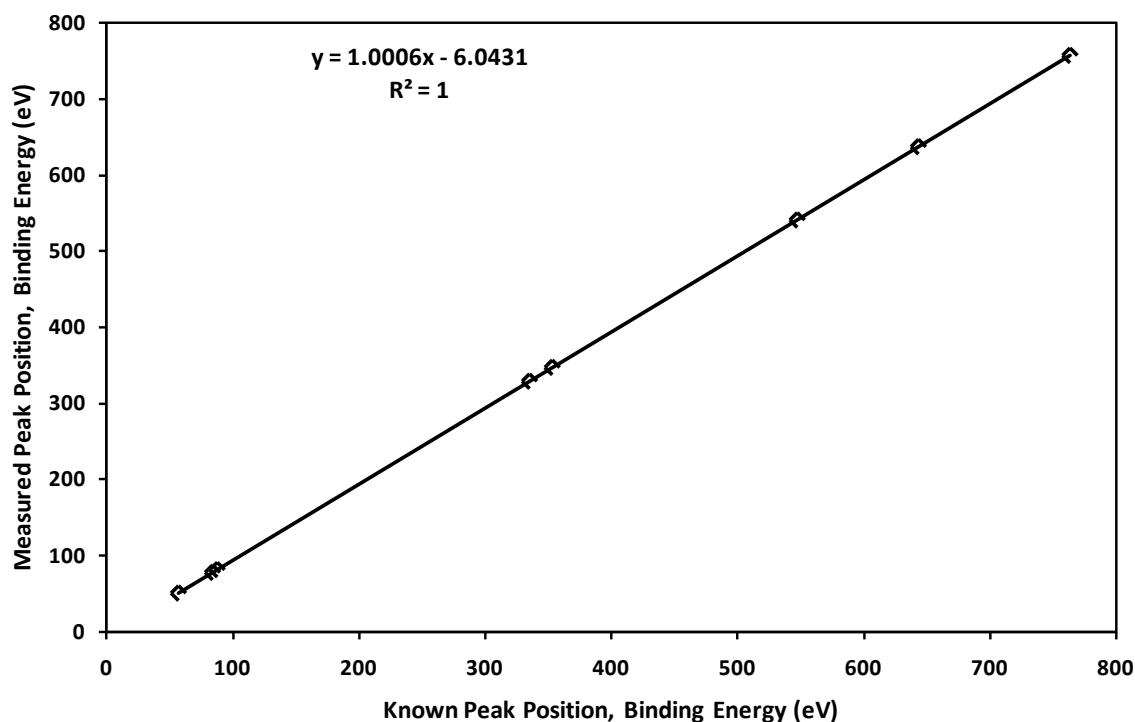


**Figure B.2.** A calibration curve created from table B.1 allowing the work function to be determined from the equation of the linear fit to the data.

is used to collect high resolution data for quantification. Survey spectra are often collected in CRR mode on the LHS-10 at Flinders as it enables a greater signal to noise ratio and is particularly suitable for qualitative analysis. In this case a similar procedure would be performed to obtain the calibration for this alternate mode.

#### *Adventitious Carbon Referencing*

It is not always the case that a surface under analysis is perfectly conducting. Quite often an experiment may want to be performed on a substrate that is semiconducting, such as silicon, or possibly even an insulator such as soda glass or quartz. In these cases obtaining reliable data is complicated by the fact that the technique removes electrons from the surface thus leaving a deficit positive charge. For insulators there is no easy way for the charge to be neutralised and, if left unchecked, can greatly influence the kinetic energy of electrons being ejected from the surface. Ultimately this adds a further source for error in energy measurement whereby electrons lose kinetic energy due to the positive charge on the surface and upon detection they appear to have come from an element of higher binding energy. This effect cannot simply be accounted for by performing the calibration procedure already described.

For some systems the charging effect can be so detrimental that it reaches a point where it is impossible to collect any reliable data without serious intervention by the analyst, such as the application of an electron flood gun to stream low energy electrons towards the surface and thus compensate for the charge deficit. The LHS-10 however, through a somewhat fortuitous design, is to some extent ‘self-compensating’ whereby electrons emitted from the filament of a nearby ion gauge help to alleviate any charge build up on surfaces. The result is a far less significant shift in energy when studying samples that may exhibit charging. In these situations calibration can be performed by referencing to peaks within a collected spectrum. As was observed in figure B.1 it is very difficult to study a surface without any contamination by carbon. This can be due to a general lack of cleanliness when preparing a sample for analysis, or by the adsorption of atmospheric contaminants. Regardless of the cause, it is usually expected that some amount of carbon signal will be detected on a surface in the absence of any *in situ* sputter cleaning. This type of carbon contaminant is called ‘adventitious’ carbon and is often accepted to have a binding energy of 285 eV.<sup>227</sup> Any spectrum collected from a sample that would be expected to charge can therefore be calibrated by simply shifting the energy scale such that the adventitious carbon signal lies at 285 eV.

## **B.2. The Dependence of XPS Peak Positions on Photon Energy**

A common element among commercial X-ray sources is the application of a dual-anode system. This allows a given source to operate with one of two different excitation energies, the most common choices being Al K $\alpha$  at 1486.6 eV and Mg K $\alpha$  at 1253.6 eV. This can be useful from multiple points of view since each of the X-ray lines have different characteristics; one may have a higher flux while the other may have a narrower line width. The availability of multiple excitation energies becomes particularly useful when dealing with a surface with a multitude of elements some of which may have overlapping Auger and photo peaks in a spectrum. Depending on the energy scale upon which the spectrum is plotted, either kinetic or binding energy, changing the excitation energy will shift peaks relative to one another and can therefore aid in their deconvolution.

The two processes of interest in XPS are presented in figure B.3.<sup>115</sup> The emission of a photoelectron is depicted in (a) whereby a photon of energy  $h\nu$  is incident upon a core electron, in this case an electron in the 1s orbital (or K shell). Ignoring the work function of the sample, the kinetic energy of this electron would therefore be

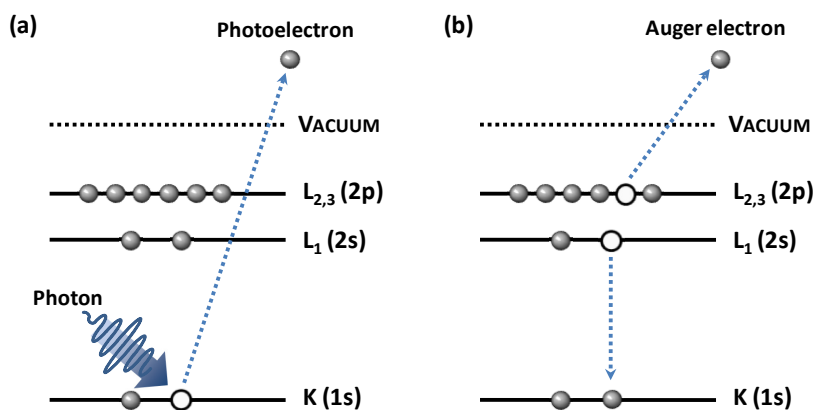


**Figure B.3.** The two processes involved in XPS: (a) the ejection of a photoelectron from a core shell upon irradiation by a photon and (b) the secondary Auger electron emission process. Modified from Kibel.<sup>115</sup>

$$E_k = h\nu - E_{1s} . \quad (\text{B-3})$$

This electron is named a photoelectron and peaks in spectra that arise due to this process are often named photo peaks. Traditionally the nomenclature used to designate which shell a given peak corresponds to is that of the molecular orbital, i.e. s, p, d or f.

The secondary process is described in (b) whereby upon the ejection of a core shell electron, another from a higher energy level relaxes down to fill the hole and in doing so transfers energy to a third electron which can then be ejected. The kinetic energy of the electron in this case is

$$E_k = E_K - E_{L_1} - E_{L_{2,3}} \equiv E_{KLL} . \quad (\text{B-4})$$

This electron is called an Auger electron named after the French physicist Pierre Auger. Traditionally these are designated by the energy levels K, L, M and N (also V for valence band) rather than the orbitals as was previously used.

Consider figure B.4 showing artificial XPS spectra consisting of one photo peak and one Auger peak. In (a) the data is presented on a kinetic energy scale and from equations (B-3) and (B-4) the energies at which those peaks should be are given. From this it can be seen that since the kinetic energy of a photoelectron is dependent on the energy of the incident photon, variation in the excitation energy will shift the position of the photo peak while the Auger peak will remain stationary.

More often than not however XPS data is presented on a binding energy scale. The conversion from kinetic to binding energy comes from equation (B-1). The peak positions on a binding energy scale are given in figure B.4(b) where it can now be seen that it is the

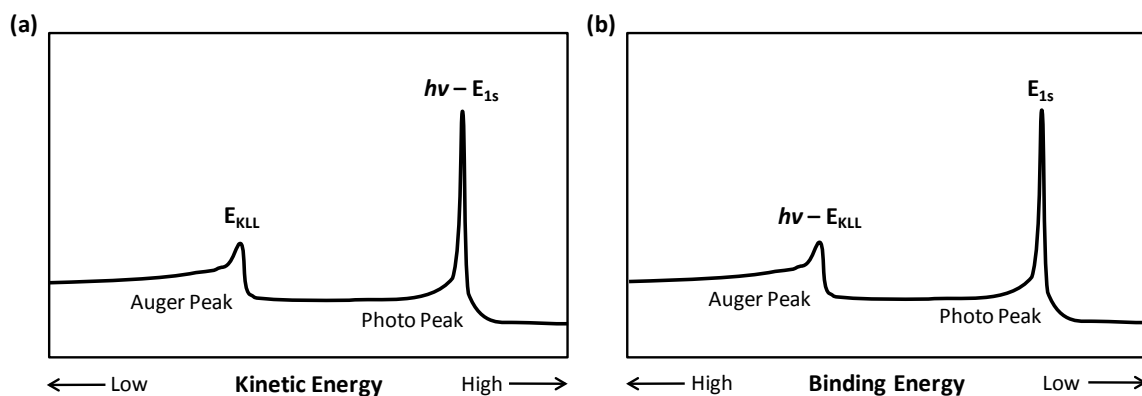


**Figure B.4.** The peak positions relative to electron and photon energy on (a) the kinetic energy scale and (b) the binding energy scale.

Auger peak that has the photon energy dependence. Intuitively these two scenarios make perfect sense. When plotted on a kinetic energy scale the Auger peak should be completely independent of the incident photon energy since the kinetic energy of such an electron is determined only by the energy levels of the atom from which it is ejected. Conversely on the binding energy scale the position of the photo peak should remain constant regardless of photon energy since the binding energy of the core shell of an element is constant.

The analysis given here is not only applicable to XPS systems with multiple excitation energies but must also be considered when performing synchrotron based PES. The strong advantage of a synchrotron light source is the continuously tunable X-ray energy, allowing an experimentalist to increase the ionisation cross-section of a particular element and hence increase the sensitivity. As has been observed however when data is plotted against binding energy a reduction in the photon energy to enhance sensitivity will also shift Auger peaks to lower energies on the scale. In the presence of multiple elements this could become detrimental as multiple peaks may begin to overlap and become convoluted, complicating analysis. Thus care must be taken when performing such an experiment to ensure that no peaks will overlap and cause unwanted interference.

### B.3. XPS Peak Widths

The width and shape of peaks in XPS spectra arise from a superposition of contributions from various aspects of the technique;

- the X-ray source,
- the uncertainty in the lifetime of the ionised state and
- the resolution of the analyser.

In an ideal spectrometer each of these contributions would be discrete, giving rise to essentially a single line for each peak in a collected spectrum. In reality this is not the case and XPS peaks have quite complex structure that is dependent on many factors.

Often when quantifying XPS data the analyst would employ a synthetic curve-fitting procedure to aid in the deconvolution of a given peak and this therefore requires a strong theoretical understanding of the mechanisms underlying the shapes and widths of observed XPS peaks. Furthermore, the properties of the synthetic curve that is best suited to a data set obtained from one instrument will likely vary from that obtained on another, and as such the requirement for understanding of these mechanisms is even greater.

#### *The X-ray Source*

It is usually accepted that a majority of the observed peak width and shape in XPS spectra comes predominantly from the X-ray line in use.<sup>195</sup> In a typical XPS instrument X-rays are generated by the acceleration of electrons thermionically emitted from a filament into a target composed of a pure material. The result is an X-ray emission spectrum similar to that depicted in figure B.5(a), where a combination of characteristic X-rays from the anode material and a background known as bremsstrahlung is observed.<sup>228</sup> Bremsstrahlung radiation occurs when a charged particle is decelerated by an external force, such as the deceleration of an electron by an atomic nucleus. In fact, the term bremsstrahlung translates to ‘braking radiation’ from the German words bremsen, meaning ‘to brake’, and strahlung, meaning ‘radiation’.<sup>228</sup> Bremsstrahlung radiation creates a continuous background of X-ray emission that drops off sharply at a wavelength corresponding to the maximum energy possible for a given accelerating voltage, i.e. the case where an electron loses all of its kinetic energy through the emission of a single photon. Superimposed onto this background are the peaks in the emission spectrum that correspond to X-rays characteristic of the target material. This type of X-ray emission occurs when the incident

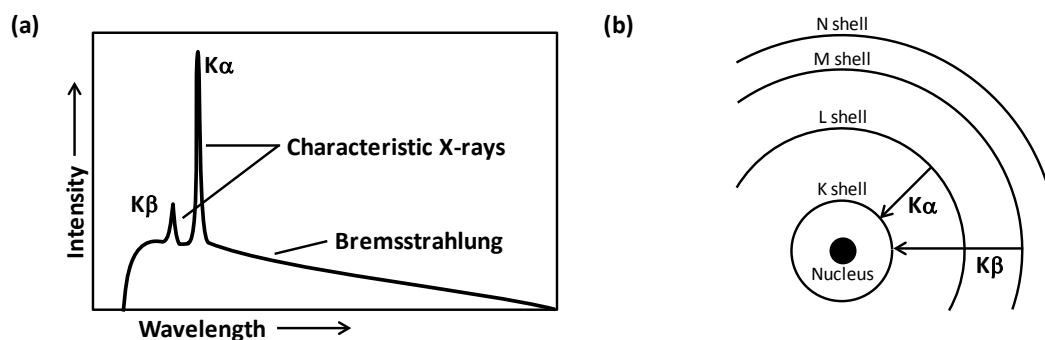


**Figure B.5. (a) An artificial X-ray emission spectrum from an element that emits two characteristic X-ray energies,  $K\alpha$  and  $K\beta$ , and (b) the electronic transitions that correspond to these characteristic X-rays.**

electron energy is sufficient enough to cause the ejection of a core electron, in this case from the K shell. The resulting hole that is left in the atom is filled by an electron from one of the outer shells, with the subsequent emission of an X-ray photon of energy equivalent to the difference between the two shells, a process known as X-ray fluorescence. The designation  $K\alpha$  and  $K\beta$  are used to indicate that the emission is a result of a transition *into* the K shell from the L shell ( $\alpha$ ) and M shell ( $\beta$ ) respectively. These transitions are depicted in figure B.5(b). In some instances, usually for greater accelerating voltages, transitions can occur into the L shell from the M and N shells and in this case the lines would be labelled  $L\alpha$  and  $L\beta$  respectively.<sup>228</sup>

Common X-ray sources utilise aluminium or magnesium as the anode material. These sources emit characteristic  $K\alpha$  and  $K\beta$  lines under typical accelerating voltages of up to 15 kV. Table B.2 summarises the energies of these lines including their relative intensities.<sup>115,229</sup> The line of interest for XPS instruments is the  $K\alpha$  line as it is the most intense emission at these voltages. Presented in the table are also widths of the  $K\alpha$  lines for both anode materials and as is clear from this data they are far from discrete emissions. The magnitude of this width is largely due to the fact that the  $K\alpha$  emission lines are actually the unresolved convolution of two distinct transitions  $K\alpha_1$  and  $K\alpha_2$ . The convoluted line is sometimes denoted as  $K\alpha_{1,2}$  rather than simply  $K\alpha$ . The transitions have a linewidth of 0.36 eV for Mg and 0.43 eV for Al, however the intensities between each pair are not equal, presenting with a ratio of 2:1 ( $\alpha_1:\alpha_2$ ). Although the total width of the  $K\alpha_{1,2}$  line is a result of this convolution there are a number of causes for the broadening of each of the individual lines. The observed widths are usually associated solely with the uncertainty in the lifetime of the hole produced in the ionised level upon electron impact.<sup>195,229</sup> This lifetime is governed by factors such as multiple ionisation processes

**Table B.2. K lines from aluminium and magnesium anodes showing the energy and relative intensity of the  $\alpha$  and  $\beta$  transitions. The linewidth given is for the  $\alpha$  transition only. Data reproduced from Kibel<sup>115</sup> and Krause.<sup>229</sup>**

Anode Material	Photon Energy (eV)		Linewidth (FWHM, eV)		
	$\alpha_{1,2}$	$\beta$ ( $\Delta$ )	$\alpha_{1,2}$	$\alpha_1$	$\alpha_2$
<b>Al</b> (relative intensity)	1486.6 (100)	1556.3 (69.7) (0.55)	0.85 (100)	0.43 (67)	0.43 (33)
<b>Mg</b> (relative intensity)	1253.6 (100)	1302.1 (48.5) (0.50)	0.70 (100)	0.36 (67)	0.36 (33)

leading to more than one hole present at any one time, and the natural width of the levels themselves. These factors result in a far less than discrete X-ray emission energy.

In the absence of a monochromator the experimentalist would ideally use the emission line that gives the greatest resolution, and from the data presented here that choice would be the Mg K $\alpha$  line. As already discussed the choice of X-ray energy can cause unwanted convolution of Auger and photo peaks and so there is always a balance between maximum resolution and obtaining appropriate data for analysis.

#### *Broadening Mechanisms during the Photo-Emission Process*

The effects that create uncertainty during characteristic X-ray emission are also present during the ionisation of the atoms within a surface under study. Just like with X-ray emission, the final kinetic energy with which an electron may be ejected from a surface can be affected by intrinsic mechanisms such as the linewidth of the core level, and various extrinsic mechanisms such as thermal and phonon broadening. All of these factors coupled together results in a distribution of electron velocities coming from a single state that has been ionised with a given photon energy.

The linewidth of a core level is directly related to the uncertainty in the lifetime of the photo-ionised state. It is governed largely by the means through which the ion dissipates the excess energy gained through the photoemission process; either X-ray fluorescence, or the subsequent ejection of a secondary electron. From Heisenberg's uncertainty principle

$$\Delta E \Delta t \geq \hbar$$

and as such the natural linewidth  $\Gamma$  is related to the lifetime  $\tau$  by

$$\Gamma = \frac{\hbar}{\tau}$$

This can be expressed as

$$\Gamma = \frac{h}{\tau} = \frac{4.1 \times 10^{-15}}{\tau} \text{ eV}$$

where Planck's constant is expressed in eV.s (electron volt seconds) and the lifetime is in seconds.<sup>228,230</sup> The lifetime can also be affected by multiply ionised states, an effect that is more prevalent in the light elements than the heavy elements.<sup>229</sup>

The observed kinetic energy of an electron is also affected by the motion of the particles themselves.<sup>231</sup> This leads to the extrinsic mechanism of thermal broadening, also referred to as Doppler broadening although the latter term is more often used to describe the broadening of photon emission processes rather than electron emission. Thermal broadening results from the fact that the atoms are not at rest when an electron is ejected, they have some finite amount of thermal energy and thus a velocity. This velocity acts upon the kinetic energy of the electron by either increasing its energy if the atom is moving with the electron trajectory, or decreasing its energy if the atom is moving opposite to the trajectory. Within an entire ensemble of particles the motion is completely random however the observed velocities adhere to the normal distribution function.<sup>228</sup> This results in the kinetic energy being broadened by this distribution of particle velocities.

#### *Analyser Resolution*

Electron energy analysers do not transmit only those electrons with a kinetic energy at which the analyser is set, but rather they transmit electrons that have energies within a small range of the set kinetic energy. In a Concentric Hemispherical Analyser (CHA) the width of this range, i.e. the analyser resolution, is defined by numerous factors; the radius of the hemispheres, the dimensions of the entrance and exit slits within the analyser and the pass energy. It is of course unreasonable to have an analyser with a variable radius, and thus the user operable parameters that define the resolution of a spectrometer are usually the slit widths and the pass energy. In the EA10/100 analyser the slit widths are fixed and as such only the pass energy can be adjusted.

For a CHA the pass energy  $E_0$  defines the absolute resolution  $\Delta E$  by the relation

$$\Delta E = E_0 \frac{W_1 + W_2}{2R_0}$$

where  $W_1$  and  $W_2$  are the entrance and exit slit widths and  $R_0$  is the mean radius of the analyser.<sup>115,191</sup> If the mean slit width is defined by  $S$  such that

$$S = \frac{W_1 + W_2}{2}$$

then the absolute resolution can be given by

$$\Delta E = E_0 \frac{S}{R_0}.$$

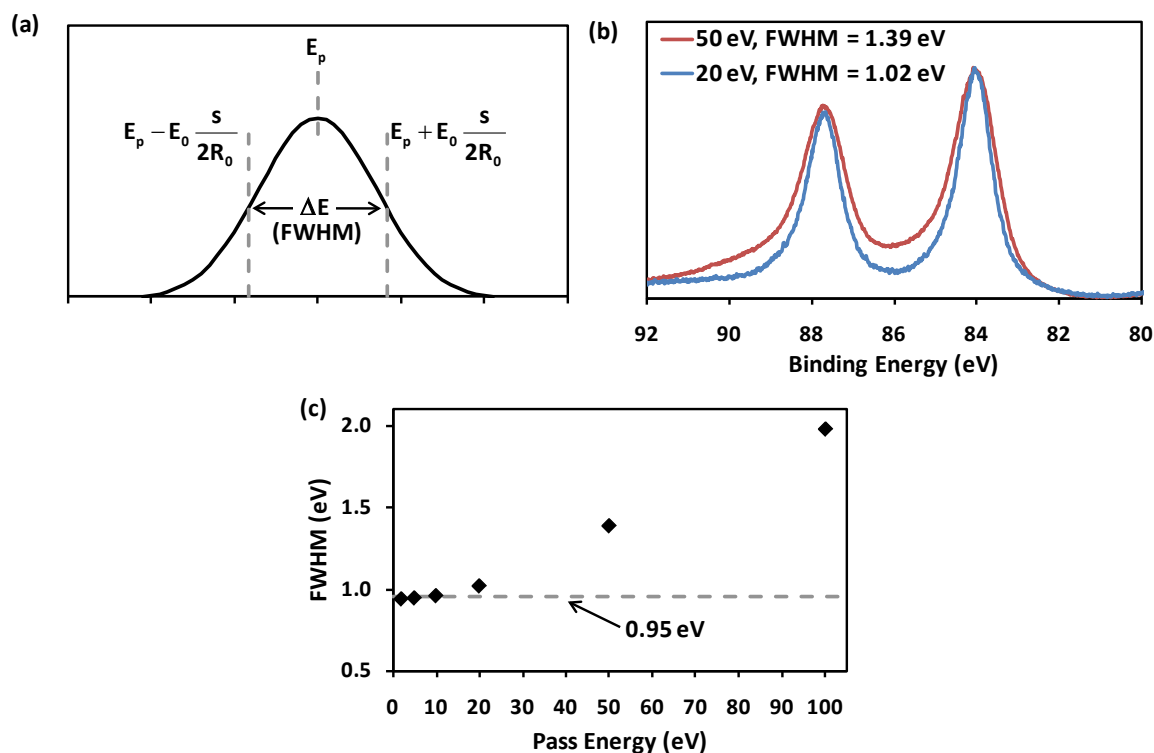


**Figure B.6.** (a) Synthetic data showing the relationship between the pass energy and the FWHM of a measured peak. (b) Measured gold 4f doublets at pass energies of 20 eV (blue trace) and 50 eV (red trace) demonstrating the relationship in (a). (c) The FWHM of the Au 4f<sub>7/2</sub> peak with varying pass energy.

The absolute resolution  $\Delta E$  is also found by determination of the FWHM of a measured peak.<sup>115</sup> This is represented in figure B.6(a) for synthetic data. If the centre of a measured peak is defined as  $E_p$  then the peak would occupy the energy range

$$E_p \pm \frac{1}{2} \Delta E$$

$$\equiv E_p \pm E_0 \frac{s}{2R_0}$$

at half maximum. From these relationships it becomes clear that for a fixed radius a reduction in either the slit width or the pass energy would result in an increase in resolution and thus a reduction in the FWHM of measured peaks. This is of course an idealised case that is not entirely accurate for real data, but nevertheless it provides the link between pass energy and resolution. Figure B.6(b) demonstrates this experimentally. Spectra of the gold 4f doublet were obtained under identical conditions at two pass energies; 20 eV (blue trace) and 50 eV (red trace). For clarity the spectra have been normalised. At 50 eV pass energy the peaks have a measured FWHM of 1.39 eV while at 20 eV pass energy this width is reduced to 1.02 eV, a significant improvement in resolution.

Ultimately the absolute resolution attainable for a given instrument will depend on the width of the exciting line and as such reduction in the pass energy and thus improvement in the resolution of the analyser can only do so much. Figure B.6(c) shows this limit experimentally. The FWHM of the Au 4f<sub>7/2</sub> peak was monitored for a wide range of pass energies and as is clear a limit in the resolution is reached at pass energy of 10 eV, with the best attainable FWHM being 0.95 eV.

It must be noted that improvements in resolution come at the sacrifice of signal intensity. Within a CHA narrowing the slit widths or reducing the pass energy improves resolution through a consequential rejection of electrons that fall outside of a decreasing ‘acceptance’ energy window, and thus much signal is discarded when high resolution is desired. While the spectra used to obtain the presented FWHM data could still be analysed at the lowest pass energies the signal was severely decreased to the point that they would not be suitable under normal circumstances. It was possible to still measure the FWHM since gold is very sensitive to X-rays and there was sufficient signal. For samples composed of the light elements such as carbon the sensitivity to X-rays is much lower and so data collection at pass energies less than 20 eV is not generally feasible for reliable quantification.

#### **B.4. XPS Peak Curve Fitting**

The kinetic energy of an electron ejected from a core level can be affected, among other things, by the chemical state of the atom. For example electrons ejected from a carbon atom bound only to other carbon atoms, such as in graphite, will exhibit a binding energy of 284.5 eV. However if those carbon atoms were all bound to an oxygen atom, the peak energy would shift to between 285 – 286 eV. Lattice structure is also observed to have an effect on peak position with sp<sup>3</sup> hybridised carbon displaying a higher binding energy than that of sp<sup>2</sup> carbon. Thus from these subtle shifts in peak positions chemical state information can be elucidated from XPS spectra. More often than not there are contributions from multiple chemical states on the sample surface and as such the information becomes convoluted and results in an asymmetric ‘shoulder’ on a given elemental peak in an XPS spectrum, usually on the higher binding energy side of the peak. This leads to the desire to deconvolute these contributions using synthetic curve fitting and background subtraction procedures.

### *Background Subtraction*

Once liberated from an atom after photoionisation an electron may travel unimpeded until detection, with its kinetic energy remaining constant. However, due to the short IMFP of electrons there is also the distinct likelihood that some of the kinetic energy will be lost through inelastic processes such as the collision with neighbouring nuclei, or the interaction with other electrons. As a consequence XPS spectra are a superposition of peaks onto a background signal that rises with decreasing kinetic energy. When presented on a binding energy scale a given peak will have a greater background signal on the high binding energy side than the low side, requiring some level of background subtraction prior to the fitting of curves to the peak.

A trivial solution would be to perform a linear background subtraction between two points in the data set that span the base of the peak under examination as demonstrated in figure B.7(a) for the Au 4f doublet. While this method is the simplest, it is also prone to inducing serious error and asymmetry for data with significant background variation.<sup>232</sup> A more sophisticated approach was introduced by Shirley in 1972 and consequently named the ‘Shirley Background’.<sup>233</sup> This method, demonstrated in figure B.7(b), increases the background at a rate proportional to the peak intensity, with the provision that the background and measured intensity are equal either side of the peak. The Shirley background has received criticism for its potential to misinterpret intensity as being due to inelastic scattering rather than important peak structure,<sup>232,234</sup> although this is more of an issue for the heavy elements where scattering creates large background variations around a peak. Tougaard addressed these concerns and developed a background subtraction method based on the physical attributes of a sample rather than the mathematical derivation of the Shirley background.<sup>234</sup> Despite these criticisms the Shirley background is still commonly used even today as the choice for analysis due to its relative simplicity and wide availability in peak fitting software, and was the choice for this work.

### *The Gaussian-Lorentzian Peak Shape*

It is now known that the shape and width of a measured peak in an XPS spectrum is the result of a complex convolution of factors throughout the technique. The total contribution is often quantified as the sum of the squares of each contribution,

$$\Delta E^2 = \Delta E_n^2 + \Delta E_p^2 + \Delta E_a^2 ,$$

where  $\Delta E$  is the final width of the peak,  $\Delta E_n$  is the natural width of the excited core

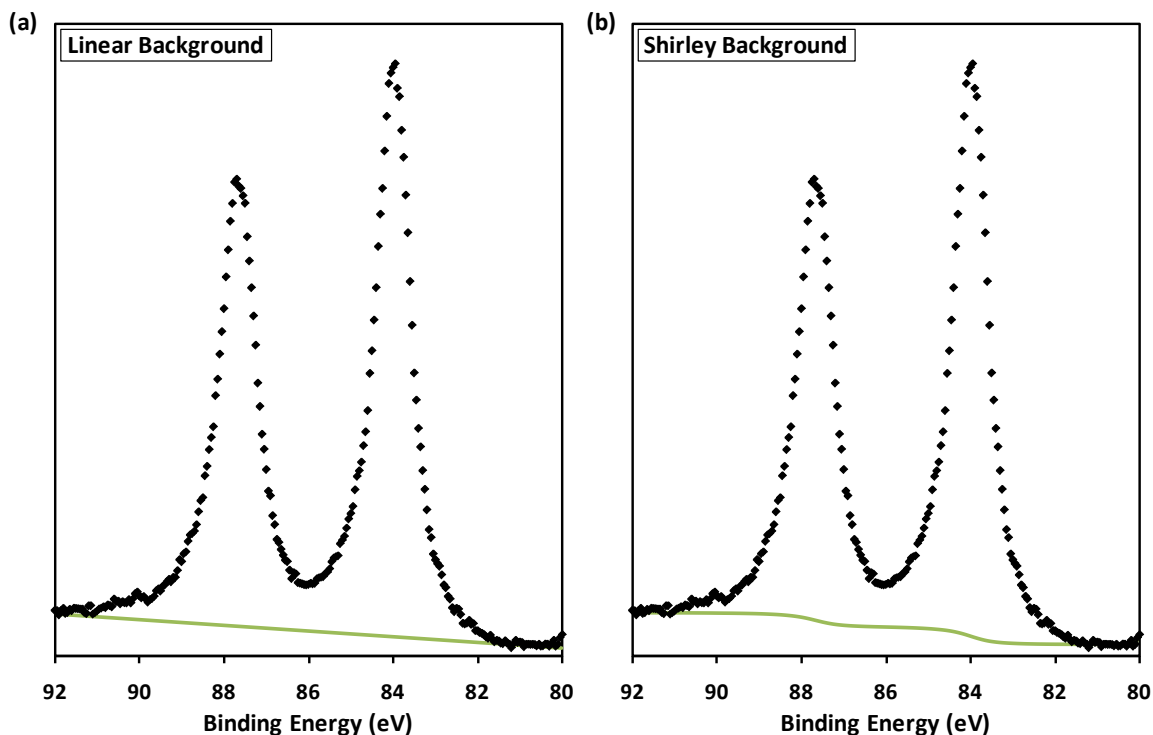


**Figure B.7.** Two background subtraction methods for XPS spectra; (a) linear and (b) the Shirley background.

level,  $\Delta E_p$  is the width of the X-ray source and  $\Delta E_a$  is the analyser resolution.<sup>230</sup> This quantification is somewhat simplistic however as it assumes that all contributions have a Gaussian shape. In general, peaks in XPS are expected to be Lorentzian, a result of the shape of the X-ray line and the natural width of the core level, which is then broadened by a Gaussian contribution from extrinsic processes such as thermal broadening and instrumental factors such as the analyser resolution.<sup>232</sup> Consequently XPS peaks cannot be appropriately fitted with a simple Gaussian or Lorentzian curve.

Presented in figure B.8 are various fits to the 4f doublet from a gold sample. A pure Gaussian of the form

$$G(x; F, E) = \left[ e^{\left( \frac{4 \ln 2 (x-E)^2}{F^2} \right)} \right]^{-1}$$

is fitted to the data in (a), while a pure Lorentzian of the form

$$L(x; F, E) = \left[ \left( 1 + \frac{4(x-E)^2}{F^2} \right) \right]^{-1}$$

is fitted to the data in (b). In both cases  $E$  is the peak centre and  $F$  is the FWHM. Neither case would be considered a good fit, although it is apparent that the Lorentzian is much more suitable than the Gaussian, in agreement with what is expected.

For some time analysts have been using mixed Gaussian-Lorentzian (GL) curves to approximate the shape of XPS peaks with varying levels of success.<sup>232</sup> These curves generally take the form

$$GL(x; F, E, m) = \left[ \left( 1 + \frac{4m(x-E)^2}{F^2} \right) e^{\left( \frac{4\ln 2(1-m)(x-E)^2}{F^2} \right)} \right]^{-1}, 0 \leq m \leq 1$$

where  $m$  is the mixing ratio. The curve is purely Gaussian when  $m$  is 0 and purely Lorentzian when  $m$  is 1. This allows for a continuous variation between the two forms to determine the most suitable curve to fit data from a given instrument. Figure B.8(c) shows the 4f doublet now fitted with a mixed Gaussian-Lorentzian form with  $m = 0.95$ , resulting in a curve that is 95% Lorentzian and 5% Gaussian, denoted GL(0.95). The quality of the fit is far superior for this mixed form than either of the pure forms as evidenced by the strong overlap between the sum curve (blue) and the raw data points (black).

Although the GL(0.95) line shape provides a suitable curve for fitting the 4f doublet from gold it should not be assumed that this line shape will fit all data obtained on the LHS-10. This is particularly true when fitting data from a different element, such as carbon, that may require a different mixing ratio due to different underlying broadening processes in the element. There are also factors that may introduce asymmetry in a given peak, resulting in an exponential ‘tail’ for binding energies greater than the peak maximum. These features must be accounted for, and generally require a modification to the GL form.<sup>232</sup> In this work however the basic GL line shape was found to provide a sound synthetic curve for peak deconvolution on all elements found in a routine analysis.

### *Error Analysis*

Quantification in XPS is usually performed by summing together the total peak area in a given spectrum and then finding the relative contribution of each element to that total area. The individual elemental contribution is then reported as a ‘relative atomic percentage’. Any error that may be present in this percentage is therefore a direct result of error in the area calculation. In 2000 Quinton discussed a procedure enabling the calculation of the uncertainty in a peak area as part of a PhD dissertation,<sup>235</sup> and the same method was applied in this work. Since it is given in detail in the referenced work it will only be reproduced here in brief.

At the most fundamental level, an XPS measurement is the counting of pulses from an electron multiplier as the result of a photoelectron passing through the analyser. For each

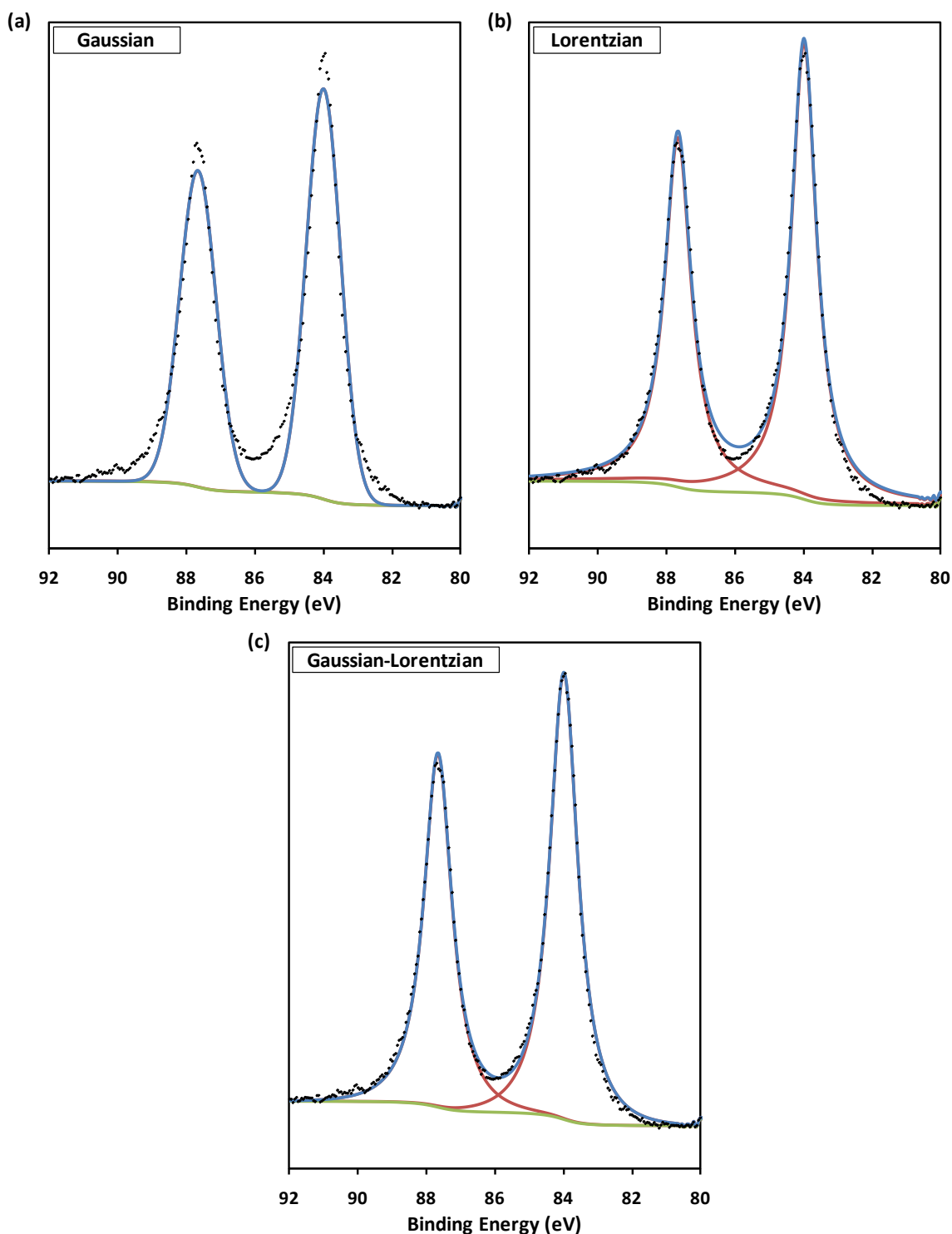


**Figure B.8. Various fits to the Au 4f doublet; (a) pure Gaussian, (b) pure Lorentzian and (c) a Lorentzian modified by a 5% Gaussian contribution.**

energy step the instrument will count the number of pulses and output this value. The entire spectrum is then made up of the total number of counts per energy step. From counting statistics it is known that a measurement of  $N$  events across a given time will be subject to a statistical uncertainty of  $\sqrt{N}$ .<sup>236</sup> That is

$$\Delta N = \sqrt{N} .$$

Thus the fractional error is given by

$$\begin{aligned} \frac{\Delta N}{N} &= \frac{\sqrt{N}}{N} \\ &= \frac{1}{\sqrt{N}} \end{aligned}$$

which shows that as the number of counts increases, the fractional error decreases. In XPS often the experimentalist will attempt to improve data quality, and thus decrease the error, by counting at each energy step for a greater time interval.

Upon careful analysis the uncertainty in the number of counts can be applied to an idealised Gaussian curve where each data point describing the curve has a magnitude of  $N_i(E)$  counts and a width of  $\Delta E$  where  $i$  spans the curve. Thus the area under each point is given by  $N_i(E)\Delta E$ . The total area under the curve is

$$Area = \lim_{\Delta E \rightarrow 0} \sum_i N_i(E)\Delta E \equiv \int_{-\infty}^{\infty} N(E)dE$$

and the error in this area is

$$\Delta Area = \lim_{\Delta E \rightarrow 0} \sum_i \sqrt{N_i(E)}\Delta E \equiv \int_{-\infty}^{\infty} \sqrt{N(E)}dE .$$

If one makes the assumption that the area can be approximated by a Gaussian function then upon solving the integral it is found that

$$\Delta Area = \sqrt{\frac{2}{G}} Area$$

where the intensity of the peak is given by  $G$ . Using properties of the function this relationship can be described in terms of the FWHM of the peak as follows

$$\Delta Area \cong \left(\frac{\pi}{\ln 2}\right)^{1/4} \sqrt{F \cdot Area} .$$

Since the FWHM of most peaks from the LHS-10 is approximately 1 – 1.1 eV this can be further simplified to

$$\Delta Area \cong 1.5\sqrt{Area} .$$

Therefore, the error in a given area measurement can be determined from the square-root of the measured area.

---

## Appendix C.

# CALCULATION OF ATOMIC SENSITIVITY FACTORS FOR SXPS

### C.1. Photoelectron Intensity

The photoelectron intensity per photon of energy  $h\nu$ , per unit solid angle, is given by

$$I_{AX_i}^\infty(h\nu) = n_{AX_i} \sigma_{AX_i}(h\nu) \sec \alpha N_A Q_A(E_{AX_i}) \lambda_A(E_{AX_i}) \quad (\text{C-1})$$

for a homogeneous system where  $n_{AX_i}$  is the electron population in subshell  $i$  of core level  $X$  of element  $A$ ,  $\sigma_{AX_i}(h\nu)$  is the ionisation cross-section of that shell for photons of energy  $h\nu$ ,  $\alpha$  is the incidence angle of the photon beam relative to the surface normal,  $N_A$  is the atomic density of the element  $A$ ,  $Q_A(E_{AX_i})$  is the overall intensity reduction of electrons of energy  $E_{AX_i}$  due to inelastic scattering and  $\lambda_A(E_{AX_i})$  is the IMFP for those electrons.<sup>237</sup>

This equation can be simplified by relating the intensity to the atomic density multiplied by some factor  $S_{AX_i}$  such that

$$I_{AX_i}^\infty(h\nu) = N_A S_{AX_i}$$

where

$$S_{AX_i} = n_{AX_i} \sigma_{AX_i}(h\nu) \sec \alpha Q_A(E_{AX_i}) \lambda_A(E_{AX_i}). \quad (\text{C-2})$$

Since most experiments are performed at a fixed geometry, and sensitivity factors are

generally presented relative to a particular element where that factor is set to unity (commonly the fluorine 1s shell), the angular factor  $\sec \alpha$  can be eliminated giving

$$S_{AX_i} = n_{AX_i} \sigma_{AX_i}(h\nu) Q_A(E_{AX_i}) \lambda_A(E_{AX_i}) . \quad (\text{C-3})$$

This defines the atomic sensitivity factor (ASF) for subshell  $i$  of core level  $X$  from element  $A$  when irradiated by a photon of energy  $h\nu$ . The calculation of each of the terms in (D-3) comes from multiple sources and as such will be treated here individually.

#### *Ionisation Cross Section*

The first two terms in (C-3),  $n_{AX_i} \sigma_{AX_i}(h\nu)$ , are generally treated as a single term taken as the product of the electron population and the ionisation cross-section. When using standard X-ray energies, a common source for these values comes from Scofield, where they were calculated using the Hartree-Slater method.<sup>196</sup> However, in this work the photon energy was not standard and thus a more general source was required. Yeh and Lindau documented atomic subshell photoionisation cross-sections for varying photon energy for the elements in the range  $1 \leq Z \leq 103$ .<sup>144</sup> Table C.1 gives the atomic subshell photoionisation cross-sections from this work for carbon, nitrogen, oxygen and fluorine at photon energies of 1486.6, 1253.6 and 760 eV. The values in the table have units of  $10^6$  barn, but note that units become meaningless upon calculation of the final relative sensitivity factor.

#### *Intensity Correction Factor*

The photoelectron intensity is affected by the inelastic scattering of electrons as they exit the material. The factor  $Q_A$  takes these effects into account, ultimately reducing the overall calculated intensity. Jablonski suggested that the correction factor could be approximated by a simple polynomial function

$$Q_x = b_1 \cos^2 \alpha + b_2 \cos \alpha + b_3$$

and published values of  $b_1$ ,  $b_2$  and  $b_3$  for a wide range of elements and shells for Al  $K\alpha$  and Mg  $K\alpha$  excitation.<sup>238</sup> Seah and Gilmore increased its generality by relating the correction factor to the atomic number and electron kinetic energy such that

$$Q_i = Q_i^* \times (b_1 \cos^2 \alpha + b_2 \cos \alpha + b_3)$$

and

$$\begin{aligned} Q_i^* = & 0.912 + 0.0148(Z + 16.21)\exp[-(Z + 16.21)/16.21] \\ & + (3.07 \times 10^{-5} - 2.09 \times 10^{-7}Z) \times (E_i - 1200) \\ & - (7.75 \times 10^{-8} - 1.45 \times 10^{-9}Z) \times (E_i - 1200)^2 \end{aligned}$$

**Table C.1. Values of  $n_{AX_i}\sigma_{AX_i}(h\nu)$  in units of  $10^6$  barn.**

	$h\nu = 760$ eV	$h\nu = 1253.6$ eV	$h\nu = 1486.6$ eV
<b>C1s</b>	0.09378	0.02235	0.01436
<b>N1s</b>	0.1596	0.04167	0.02579
<b>O1s</b>	0.2451	0.06697	0.04221
<b>F1s</b>	0.3540	0.1004	0.06394

where  $E_i$  is the electron kinetic energy and  $Z$  is the atomic number.<sup>239</sup> Table C.2 gives the calculated correction factors  $Q_i$  for the elements and X-ray energies used in this work.

#### *Inelastic Mean Free Path*

Calculation of the IMFP for electrons often comes from the work of Tanuma *et al.*, using their TPP-2M formula.<sup>180</sup> The IMFP calculations presented here were performed using the Quases-IMFP-TPP-2M software developed by Tougaard. Table C.3 gives the IMFP values as well as the input kinetic energies (given in parentheses after each of the IMFP values). It was assumed that electrons travelled through carbon prior to escaping the surface and thus for the calculations this was the material chosen. Kinetic energies were based on the shell being ionised and the photon energy and are given in eV.

#### *Atomic Sensitivity Factors*

Atomic sensitivity factors were calculated by simply multiplying the determined values for  $n_{AX_i}\sigma_{AX_i}(h\nu)$ ,  $Q_i$  and  $\lambda_A(E_{AX_i})$  in tables C.1 – C.3. Table C.4 gives the ASF values calculated for carbon, nitrogen, oxygen and fluorine when illuminated by photons of energy 1486.6, 1253.6 and 760 eV. These values are the raw results and as suggested most sensitivity factors are presented relative to another element. Common databases set the sensitivity factor for the F1s shell to unity with all other factors determined relative to this. Table C.5 gives the calculated ASFs adjusted such that F1s is unity, and compared against known values for excitation at 1486.6 eV and 1253.6 eV based on the work by Seah.<sup>237</sup> These values are also graphically compared in figure C.1 where the known values are given as the diamonds and the theory as the lines. As can be seen from these results there is excellent agreement between already published values and those calculated in this work. Strong agreement would suggest the correct application and implementation of the theory, thus leading to confidence in the calculated ASFs for the elements at 760 eV for which there is no direct comparison.

**Table C.2. Values of  $Q_i$ .**

$h\nu = 760 \text{ eV}$	$Z$	$E_i$	$Q_i^*(0)$	$Q_i$
C1s	6	475	0.9380	0.9229
N1s	7	362	0.9225	0.9077
O1s	8	229	0.9021	0.8875
F1s	9	70	0.8744	0.8603
$h\nu = 1253.6 \text{ eV}$	$Z$	$E_i$	$Q_i^*(0)$	$Q_i$
C1s	6	969	0.9850	0.9692
N1s	7	856	0.9772	0.9615
O1s	8	723	0.9658	0.9502
F1s	9	564	0.9490	0.9337
$h\nu = 1486.6 \text{ eV}$	$Z$	$E_i$	$Q_i^*(0)$	$Q_i$
C1s	6	1202	0.9955	0.9795
N1s	7	1089	0.9914	0.9754
O1s	8	956	0.9842	0.9684
F1s	9	797	0.9725	0.9568

**Table C.3. Values of  $\lambda_A(E_{AX_i})$  in units of Angstroms ( $\text{\AA}$ ). Kinetic energy of these electrons given in parentheses in units of eV.**

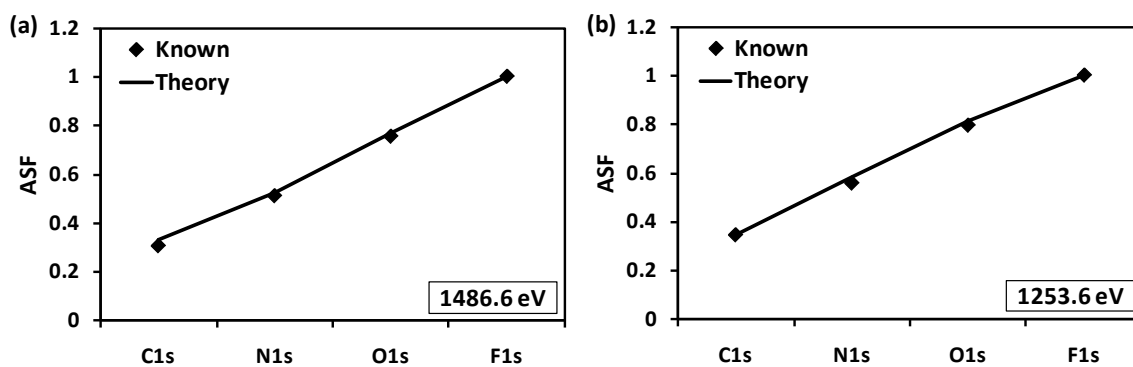
	$h\nu = 760 \text{ eV}$	$h\nu = 1253.6 \text{ eV}$	$h\nu = 1486.6 \text{ eV}$
C1s	16.61 (475)	27.98 (969)	33.05 (1202)
N1s	13.85 (362)	25.47 (856)	30.61 (1089)
O1s	10.53 (229)	22.45 (723)	27.70 (956)
F1s	7.42 (70)	18.74 (564)	24.14 (797)

**Table C.4. Atomic sensitivity factors.**

	$h\nu = 1486.6 \text{ eV}$	$h\nu = 1253.6 \text{ eV}$	$h\nu = 760 \text{ eV}$
C1s	0.465	0.606	1.438
N1s	0.743	1.020	2.006
O1s	1.086	1.429	2.291
F1s	1.416	1.757	2.260

**Table C.5. Atomic sensitivity factors adjusted such that F1s is unity.**

	$h\nu = 1486.6 \text{ eV}$		$h\nu = 1253.6 \text{ eV}$		$h\nu = 760 \text{ eV}$
	Theory	Known	Theory	Known	Theory
<b>C1s</b>	0.328	0.306	0.345	0.347	0.636
<b>N1s</b>	0.525	0.511	0.581	0.559	0.888
<b>O1s</b>	0.767	0.755	0.813	0.795	1.014
<b>F1s</b>	1.000	1.000	1.000	1.000	1.000

**Figure C.1. Comparison between known ASF values (diamonds) and those calculated here (lines) for (a) Al K $\alpha$  and (b) Mg K $\alpha$  X-ray sources.**



---

## **Appendix D.**

# **XSPECT: DATA ACQUISITION SOFTWARE FOR THE LHS-10 AT FLINDERS**

During the research detailed in this dissertation the LHS-10 instrument was decommissioned for a significant period for repairs after a serious failure of a critical component. During this time it was deemed prudent to investigate ways in which the instrument could be upgraded to add enhanced features, improve the quality of the data acquired and also to improve the handling of such data. Prior to this work, the computer used to acquire data was an outdated system running on a Windows 3.1 platform. While this was appropriate for the instrument when it was first installed, it was lacking severely in several key areas compared to modern instruments. Most notably, it had no control over the instrument, data was collected as a single column of data that needed to be interpreted and the data could only be retrieved through a 3.5' floppy disk drive. This prompted the design and installation of a computer controlled sweep generator by the Electronics Workshop in the School of Chemical and Physical Sciences. This device was interfaced with the existing electronics that controlled the LHS-10, details of which were given in the experimental chapter of this thesis. Control over this device was achieved through software written in the LabVIEW programming environment and named XSpect. Details regarding the design and operation of this software are given in this appendix.

## D.1. The XSpect Front Panel and its Operation

The front panel of XSpect is pictured in figure D.1. Broadly, it can be separated into three sections; scan control, scan browser and data output (i.e. the spectral plot). These sections will be discussed individually below, with each control discussed in detail.

### *Scan Control*

This section of the front panel allowed the user to setup each of their scans. Through the sweep generator the user had complete control over the width of the sweep, the step size of this sweep (i.e. how many points to collect in the designated range), how long to average on each point and how many scans to collect. The user also had control over several passive details such as the naming of the sample, the region being scanned and the excitation energy used. This last quantity was not tied to the X-ray source it was merely there to aid in the application of the correct energy scale calibration.

A majority of the advanced control of the software could be performed through this section of the software. To aid in the consistency of scans, a feature was added whereby the user could select from a series of preset scans. The user would simply select the region of the spectrum to be analysed, for example the C1s region, and the software would set the start and end of the scan, as well as the step size and time spent at each point. The user could then set the number of scans to be performed. During data collection the software would collect each spectrum sequentially and perform an average after each complete acquisition. Prior to collection, each scan needed to be checked by pressing 'Validate'. This process verified each of the settings input by the user to ensure that they were within range of what the sweep generator could output and also that they made sense. For example, due to the way in which the system was configured the start energy (in binding energy) always needed to be greater than the end energy. If this was not the case, upon pressing validate the conflicting controls would flash red, a message would be displayed in the dialog box and the acquire button would remain disabled. This would force the user to correct the problem, and validate the scan again prior to data collection.

If the scan was validated, it would then be added to the scan queue (the list box immediately beneath the validate button). If desired, the user could then set up another scan, validate it, and have it added to the scan queue. In effect, this allowed the user to set up a suite of scan regions for a given sample. Upon pressing the 'Acquire' button, the

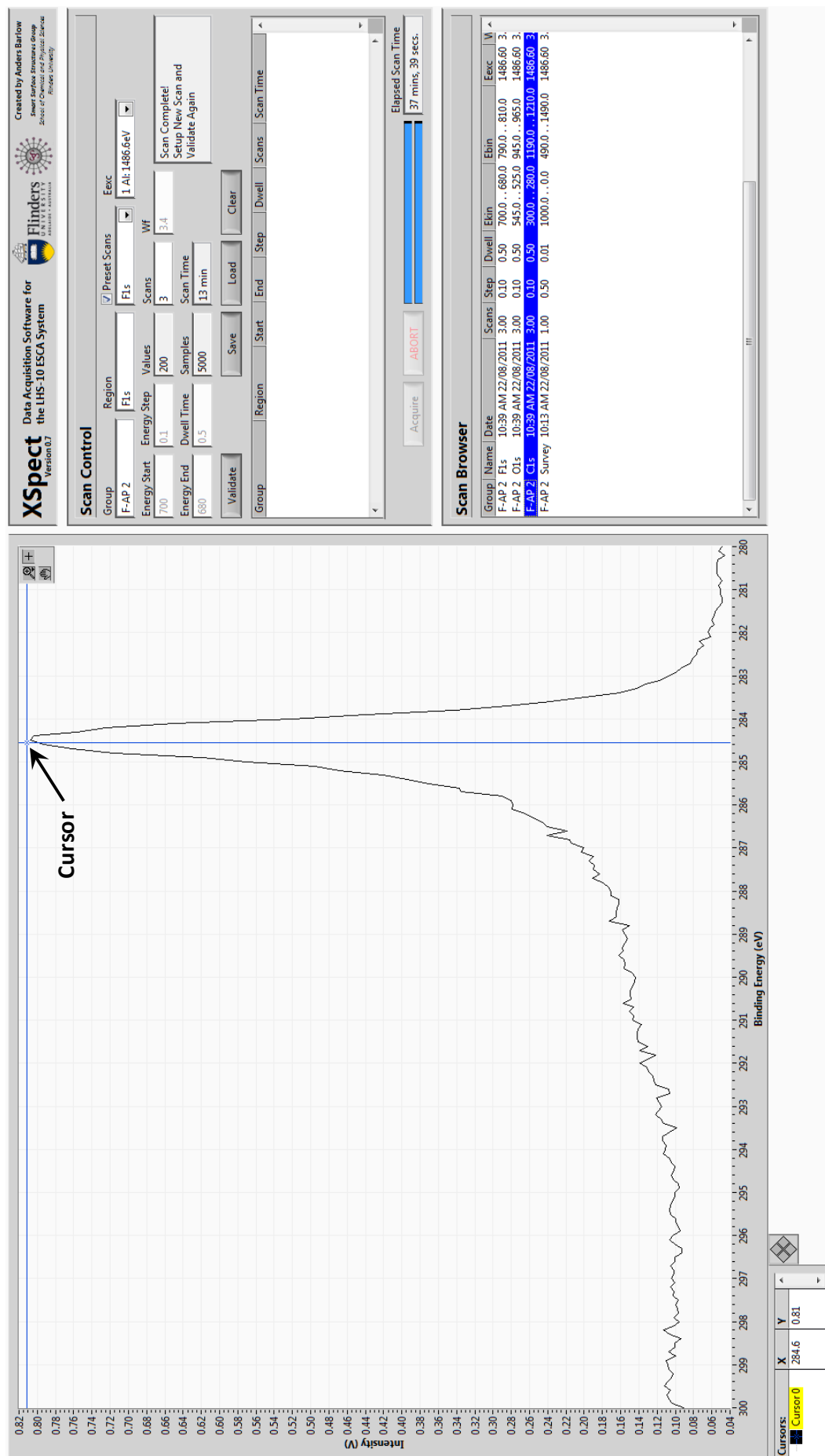


Figure D.1. The front panel of XSpec, the data acquisition software designed and written as part of this dissertation.

software would then begin collecting data from the first region in the scan queue and upon completion it would then continue to the next region in the queue. Not only was this found to save significant time by minimising dead time for the spectrometer, it was also found to greatly aid consistency, especially when used in conjunction with the preset scans.

This was further enhanced through the ability to save an entire scan queue as a scan file. Upon completing a list of regions to be analysed, for example the C1s, O1s and F1s regions as would be common in this research, the user then had the option to save this queue as a separate file. When beginning a new sample, the user could then open this file and import the queue that was used for previous samples and immediately begin taking data. Again, this was found to greatly improve consistency within a large set of samples.

Scan progress could be monitored via the progress bars and by checking the time elapsed against the estimated time for acquisition. Upon completion, the software would then ask the user if they would like to keep the scan queue (i.e. to repeat the scans in the case of an anomaly) or to clear the queue. This same behaviour was programmed in the case of the user aborting the acquisition for some reason, such as if the sample was not appropriately aligned in the spectrometer, or a setting was incorrect at the instrument. If desired, the scan queue could also be manually cleared by pressing the button labelled 'Clear'.

Below is a glossary of the controls with a brief description of their function:

- Group** This control served as the 'global' name for the data that will be saved and is the foremost label in the name of the saved data file.
- Region** This control served as the label for the region of the XPS spectrum being studied, eg. C1s. This was the second label in the filename and served to identify the region of data that was in each file. When preset scans were being used this box was controlled by the drop down box and received its value from the preset scan chosen.
- Preset Scans** This drop down box was activated when the check box was set to 'true'. When active it would write preset values to the 'Region', 'Energy Start', 'Energy End', 'Energy Step' and 'Dwell Time' controls. By pulling down the list the user could select from a range of common preset scans. If desired, the user could use a preset, then de-check the box and adjust the scan to suit a given sample.

---

<b>Eexec</b>	This pull down box allowed to user to inform the software of which anode was being used to ensure the correct calibration was used. It had no physical connection to the source, i.e. it did not select the anode being used.
<b>Energy Start</b>	This control would set the start energy for a scan in binding energy. It was constrained such that a user could not select a value outside of the range capable of the sweep generator, i.e. 0 – 2000 eV. Its value was also required to be greater than that of ‘Energy End’.
<b>Energy End</b>	This control would set the end energy of a scan. It was constrained in much the same way as ‘Energy Start’, excepting that it was required to be less than ‘Energy Start’.
<b>Energy Step</b>	This allowed the step size of a scan to be adjusted. It was continuously variable within a range defined by the resolution of the sweep generator. Its minimum value was thus 0.01 eV.
<b>Dwell Time</b>	This indicated how long (in seconds) the software would average at a given energy. Its minimum value was 0.1 seconds.
<b>Values</b>	This was an indicator that simply calculated how many points would be collected for the given scan settings.
<b>Samples</b>	This indicated how many measurements would be made at each point and was a function of the dwell time and the sampling rate of the data acquisition card.
<b>Scans</b>	This control defined how many scans would be collected and averaged for each region. It was limited to integer values.
<b>Scan Time</b>	This was an indicator giving an estimated scan time based on the parameters chosen by the user.
<b>Wf</b>	This was an indicator to show the current calibration factor as taken from a text file saved within the XSpect directory. It was not variable by the user.
<b>Dialog</b>	This indicator would inform the user of the current status of the software. If a scan did not validate properly it would inform the user where and why the problem was found. When scanning it would inform the user of what time the acquisition began.
<b>Validate</b>	This button committed the input scan parameters to a check by the software and if appropriate added the scan to the queue. The ‘Acquire’ button was not enabled until this button was pressed.

---

- Save** This button would save the current scan queue to a text file for loading at a later date.
- Load** This button would open a dialog box to allow the user to import a scan file.
- Clear** This button would clear the scan queue of all its current values.
- Scan Queue** This list box gave all the scans queued to be collected.
- Acquire** This button enabled data acquisition. Until at least one scan was validated this button remained unavailable to the user to prevent erroneous data collection.
- Abort** This button allowed the user to abort a current scan. A data file with any collected data would still be saved after pressing this button.
- Progress Bar** Two progress bars were programmed into the software to show the progress of the current scan (the top bar) and the progress through the number of scans selected for that region (the bottom bar). For example, if the software was halfway through the first of five scans, the top bar would show 50% progress while the bottom bar would show 20%.
- Elapsed Time** This indicator showed how much time had elapsed since the acquisition was started.

### *Scan Browser*

Upon completing the acquisition of a set of data, the scan would be added to the list box labelled 'Scan Browser'. This would collect all of the scans for a given XSpect session and list them chronologically with the most recent scan at the top of the list. All details regarding each scan would be present in this list, allowing the user to appropriately plan for upcoming data collection. When the software was not actively collecting data this list box also allowed the user to actively browse through the data sets that have already been collected by double-clicking on a given data set. The data within that file would be plotted for the user to view. This further allowed the user to appropriately plan upcoming scans, or to collect extra data if necessary.

### *Data Output*

This is where the data is plotted. The  $x$  and  $y$  axes (binding energy and intensity respectively) auto scale as the data is collected. The user can apply a cursor to the spectrum if desired, allowing the quick analysis of peak positions and relative intensities. The position of the cursor is displayed in the box on the bottom left of the plot.

---

## Appendix E.

# UNITS, SYMBOLS AND ABBREVIATIONS

The following is a list of all the units, symbols and abbreviations that have been used throughout this text. In the case of the various units used, examples of different magnitudes of these units are also given.

### E.1. Units

A	Ampere	mA, $10^{-3}$ A
Å	Angstrom, $10^{-10}$ m	
C	Coulomb	
cm <sup>-1</sup>	wavenumber	
cps	counts per second	
eV	electron volt	keV, $10^3$ eV
F	farad	pF, $10^{-12}$ F
g	gram	mg, $10^{-3}$ g
H	Henry	μH, $10^{-6}$ H
Hz	Hertz	kHz, $10^3$ Hz; MHz, $10^6$ Hz; GHz, $10^9$ Hz
J	Joule	
S/s	Samples/second	kS/s, $10^3$ S/s

K	Kelvin	
L	litre	mL, $10^{-3}$ L
m	metre	nm, $10^{-9}$ m; $\mu\text{m}$ , $10^{-6}$ m; mm, $10^{-3}$ m; cm, $10^{-2}$ m
min	minute	
N	Newton	
s	second	ms, $10^{-3}$ s
Torr	torr	mTorr, $10^{-3}$ Torr
V	volt	mV, $10^{-3}$ V; kV, $10^3$ V
W	Watt	kW, $10^3$ W
$^{\circ}\text{C}$	degrees Celcius	
$\Omega$	ohm	

## E.2. Symbols

C	capacitance
e	elementary charge ( $1.6 \times 10^{-19}$ C)
E	energy
I	current
j	current density
$k_{\text{B}}$	Boltzmann constant ( $1.381 \times 10^{-23}$ JK $^{-1}$ )
L	inductance
m	mass
n	particle density
N	particle density per unit volume
p	pressure
R	resistance
T	temperature (in units of K)
$\lambda$	mean-free-path
$\Phi$	work function
$\sigma$	cross section
v	velocity

**E.3. Abbreviations**

AISI	American Iron and Steel Institute
ANSTO	Australian Nuclear Science and Technology Organisation
APC	automatic pressure controller
CAE	constant analysis energy
CHA	concentric hemispherical analyser
CNT	carbon nanotube
CPU	central processing unit
CRR	constant retarding ratio
DAC	digital to analog converter
dc	direct current
DMF	n,n-dimethylformamide
DOS	density of states
EPU	elliptically polarised undulator
ESCA	electron spectroscopy for chemical analysis
FAT	fixed analyser transmission
FWHM	full width at half maximum
HiPco	high-pressure carbon monoxide conversion
HOPG	highly oriented pyrolytic graphite
I-V	current-voltage
ICP	inductively coupled plasma
ISM	Industrial, Scientific and Medical
JDOS	joint density of states
LP	Langmuir probe
MWCNT	multi-walled carbon nanotube
Nd:YAG	neodymium doped yttrium aluminium garnet
NEXAFS	near-edge X-ray absorption fine structure
NI	National Instruments
OML	orbital motion limit
PC	personal computer
PCI	peripheral component interconnect
PES	photoemission spectroscopy
PGM	plane grating monochromator

rf	radio frequency
RMS	root-mean-square
SWCNT	single-walled carbon nanotube
SXR	soft X-ray
TTL	transistor-transistor logic compatible logic levels
UHV	ultra-high vacuum
UNE	University of New England
USB	universal serial bus
vHS	van Hove singularity
VI	virtual instrument
XPS	X-ray photoelectron spectroscopy